RIGA TECHNICAL UNIVERSITY

Sandis Migla

# DESIGN AND EXPERIMENTAL VALIDATION OF HIGH-RESOLUTION PULSE POSITION MODULATION TECHNIQUES FOR INTEGRATED SENSING AND COMMUNICATIONS

Doctoral Thesis



RTU Press
Riga 2026

**RIGA TECHNICAL UNIVERSITY**
Faculty of Computer Science, Information Technology and Energy
Institute of Photonics, Electronics and Telecommunications

**Sandis Migla**
Doctoral Student of the Study Programme "Electronics"

# DESIGN AND EXPERIMENTAL VALIDATION OF HIGH-RESOLUTION PULSE POSITION MODULATION TECHNIQUES FOR INTEGRATED SENSING AND COMMUNICATIONS

**Doctoral Thesis**

Scientific supervisor

Professor Dr. sc. ing.
ARTŪRS ĀBOLTIŅŠ

Riga 2026

# ABSTRACT

This Thesis is devoted to the design, implementation, and experimental validation of pulse position modulation (PPM)-based communication systems, with the main objective being to develop and experimentally validate a PPM-based integrated sensing and communications (ISAC)-capable joint radar and communication system utilizing analog radio-over-fiber (ARoF) technology and a custom-built PPM modulator with a commercial time-tagger as the demodulator, which can serve as a testbed for future ultra-wideband (UWB) sensing, as well as space communication research.

The Thesis investigates various PPM schemes, generation and detection methods, and their use in ISAC. It for the first time experimentally demonstrates the use of a commercial high-precision time-tagger (event timer), which is intended for use in satellite laser ranging (SLR), as a demodulator in a PPM communication system. The design and validation of a programmable digital delay line (DDL) integrated circuit (IC)-based PPM modulator is presented.

The Thesis explores electrical and optical means of ultra-short pulse expansion for use in time-tagger-based systems. Electrical pulse expansion using low-pass filters (LPFs) and optical expansion using a fiber Bragg grating (FBG) are explored, and experimental data transmission test results are presented.

In the Thesis, a novel ARoF-based ISAC-capable pulse radar system is proposed, which features a custom-built PPM modulator employing a digital-to-time converter (DTC) and a high-accuracy time tagger as the demodulator, allowing for pulse time of arrival (ToA) measurements with a root mean square (RMS) accuracy up to 1.5 ps. The experimental results show a 5 Mbit/s data transmission along with a bit error ratio (BER) less than $5.86 \times 10^{-7}$ at a 95 % confidence level, using a PPM slot duration of 750 ps in an optical system featuring more than 40 km of single-mode optical fiber (SMF) and a simultaneous range measurement with error less than 0.86 cm. In addition to ISAC exploration, the impact of fiber-induced chromatic dispersion on the PPM waveform was explored.

The Thesis is written in English as a summary of thematically unified scientific publications. It consists of an Introduction, 3 chapters, Conclusions, 45 figures, 8 tables, and 7 appendices; the total number of pages is 82, not including appendices. The Bibliography contains 180 titles.

# ANOTĀCIJA

Šajā promocijas darbā ir aplūkota uz impulsa pozīcijas modulāciju (PPM) balstītu sakaru sistēmu projektēšana, īstenošana un eksperimentālā validācija. Darba galvenais mērķis ir projektēt un eksperimentāli validēt PPM balstītu, integrētās jušanas un komunikācijas (ISAC) funkcionalitāti nodrošinošu apvienoto radara un sakaru sistēmu, kurā izmantota analogā radio caur šķiedru (ARoF) tehnoloģija, īpaši izstrādāts PPM modulators un komerciāls laikatzīmētājs (notikumu taimeris) kā demodulators. Šāda sistēma var kalpot par eksperimentālo platformu turpmākiem ultraplatjoslas (UWB) jušanas, kā arī kosmisko sakaru pētījumiem.

Promocijas darbā ir pētītas dažādas PPM metodes, to ģenerēšana un detektēšana, kā arī to izmantošana ISAC sistēmās. Darbā pirmo reizi eksperimentāli demonstrēta komerciāla augstas precizitātes laikatzīmētāja jeb notikumu taimera, kas paredzēts satelītu lāzerlokācijai (SLR), izmantošana par demodulatoru PPM sakaru sistēmā. Tāpat izklāstīta uz programmējamas ciparu aiztures līnijas (DDL) integrālās shēmas (IC) balstīta PPM modulatora izstrāde un validācija.

Promocijas darbā ir izpētītas elektriskas un optiskas ārkārtīgi īsu impulsu paplašināšanas metodes izmantošanai uz laikatzīmētājiem balstītās sistēmās. Pētīta gan elektriska impulsu paplašināšana, izmantojot zemfrekvences filtrus (LPF), gan optiska impulsu paplašināšana, izmantojot šķiedras Brega režģi (FBG), kā arī sniegti eksperimentālo datu pārraides pārbaužu rezultāti.

Promocijas darbā ir piedāvāta jauna, ARoF balstīta un ISAC funkcionalitāti nodrošinoša impulsu radara sistēma. Tajā izmantots īpaši izstrādāts PPM modulators ar ciparu-laika pārveidotāju (DTC) un augstas precizitātes laikatzīmētājs demodulatora funkcijai, kas ļauj veikt impulsu pienākšanas laika (ToA) mērījumus ar vidējo kvadrātisko (RMS) precizitāti līdz 1,5 ps. Eksperimentālie rezultāti apliecina iespēju nodrošināt datu pārraidi ar ātrumu 5 Mbit/s un bitu kļūdu attiecību (BER), kas ir mazāka par $5.86 \times 10^{-7}$ pie 95 % ticamības līmeņa, izmantojot 750 ps ilgu PPM laika intervālu optiskajā sistēmā, kurā ietilpst vairāk nekā 40 km vienmodas optiskās šķiedras (SMF). Vienlaikus veikts arī attāluma mērījums ar kļūdu, kas mazāka par 0,86 cm. Papildus ISAC izpētei ir analizēta arī optiskās šķiedras izraisītās hromatiskās dispersijas ietekme uz PPM signāla formu.

Promocijas darbs uzrakstīts angļu valodā kā tematiski vienotu zinātnisko publikāciju kopa, tajā ir ievads, trīs nodaļas, secinājumi, 45 attēli, 8 tabulas un 7 pielikumi; kopējais lappušu skaits ir 82, neieskaitot pielikumus. Literatūras sarakstā ir 180 avoti.

# CONTENTS


INTRODUCTION . . . . . 11
Rationale . . . . . 11
Objective, Tasks, and Thesis to be Defended . . . . . 13
Scientific Novelty and Main Results . . . . . 14
The Approbation and Publications . . . . . 15
The Structure of the Thesis . . . . . 16
1 PPM SIGNAL GENERATION, DETECTION, AND MODULATOR PERFORMANCE EVALUATION . . . . . 18
1.1 Pulse Position Modulation Types . . . . . 18
1.2 PPM Signal Detection Methods . . . . . 21
1.3 Digital Discovery-Based Testbed . . . . . 23
1.4 Ultrashort Slot Duration Differential PPM . . . . . 25
1.5 Digital Delay Line-Based PPM Modulator . . . . . 28
1.6 Error Analysis and Correction Techniques . . . . . 33
1.7 Summary of the First Thesis . . . . . 39
2 ULTRASHORT PULSE EXPANSION IN PPM SYSTEMS . . . . . 40
2.1 Electrical Pulse Expansion . . . . . 40
2.2 Optical Pulse Expansion . . . . . 44
2.3 Pulse Expansion Method Experimental Validation . . . . . 45
2.4 Summary of the Second Thesis . . . . . 48
3 EVALUATION OF PPM-BASED ISAC SYSTEM PERFORMANCE WITH AROF-BASED TRANSMISSION NETWORK . . . . . 49
3.1 Design and Evaluation of 28 GHz Microwave/Optical Transmission System Utilizing PPM . . . . . 49
3.2 Design and Evaluation of ISAC-Capable PPM-Based Radar System . . . . . 54
3.3 Summary of the Third Thesis . . . . . 63
CONCLUSIONS . . . . . 64
REFERENCES . . . . . 66
ANNEXES . . . . . 83

# LIST OF FIGURES


1 Diagram of the Thesis structure, where "P" denotes the publications contained within the Thesis. . . . . 17
1.1 An example coherent PPM signal structure. . . . . 18
1.2 An example TR-PPM signal structure. . . . . 20
1.3 An example DPPM signal structure. ©2023 IEEE . . . . . 20
1.4 Comparison of data rates as a function of bits per position for DPPM and TR-PPM. ©2023 IEEE . . . . . 21
1.5 Testbed setup diagram. ©2022 IEEE . . . . . 23
1.6 Testbed software layer diagram. ©2022 IEEE . . . . . 24
1.7 BER as a function of noise RMS for pulse durations 20 ns and 40 ns. ©2022 IEEE 25
1.8 Experimental setup for DPPM transmission including PEXM. ©2023 IEEE . . 26
1.9 Pulse deviation from ideal positions. ©2023 IEEE . . . . . 27
1.10 Block diagram of the DDL-based modulator implementation. ©2024 IEEE . . 29
1.11 DPPM transmission test setup block diagram. ©2024 IEEE . . . . . 30
1.12 Modulator jitter distribution measured by the ESTT. ©2024 IEEE . . . . . 30
1.13 Experimental results for DPPM transmission tests. ©2024 IEEE . . . . . 31
1.14 Conceptual block diagram of the PPM modulator. . . . . 31
1.15 Jitter distribution test results for the developed modulator: (a) jitter distribution; (b) pulse deviation from ideal positions. . . . . 33
1.16 Jitter distribution function. ©2024 IEEE . . . . . 35
1.17 Pulse deviation from the ideal positions without calibration. ©2024 IEEE . . . 36
1.18 Pulse deviation from the ideal positions after calibration. ©2024 IEEE . . . . . 36
1.19 Simulation results without clock drift error. ©2024 IEEE . . . . . 38
1.20 Simulation results with added clock drift error. ©2024 IEEE . . . . . 38
2.1 Pulse expanded using Mini-Circuits SLP-2400 filter: (a) waveforms of the pulses; (b) normalized magnitude spectra. . . . . 41
2.2 Custom-designed filters: (a) Magnitude-Normalized, and (b) Classical, with cutoff frequencies $f_c = 1.8$ GHz. . . . . 42
2.3 Ansys HFSS simulation results and custom-designed filter measurement results for $|S_{21}|$ magnitude. . . . . 42
2.4 Ansys HFSS simulation results and custom-designed filter measurement results for group delay. . . . . 43
2.5 Block diagram of electrical pulse expansion test setup. . . . . 43
2.6 Pulse expanded using Classical custom-designed filter: (a) waveforms of the pulses; (b) normalized magnitude spectra. . . . . 43
2.7 Pulse expanded using Magnitude-Normalized custom-designed filter: (a) waveforms of the pulses; (b) normalized magnitude spectra. . . . . 43

2.8 Block diagram of optical pulse expansion test setup. . . . . 45
2.9 Pulse expanded using tunable FBG: (a) captured waveform, and (b) normalized magnitude spectra. . . . . 45
2.10 Block diagram of a PPM transmission link with an event timer for the demodulation. . . . . 46
2.11 BER versus average received optical power with optical pulse expansion with FBG module. . . . . 47
2.12 BER versus average received optical power with electrical pulse expansion with LPF. . . . . 48
3.1 Experimental setup of the PPM-based ARoF communication system. . . . . 50
3.2 Optical spectra: (a) back-to-back (B2B) connection, (b) connection with 20 km long SMF. . . . . 51
3.3 Captured pulse waveforms for B2B connection with duration: (a) 100 ps, (b) 200 ps, (c) 500 ps. . . . . 52
3.4 Captured pulse waveforms for connection with 20 km SMF, with duration: (a) 100 ps, (b) 200 ps, (c) 500 ps. . . . . 52
3.5 Data transmission experiment results for the B2B connection. . . . . 53
3.6 Data transmission experiment results for the connection with 20 km SMF. . . . 53
3.7 Setup block diagram of the ISAC-capable PPM-based radar system utilizing ARoF. 55
3.8 Bit rate as a function of bits per symbol. . . . . 57
3.9 Captured pulse waveforms: (a) electrical B2B connection, (b) optical B2B connection, (c) optical connection with 40 km SMF, (d) optical connection with 40 km SMF and DCM. . . . . 59
3.10 BER as a function of pulse duration. . . . . 60
3.11 Measured BER as a function of slot duration: (a) without Gray coding, (b) with Gray coding. . . . . 61
3.12 Range measurement errorbar plot: (a) optical B2B connection, (b) optical connection with 40 km SMF, (c) optical connection with 40 km SMF and DCM. . 62

# LIST OF TABLES

1.1 UWB Testbed Experimental Parameters ©2022 IEEE . . . . . 24
1.2 DPPM Transmission Experimental Parameters and Results ©2023 IEEE . . . . 27
1.3 Parameters of the DPPM Modulator ©2024 IEEE . . . . . 29
1.4 Fixed Parameters of the DPPM Data Transmission Tests ©2024 IEEE . . . . . 30
1.5 Simulation Parameters ©2024 IEEE . . . . . 37
2.1 TR-PPM Transmission Experiment Parameters . . . . . 46
3.1 Summary of the Main Experimental Parameters . . . . . 57
3.2 Range Measurement Results . . . . . 62

# ABBREVIATIONS

**ADC** analog-to-digital converter
**ARoF** analog radio-over-fiber
**AWG** arbitrary waveform generator
**B2B** back-to-back
**BER** bit error ratio
**BPF** bandpass filter
**C-RAN** centralized radio access network
**CCSDS** Consultative Committee for Space Data Systems
**CD** chromatic dispersion
**CDMA** code division multiple access
**CO** central office
**CS** compressed sensing
**CW** continuous wave
**D-MIMO** distributed multiple-input multiple-output
**DAC** digital-to-analog converter
**DC** direct current
**DCM** dispersion compensation module
**DDL** digital delay line
**DPPM** differential pulse position modulation
**DSO** digital storage oscilloscope
**DTC** digital-to-time converter
**ECC** error correcting code
**ED** envelope detector
**EDFA** erbium-doped fiber amplifier
**ESA** European Space Agency
**ESTT** Eventech Stream Time Tagger
**FBG** fiber Bragg grating
**FEC** forward error correction
**FMCW** frequency modulated continuous wave
**FPGA** field-programmable gate array
**FSO** free-space optical
**FWHM** full width at half maximum
**FWM** four-wave mixing
**IC** integrated circuit
**IM/DD** intensity modulation / direct detection
**IoT** Internet of Things
**IR** impulse radio

**IR-UWB** impulse radio ultra-wideband
**ISAC** integrated sensing and communications
**LDPC** low-density parity check
**LO** local oscillator
**LPF** low-pass filter
**LVTTL** low-voltage transistor–transistor logic
**MZM** Mach–Zehnder modulator
**NASA** National Aeronautics and Space Administration
**NOE** nonlinear optical effects
**OOK** on-off keying
**OPM** optical power meter
**PAM** pulse amplitude modulation
**PC** personal computer
**PCB** printed circuit board
**PD** photodetector
**PEXM** pulse expansion module
**PLC** power line communication
**PLL** phase locked loop
**PON** passive optical network
**PPM** pulse position modulation
**PRBS** pseudorandom binary sequence
**PWM** pulse width modulation
**PWPM** pulse-width and pulse position modulation
**RAU** remote antenna unit
**RF** radio frequency
**RMS** root mean square
**RoF** radio-over-fiber
**RS** Reed–Solomon
**SDK** software development kit
**SDR** software-defined radio
**SHF** super-high-frequency
**SLR** satellite laser ranging
**SMF** single-mode optical fiber
**SNR** signal-to-noise ratio
**SoC** system-on-chip
**T-PPM** Trellis-coded pulse position modulation
**TDC** time-to-digital converter
**ToA** time of arrival
**ToF** time-of-flight

**TR-PPM** transmitted reference pulse position modulation
**UAV** unmanned aerial vehicle
**UWB** ultra-wideband
**V2V** vehicle-to-vehicle
**V2X** vehicle-to-everything
**VOA** variable optical attenuator
**WGN** white Gaussian noise
**WPAN** wireless personal area network

# INTRODUCTION

## Rationale

Energy efficiency is an essential aspect of a communication system, and it is crucial in applications with limited power budgets, i.e., space communications, sensor networks, and other autonomous systems using ultra-short pulses for transmitting information, as well as applications in integrated sensing and communications (ISAC), radar technology, and distributed sensor networks [1]. Ultra-wideband (UWB) technology provides an efficient means for creating power-efficient radio and optical communication systems. Well-known impulse radio ultra-wideband (IR-UWB) modulation schemes like IEEE 802.15.4a and its derivatives [2, 3] are designed for short-range wireless personal area networks (WPANs) and provide data rates of about 0.5 Mbit/s. There is numerous research for applying IR-UWB schemes and commercial devices for vehicle-to-vehicle (V2V) communications [4], railway [5], power line communication (PLC) [6], etc. However, due to limitations in achievable bitrate, impulse radio (IR) has not gained much popularity in high-speed terrestrial and space radio links, and most of the current research is concentrated on the employment of IR-UWB for localization and ranging [7]. However, with the introduction of 6G mobile networks, where it is predicted that ISAC will be one of the core functions of the radio network, excellent capabilities of IR-UWB for localization can facilitate the use of this technology also for communication [2].

Over the last decade, the amount of transmitted data and the data transmission speed have increased significantly. The urgency of the energy consumption associated with data transmission has increased correspondingly. Nowadays, communication systems designed to perform bandwidth-intensive high-speed data transmission extensively exploit microwave and optical frequency bands, thereby becoming increasingly demanding in energy consumption. With the transition to millimeter-wave carrier frequencies, power consumption plays an increasingly important role [8]. On the other hand, the availability of the spectrum at a millimeter band and the possibility of transmitting focused beams of optical or radio signals make UWB technology an attractive choice. Moreover, UWB signals allow for very accurate time-of-flight (ToF) measurements and precise localization, which is a feature in high demand.

To provide exceptional energy efficiency, the transmitted pulses must be as short as possible, and the only limitation is the communication channel's available bandwidth and the transceiver's capabilities. In radio communications, the bandwidth is determined by the radio frequency (RF) part and antenna. Nowadays, the bandwidth of the radio communication channel can reach hundreds of GHz. Therefore, pulses with a duration of a few picoseconds, theoretically, can be used. In the case of optical transmission, the length of the pulses can be below 1 ps.

Pulse position modulation (PPM) is UWB technology where information is encoded into the absolute or relative times of the signalling pulses [9–12], allowing ultra-short pulses to transmit data, increasing the power efficiency [13]. Because in PPM, the pulse duration does not carry

any information, average power and signal-to-noise ratio (SNR) of the transmitted signal do not directly affect the bit error ratio (BER). Instead, the instantaneous power of the signalling pulses plays a vital role in determining the communication system's performance. By shortening the signalling pulses, it is possible to decrease the average power and SNR without significant impact on BER [14]. Alternatively, it is possible to decrease BER, shortening the signalling pulses and increasing the instantaneous power. The benefits in both cases come at the expense of the frequency spectrum occupation. Therefore, there is no contradiction with the well-known Shannon formula for channel capacity.

PPM allows for substantial energy savings at the cost of spectrum occupation, which makes the proposed modulation technique of particular interest to users with limited energy resources and significant signal power losses in the communication channel, for example, deep space communications, terrestrial and underwater optical wireless sensor networks, etc. It might also be important for other users, since using the proposed modulation method can reduce overall energy consumption [15, 16].

While PPM was originally employed in analog low-frequency radio and microwave systems [17], it has subsequently found use in digital communications [18–20] and microwave applications. In the optical frequency range, PPM is used in free-space optical communication and wired communications [21–23]. Furthermore, PPM is still in use in semi-analog radio control systems [24].

An overview of the benefits, disadvantages, and applications of PPM can be found in [25]. The main advantage of PPM is that it ensures higher energy efficiency than other modulation techniques and is tolerant of nonlinear distortions [26–28]. Those properties provide a solid foundation for future use of PPM, as pointed out in [17, 29, 30]. The development of the PPM technique has led to novel hybrid modulation types, such as multi-pulse-position modulation [31], where the symbol is composed of several pulses. It is worth mentioning that PPM can be combined with pulse amplitude modulation (PAM) and pulse width modulation (PWM) techniques to increase the spectral efficiency of the transmission.

PPM is also used in space communications [32–37], and study [34] shows the implementation of a PPM modem capable of using a slot width as narrow as 0.5 ns for deep space communication experiment.

UWB modulation schemes [38, 39] are also used in optical communication systems using analog radio-over-fiber (ARoF) [40–42] and free-space optical (FSO) physical layers, allowing for competitive bitrates [43, 44] suitable for space communication, Internet of Things (IoT) applications, and underwater optical communications to be achieved [45]. Such communication systems widely employ the PPM technique [46–48].

The most significant challenges for transitioning to optical communication are providing high pointing accuracy and mitigating the atmospheric turbulence impact [49, 50]. The latest developments of optical ISAC for space and ground applications are highlighted in [51]. The employment of PPM in optical communication systems is especially appealing as optical circuitry

naturally operates at large frequency bandwidths, and optical fibers typically have very low signal attenuation. At the same time, traditional on-off keying (OOK) modulation techniques have higher optical power utilization and lower sensitivity to nonlinear distortions.

ISAC systems present a wide range of perspectives in the pursuit of launching 6G networks [52, 53] which promise to focus on more than just a communication-only standpoint, but to utilize existing infrastructure for novel applications, e.g., vehicle-to-everything (V2X) communication [54, 55], IoT [56], and unmanned aerial vehicle (UAV) surveillance [57]. ISAC has proven itself as a valuable method for enhancing energy and spectrum efficiency in IR-UWB systems and is used for range and Doppler shift sensing, as well as data transmission [58–60].

PPM is also one of the modulation formats used in ISAC applications, such as simultaneous communication and LiDAR [61, 62], or radar sensing based on chirp sequences [63], with its key advantages being high energy efficiency and resilience [64]. The study [65] shows a 45.2 % energy efficiency improvement compared to OOK.

Another application of PPM is in joint radar communication [63], which is explored in this Thesis. This PPM communication system with radar capabilities can work as an ISAC system, where the PPM transceiver's receiving antenna unit acts as a radar receiver. In this implementation, the transmitted signal can be locally used for symbol synchronization of the received waveform. Depending on the received reflections and pulses from other transmitters, distances and velocities of objects and receivers can be measured.

## Objective, Tasks, and Theses to be Defended

**The objective of the Thesis**

Develop and experimentally validate a PPM-based ISAC-capable joint radar and communication system utilizing ARoF technology and a custom-built PPM modulator with a commercial time-tagger as the demodulator, which can serve as a testbed for future UWB sensing, as well as space communication research.

**The defined tasks to achieve the objective**

- Analyze and investigate the advantages and drawbacks of various PPM modulation schemes.
- Investigate and evaluate the use of a time-tagger for satellite laser ranging applications as a demodulator in PPM-based systems.
- Design, develop, and experimentally validate a digital delay line-based PPM modulator.
- Investigate error correction techniques in PPM-based systems.
- Investigate electrical and optical means of pulse expansion in systems utilizing a time tagger as the demodulator.
- Design, develop, and test a fiber optic-based PPM communication system.

- Develop and validate the concept of PPM-based integrated sensing and communications in a radar system.
- Investigate radio-over-fiber-based transmission of PPM signals.
- Investigate and evaluate the impact of various lengths of optical fiber in PPM data transmission and sensing systems.

**Theses to be defended**

1. A PPM modulator implemented using programmable gate and multiplexer-based digital delay line (DDL) integrated circuit (IC) technology is capable of achieving PPM pulse sequence generation with root mean square (RMS) timing jitter below 10 ps.
2. In time tagger-based PPM systems, a pulse with duration 50–100 ps can be expanded passively by electrical and optical means to more than 2 times its original full width at half maximum (FWHM) duration while preserving the pulse's waveform shape enough for stable detection.
3. In optical PPM-based ISAC systems, a BER below $1 \times 10^{-6}$ along with a sensing accuracy below 5 cm at a range of at least 4 m with optical transmission distance exceeding 40 km can be achieved by using high-order PPM and a time tagger for satellite laser ranging (SLR) applications as the receiver.

## Scientific Novelty and Main Results

**The main scientific contributions of this Thesis**

1. Experimentally demonstrated the concept of using digital delay line integrated circuits for high-order high-precision PPM pulse sequence generation.
2. Experimentally proved the concept of using a high-precision time tagger for satellite laser ranging applications to achieve high-order PPM signal demodulation.
3. Experimentally proven electrical and optical pulse stretching techniques for use in PPM communication systems.
4. For the first time experimentally demonstrated joint radar sensing and communications using PPM in a system employing analog radio-over-fiber technology with long fiber spans.

**The main results of the presented Thesis have been utilized in three research projects**

1. EU Recovery and Resilience Facility Project No. 5.2.1.1.i.0/2/24/I/CFLA/003 academic career doctoral grant (ID 1008).
2. Latvian Council of Science grant No. lzp-2021/1-0475, "Picosecond-resolution pulse position modulation for beyond-the-limits energy efficiency of communications."
3. EU Cohesion Policy Fund Project No. 1.1.1.8/1/24/I/007 academic career doctoral grant (ID 8110).

## The Approbation and Publications

The main results presented in this Thesis have been published in three peer-reviewed international journals ranking in the top 25th percentile (Q1) by citation index, as well as four peer-reviewed international conference proceedings.

**Dissemination in international conferences**

1. 2022 IEEE 2nd Ukrainian Microwave Week (UkrMW), November 14–18, 2022, Kharkiv, Ukraine.
2. 2023 IEEE 10th Jubilee Workshop on Advances in Information, Electronic and Electrical Engineering (AIEEE), April 27–29, 2023, Vilnius, Lithuania.
3. 2024 Joint European Conference on Networks and Communications & 6G Summit (EuCNC/6G Summit), June 3–6, 2024, Antwerp, Belgium.
4. 2024 IEEE International Conference on Microwaves, Communications, Antennas, Biomedical Engineering and Electronic Systems (COMCAS), July 9–11, 2024, Tel Aviv, Israel.

**Publications in conference proceedings**

**Annex 1**. Migla, S., Selis, O., Sics, P. E., Pudzs, M., Zeltins, M., and Aboltins, A. "A Design of UWB Communication Testbed with Event Timer-based PPM Demodulator." *2022 IEEE 2nd Ukrainian Microwave Week (UkrMW)*. 2022, pp. 691–694. DOI: 10.1109/UkrMW58013.2022.10037100

**Annex 2**. Selis, O., Migla, S., Sics, P. E., Zeltins, M., Spolitis, S., and Aboltins, A. "Demonstration of 50 ps Per-Position Differential Pulse Position Modulation Data Transmission." *2023 IEEE 10th Jubilee Workshop on Advances in Information, Electronic and Electrical Engineering (AIEEE)*. 2023, pp. 1–4. DOI: 10.1109/AIEEE58915.2023.10134802

**Annex 3**. Sics, P. E., Tihomorskis, N., Migla, S., Ratners, J., Kurtenoks, V., and Aboltins, A. "Implementation of Reconfigurable 149Mbps TDC-Based PPM Transceiver." *2024 Joint European Conference on Networks and Communications & 6G Summit (EuCNC/6G Summit)*. 2024, pp. 706–710. DOI: 10.1109/EuCNC/6GSummit60053.2024.10597124

**Annex 4**. Migla, S., Selis, O., Sics, P. E., and Aboltins, A. "Error Analysis and Correction Techniques for PPM Communication Links with Jitter and Clock Drift." *2024 IEEE International Conference on Microwaves, Communications, Antennas, Biomedical Engineering and Electronic Systems (COMCAS)*. 2024, pp. 1–4. DOI: 10.1109/COMCAS58210.2024.10666259

**Publications in scientific journals**

**Annex 5**. Aboltins, A., Solovjova, T., Semenako, J., Kusnins, R., Migla, S., Sics, P. E., Selis, O., Tihomorskis, N., Prigunovs, D., Ostrovskis, A., and Spolitis, S. "Passive Electrical and Optical Methods of Ultra-Short Pulse Expansion for Event Timer-Based TDC in PPM Receiver." *Electronics* 12.22 (2023). DOI: 10.3390/electronics12224634

**Annex 6**. Migla, S., Rubuls, K., Tihomorskis, N., Salgals, T., Ozolins, O., Bobrovs, V., Spolitis, S., and Aboltins, A. "Ultra-Wideband Analog Radio-over-Fiber Communication System Employing Pulse-Position Modulation." *Applied Sciences* 15.8 (2025). DOI: 10.3390/app15084222

**Annex 7**. Migla, S., Tihomorskis, N., Rubuls, K., Cirjulina, D., Murans, I., Kurtenoks, V., Braunfelds, J., Spolitis, S., Ozolins, O., Vovchuk, D., Salgals, T., Ginzburg, P., Bobrovs, V., and Aboltins, A. "Demonstration of Integrated Sensing and Communications in an ARoF-Based Radar System Utilizing Pulse Position Modulation." *IEEE Access* 14 (2026), pp. 76251–76264. DOI: 10.1109/ACCESS.2026.3693952

## The Structure of the Thesis

The Thesis is written as a summary of thematically unified scientific publications. Each chapter is devoted to its corresponding thesis.

Chapter 1 introduces the used PPM types and detection methods. A Digital Discovery-based testbed is presented, which serves as the first stepping stone in this research. This chapter introduces the concept of using a commercial time-tagger (also known as an event timer) for SLR applications as a PPM demodulator. The main focus point of this chapter is the design and performance evaluation of a digital delay line integrated circuit-based PPM modulator. The chapter is concluded with systematic error and jitter mitigation techniques in PPM communication systems.

Chapter 2 is devoted to the electrical and optical pulse expansion techniques in PPM communication systems. Custom-built filter-based and fiber Bragg grating (FBG)-based optical pulse expansion setups are presented. This chapter is concluded with the experimental evaluation of both methods in a fiber optic-based PPM communication system by transmitting pseudorandom binary sequence (PRBS).

Chapter 3 introduces ARoF as a viable method for RF-modulated PPM signal transmission over long distances. An experimental setup for an ARoF-based communication system using PPM is presented. The chapter is concluded with an experimental demonstration of ISAC using PPM in an ARoF-based radar system, presenting BER measurements and sensing distance accuracy measurements.

Finally, the Thesis is concluded by summarizing the main findings presented in the men-

tioned chapters, conclusions drawn about each thesis to be proved, and discussing future prospects of UWB-based ISAC research.

The overview of publications contained within this Thesis and their relationships with chapters and research objectives is shown in Fig. 1.

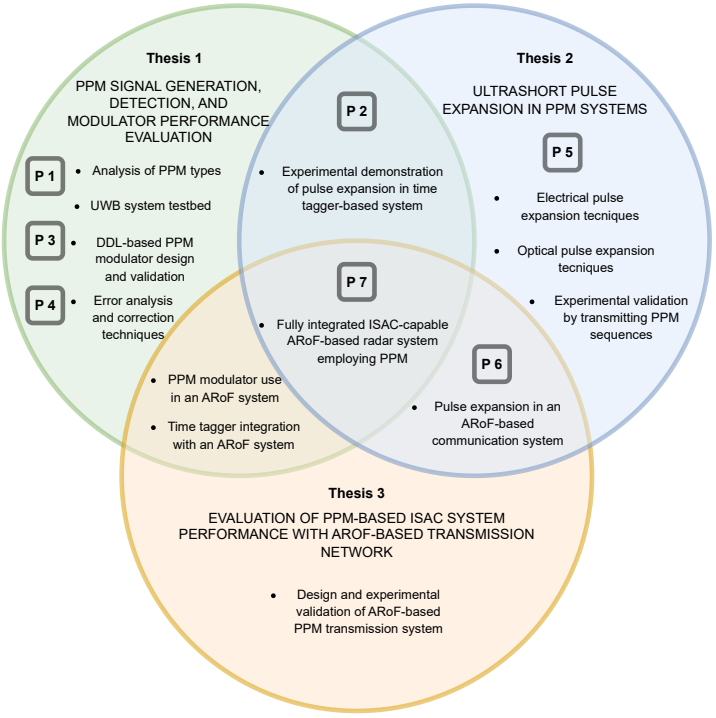



Fig. 1. Diagram of the Thesis structure, where “P” denotes the publications contained within the Thesis.

# 1 PPM SIGNAL GENERATION, DETECTION, AND MODULATOR PERFORMANCE EVALUATION

## 1.1 Pulse Position Modulation Types

There are many types of pulse position modulation (PPM) schemes, such as coherent PPM, differential PPM, transmitted reference pulse position modulation (TR-PPM) [66, 67], variable PPM [68], overlap PPM and more [69]. In this Thesis, the following sections focus on coherent PPM, TR-PPM and differential PPM.

### Coherent PPM

This Subsection focuses on the coherent PPM following the Consultative Committee for Space Data Systems (CCSDS) recommended standard 142.0-B-1 "Optical communications coding and synchronization" [70]. An example signal structure is shown in Fig. 1.1.

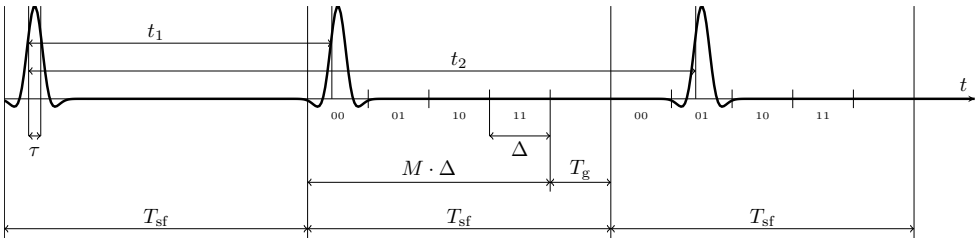



Fig. 1.1. An example coherent PPM signal structure.

In coherent PPM, the sequence of pulses, called a PPM transfer frame, consists of a start pulse, with respect to which all time tags are calculated, and $N$ PPM subframes that contain the data pulses. In a PPM symbol, which is part of the subframe, the pulse can be located in one of $M$ time slots with the slot duration $\Delta$. The number of time slots $M$ is determined by how many bits are encoded in a single PPM symbol, $M = 2^b$, where $b$ is the number of bits per symbol. The total symbol duration is $M \cdot \Delta$. Together with the guard slot duration $T_g$, the symbol makes up the subframe with the duration [64]

$$T_{sf} = M \cdot \Delta + T_g \,, \tag{1.1}$$

where $T_{sf}$ is the subframe duration, $M$ is modulation order, $\Delta$ is the slot duration and, $T_g$ is the guard slot duration.

The guard slot compensates for the hardware's inherent dead time, encompassing signal propagation delays and the duration required for processing, as explored in Section 1.2. The guard slot is added at the end of the subframe as defined in [70] to preserve a clear subframe start at the "0" position. It should be noted that in PPM-based integrated sensing and communications (ISAC) systems, the guard slot is not intended to prevent the reflected echo overlap, as

the received signal's relative time scale is calculated with respect to its start pulse. If multipath propagation is considered, then this aspect becomes relevant, as a delayed replica of the pulse can appear in the next subframe, causing bit errors and erroneous distance calculation.

The time tags for each pulse in the sequence [70] with respect to the PPM transfer frame start pulse can be calculated as

$$t_{\mathrm{k}} = k \cdot T_{\mathrm{sf}} + K \cdot \Delta \,, \tag{1.2}$$

where $t_{\mathrm{k}}$ is the time tag with the index $k$ (1 to $N$) and $K$ is the encoded decimal data (0 to $M-1$) in the subframe.

For this modulation format, the maximum achievable continuous data transfer speed can be calculated by Equation (1.3):

$$R_{\mathrm{b}} = \frac{N \cdot \log_2 M}{(N+1) \cdot T_{\mathrm{sf}} + T_{\mathrm{break}}} \,, \tag{1.3}$$

where $R_{\mathrm{b}}$ is the bit rate, $M$ is modulation order, $N$ is the number of symbols in the PPM transfer frame, and $T_{\mathrm{break}}$ is the time between subsequent PPM transfer frames.

By decreasing the time bins' width $\Delta$, more data in PPM can be allocated, increasing data transmission speed. It is worth noting that although in some PPM applications, a simplified scheme with $\Delta = \tau$ is used, the information is carried solely by the timing of the pulses' rising edges. Hence, the pulse duration $\Delta$ is not critical from an information-carrying perspective. However, pulse duration affects both the link's energy efficiency and the signal's frequency bandwidth. Consequently, the narrower pulses create more energy-efficient transmission, whereas longer pulses require smaller bandwidth and are easier to detect.

A custom-built PPM modulator using this technique is presented in Section 1.5, and a full ISAC-capable system is presented in Section 3.2.

#### Transmitted Reference PPM

This subsection introduces TR-PPM, which uses the same basic principle as described above, and additionally includes a reference pulse at the beginning of each frame that helps to calculate the value of the received symbols. The first time bin starts after $\mathrm{M} \cdot \Delta + T_{\mathrm{g}}$ seconds from the reference pulse. An example of a TR-PPM frame is shown in Fig. 1.2.

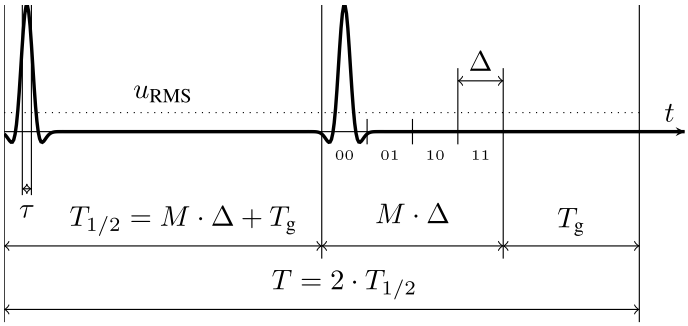



Fig. 1.2. An example TR-PPM signal structure.

The main advantage of TR-PPM is its stability, especially in long-distance transmission, as the time measurement is done between each reference and data pulse pair in the sequence; however, this comes at an efficiency cost, as twice as many pulses are needed to encode the same amount of data.

**Differential PPM**

This subsection is focused on differential pulse position modulation (DPPM) – one of the most efficient and simple PPM modulation types. It provides higher channel capacity compared to fixed-length symbol modulation types [14]. DPPM is also more robust against disturbance caused by atmospheric turbulence and the signal-to-noise ratio (SNR) level when using DPPM was lower at the same bit error ratio (BER) values than in the case of classical PPM [71]. Furthermore, the error rate of DPPM can be decreased using soft decision encoding [72, 73].

Using DPPM, a data pulse can be transmitted during every symbol in one of the slots. The difference between the two pulse position techniques is that coherent PPM and TR-PPM send symbols of fixed length, whereas DPPM cuts the part of the symbol that follows the pulse. Therefore, each new symbol in DPPM starts immediately after the data pulse, which, at the same time, is the reference pulse for the next symbol. This improvement dramatically increases the amount of information that can be transmitted. An example DPPM signal structure is shown in Fig. 1.3.

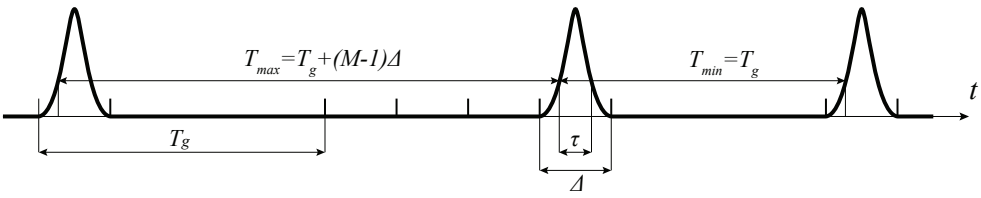



Fig. 1.3. An example DPPM signal structure. ©2023 IEEE

The mean data rate of DPPM can be calculated using the formula (1.4), considering that ***M***

positions are used. $T_{\text{mean}}$ represents the mean symbol duration in the DPPM sequence:

$$R_{\text{b}} = \frac{log_2 M}{T_{\text{mean}}} = \frac{2log_2 M}{\Delta(M+1)}. \tag{1.4}$$

The guard interval significantly increases the time between the pulses, especially if the time bin $\Delta$ is substantially smaller than $T_g$. The data rate of the DPPM signal when the guard interval $T_g$ is applied to it can be calculated using Formula (1.5):

$$R_{\text{b,guard}} = \frac{2log_2 M}{2T_g + \Delta(M-1)}. \tag{1.5}$$

The number of data bits within each pulse is determined by the number of time bins utilized in the modulation scheme. For instance, given a pulse coded with $N$ bits, there are $M = 2^N$ possible time bins where the pulse can be positioned within the symbol.

Fig. 1.4 shows theoretically achievable average data rates for DPPM and TR-PPM. To achieve the highest data rate using DPPM, 10 bits per position should be considered in the case of 50 ns guard interval and a slot duration of 50 ps. The achievable data rate for TR-PPM is twice as small as for DPPM, and the optimal number of bits is nine. This is because TR-PPM symbols, on average, are twice as long as in the case of DPPM.

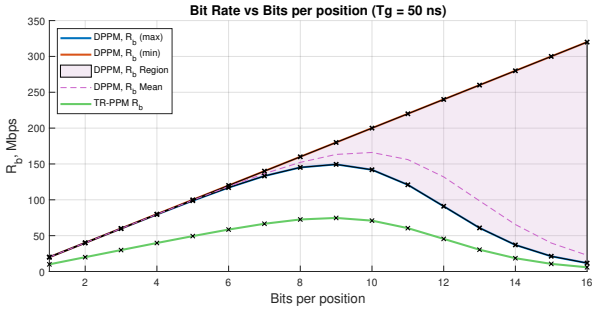



Fig. 1.4. Comparison of data rates as a function of bits per position for DPPM and TR-PPM. ©2023 IEEE

## 1.2 PPM Signal Detection Methods

Several methods for PPM signal demodulation have been proposed [17, 23, 30, 63]. Early PPM demodulators employed energy-based detection [74, 75]. However, the most commonly used technique in low-speed applications is first to convert PPM to pulse width modulation (PWM), then use an integrator circuit to produce an approximation of the signal.

Correlation receivers are one of the most common approaches to the demodulation of ultra-wideband (UWB) radio frequency (RF) signals [76–78], which is especially attractive in the case of non-coherent TR-PPM [79]. In the RAKE receivers, which are widely used in UWB and code division multiple access (CDMA) systems [80], demodulation is performed by correlation

with multiple copies of the locally generated template. Designing a template signal is difficult as linear and nonlinear distortions corrupt the received signal. Moreover, the correlation receiver has to track and record the energy of as many replicas as possible for better performance [81]. Non-coherent UWB modulation schemes [81, 82], which involve transmitted reference pulses along with an information-carrying UWB pulse train [76] allow overcoming those issues. In TR-PPM, the transmitter sends a pair of pulses, i.e., a reference pulse at the beginning of the symbol and a data pulse located at a certain time slot. The non-coherent receiver uses the first pulse as a reference for demodulation and recovering the information encoded in the second pulse time offset. Since both pulses will be distorted the same way, the matching process is much simpler, and strict timing synchronization between the transmitter and receiver is unnecessary.

Detection of high-speed PPM signals with a large number of symbol positions using digital correlation-based methods becomes impractical due to computational complexity and speed requirements. Moreover, high-accuracy timing is necessary for distinguishing pulse positions and symbol timing, in the case of coherent demodulation.

Other, more advanced approaches have been developed, including iterative demodulation methods [83] and even chaotic synchronization-based techniques [84]. Advanced methods like compressed sensing (CS) theory can be employed for the demodulation of PPM signals using low-speed analog-to-digital converter (ADC) [85].

One of the most elegant ways to implement a highly efficient PPM demodulator is to employ a time-to-digital converter (TDC) [14, 86, 87]. TDCs are employed in event timers, also known as time taggers, which are widely used in time measurement applications where precise time measurements, and therefore distance measurements, are crucial, particularly for time-of-flight (ToF) measurements [88], such as satellite laser ranging (SLR) [89, 90], LiDAR, and ISAC applications. This method is based on the idea of direct time measurement using a time tagger [91–93]. The employment of accurate event timers allows the use of a high number of positions in the symbol, achieving a very low duty cycle and exceptional energy efficiency. However, two major challenges exist when using an event timer to demodulate the PPM signal. Using a time tagger imposes specific requirements concerning the minimal pulse duration at the input of the timer. If the pulse duration is too small, the event timer will not detect the event (incoming pulse). Additionally, time measurement by the event timers requires a relatively large guard time, during which the timer estimates the time and does not react to the incoming signal. This time, sometimes called “dead time,” cannot be efficiently employed for data transfer and affects the achievable bitrate.

In this Thesis, two time taggers (event timers) have been utilized. Eventech A033-ET and Eventech Stream Time Tagger (ESTT) 7 Series. A033-ET can detect events with single-shot root mean square (RMS) resolution better than 5 ps combined with a high measurement rate of up to 20 million events in a burst and featuring a dead time of 50 ns. The incoming events are registered on the rising edge of a low-voltage transistor–transistor logic (LVTTL) signal. This timer can be used for the demodulation of high-order digital PPM signals. The first attempt to

use this timer for PPM was made in 2015 [94].

The ESTT features two inputs, thereby enabling ToF and range calculations for ISAC. The event is triggered by a programmatically set voltage threshold value in the range of −2 V to 3 V with a step of 1.2 mV. Different threshold values can be set for the two inputs, allowing the use of signals with varying amplitudes. ESTT features a single-shot RMS accuracy of 1.5 ps and has a dead time of 40 ns, which was the key limiting factor when selecting the PPM parameters, especially the subframe duration $T_{sf}$. As the ESTT triggers on the rising edge of the pulse, it is critical to have an edge with as short a rise time as possible, but the pulse duration is not crucial, as long as it is above the minimum required duration of 150 ps.

In the presented studies, the PPM demodulation and range data processing were performed in real-time on the personal computer (PC) using custom software. The time tags from the two channels were saved as separate files on the PC, allowing for later processing and range estimation. Additionally, the software enabled saving of the received data for BER calculation.

## 1.3 Digital Discovery-Based Testbed

This section presents the first developed software framework and testbed for exploring PPM communication using short electrical pulses with a duration between 20 ns and 40 ns, employing a high-accuracy event timer for the PPM demodulation.

Experiment hardware consists of a Digital Discovery device, with additional circuitry at digital output pins to provide sufficient signal voltage to ensure that the event timer will receive the incoming signal, an Eventech A033-ET event timer, and a source of white Gaussian noise (WGN). The signal from the Digital Discovery is added to the signal of the WGN generator and sent to the event timer's input as shown in Fig. 1.5.

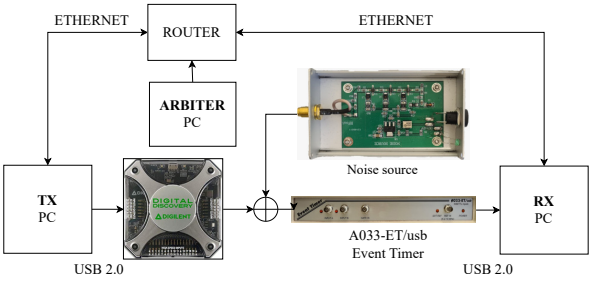



Fig. 1.5. Testbed setup diagram. ©2022 IEEE

A Python script performs communication with the Digital Discovery device using WaveForms software development kit (SDK) and the A033-ET event timer using TCP/IP messages. The software diagram is presented in Fig. 1.6.

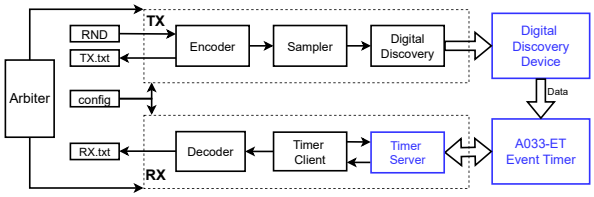



Fig. 1.6. Testbed software layer diagram. ©2022 IEEE

Generally, slot duration $\Delta$ and pulse duration $\tau$ are independent; as in PPM, the duration of the pulse does not play any role in the signaling; therefore, to save energy, pulses must be as short as possible. Since the maximum sample rate of the Digital Discovery is 100 MSa/s and the analog bandwidth is about 50 MHz, the minimal time slot $\Delta$ is 10 ns and the duration of the generated pulse $\tau$ is 20 ns. In the presented experiments, a simplified scheme where $\delta = \tau$, i.e., the pulse duration is equal to the time slot for one position, was employed.

Verification of the testbed has been performed using transmission of pseudorandom binary sequence (PRBS), encoded using the TR-PPM scheme. Pulse duration and duration of the time slot are limited by the sample rate of the Digital Discovery. The number of symbols in the packet was selected based on the event timer's limitations. It can detect 64 pulses at a time, so no more than 31 symbols can be sent, considering the empty symbol with one pulse and payload symbols with two pulses. The Guard time was 40 ns. The additive WGN has been controlled manually with 10 mV RMS step. The summary of experimental parameters is shown in Table 1.1, and the results are presented in Fig. 1.7.

Table 1.1

UWB Testbed Experimental Parameters ©2022 IEEE

| **Parameter** | **Parameter symbol** | **Parameter value** |
|---|---|---|
| Number of positions | $M$ | 32 |
| Pulse duration | $\tau$ | 20 ns (40 ns) |
| Slot duration | $\Delta$ | 20 ns (40 ns) |
| Symbols per packet | $N$ | 31 |
| Guard time | $T_g$ | 40 ns (80ns) |

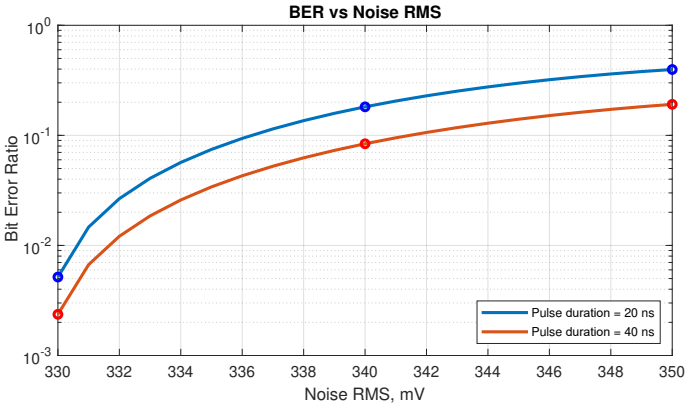



Fig. 1.7. BER as a function of noise RMS for pulse durations 20 ns and 40 ns. ©2022 IEEE

The first errors appear at 330 mV RMS and continue to rise as the noise intensity increases. The use of 40 ns pulses leads to a lower bit-error rate than the 20 ns pulse sequence. With 20 ns pulses the signal RMS is approximately 730 mV, whereas with 40 ns it is 980 mV. Moreover, the signal waveform is imperfect and oscillates.

The jitter of the pulses increases as SNR of the signal decreases. At SNR = 13 dB it is 1.1 ns, and at SNR = 7 dB it is 2.6 ns. The main reason why the BER starts to rise is that the timer has a threshold voltage of around 1.2 V at which it reacts to incoming pulses. The WGN peaks can already reach the threshold voltage and cause a false timer reaction and false time tags. In ideal conditions, the RMS of WGN might not exceed 330 mV. In this modulation scheme, the software can filter false time tags because the time between the pulses can not be less than guard time $T_g$. Because of the smaller signal RMS of the Digital Discovery's output when using narrower pulses, the 20 ns pulses will require higher SNR for achieving certain BER.

The jitter of the rising edge does not exceed 2.8 ns. Therefore, the jitter does not affect the timer's decisions and does not decrease BER in the presented setup.

The limitation for the employment of shorter pulses is at the transmitter side. The maximum sample rate of the Digital Discovery, which is used as digital-to-time converter (DTC) in the transmitter, is 100 MSa/s. For the use of shorter pulses and, hence, more and shorter PPM slots, it is necessary to use a more advanced modulator solution.

The presented testbed served as an important stepping stone in PPM research, and **the full publication can be seen in Annex 1 ©2022 IEEE.**

## 1.4 Ultrashort Slot Duration Differential PPM

This section presents DPPM modulation scheme and demonstrates possibilities for demodulation of DPPM using the highly accurate A033-ET event timer, demonstrating data transmission using a high-order DPPM signal in a laboratory environment.

The DPPM signal generation is achieved using the Keysight M8195A arbitrary waveform

generator (AWG), featuring a 25 GHz analog bandwidth and a 65 GSa/s sampling rate, which is a significant upgrade from the Digital Discovery device presented in the previous section. The AWG allows for the PPM duration to be as short as 100 ps, significantly increasing the energy efficiency in the transmission channel. The A033-ET event timer served as the PPM demodulator. Since the event timer cannot detect such short pulses, a custom pulse expansion module (PEXM) was employed that contains the following hardware in the following order:

1) 6 dB RF attenuator to remove possible back-reflection from custom low-pass filter (LPF);
2) In-house manufactured custom LPF [95];
3) VLFX-1300+ commercial LPF;
4) 30 dB RF amplifier with bandwidth 30-4000 MHz;
5) SHF BT45 broadband bias tee with bandwidth 20 kHz - 45 GHz.

The full experimental setup, including the PEXM, is shown in Fig. 1.8.

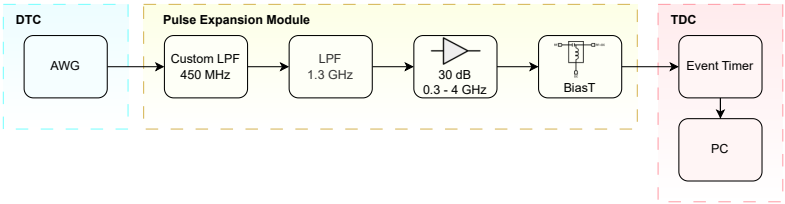



Fig. 1.8. Experimental setup for DPPM transmission including PEXM. ©2023 IEEE

The software framework, presented in Section 1.3, was employed. The event timer received the signal sequence with DPPM pulses at specific absolute times (also known as time tags). From each time tag, guard time $T_g$ was subtracted, and the resulting time was divided by slot duration $\Delta$, obtaining relative time tags converted to the pulse positions. Finally, the positions were reversed to binary data.

Experimental validation was performed by transmitting PRBS with parameters shown in Table 1.2. Each experiment consisted of one transmitted data packet of 63 data pulses. To ensure that a valid output signal was obtained, a periodic sequence of 100 ps pulses was transmitted before data transmission. Each experiment file was loaded in AWG individually. At the same time, the event timer was being configured for event measurement. The AWG generated pulse was expanded by the PEXM to about 750 ps, which is an optimal and valid signal width for event detection. A 300 mV direct current (DC) level to all signals is applied to ensure optimal signal level for the event timer because the event timer uses LVTTL signal levels, but the PEXM output voltage is 1500 mV peak-to-peak, i.e., slightly above the threshold level. Signal parameters after the pulse expansion module were as follows: $V_{\mathrm{pp}} = 1500\mathrm{mV}$, $V_{\mathrm{DC}} = 300\mathrm{mV}$, $\tau = 750\mathrm{ps}$, $t_{\mathrm{rise}} = 350\mathrm{ps}$.

Table 1.2 summarizes the results of decoded DPPM test signals where BER was calculated

for each test. The test did not detect any bit errors at slot duration $\Delta = 200$ ps. At 100 ps and 50 ps the error rate increases significantly $1.781 \cdot 10^{-2}$ and $7.935 \cdot 10^{-4}$, accordingly. Fig. 1.9 shows how each detected pulse is shifted from the expected time position. The shaded region denotes the time bin where the pulse should be registered. It shows that the maximum offset is less than one 50 ps position bin.

Table 1.2

DPPM Transmission Experimental Parameters and Results ©2023 IEEE

| **Test nr.** | **$\tau$, ps** | **$\Delta$, ps** | **M** | **$T_g$, ns** | **Total bits** | **BER** |
|---|---|---|---|---|---|---|
| 1 | 100 | 200 | 128 | 50 | 4410 | 0 |
| 2 | 100 | 100 | 256 | 50 | 5041 | $7.935 \cdot 10^{-4}$ |
| 3 | 100 | 50 | 512 | 50 | 5670 | $1.781 \cdot 10^{-2}$ |

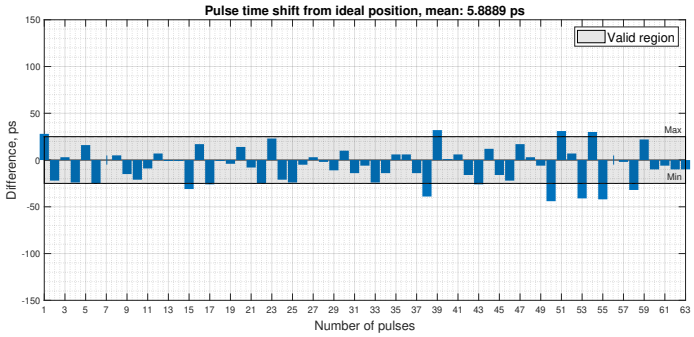



Fig. 1.9. Pulse deviation from ideal positions. ©2023 IEEE

The implemented DPPM transmission test setup has demonstrated excellent results, as indicated by the low bit error rate observed. Despite the jitter and systematic timing error, the test system could accurately detect the pulses with an error rate of no more than one position.

The main contributing factor to the test's success was the robust design of the A033-ET event timer, which could effectively detect events even in the presence of a noisy signal and an insufficiently steep rising edge of the expanded pulses. However, it should be noted that the signal amplitude could also impact the accuracy of the detection process, as the time walk may occur at different pulse amplitudes. The achieved data rate in the case of 50 ps slot duration was about 160 Mbit/s, which is an improvement compared to [14] even considering relatively high BER. Nevertheless, the data rate was not the most critical aspect of these tests, as the goal was to demonstrate DPPM at the narrowest slot durations possible.

**Full description can be seen in Annex 2 ©2023 IEEE.**

## 1.5 Digital Delay Line-Based PPM Modulator

Development of a more capable means of PPM generation was the logical next step in the presented research. This section presents the design and validation of custom-built PPM modulators based on digital delay line (DDL) technology, which offer advantages over widely used field-programmable gate arrays (FPGAs) for PPM signal generation [96], and other hardware-based pulse generators [3], which are limited in available PPM slot width and accuracy.

### DPPM Modulator

This subsection is focused on the design, implementation, and testing of a modulator intended for DPPM applications. The novelty of the proposed modulator lies in the implementation of a DDL-based DTC for the modulation of the PPM signal. The employment of this technology allows the integration of software-defined radio (SDR) concepts [97, 98] to UWB, which, in turn, allows to easily switch between different PPM modulation formats and bandwidths. Typical SDR bottleneck is the interface between ADC/digital-to-analog converter (DAC) and the computer. The proposed system must be capable of streaming the time tags at very high speed between the computer running the software and the hardware performing the DTC functions.

A custom printed circuit board (PCB) has been developed for generating PPM signals, which is controlled by a PC. The main components of the modulator are the MC100EP196B high-precision programmable DDL, SI5394J-A phase locked loop (PLL) jitter attenuator and Cyclone IV FPGA system-on-chip (SoC). The jitter attenuator features an ultra-low jitter of 69 fs and a frequency output range of up to 1028 MHz and delivers a 0.09 ps RMS phase jitter performance with a 0 ppm error.

The Altera Cyclone IV FPGA SoC controls and commands the modulator. FPGA was chosen because of its high-speed digital logic capabilities. It interprets the commands and serves as an interface between the PC and the rest of the modulator board. The connection to the PC is achieved using USB 3.0. The FT601Q USB 3.0 Super-Speed to 32-bit Sync FIFO was selected for the interface due to its high speed (66 MHz) and 32-bit bus width. The software architecture of the FPGA SoC part of the modulator is implemented as a Nios II virtual processor with custom IO procedures written in VHDL. Employment of the Nios soft microprocessor allows part of the software modules to be developed in C++.

The MC100EP196B high-precision programmable DDL has a maximum time resolution of 10 ps and a programmable range of 10450 ps when using all data inputs (D0 to D9). The total delay range of the DTC is 2.2 ns to 12.4 ns, including the minimum fixed delay.

For each PPM symbol, a pulse is generated based on the 10 MHz reference clock, which can be delayed in 10 ns increments (coarse delay) and also delayed by the DDLs to achieve fine control over the pulse location in time (precision delay).

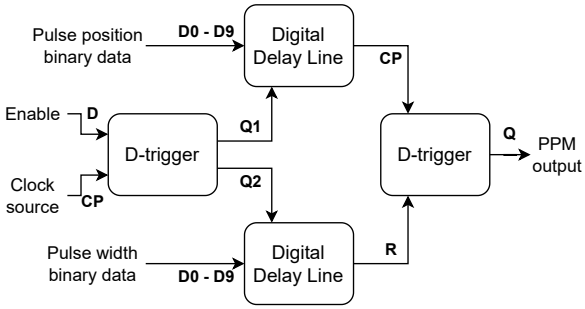



Fig. 1.10. Block diagram of the DDL-based modulator implementation. ©2024 IEEE

The pulse duration can be adjusted by using a second DDL in parallel with the DDL used to precisely adjust pulse location in time. The delay value set in the second DDL is the sum of the delay required in the PPM symbol and the desired pulse duration. The second DDL output is used to reset a D-trigger, generating a short pulse with the required width. The block diagram of this arrangement is shown in Fig. 1.10, and the summary of the modulator's parameters is presented in Table 1.3.

Table 1.3

Parameters of the DPPM Modulator ©2024 IEEE

| **Parameter** | **Value** |
|---|---|
| DTC granularity (minimum step) | 10 ps |
| Maximum precision delay | 10450 ps |
| Bits for precision delay | 10 |
| Maximal coarse delay | 655.35 µs |
| Bits for coarse delay | 16 |
| Maximal number of pulses per second | $10^6$ |
| Minimal pulse repetition interval | 10 ns |

The testing of the modulator was carried out by directly connecting its output to the ESTT 7 Series event timer. The block diagram of the connection scenario and full software stacks is shown in Fig. 1.11.

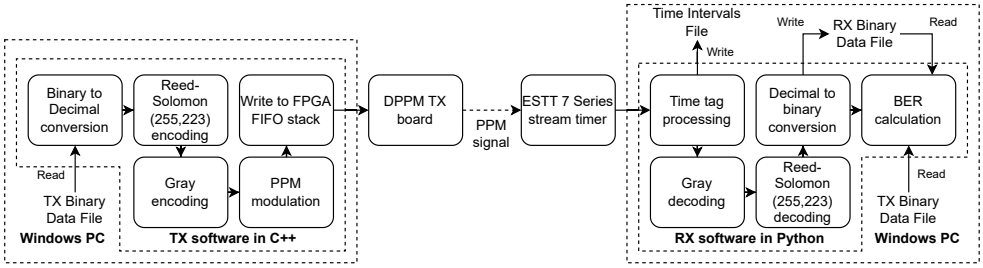



Fig. 1.11. DPPM transmission test setup block diagram. ©2024 IEEE

The jitter distribution shown in Fig. 1.12 was obtained by analyzing the deviations of measured pulse positions from expected ones. The resulting RMS of pulse position deviation was 18.9 ps. Considering that the jitter distribution is close to normal, 99.7 % of deviations fall within the $3\sigma$ range, i.e., 56.7 ps.

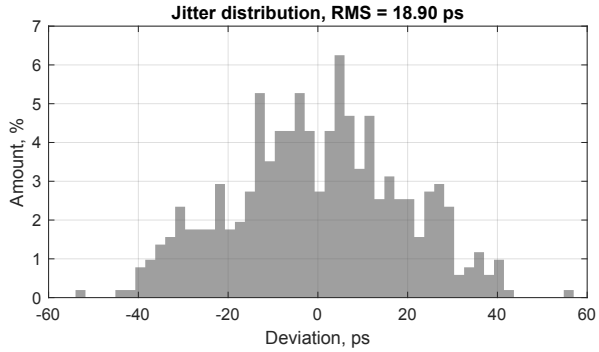



Fig. 1.12. Modulator jitter distribution measured by the ESTT. ©2024 IEEE

For the data transmission tests, a PRBS was used with a length of one million bits and encoded using DPPM. The impact of different time bin duration values and number of positions with various forward error correction (FEC) codes has been explored, and BER calculated for each case. The fixed experimental parameters are shown in Table 1.4 and the experimental results in Fig. 1.13.

Table 1.4

Fixed Parameters of the DPPM Data Transmission Tests ©2024 IEEE

| Parameter | Description | Value |
|---|---|---|
| Modulation scheme | Modulation scheme | DPPM |
| Bit count | Number of bits sent | $10^6$ |
| $t_g$ | Guard time, ns | 50 |
| $\tau$ | Pulse duration, ps | 150 |
| x | Bit pattern | Pseudo-random |

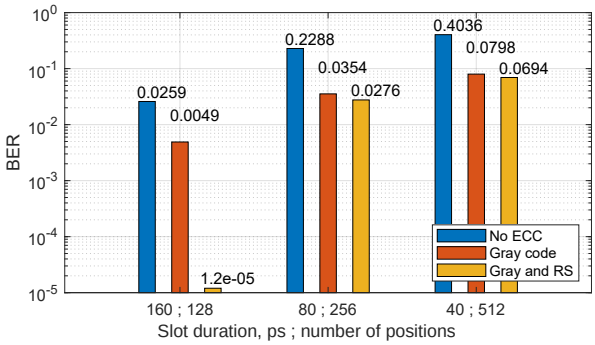



Fig. 1.13. Experimental results for DPPM transmission tests. ©2024 IEEE

The results show that the designed modulator provides real-time data communication, and the implemented error correction algorithms are working as intended. The most significant impact on the BER is achieved using the Gray code, further enhanced by the Reed–Solomon (RS) error correction algorithm. When combined, these error correction schemes provide a BER of $1.2 \cdot 10^{-5}$ at a slot duration of 160 ps. Even for an extremely small 40 ps slot duration, using error correcting code (ECC), it is possible to reduce BER to 0.07, which can be further reduced using more advanced codes, such as low-density parity check (LDPC).

Considering the guard time, the presented modulator using the DPPM scheme can theoretically achieve a data rate up to 149 Mbit/s using 512 positions and a slot duration of 40 ps. In practice, the developed transceiver prototype achieved a real-time transmission speed of about 10 Mbit/s due to PC software limitations.

**Full description can be seen in Annex 3 ©2024 IEEE.**

### Coherent PPM Modulator

This subsection presents the design of the next evolution of the DTC-based PPM modulator, which utilizes the same core component – DDL. The conceptual diagram of the DTC is shown in Fig. 1.14. The device is compliant with the CCSDS recommended standard 141.0-B-1 “Optical communications physical layer” [99].

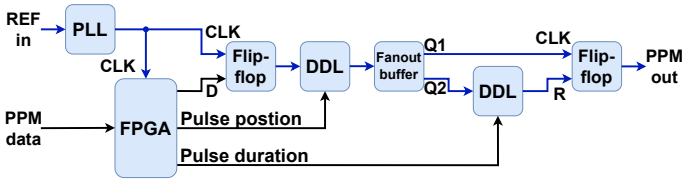



Fig. 1.14. Conceptual block diagram of the PPM modulator.

The core of the DTC is the MC100EP196B programmable DDL with the programmable delay range 0–10.24 ns in 10 ps increments, and it features a ±11 ps linearity across the whole

delay range. The purpose of the DDL is to delay a pulse at its input by a specified time interval, set via the 10-bit-wide input bus, allowing 1024 unique delay values.

The DDL receives the clock signal from a highly stable D flip-flop. The flip-flop is clocked by a 100 MHz signal generated by a very low-jitter PLL, while its "D" input is driven by the FPGA. The clock phase is slightly delayed relative to the FPGA reference clock of the same frequency. This technique minimizes the contribution of FPGA output jitter.

For precise control of the pulse duration, the signal at the output of the DDL is split using a fanout buffer, one output of which ("Q1") is directly connected to the "CLK" input of a D flip-flop, and the other output ("Q2") is passed through a second DDL of the same model and then connected to the reset ("R") input of the flip-flop. This arrangement allows for adjustment of the pulse full width at half maximum (FWHM) in the range of 2.4 – 12.6 ns, as there is a 2.4 ns inherent propagation delay in the DDL even with "0" delay set on the input bus.

The DTC is controlled by the Altera Cyclone IV FPGA, which is connected to the PC via a USB 3.0 interface. Custom software, built in C++ and running on the PC, is responsible for data preparation and transfer to the FPGA. When the software initiates a transmission, an entire PPM transfer frame is sent to the FPGA and stored in memory. Each PPM symbol in the transfer frame is stored at a separate memory address as a 24-bit binary number, where 10 bits specify the pulse delay from the start of the current clock cycle and 14 bits specify the number of clock cycles until the next pulse in the sequence. At the start of the PPM transfer frame, a start pulse is generated, from which the clock cycles are counted. At this time, the FPGA also already prepares and outputs the 10-bit delay value for the next pulse in the sequence. When the FPGA receives a set number of clock cycles (14 bits in the memory address), it sets the "D" input of the flip-flop for one clock cycle, thereby generating a single pulse which is delayed by the value already set in the DDL. Then the FPGA moves to the next memory address, where the data for the next pulse in the sequence is stored, and the same process repeats until the end of the PPM transfer frame. The pulse duration can be set separately via a 10-bit register that stores the pulse duration value.

Since the operating clock frequency is 100 MHz, corresponding to the clock period 10 ns, and the programmable delay range of the DDL is 0 – 10.24 ns, all possible time slots can be covered with the step of 10 ps by setting the DDL delay value and counting the clock cycles.

As the pulse duration can be programmatically controlled, the given modulator enables the use of advanced UWB modulation schemes, such as the pulse-width and pulse position modulation (PWPM).

The device can transmit a 16000-symbol-long PPM transfer frame at a time, with about 20 ms between PPM transfer frames, a software limitation that can be further improved to significantly increase the continuous data transfer rate. For example, with $M = 16$ and $\Delta = 100$ ps, the modulator can achieve a data transfer speed of 2 Gbit/s if the guard slot duration and break are nearly eliminated.

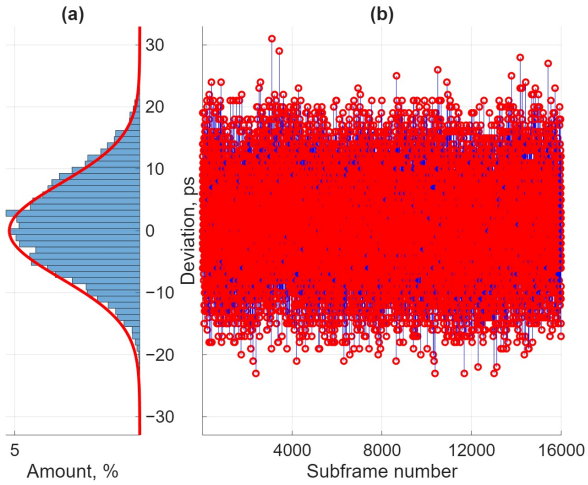



Fig. 1.15. Jitter distribution test results for the developed modulator: (a) jitter distribution; (b) pulse deviation from ideal positions.

The testing of the modulator was performed by connecting the modulator directly to the ESTT via a coaxial cable, in an electrical back-to-back (B2B) configuration. The jitter distribution and pulse position deviation from expected values over a 16000-symbol-long PPM transfer frame are presented in Fig. 1.15. The red line in Fig. 1.15 (a) represents the distribution of jitter. As can be observed, the pulse position jitter is approximately normally distributed, with a RMS jitter of 7.65 ps.

**The presented modulator is employed in research shown in Annex 7.**

## 1.6 Error Analysis and Correction Techniques

FEC is widely used in PPM-based communication systems that use transmission channels that are noisy and can be unreliable. Furthermore, the errors in the received information tend to increase when moving closer to the limits of the data transmission capacity for the channel. The FEC algorithm must be selected depending on the application and computational capabilities of the communication modem.

This section is devoted to the theoretical study and simulation of custom error-correction algorithms in conjunction with FEC for the improvement of TR-PPM transmission links [100]. In this section, major PPM link degradation reasons and respective mitigation methods are investigated. Special attention is paid to FEC methods and their suitability for PPM communication links. A theoretical framework describing the impact of jitter and systematic errors, such as clock drift, on the performance of PPM link is developed. Using computer simulation, the contribution of Gray coding and RS coding to the reduction of BER of TR-PPM communication link with an event timer-based demodulator is found.

There is a great variety of FEC algorithms, and this area continues evolving. The most

straightforward approach, which is widely used in communications, is Gray coding [101], where adjacent symbols are encoded by maximally similar bit combinations. LDPC was one of the first error correction codes that allowed the achievement of data transmission rates close to transmission channels' maximum capacity, which is dictated by the Shannon theorem [102]. For the last 30 years, Turbo and RS coding have been widely used in 3G/4G mobile communications, deep space satellite communication, and other data transmission environments. Turbo coding has significantly increased channel reliability under extreme turbulence conditions in an free-space optical (FSO) system [103]. By using RS hard decision coding for FEC, it is possible to greatly increase the sensitivity of the receiver in FSO applications [104, 105]. There are also FEC methods that combine RS and Turbo coding. Trellis-coded pulse position modulation (T-PPM) can be used to improve the performance of optical communication systems that employ high-power Q-switched lasers and in which pulse duration inaccuracies are present [106].

**Theoretical Framework**

In setups where PPM slot duration below 100 ps is used, it is challenging to maintain precision due to various conditions that can cause position errors. For instance, temperature can affect the internal circuitry, which generates clock signals, resulting in position errors. Additionally, errors may occur as a result of the inability of the generator to provide an exact clock divisor, leading to tiny pulse shifts in time. Also, the movement of the transmitter and receiver stations will lead to various issues.

Moreover, these errors can arise if a jitter is introduced in the signal, causing the receiver to detect the pulse position differently from what was expected. Earlier tests [107] and Section 1.5 of this Thesis have shown that the values of the jitter are distributed approximately normally. The BER of PPM data transmission can be found via calculation of the probability of the pulse appearing at different positions using Formula (1.6).

$$P(\sigma, \mu) = 1 - \int_{-\frac{1}{2}\Delta}^{\frac{1}{2}\Delta} \frac{1}{\sigma\sqrt{2\pi}} e^{-\frac{1}{2}(\frac{x-\mu}{\sigma})^2} \, dx, \tag{1.6}$$

where $x$ is the deviation from ideal position, $\mu$ is systematic error caused by the clock drift, and $\sigma$ is standard deviation of the jitter. For the normal distribution function, 99.73 % of cases are within $\pm 3\sigma$ interval. If the jitter is limited in range $(-t_j/2, t_j/2)$, using the $3\sigma$ rule, the standard deviation can be found as $\sigma = t_j/6$, where $t_j$ is the jitter amplitude. The visualized distribution function is shown in Fig 1.16.

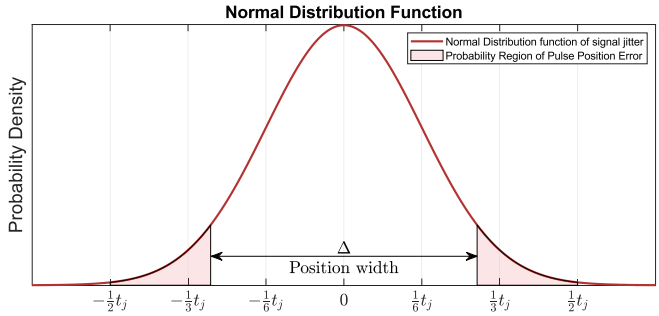



Fig. 1.16. Jitter distribution function. ©2024 IEEE

If the PPM signal structure where bits per symbol $N = 8$ is used, and a position error occurs where the time drift does not exceed $\frac{3}{2}\Delta$, then a one-bit error will be determined in 8-bit symbol. If deviation $x$ does not exceed one position, and it leads to only a 1-bit error, the BER $B$ can be calculated by using Formula (1.7):

$$B(\sigma,\mu) = \frac{P(\sigma,\mu)}{N} = \frac{1}{N} - \frac{1}{N}\int_{-\frac{1}{2}\Delta}^{\frac{1}{2}\Delta} \frac{1}{\sigma\sqrt{2\pi}} e^{-\frac{1}{2}(\frac{x-\mu}{\sigma})^2} dx. \tag{1.7}$$

If the time shifts from expected positions are linear for all pulses, a simple time shift averaging method called the zero position interval method could be used. This method requires a certain number of frames in which the pulse is fixed at the first symbol position. Based on the PPM parameters, an average time shift for several frames containing fixed interval pulses can be calculated. A higher number of fixed intervals will result in more precise averaging. The receiver will apply this average value to the remaining pulses, assuming that the other pulses have the same average time shift.

If an averaging is performed on the time intervals, which corrects the described clock drift $\mu$, it is possible to calculate the improvement $\gamma$ of the correction by the formula (1.8).

$$\gamma = \frac{B(\sigma,\mu)}{B(\sigma,0)}. \tag{1.8}$$

Due to the high probability of position error if $t_j \geq \Delta$, appropriate FEC codes should be implemented. If the PPM pulse is detected in a different position, the binary code of the symbol will change with respect to the new position. Employment of Gray coding of the PPM positions ensures that one position shift will result in a single-bit error.

A much more advanced technique is the RS code, an error correction code widely used in communications. This error correction adds redundant correction bits to the data to be used for the decoding process. It encodes and decodes the data by symbols, which are perfect for PPM communication since they consist of $N$ bits each. RS encoding requires two parameters: the total symbol length $n$ and the number of redundant bits $k$. These parameters are usually determined by

the expected error rate and the length of the signal frame block. The data symbols are separated into blocks, with each block transformed into coefficients of a polynomial representing the data. The block length determines the degree of the polynomial. The redundant bits are generated based on the polynomial, which means the redundant symbols act as coefficients that are part of the polynomial. This data block is then sent to the receiver for decoding.

### Validation of Clock Drift Correction Algorithm

The experimental validation of the clock drift correction algorithm has been performed using TR-PPM and the setup presented in Section 1.4.

A calibration sequence consisting of five TR-PPM data frames in the ”0” position was used before the main data frame sequence. The receiver software corrected the clock drift error by comparing the expected time interval between the reference and data pulses and the actual received interval for each calibration frame. The average difference was calculated and applied to the entire TR-PPM data sequence. The pulse deviation from the ideal positions without calibration is shown in Fig 1.17 and with calibration in Fig 1.18.

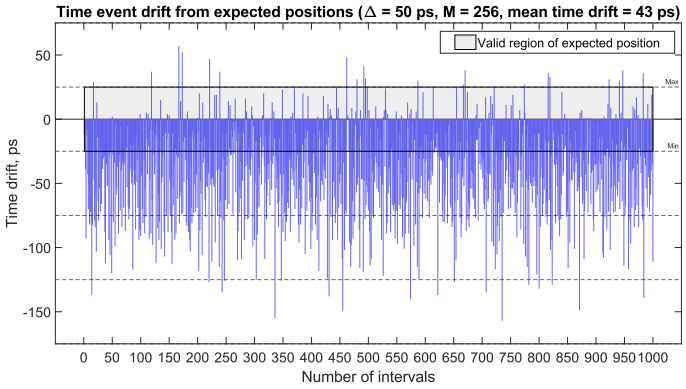



Fig. 1.17. Pulse deviation from the ideal positions without calibration. ©2024 IEEE

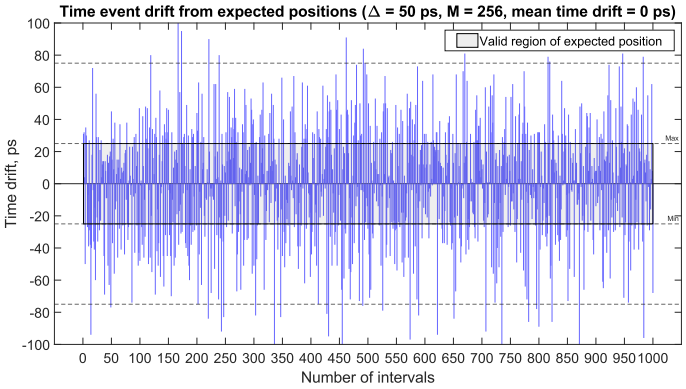



Fig. 1.18. Pulse deviation from the ideal positions after calibration. ©2024 IEEE

The results show that clock drift error manifests as an offset of the entire TR-PPM by a specific value. The implemented correction algorithm can determine the offset, and applying the correction leads to significantly lower BER as reported in Section 1.4.

**Validation of Error Correction Algorithms**

A simulation was performed in the MATLAB environment and employed experimentally determined jitter and clock drift values of the custom-designed modulators presented in Section 1.5. In the hardware prototypes, the deviation of the data pulses from their expected positions was distributed semi-normally. In contrast, the errors introduced by the clock drift were almost constant during one PPM frame. As the clock drift does not significantly increase for the duration of the PPM sequence, it can be modeled as a constant offset from the expected data pulse position values.

In the simulation, the RS error correction algorithm was implemented. The RS(255, 223) code was used, in which a block consists of 223 data bits with 255 total bits. The experiment was repeated using various parameters listed in Table 1.5. The position count in all experiments was 256 and the slot duration 155 ps. The transmitted data was generated as a 255-symbol-long (8 bits per symbol, 1784 total bits) PRBS and encoded using RS(225, 223) code and Gray code, if applicable for the specific experiment.

Table 1.5

Simulation Parameters ©2024 IEEE

| Test nr. | Jitter RMS range, ps | Clock drift, ps | Error correction used |
|---|---|---|---|
| 1 | 30-55 | 0 | No error correction |
| 2 | 30-55 | 0 | Gray code |
| 3 | 30-55 | 0 | Reed-Solomon code |
| 4 | 30-55 | 0 | Reed-Solomon code and Gray code |
| 5 | 10-22 | 43 | No error correction |
| 6 | 10-22 | 43 | Gray code |
| 5 | 10-22 | 43 | Reed-Solomon code |
| 6 | 10-22 | 43 | Reed-Solomon code and Gray code |

The event timer was simulated by adding 3 ps RMS jitter to the simulated received data. The experimentally obtained BER as a function of RMS jitter for the previously mentioned error correction schemes without clock drift error can be seen in Fig. 1.19 and with added clock drift error in Fig. 1.20.

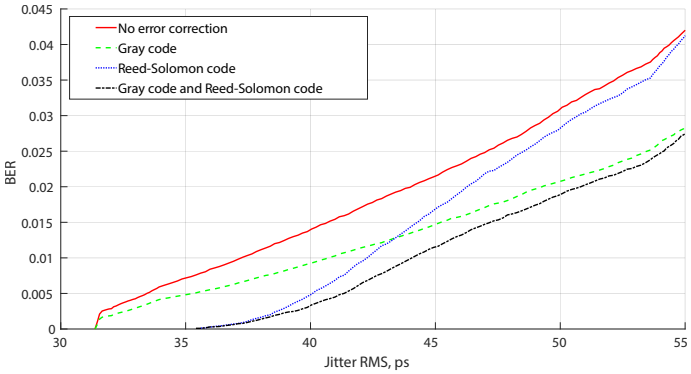



Fig. 1.19. Simulation results without clock drift error. ©2024 IEEE

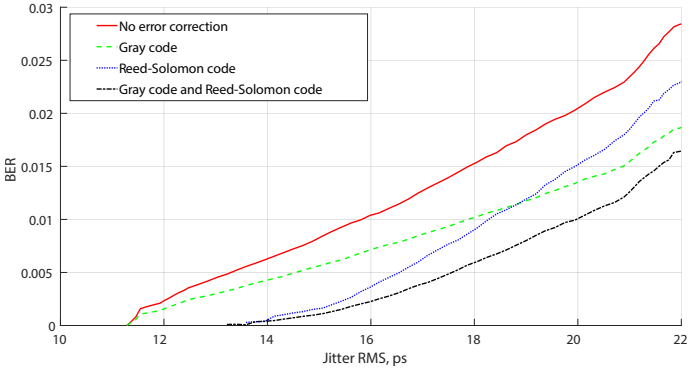



Fig. 1.20. Simulation results with added clock drift error. ©2024 IEEE

The results show that the RS error correction scheme performs well up to a jitter RMS of about 45 ps. As the jitter further increases, the gain from the error correction is minimal. In contrast, bit errors emerge at a jitter RMS of 32 ps in the case of no error correction and Gray code only. This is expected, as errors should appear when the deviation exceeds position limits. The Gray code provides the most significant decrease of the BER as it provides for a single bit error in the PPM symbol in case the data pulse is shifted by a value equal to or less than one slot duration.

Clock drift correction via averaging offsets from the ideal positions significantly reduces BER. However, it requires data-aided estimation of the clock drift via transmission of known training sequences before sending actual data. In TR-PPM, time measurement between the reference pulses can be employed to estimate the clock drift without sending the training sequence.

FEC based on RS code allows for the reduction of bit errors caused by both jitter and clock drift. However, after a certain point, RS code cannot correct the bit errors caused by the jitter since RS(255,223) code can correct 16 bit errors per block. For this reason, data should also be encoded using Gray code, since it improved in BER over the whole range of jitter RMS values used in this experiment.

**Full description can be seen in Annex 4 ©2024 IEEE.**

## 1.7 Summary of the First Thesis

The first thesis was devoted to proving that a PPM modulator implemented using programmable gate and multiplexer-based DDL integrated circuit (IC) technology is capable of achieving PPM pulse sequence generation with RMS timing jitter below 10 ps. To achieve this objective, a testbed was developed to research concepts used in PPM data transmission; high-precision time-taggers were tested and validated for use in PPM systems, and for the first time, a data transmission experiment using PPM and a time-tagger intended for SLR applications was performed. Two MC100EP196B high-precision programmable DDL-based modulators were developed and tested using the ESTT, at first achieving an RMS jitter of 18.9 ps and the latter model 7.65 ps, thereby proving the thesis. The developed modulator can transmit a 16000-symbol-long PPM transfer frame at a time, with about 20 ms between transfer frames, using slot durations as low as 10 ps and modulation order above 256. Data transmission experiments showed a BER as low as $1.2 \times 10^{-5}$ using Gray and RS code. The testing revealed that the jitter is distributed approximately normally, and finally, the systematic errors were analyzed and correction techniques proposed.

**Full description of the results presented in this chapter can be seen in Annexes 1, 2, 3, 4, and 7.**

# 2 ULTRASHORT PULSE EXPANSION IN PPM SYSTEMS

The demodulation of a PPM signal employing extremely short pulses is challenging as it requires fast electronic circuitry, such as comparators and triggers with bandwidths of tens of gigahertz. As PPM pulse duration does not carry information, the problem can be tackled by increasing the duration of the received pulses just before the demodulation. The occupation of several time positions by the single incoming expanded pulse does not create any issues with PPM demodulation, as only the rising edge of the pulse carries the information. Also, there is no stringent requirement to maximally preserve the shape of the generated pulse being transmitted via a channel to the receiver unit, provided that the pulse shape variations do not vary considerably between the pulses; one only needs to ensure that the change in the pulse shape is not too significant to provide correct demodulation.

This chapter focuses on the expansion techniques of 50–100 ps short pulses using passive electrical and optical devices for subsequent use in PPM demodulators and demonstrates that passive techniques can be successfully applied for high-bandwidth pulse expansion in both optical and electrical domains. Employment of electrical LPF and optical techniques, namely, fiber Bragg grating (FBG), for pulse duration expansion is explored.

## 2.1 Electrical Pulse Expansion

Many modern electrical and optical systems, such as UWB communication devices, signal processing circuits, radar systems, and more, are dealing with the transmission, measurement, and processing of short pulses [108, 109]. These operations often require the pulse to be expanded or compressed with minimal waveform distortion. Various delay lines [110–114] and other devices operating in the frequency domain (for example, filters) and making changes to it [115–125] and combinations of delay lines and filters are widely used for pulse expansion. Both digital and analog signal processing techniques are used, and each has advantages and disadvantages.

An option for pulse shaping involves using filters that influence the pulse magnitude spectrum. Passive and active filters [126, 127] can be utilized for this purpose. The simplest active filters are built around transistor and op-amp circuits as their fundamental components [128], although, in most cases, they tend to be more complex [129]. Active filters offer greater flexibility, allowing for reconfigurable bandwidths ranging from narrow/mid-band to ultra-wideband states, as described in [130]. Active filters can implement intricate filter functions such as low-pass, band-pass, and various filter types, and they can be designed with a reconfigurable magnitude response and phase-frequency dependence. Due to the presence of active components, they tend to be more costly than passive filters. Additionally, they require an external power supply, which can introduce noise or interference.

To ensure an unambiguous event timer response and the minimum possible jitter in time interval detection as well as the stable operation of the event timer and initial state recovery, it is necessary to ensure that the initial pulse is extended to about 150 ps, that the filtered pulse

does not have noticeable ripples or a long tail, and that the rising edge of the filtered pulse is preferably as steep as possible.

LPFs perform the signal's energy accumulation, leading to a situation where the signal at the output of the filter lasts longer than the excitation. Therefore, when unipolar pulses are used in the PPM transmission channel, one of the most rational ways for pulse expansion is to utilize a LPF. It is sufficient to design a filter whose attenuation in the passband (up to the cutoff frequency $f_c$) is almost constant, whose stopband up to the frequency $3f_c$ decreases by 10 dB, and whose group delay has minimal variations up to the frequency $2f_c$.

Analytical derivations and numerical modeling in [95] have confirmed that, of all the filter types, the Bessel-type filter is the most suitable for pulse expansion, as it has a maximally flat group delay and a maximally linear phase response. Those characteristics ensure negligible ringing in the impulse response [131] and minimize overshoots in the pre-transition and post-transition aberration regions of the expanded PPM pulses.

Experiments were performed with commercially available LPFs to determine if an off-the-shelf filter could be used for pulse expansion. An example of pulse expansion using the Mini-Circuits SLP-2400+ filter [132] is shown in Fig. 2.1. The commercial filter introduced noticeable oscillations in the post-transition region. Moreover, it significantly flattened the pulse's rising edge, increasing the timer's sensitivity to the additive noise. Experiments with commercial filters showed that it would be difficult to find a suitable filter, so it was decided to design and build a custom filter. Microstrip technology was chosen because its fabrication is possible without the involvement of complicated and expensive technological processes.

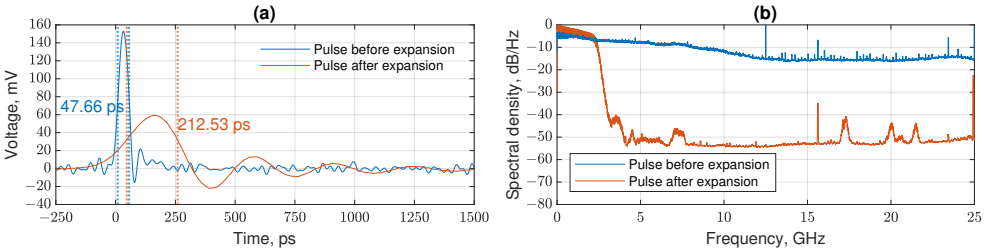



Fig. 2.1. Pulse expanded using Mini-Circuits SLP-2400 filter: (a) waveforms of the pulses; (b) normalized magnitude spectra.

### Custom-Built Electrical Pulse Expanders

Two microstrip LPF filters were designed to extend the pulse duration from 50 ps up to about 170 ps, which is slightly above the event timer's minimum pulse duration threshold of 150 ps, to ensure that the timer will definitely respond. Analytical and numerical calculations, computer modeling, and measurements showed that the third-order Bessel LPF capacitor–inductor–capacitor filter, which is normalized by the group delay (hereafter called Classical), is the most suitable for the expansion task. The filter's group delay was normalized so that in the passband, it is $1/\omega_c$, where $1/\omega_c$ is the angular cutoff frequency, which was chosen to give the required pulse

extension. The normalization of the second filter (hereafter called Magnitude-Normalized) was performed using the traditional magnitude normalization methodology, where the gain is $-3$ dB at the cutoff frequency. The filters are shown in Fig. 2.2.

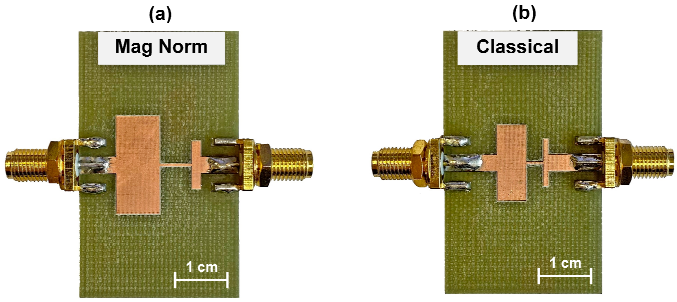



Fig. 2.2. Custom-designed filters: (a) Magnitude-Normalized, and (b) Classical, with cutoff frequencies $f_c = 1.8$ GHz.

Simulated and measured curves of the transmission coefficient magnitude $|S_{21}|$ and group delay for both filters are shown, respectively, in Fig. 2.3 and Fig. 2.4. The group delay curves obtained in the simulation and the experimental ones are in good agreement if the slopes of the curves are compared. The differences in group delay seen in the figures are almost constant across the whole frequency range, and they can be caused by different reference planes used in the simulation and experiments, as the actual board included the SMA connectors but the simulations did not.

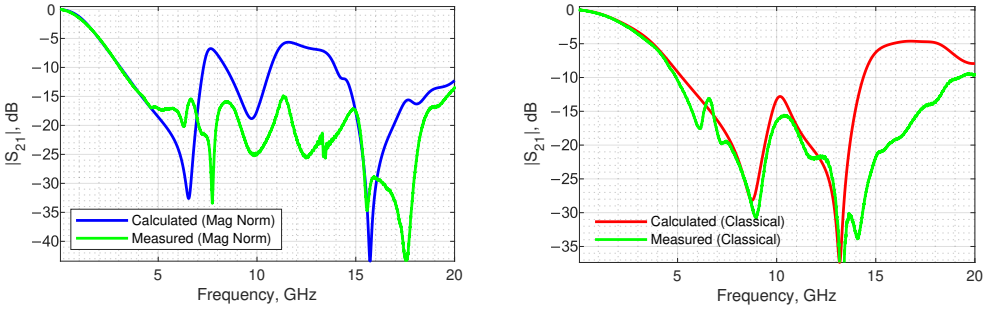



Fig. 2.3. Ansys HFSS simulation results and custom-designed filter measurement results for $|S_{21}|$ magnitude.

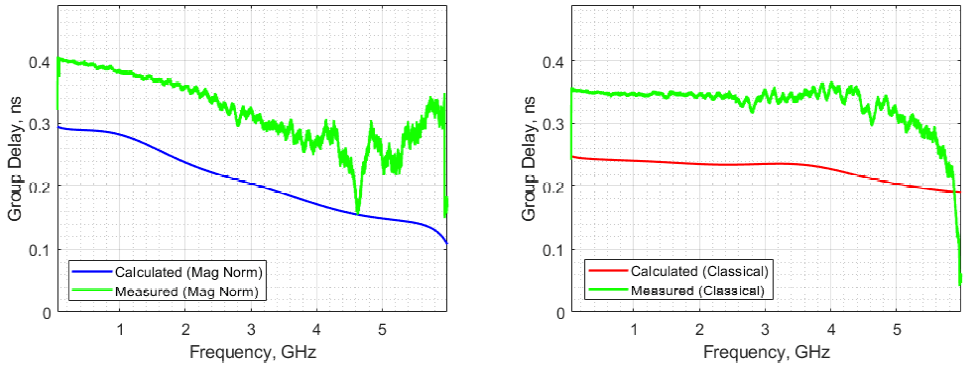



Fig. 2.4. Ansys HFSS simulation results and custom-designed filter measurement results for group delay.

### Testing of the Custom Filters

Fig. 2.5 shows the block diagram of the LPF-based electrical pulse expansion test setup. The results of a 50 ps input pulse expansion by the Classical LPF filter can be seen in Fig. 2.6, whereas those of the Magnitude-Normalized LPF filter can be seen in Fig. 2.7.

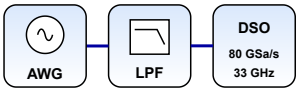



Fig. 2.5. Block diagram of electrical pulse expansion test setup.

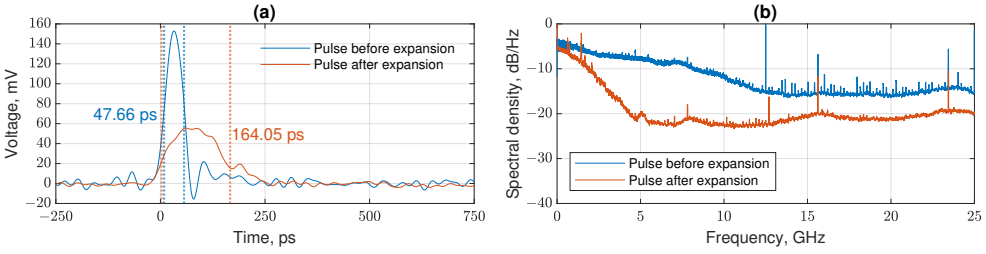



Fig. 2.6. Pulse expanded using Classical custom-designed filter: (a) waveforms of the pulses; (b) normalized magnitude spectra.

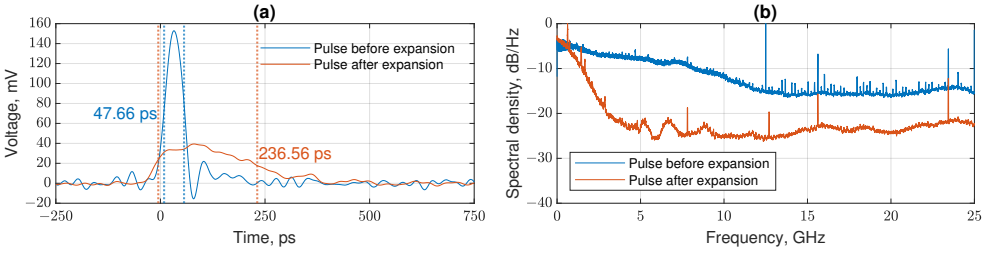



Fig. 2.7. Pulse expanded using Magnitude-Normalized custom-designed filter: (a) waveforms of the pulses; (b) normalized magnitude spectra.

It can be seen that the pulse expanded by the Classical filter to 146 ps is close to the desired pulse waveform, as it meets the waveform requirements. The Magnitude-Normalized filter expands the pulse to 237 ps, and this pulse waveform has a first transition duration that is too large, a long tail, and ripples in the tail. These differences can be explained by the fact that the group delay of the Classical filter is less variable across the frequency range, and the transfer coefficient magnitude is flatter and significantly larger at frequencies above 3 GHz compared to the Magnitude-Normalized filter. Those features affect the pulse waveform, especially the rise time, which should be small enough to comply with the set-out parameters.

## 2.2 Optical Pulse Expansion

PPM pulses can be expanded not only in the electrical domain but also in the optical domain when signal transmission over optical fiber is realized. To increase optical pulse duration, so-called optical pulse stretchers or techniques are used [133, 134]. Stretching optical pulses can be helpful in scenarios where it is necessary to increase the duration of a pulse without altering its waveform. These are crucial elements, for example, in ultra-fast lasers, to expand the pulse in the time domain and reduce the pulse's peak power, eliminating adverse nonlinear effects [135]. Also, optical pulse stretching is a commonly employed technique to safeguard the input faces of optical fibers from damage [136]. In general, pulse stretchers can be classified into two categories: coherent and incoherent. Coherent pulse stretchers, such as grating pulse stretchers, stretch a pulse in a way that can later be undone. They provide positive or negative group delay dispersion and typically are based on dispersive elements like diffraction grating pairs, grisms (grating and prism), FBG, chirped Bragg gratings, or ring resonators. On the other hand, incoherent pulse stretchers irreversibly stretch a pulse [133, 137]. An incoherent pulse stretcher can be realized by circulating cavities, which divide an incident pulse into many smaller pulses spread over a time period [134]. In the presented experiments, a tunable FBG to introduce positive dispersion and broaden the input optical PPM pulses was used.

The target of this experiment was to expand 50 ps optical PPM pulses up to at least 150 ps. This is necessary as the duration of the incoming PPM pulse on the input of the event timer should be at least 150 ps to provide stable operation.

The transmitter side included a Keysight M8195A AWG, RF amplifiers, 40 GHz Mach–Zehnder modulator (MZM), Cobrite DX4 continuous wave (CW) C-band laser tuned at 1550 nm, and power supplies. The receiver part contained a linear variable optical attenuator (VOA), optical power meter, Amonics PR10G 10 ac-coupled photodetector (PD), and a Keysight DSAZ334A digital storage oscilloscope (DSO) (80 GSa/s, 33 GHz) with a connected DC blocker. The tunable FBG was placed right between the transmitter and receiver sides of the experimental setup, as shown in Fig. 2.8.

The tunable FBG was set to the chromatic dispersion (CD) value of +1200 ps/nm, which was equal to around the dispersion value introduced by 75 km of standard ITU T G.652 single-mode

optical fiber (SMF). As a result, FBG set to this value of CD expanded the PPM pulses up to 154.03 ps, as shown in Fig. 2.9. It can be concluded that FBG behaved as a slight band-rejection filter with a center frequency around 6 GHz.

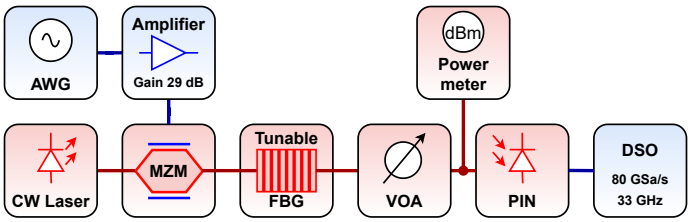



Fig. 2.8. Block diagram of optical pulse expansion test setup.

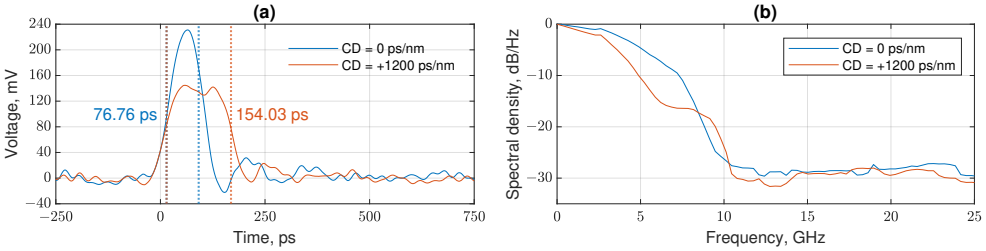



Fig. 2.9. Pulse expanded using tunable FBG: (a) captured waveform, and (b) normalized magnitude spectra.

The experiment successfully demonstrated the optical pulse expansion capacity of the tunable FBG module.

## 2.3 Pulse Expansion Method Experimental Validation

The PPM transmission experiments have been carried out using optical and electrical pulse expansion methods with TR-PPM waveforms. The PPM pulses were kept as short as possible to demonstrate energy-efficient transmission.

The block diagram of the PPM transmission system is illustrated in Fig. 2.10. Key components of the system are a pulse expander module (optical FBG or electrical LPF) and a high-precision event timer used for the demodulation. AWG acts as a PPM transmitter, generating the desired signal waveform following our loaded sampled data. Unipolar PPM pulses with a time duration of 50 ps were used. When pulse expansion was realized by the LPF, the CD value of FBG was set to 0 ps/nm.

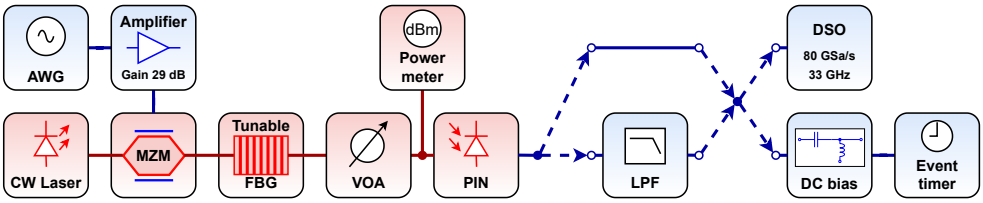



Fig. 2.10. Block diagram of a PPM transmission link with an event timer for the demodulation.

First, the ideal 50 ps pulses with a rectangular shape and intervals between pulses determined by the random data were generated by MATLAB. Then, the waveform was saved into an AWG-specific file format and loaded into its memory. Next, the prepared waveform was played on the AWG's output port at a maximal sampling speed of 65 GSa/s. The AWG output signal was amplified to drive the MZM intensity modulator. The optical MZM output was connected to the Teraxion FBG module. The output of this module was connected to a VOA and through a 10%/90% optical coupler to the PD, where the optical signal was converted to electrical. The 10% port of the optical coupler was connected to the optical power meter (OPM). The PPM pulse duration on the output of the PD was measured to be about 76.76 ps due to the limited bandwidth of the PD, which was lower than the bandwidth of the original signal generated by AWG. The bias tee circuit was connected before the event timer to adjust the PPM signal's DC level so that the half-magnitude of the incoming pulses was approximately at the timer-triggering threshold of 1.2 V.

The experiment has been conducted using TR-PPM waveforms [67] with the parameters listed in Table 2.1 by employing optical or electrical pulse expansion methods. In both cases, BER measurements were relative to the average optical power received before the PD. The BER versus the average received optical power with optical pulse expansion for multiple slot duration values is shown in Fig. 2.11, whereas in the case of electrical pulse expansion, the results can be seen in Fig. 2.12. The range of the average received optical power values was selected to represent the region around which the data transmission transitions from error-free to completely unintelligible (BER value of 0.5). This range was experimentally determined for the given system and corresponds to the amplitude values of the electrical pulse on the edge of the detection threshold of the event timer.

Table 2.1

TR-PPM Transmission Experiment Parameters

| **Number of positions, $N$** | **Slot duration $\Delta$, ps** | **Pulse duration $\tau$, ps** | **Expansion method** |
|---|---|---|---|
| 512 | 50 | 50 | Optical |
| 256 | 100 | 50 | Optical |
| 128 | 200 | 50 | Optical |
| 512 | 50 | 50 | Electrical |
| 256 | 100 | 50 | Electrical |
| 128 | 200 | 50 | Electrical |

The FEC limit represents the BER threshold at which the Reed–Solomon RS(255, 223) FEC algorithm is capable of correcting the errors in the received data pattern. This BER value is $6.27 \times 10^{-2}$ as the RS(255, 223) algorithm can correct up to 16 erroneous symbols in the block.

For the experiments conducted using a slot duration of 200 ps, the results reveal a distinct point where the data transmission becomes error-free. This happens when the incoming PPM signal at the input of the event timer significantly exceeds the threshold set by the DC bias voltage so that no adverse effects, such as noise and jitter, significantly impact the BER. In contrast, if the magnitude of the incoming pulses, which corresponds to a certain average received optical power, falls below the voltage threshold of the event timer, very low BER values are observed in all cases. The threshold effect is observable at a slot duration of 200 ps. In contrast, in the case of slot durations of 50 and 100 ps, the experiments show an error floor, especially in the case of optical pulse expansion. This is expected behavior, as smaller slot durations require more precise modulation in the transmitter and demodulation in the receiver. Adverse effects such as jitter and additive noise in all system components considerably impact the PPM signal with smaller slot durations. As the slot durations of PPM pulses decrease, the jitter can more likely cause the estimated pulse position in the receiver to shift to a different pulse position than the one generated by the modulator. The additive noise in the signal waveform can also cause errors by falsely triggering the event timer when the time corresponds to a different pulse position. The effect of the noise is especially pronounced when considering slot durations smaller than the pulse duration, as this provides a large time window (the entire pulse) where noise may falsely trigger the timer.

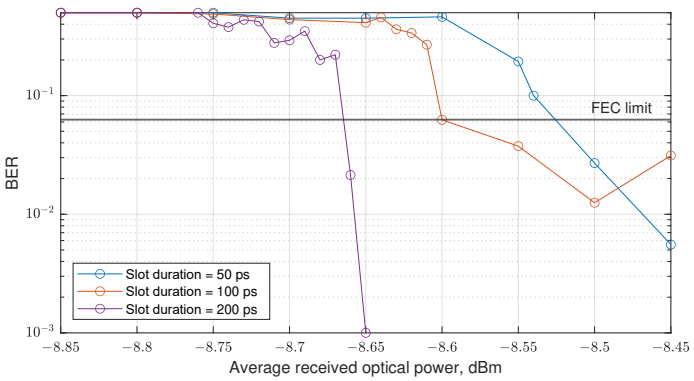



Fig. 2.11. BER versus average received optical power with optical pulse expansion with FBG module.

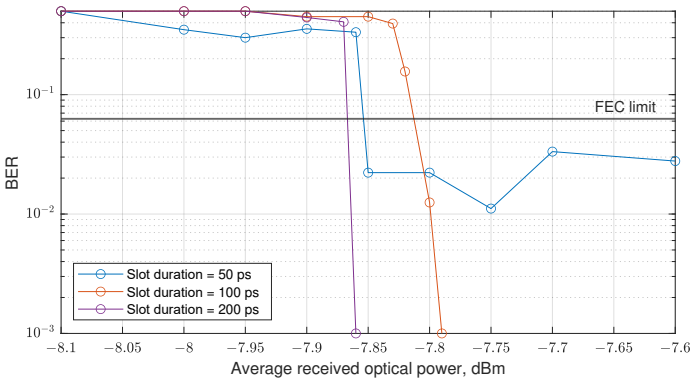



Fig. 2.12. BER versus average received optical power with electrical pulse expansion with LPF.

The results validate the concept of both electrical and optical pulse expansion methods for use with the event timer, as the BER values, even at very small slot durations of 50–100 ps, are acceptable. The lower BER values in the case of electrical pulse expansion at a similar average received optical power can be attributed to the excellent pulse shape at the output of the custom LPF, which leads to higher accuracy in the triggering of the event timer, resulting in less error-prone transmission. Employment of new pulse expansion techniques in conjunction with a more capable TDC allowed to achieve a much lower BER compared to the results presented in [100].

## 2.4 Summary of the Second Thesis

The second thesis was devoted to proving that in time tagger-based PPM systems, a pulse with duration 50–100 ps can be expanded passively by electrical and optical means to more than 2 times its original FWHM duration while preserving the pulse's waveform shape enough for stable detection. In this chapter, two methods of passive pulse expansion were discussed: electrical and optical. A commercial Mini-Circuits SLP-2400 LPF was tested and found to have expanded the 47.66 ps pulse to 212.53 ps with noticeable ripples in the falling edge. Two custom-built filters were presented and tested, achieving expansion to 164.05 ps and 236.56 ps, respectively; however, in the latter case, the falling edge was highly stretched. Optical pulse expansion using an FBG was experimentally tested, stretching the pulse to 154.03 ps with excellent waveform shape. Both methods were validated in experiments involving data transmission in an optical PPM communication system, achieving BER values below $1 \times 10^{-3}$.

**Full description containing the results presented in this chapter can be seen in Annex 5.**

# 3 EVALUATION OF PPM-BASED ISAC SYSTEM PERFORMANCE WITH AROF-BASED TRANSMISSION NETWORK

Achieving tight sub-nanosecond timing tolerances required for distributed sensing, especially in PPM applications, is challenging. To address this issue, fiber-optic technologies provide low-jitter, long-distance physical links with an established functional model: radio-over-fiber (RoF) [138, 139]. RoF has gained considerable popularity, as optical fiber links and passive optical network (PON) infrastructure are deployed to consolidate these technologies in centralized radio access network topologies [140–142]. Additionally, RoF has already proven itself to be a valuable addition to interconnected radar architectures [143], enabling simplified radar data transmission [144–146]. A sub-branch of RoF, analog radio-over-fiber (ARoF), further simplifies the system by sending an analog signal directly over an optical fiber without analog-to-digital conversion. This approach preserves the signal's continuous form and analog nature, which can be beneficial for subsequent signal processing and synchronization, especially in PPM-based systems, which require high timing accuracy. Consequently, ARoF technology has been explored in recent research for millimeter-wave [147, 148] and terahertz links [149, 150]. Additionally, ARoF is being considered for future distributed multiple-input multiple-output (D-MIMO) systems in 6G networks [142, 151–155], as well as wireless communications, distributed sensor networks, radars, space communication systems, and many other applications [156–159].

This chapter is focused on the design, implementation, and evaluation of PPM-based communication systems using the ARoF technology for long-distance optical signal transmission, and exploring range measurement capabilities in an ISAC system that uses a time tagger as the demodulator.

## 3.1 Design and Evaluation of 28 GHz Microwave/Optical Transmission System Utilizing PPM

This section presents a novel, experimentally validated communication system employing TR-PPM transmission over ARoF. In this implementation, the central office is equipped with a local analog RoF transmitter; in turn, the base station consists of a remote antenna unit (RAU) serving as the RF transmitter in the access network. The demodulation of PPM signal is performed by TDC based on a commercial event timer. The presented system functions as a testbed for the investigation of impulse radio ultra-wideband (IR-UWB) communication and future use cases of UWB ISAC.

### Experimental Setup

The experimental system mainly consists of three parts: (a) ARoF transmitter, (b) RAU transmitter, and (c) RAU receiver, as shown in Fig. 3.1. In the experimental setup, the following

primary assumptions have been made: firstly, the radio channel is exclusive to the presented experiment; secondly, both the transmitter and receiver remain stationary; and, thirdly, multipath propagation effects are negligible due to the controlled environment.

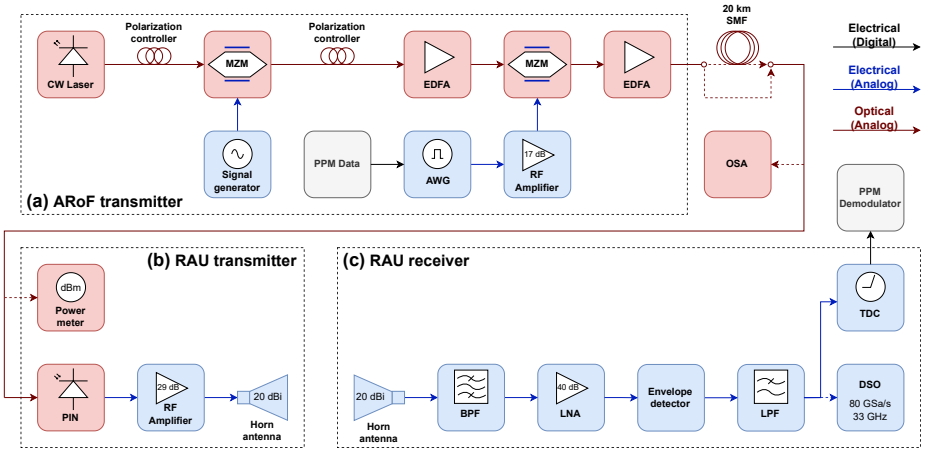



Fig. 3.1. Experimental setup of the PPM-based ARoF communication system.

In the setup, the optical output (1550 nm wavelength) from the Cobrite DX-1 CW laser was first directly connected to a 40 GHz MX-LN-40 MZM. The bias point was adjusted near its zero level. A sinusoidal signal generator, producing a 14 GHz sinusoidal electrical signal (half of the proposed intermediate frequency), was directly connected to the electrical signal input of the first MZM. As a result, the desired RF of 28 GHz was achieved between the generated tones in the optical domain at the output of the first MZM. The output of the first MZM, comprising two equal optical tones (carriers) spaced 28 GHz apart, was subsequently amplified using an erbium-doped fiber amplifier (EDFA) to compensate for optical power loss. The optical signal was then modulated with the TR-PPM waveform using a second MZM. The TR-PPM waveform was generated using the Keysight M8195A AWG with a 25 GHz analog bandwidth and a 65 GSa/s sampling rate.

An optical signal pre-amplification by a second EDFA with an optimized gain was performed before launching the optical signal into a 20 km long ITU-T G.652 rec. compliant SMF span, which has 0.02 dB/km attenuation and a 17 ps/nm/km dispersion coefficient at 1550 nm.

As for the optical receiver, a DSC10H PD with 50 GHz 3-dB electrical bandwidth was used, which realized the photodetection-based RF generation from the optical beat note. The optical spectra before the PD are shown in Fig. 3.2. The RF signal output power from the PD was amplified before being transmitted to the Ka-band (26.5–40 GHz) horn-type antenna with 20 dBi gain. Free space path loss of the transmitted 28 GHz signal at 5 m was 35.36 dB; at 10 m, it was 41.38 dB, and at 20 m it was 47.40 dB. The most critical insertion losses are at the beginning of the transmission distance.

The receiver was located 5 m away from the RAU transmitter. The transmitted mm-wave signal was received by an identical Ka-band antenna and filtered using the bandpass filter (BPF), which has a center frequency of 27.38 GHz and a 3-dB passband of 8.3 GHz. After filtering, the signal was amplified, allowing further processing in the mm-wave RAU receiver. The amplified signal was then sent to the envelope detector with GHz bandwidth, which performed frequency down-conversion of the 28 GHz intermediate frequency signal. The down-converted baseband signal was then sent to the DSO and the ESTT event timer via a custom-made LPF with a bandwidth of up to 1.8 GHz for analysis. This specific LPF (see Chapter 2) was purposefully utilized to broaden the received pulses for accurate detection with the ESTT, as the group delay of this filter remains nearly constant for frequencies up to 3 GHz, thus reducing pulse shape distortions. Additionally, the Keysight DSOZ334A DSO was initially used for signal visualization and optimization after wireless transmission and was later replaced with the ESTT for experimental measurements. The pulse waveforms for various pulse duration values $\tau$, captured by the DSO, for the B2B experimental setup and the setup involving 20 km SMF are shown in Figs. 3.3 and 3.4, respectively.

The Kerr nonlinear optical effects (NOE), e.g., the four-wave mixing (FWM) impact on the PPM modulated intermediate frequency optical signal, is illustrated, which affects the signal transmission through the optical distribution network. Additional spectrum peaks are caused by the high optical power level output ($\sim +15$ dBm) of the second EDFA before launching the optical signal in the optical distribution network and are more pronounced than in the case of the B2B setup due to the nonlinear coefficient and the mode effective area of the SMF. Nevertheless, this does not significantly impact the BER, as NOE does not considerably affect PPM signals. The optical power of the three optical tones after the 20 km long SMF is about 3 dB lower due to the attenuation in the fiber.

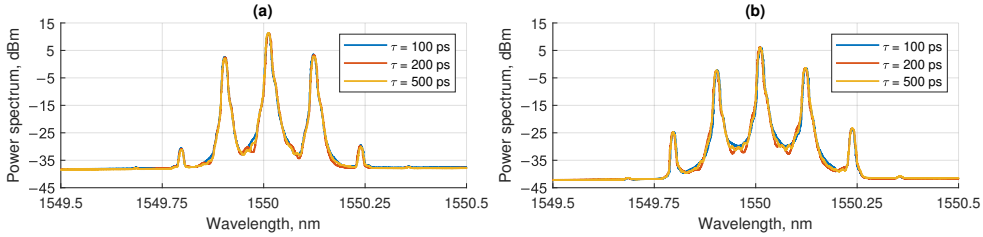



Fig. 3.2. Optical spectra: (a) B2B connection, (b) connection with 20 km long SMF.

The pulses after the LPF in the RAU receiver are broadened to approximately 500 ps, facilitating their detection by the ESTT. However, the expansion comes at the cost of the pulse waveform amplitude.

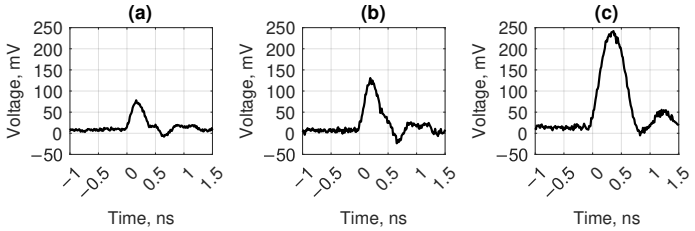



Fig. 3.3. Captured pulse waveforms for B2B connection with duration: (a) 100 ps, (b) 200 ps, (c) 500 ps.

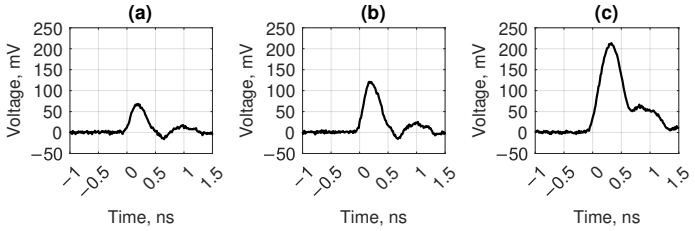



Fig. 3.4. Captured pulse waveforms for connection with 20 km SMF, with duration: (a) 100 ps, (b) 200 ps, (c) 500 ps.

**Data Transmission Experiments**

The transmitted data were generated as a $1.224 \times 10^6$ bit long PRBS using the Mersenne Twister pseudo-random number generator with the order of 623, establishing a minimum detectable BER of $8.17 \times 10^{-7}$ corresponding to a single error in the demodulated data. The data were saved for later comparison with the demodulated data. The TR-PPM waveforms were generated offline in MATLAB with pulse durations varying from 500 ps to 100 ps and time bin durations ranging from 200 ps to 50 ps and then loaded into the AWG. The number of pulse positions was adjusted for each configuration to achieve optimal data rates for the given parameters. Additionally, these waveforms were generated with and without ECC. Error correction was implemented using Gray code alone and Gray code with RS ECC, which can correct up to 16 error bytes in the encoded data. In the case of RS encoding, the waveform was generated with the number of positions $M = 256$, so that one byte of data takes up an entire TR-PPM frame and is not split across multiple frames.

Two sets of experiments were performed, with and without a 20 km SMF link, and BER measurements were made with and without ECC. The results are presented in Figs. 3.5 and 3.6. For error-free demodulation, the BER is reported as $<8.17 \times 10^{-7}$, as lower BER values cannot be measured with the given data set size.

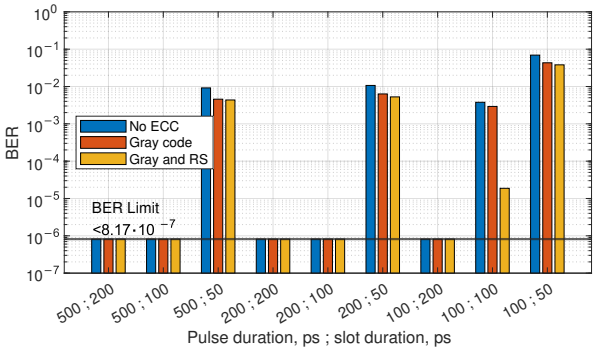



Fig. 3.5. Data transmission experiment results for the B2B connection.

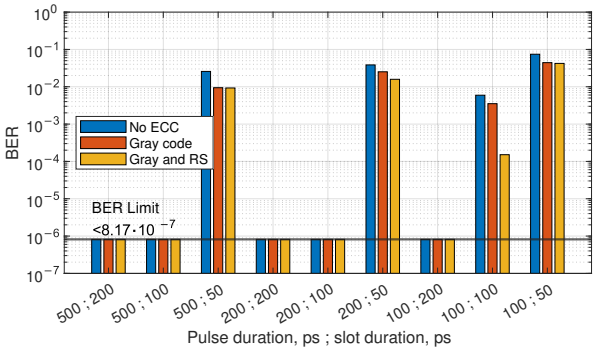



Fig. 3.6. Data transmission experiment results for the connection with 20 km SMF.

All measurements with a time bin duration of 200 ps demonstrate error-free transmission. Error-free transmission was also achieved with both 500 ps and 200 ps pulse durations, using a time bin duration of 100 ps.

It can be seen that the employment of Gray code, which ensures that only one bit is flipped if the received pulse is located in the adjacent time bin, slightly decreases the BER, which is further reduced by the use of RS (255, 223) code. Employment of RS code significantly reduces the BER for measurements with the pulse duration of 100 ps and time bin duration of 100 ps. For all measurements involving the time bin duration of 50 ps, the impact of the RS code is negligible, which can be attributed to the high amount of flipped bits in the TR-PPM frames that carry the parity bytes. When considering time bin durations smaller than the pulse duration, the effect of the additive noise is especially significant, as the detection threshold may be reached over a time span longer than the time bin duration in systems employing a timer-based TDC.

Comparing measurements with and without the 20 km SMF, the B2B measurements result in a lower overall BER than when the 20 km fiber is connected. BER degradation in the latter case can be attributed to dispersion in the fiber, which causes degradation of the pulse shape and a reduction in the steepness of the rising edge. This, in turn, increases sensitivity to additive noise, resulting in errors in pulse position measurements by the ESTT.

The presented pulse waveforms after the RF transmission show distortions not dissimilar to existing research on RoF systems, where waveforms were captured after the optical transmission network.

The primary factor influencing the performance of the ARoF TR-PPM communication system is the time bin duration, which directly determines the system's tolerance to jitter. The results validate the effectiveness of the implemented encoding algorithms, as enabling ECC reduces the BER in both the 20 km SMF and B2B setups. Tests with a 20 km SMF show only a slight BER increase over the B2B setup, which remains negligible for data transmission. In both configurations, multiple combinations of pulse durations and time bin durations resulted in a BER of $<8.17 \times 10^{-7}$, which is below the threshold corresponding to a single bit error after PPM signal demodulation.

**Full description can be seen in Annex 6.**

## 3.2 Design and Evaluation of ISAC-Capable PPM-Based Radar System

This section presents the first implementation of an ARoF-based ISAC-capable radar system utilizing PPM, with a custom-built modulator and a high-precision time tagger, the ESTT 7 Series [160], enabling sub-nanosecond PPM slot durations and transmission over a long SMF span.

Compared to commonly used radar sensing solutions, such as those used in autonomous driving, aerial and ground object monitoring, and weather monitoring [161–164], namely frequency modulated continuous wave (FMCW) and pulse-Doppler radars, both of which offer range and velocity measurement capabilities, the proposed architecture addresses several limitations. FMCW radars are usually quite power-hungry due to continuous transmission and reception and require complex RAUs; meanwhile, pulse-Doppler radars encounter limitations in performing precise absolute range measurements and in detecting slow-moving targets as they rely on Doppler shifts [165, 166]. The proposed architecture achieves precise range measurements by directly measuring the pulse time of arrival (ToA) even for low-velocity or stationary targets. When combined with ARoF, the PPM waveform used mitigates the phase noise accumulation issue in optical FMCW systems [167–169].

A 6.6 GHz pulse radar was implemented due to the extensive super-high-frequency (SHF) infrastructure [170, 171], which can be easily repurposed for ISAC systems. The impact of long SMF spans on the quality of the PPM signal, measured BER, and range accuracy was investigated. Also, the impact of fiber-induced chromatic dispersion compensation in the optical subsystem is evaluated, given that PON systems are intrinsically designed and assessed with dispersion effects accounted for.

### Experimental System Description

The experimental system consisted of the central office (CO), where the optical carrier and the RF signals were generated and detected, and the RAU, which radiated and received the RF signal, as shown in Fig. 3.7.

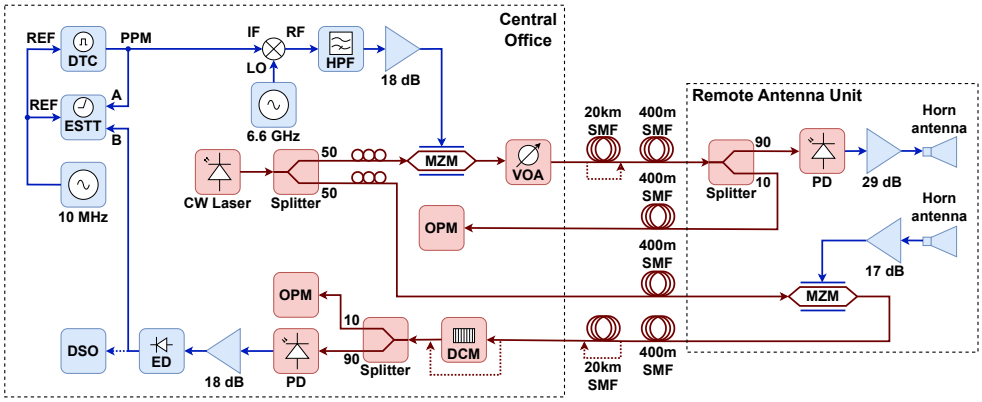



Fig. 3.7. Setup block diagram of the ISAC-capable PPM-based radar system utilizing ARoF.

The transmitted PRBS was generated in MATLAB software, using the 623-order Mersenne Twister pseudo-random number generator. In total, $5.12 \times 10^6$ bits were generated, saved as 40 data files, each containing 16000 PPM symbols (one symbol being 8 bits long, therefore the modulation order $M = 256$), and loaded into the modulator control software on the PC.

In the CO, the baseband PPM waveform was generated using the custom-built PPM modulator. The PPM waveform was mixed with the 6.6 GHz RF carrier, generated by the Anritsu MG3690C signal generator, which served as the local oscillator (LO). The up-converted signal was then filtered to remove any remaining baseband components. The filtered signal was amplified and fed into the RF input port of the MZM. An Exail Technologies MX-LN-40 MZM with a 40 GHz bandwidth was used to modulate the optical carrier with the up-converted PPM waveform. The optical carrier was generated using an ID Photonics Cobrite DX-4 CW laser. The optical carrier wavelength was 1550 nm, and the laser's optical output power was +12 dBm. The optical carrier was split by an optical splitter (ratio: 50/50) to use the same laser source for both the transmitter and receiver links, and then passed through polarization controllers. The optical output of the MZM was routed to an EXFO FVA-3150 VOA, which was used to precisely control the optical power incident on the PD in the RAU, maintaining a consistent level of $-15$ dBm across all connection scenarios. This optical power level enabled the PD to receive the signal without saturation or amplitude clipping. The optical signal was passed to the RAU through a 400 m long SMF span with the option to add an additional 20 km of SMF.

In the RAU, the optical signal from the CO was split by an optical splitter (ratio: 90/10), with 10% of the output sent to the OPM. The signal was converted to the electrical domain using the Conquer KG-PT-10G-SM-FA PD, which features 10 GHz 3-dB bandwidth. The AC-coupled

electrical output of the PD was amplified and then radiated by the Pasternack WR-159 horn antenna with 20 dBi gain and a frequency range of 4.9 GHz to 7.05 GHz.

On the receiver side, the same type of antenna as in the transmitter was used. The antennas were located next to each other, and the measured isolation between the antennas was 40 dB. The received signal was amplified and fed into the RF input of another MZM, which receives the optical carrier from the CO. The optical output of the MZM was fed into a TeraXion Clear Spectrum TDCMX tunable dispersion compensation module (DCM), which could be bypassed and replaced with a 3 dB optical attenuator to preserve the same $-15$ dBm optical power at the PD. The signal propagated through a 400 m SMF span, with the option to add 20 km of SMF. The total dispersion for both 20 km SMF (total 40 km) spools was measured to be 681 ps/nm at 1550 nm. The optical signal was subsequently delivered to the PD, and the resulting electrical signal was amplified and down-converted using a custom-built envelope detector (ED). Waveform monitoring and capture were performed with a Keysight DSOZ334A DSO, which offers a 33 GHz bandwidth and 80 GSa/s sampling rate.

The received and down-converted signal was sent to the "B" input of the ESTT, whereas the "A" input of the ESTT was connected to the modulator to record the time tags of the transmitted pulses, which are necessary for range estimation. Both the custom-built modulator and the ESTT were connected to the same ultra-stable 10 MHz reference signal generator with stability of less than $\pm 0.5$ ppb, to exclude possible clock drift-caused errors, as the internal clocks of the two devices do not share exactly the same clock frequency. It slightly varies over time, which is highly problematic when working with slot durations in the sub-nanosecond range.

**Experimental Parameters**

The subframe duration $T_{\text{sf}} = 300$ ns was chosen as such to make sure that, at every tested slot duration $\Delta$, pulses do not arrive within the dead time window of the ESTT. Although the subframe duration can be adjusted to maximize bit rate, to maintain consistency, it was kept constant.

The slot duration range of 10—1000 ps was chosen, as $\Delta = 10$ ps is the shortest possible slot duration that can be generated by the custom-built modulator, due to the limitation of the used DDL IC. The upper limit of slot duration equal to 1000 ps was chosen as it represents the lower end of the typical slot durations used in real-world state-of-the-art PPM data transmission systems, such as those used by National Aeronautics and Space Administration (NASA) and European Space Agency (ESA) [33, 34, 172]. The presented system can achieve an undetectable low error rate at this slot duration.

The PPM transfer frame size was set to the maximum allowable by the DTC, meaning that $128 \times 10^3$ bits were transmitted in a single transfer frame.

The optimal PPM order in terms of bit rate was calculated and is shown in Fig. 3.8. As can be observed, the optimal number of bits per symbol is 8; therefore, the modulation order $M = 256$.

The maximum bit rate for the given set of constraints ($T_{\text{sf}} = 300$ ns, $T_{\text{break}} = 20$ ms, $N =$

16000) is around 5 Mbit/s, and, as such, the bit rate is acceptable and close to other practically implemented systems [173]. The full list of experimental parameters is shown in Table 3.1.

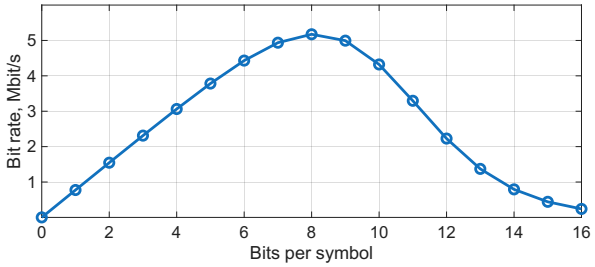



Fig. 3.8. Bit rate as a function of bits per symbol.

Table 3.1

Summary of the Main Experimental Parameters

| Parameter | Value |
|---|---|
| Modulation type | PPM |
| Slot duration $\Delta$ | 10–1000 ps |
| Modulation order $M$ | 256 |
| Bits per symbol | 8 |
| PPM transfer frame size $N$ | 16000 symbols |
| Subframe duration $T_{sf}$ | 300 ns |
| Number of transfer frames sent | 40 |
| Total number of bits sent | $5.12 \times 10^6$ |
| Pulse FWHM $\tau$ | 2.5 ns |
| RF carrier frequency | 6.6 GHz |
| Distance to the static reflector | 4 m |
| Optical B2B distance | 800 m |
| Total distance with SMF | 40.8 km |
| Optical carrier wavelength | 1550 nm |
| DCM value | −681 ps/nm |

**Experimental Configurations**

The measurements were conducted with a static metallic reflector located 4 m from the RAU due to space constraints. This distance provides optimal pulse amplitude at the receiver for data transmission and ranging tests. The data transmission experiments were conducted with and without Gray coding in four system connection configurations:

1) electrical back-to-back (B2B) connection, where the modulator was directly connected to the ESTT via a coaxial cable;
2) optical B2B connection, where the optical transmission network was connected with only the 800 m (400 m each direction) SMF;

3) optical connection with 40 km SMF, where 20 km spools were added in the optical branches that carry the PPM signal in each direction;
4) optical connection with 40 km SMF and DCM.

The range measurements were conducted for all three optical connection scenarios by measuring the ToA of the pulses on both channels of the ESTT and calculating the ToF. The actual ToF in the RF channel can be calculated by subtracting the system propagation delay from the measured time difference. The propagation delay was measured by the ESTT: 4.005752 µs for the optical B2B connection, 202.374635 µs for the connection with 40 km SMF, and 202.418792 µs for the connection with a 40 km SMF with DCM. The average ToF was calculated over each PPM transfer frame to eliminate relatively large range discrepancies that can be present when considering each transmitted and received pulse individually. The distance $d$ was calculated by knowing the propagation velocity, i.e., the speed of light:

$$d = \frac{(t_{\mathrm{m}} - t_0)}{2} \cdot c \,, \tag{3.1}$$

where $t_{\mathrm{m}}$ is the measured average time difference between the transmitted and received pulses, $t_0$ is the propagation delay in the system, and $c$ is the speed of light.

Importantly, the static propagation delay is also temperature dependent, which is especially noticeable in long SMF links. Since the propagation time through standard (solid-core) SMF optical fiber changes by approximately 40 ps/km/K at 1550 nm [174, 175]. Therefore, the 40 km SMF link configuration can experience a delay drift of approximately 1.6 ns/K (e.g., $t_{\mathrm{m}} - t_0$). From equation (3.1), this corresponds to an uncompensated apparent range shift or inaccuracy of about 24 cm/K (e.g., $d$). Thus, to maintain sub-centimeter range accuracy, the residual error in the static propagation delay must be kept below approximately 67 ps. In practice, this can be achieved by periodically or continuously recalibrating the static propagation delay using an optical loop-back system. The measured drift can then be subtracted from the subsequent range measurements to maintain sub-centimeter accuracy over time.

While the ESTT offers picosecond-level timing accuracy that enables centimeter-level range accuracy, its ability to resolve multiple targets is limited by the 40 ns dead time, which corresponds to about 6 m separation between detectable targets. If the dead time of the ESTT were to be eliminated, the range resolution $\Delta R$ is limited by the formula $\Delta R = c \cdot \tau/2$, where $c$ is the speed of light and $\tau$ is the pulse duration.

**Preliminary Testing**

Signal waveforms with a pulse duration of $\tau = 2.5$ ns were captured with the DSO for all system connection configurations and are displayed in Fig. 3.9.

Fig. 3.9. Captured pulse waveforms: (a) electrical B2B connection, (b) optical B2B connection, (c) optical connection with 40 km SMF, (d) optical connection with 40 km SMF and DCM.

A slight pulse expansion effect can be observed, with the FWHM of the pulse being expanded to about 3.1 ns. In all cases, the width of the falling edge was measured to quantify the system's jitter. The falling edge was measured because the jitter is the same for both edges of the pulse, and the DSO was triggered from the rising edge. In Fig. 3.9 (a), an edge width of 47 ps can be observed, which matches well with the jitter measurements using the ESTT. However, all three optical connection scenarios featured significantly increased jitter. For the optical B2B scenario, the recorded edge width was 227 ps. For the 40 km SMF scenario, the edge width increased to 318 ps due to accumulated positive chromatic dispersion along the fiber. In this case, the resulting group-velocity dispersion caused different spectral components of the signal to propagate at different velocities, leading to temporal pulse broadening and reduced edge slope, and thereby increasing the measured jitter due to larger noise susceptibility. Meanwhile, with the introduction of the DCM, the edge width decreased to 295 ps, as the applied negative dispersion only partially compensated the accumulated higher-order dispersion, slightly reducing the temporal spread of the pulse. Although the nominal dispersion values were matched, complete restoration of the original edge width could not be achieved due to residual higher-order dispersion and dispersion slope mismatch between the SMF and DCM.

The observed transition width increase can be explained by the chromatic dispersion effect in a double-sideband intensity modulation / direct detection (IM/DD) ARoF link. Chromatic dispersion is strongly dependent on signal bandwidth, increasing approximately quadratically with increasing bandwidth or data rate. However, under these conditions, the impact of chromatic dispersion remains sufficiently limited to allow signal transmission over optical links exceeding 100 km. Chromatic dispersion introduces deterministic frequency-dependent phase shifts and group-delay differences among the optical carrier and modulation sidebands. After square-law photodetection, this phase distortion is converted into a frequency-dependent electrical magnitude response or dispersion-induced RF power fading. Consequently, the signal components contributing to the pulse transition are delayed and attenuated non-uniformly, which causes tem-

poral pulse broadening, increases the transition time, and reduces the edge slope at the detection threshold. Since the RMS timing jitter of a threshold-triggered receiver due to additive voltage noise can be approximated as the voltage-noise RMS divided by the signal slope at the threshold crossing, the reduced slope directly increases the measured timing jitter. Using the measured transition widths as a first-order inverse indicator of edge slope, the increase from 227 ps in the optical B2B case to 318 ps after 40 km SMF corresponds to an approximately 29% normalized slope reduction and an expected jitter increase factor of about 1.4. With DCM, the transition width decreased to approximately 295 ps, corresponding to a partial slope recovery of about 8%, which confirms that dispersion compensation partially restores the pulse transition.

The impact of the pulse duration $\tau$ on the BER was explored, by measuring the BER in system connection configurations 2 to 4 and with pulse durations 2.5 ns, 5 ns, 7.5 ns and 10 ns, at slot duration $\Delta = 250$ ps. The chosen pulse durations represent the lower end of those actually used [176]. The measurements were conducted without Gray coding, and the results are shown in Fig. 3.10, from which it can be observed that the BER remains almost constant across all tested pulse durations. This is expected, as the pulse duration $\tau$ should not affect the BER, notwithstanding other system factors such as available bandwidth, since the time tagger reacts only on the rising edge of the pulse. The approximate bandwidth of the shortest tested pulse is about 400 MHz, so this pulse duration can be used in further experiments.

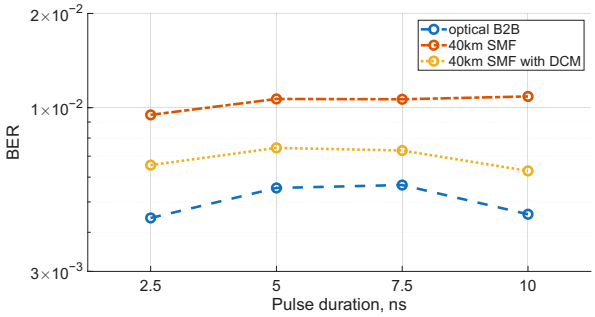



Fig. 3.10. BER as a function of pulse duration.

**Results**

The data transmission measurement results without Gray coding are shown in Fig. 3.11 (a), while the results with Gray coding are shown in Fig. 3.11 (b). The estimated BER lower limit is $5.86 \times 10^{-7}$ at a 95 % confidence level, given the number of bits sent.

As shown in the reported results, in the electrical B2B configuration, zero errors were observed over $5.12 \times 10^6$ bits at $\Delta = 100$ ps, meaning the modulator achieved error-free transmission with and without Gray coding, whereas at $\Delta = 50$ ps slot duration, the Gray code significantly reduced the BER. The optical transmission network significantly degraded the BER, achieving error-free transmission only at $\Delta = 500$ ps for the optical B2B case and at $\Delta = 750$ ps for cases with 40 km SMF.

Considering the existing methodology and testing approaches [33, 34], which focus on high photon efficiency and present the BER as a function of photons per slot, the presented PPM modulator and the transmission network show improved performance in terms of BER and meet the CCSDS 141.0-B-1 requirement [99] of the jitter RMS ≤10% of the slot duration at $\Delta \geq 100$ ps, in the electrical B2B configuration, which is the lower than the 125 ps slot duration allowed by the standard and much lower than ones practically used (1 ns). In the optical configurations, improvements were observed at $\Delta \geq 750$ ps slot durations. For all cases, when the BER does not approach the established limit, the 95 % confidence interval is less than 6 %.

It can be seen that adding a 40 km SMF span slightly degrades performance compared to the optical B2B connection scenario. The impact is not significant, as the system achieves error-free transmission at $\Delta \geq 750$ ps. This degradation is consistent with the observed edge broadening, where accumulated chromatic dispersion reduced the edge slope and increased jitter, leading to slightly increased BER in this case.

The results obtained with the 40 km SMF and DCM value of −681 ps/nm, which nominally compensated the accumulated second-order dispersion at the carrier wavelength, show a slight improvement in BER. The performance did not fully return to the level observed in the optical B2B case due to residual higher-order dispersion and practical device limitations.

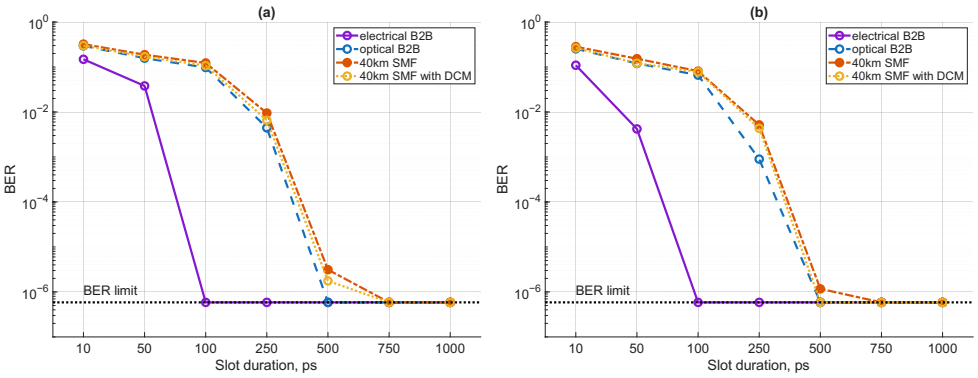



Fig. 3.11. Measured BER as a function of slot duration: (a) without Gray coding, (b) with Gray coding.

As for the range measurements, presented in Table 3.2 and Fig. 3.12, in the optical B2B connection, the absolute range deviation was approximately 0.6741 cm. With the addition of a 40 km SMF, the deviation increased slightly to 0.8610 cm, while incorporating the DCM reduced the deviation to 0.6144 cm, but in this case, the interquartile range was larger. The results are consistent with the previously described considerations and show that dispersion compensation can slightly improve the accuracy. The effect of the dispersion in the SMF is slight, at least in the tested distance, and the main factor impacting the range accuracy is the accuracy of the ESTT and the jitter introduced by other hardware (PD, envelope detector, etc.), as only the measurement of the relative ToA between the transmitted and received pulses is required, which

is not impacted by the quality of the generated pulse sequence. Conversely, the jitter present in the transmission system degrades measurement accuracy, and it is not possible to achieve ToF measurement accuracy close to the stated RMS accuracy of the ESTT of about 1.5 ps.

The presented architecture shows improved accuracy compared to existing, more complex and costly solutions [177–179]; on the other hand, newer experimental terahertz systems report sub-micron accuracy [180] using interferometric ToF.

The broader and slightly shallower pulse rising edge, which results from the dispersion in the SMF, impacts the BER and range accuracy measurements as the ESTT triggers at a set threshold voltage; therefore, additive noise in the pulse waveform may cause the triggering event to happen at a time, which is slightly before or after the expected time.

Table 3.2

Range Measurement Results

| **Connection** | **Mean range, m** | **Absolute deviation, cm** | **Standard deviation, cm** | **Interquartile range, cm** |
|---|---|---|---|---|
| Optical B2B | 4.0198 | 0.6741 | 0.1803 | 0.2789 |
| 40 km SMF | 4.0189 | 0.8610 | 0.2405 | 0.3657 |
| 40 km SMF with DCM | 4.0188 | 0.6144 | 0.1858 | 0.3330 |

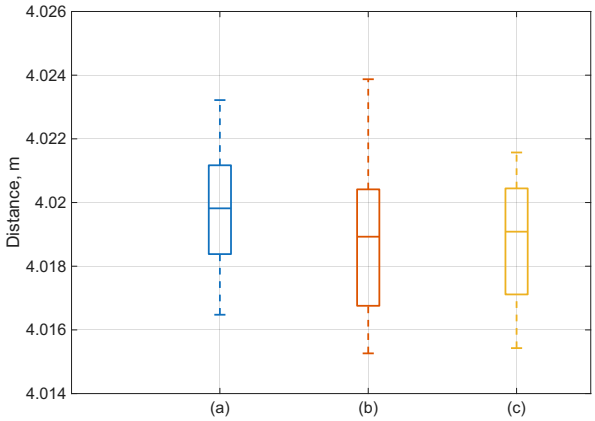



Fig. 3.12. Range measurement errorbar plot: (a) optical B2B connection, (b) optical connection with 40 km SMF, (c) optical connection with 40 km SMF and DCM.

In summary, using the optical transmission network, error-free transmission was achieved at a slot duration of 500 ps, and with an additional 40 km of SMF, at 750 ps. The system outperforms existing solutions in both BER and the minimum usable slot duration, and is ISAC-capable. Gray coding reduced the resulting BER, making it effective for PPM data transmission.

The range measurement accuracy was 0.6741 cm in the optical B2B case and increased slightly to 0.8610 cm in the case with a 40 km SMF. The effect of dispersion compensation was

tested and found to reduce the BER and to slightly increase the range accuracy. The improvement is slight and may not justify the added complexity and cost. The range accuracy achieved with the time tagger significantly outperforms that of widely used radar systems, and enables accurate range and velocity estimation with a lower power budget than an FMCW radar, without depending on Doppler-induced frequency shifts. The main limitation of the range resolution, currently 6 m for multi-target scenarios, is the dead time of the TDC. While the pulse duration does not carry information in PPM, reducing it is important for energy efficiency and range resolution in ISAC, given that the TDC dead time is kept low.

**Full description can be seen in Annex 7.**

## 3.3 Summary of the Third Thesis

The third thesis was devoted to proving that in optical PPM-based ISAC systems, a BER below $1 \times 10^{-6}$ along with a sensing accuracy below 5 cm at a range of at least 4 m with optical transmission distance exceeding 40 km can be achieved by using high-order PPM and a time tagger for SLR applications as the receiver. ARoF-based communication system using PPM was developed and tested with 20 km of SMF and 5 m 28 GHz RF link, using pulses as short as 100 ps. The experimental validation proved that the PPM waveform is highly resilient to distortions introduced by the transmission network, achieving BER values as low as $8.17 \times 10^{-7}$. This system was used as a testbed to develop a PPM-based ISAC pulse radar system, employing a time-tagger as the receiver. For the first time, joint radar sensing and communications using a 6.6 GHz PPM-based system with up to 40 km of SMF was experimentally demonstrated. The experimental results using 10–1000 ps slot durations, PPM order of 256, and a subframe duration of 300 ns achieved BER values as low as $5.86 \times 10^{-7}$ at a 95 % confidence level, with and without Gray coding. In the distance measurements, absolute deviation below 0.861 cm was observed. The data transmission and distance measurement test results significantly exceeded the target set out in this thesis, therefore proving it. Additionally, the impact of chromatic dispersion on the PPM waveform was explored and found not to significantly affect the BER and range accuracy.

**Full description containing the results presented in this Chapter can be seen in Annexes 6 and 7.**

# CONCLUSIONS

The Thesis is written as a summary of thematically unified scientific publications and is devoted to the design, implementation, and experimental validation of PPM-based communication systems, with the main objective being to design, develop, and test a PPM-based ISAC-capable joint radar and communication system utilizing ARoF technology and a custom-built PPM modulator with a commercial time-tagger as the demodulator, which can serve as a testbed for future UWB sensing, as well as space communication research. The main results and findings of the Thesis are as follows:

1. An experimental testbed and an AWG-based setup have been developed to explore PPM signal detection with a high-precision time-tagger for SLR applications. It was shown that additive noise on the PPM waveform can significantly impact the BER in time-tagger-based systems because the detection threshold level is fixed, potentially causing a false time tag in a neighboring time slot. Nevertheless, it was demonstrated that a time-tagger is a robust and highly precise means for PPM signal demodulation under the test conditions.
2. Two programmable digital delay line-based PPM modulators have been developed and experimentally validated. The tests indicate stable PPM sequence generation with RMS jitter as low as 7.65 ps. The most recently developed modulator is capable of generating a 16000-symbol-long PPM sequence with slot duration as low as 10 ps and reconfigurable modulation order. The concept of a DDL-based modulator was verified and proven to be an excellent, highly stable means of PPM signal generation in subsequent experiments.
3. The jitter distribution was analyzed and found to be distributed approximately normally, thereby enabling the use of ECC algorithms. The systematic errors, including clock drift and synchronization between the transmitter and receiver, were analyzed. It was found that the clock drift manifests as a constant offset from the expected pulse positions in the PPM sequence, while synchronization errors provide for a constantly increasing offset. Techniques such as a synchronization preamble in the pulse sequence can be used to mitigate these issues.
4. It was found that Gray coding provides for the most significant decrease in BER, as the code allows for one bit error to occur when the pulse is received in the neighboring time slot, which is the most common cause of errors. RS code was proposed to correct bit errors in the transmitted data, and simulations show that it provided the most benefit in the cases when clock drift error is present.
5. Electrical and optical pulse expansion techniques were proposed, as the time-tagger has a minimum required pulse duration. The experimental results demonstrate that a pulse can be expanded electrically using an LPF, and optically using an FBG to 2–3 times its original duration while preserving the waveform shape for stable detection

using the time-tagger.

6. An ARoF-based PPM communication system was designed and experimentally validated, achieving BER values as low as $8.17 \times 10^{-7}$ using 200 ps slot duration using 20 km long SMF span and a 5 m RF link. It was shown that NOE do not significantly affect the PPM waveform and validates PPM as an efficient and robust means for data transmission in optical communication systems.
7. An ISAC-capable ARoF-based 6.6 GHz joint radar and communication system was developed and experimentally validated. The system achieved BER values as low as $5.86 \times 10^{-7}$ at a 95 % confidence level, with and without Gray coding, and absolute range measurement deviation below 0.861 cm, using a total SMF distance of 40 km and a 4 m distance to the target. The main contributing success factor was the use of the high-precision time-tagger, which was experimentally demonstrated for the first time in this Thesis; however, the dead time of the time-tagger significantly limits the range resolution of such a system.
8. The impact of chromatic dispersion was evaluated by using a tunable DCM and found to be insignificant at least in the tested SMF span distances. While dispersion compensation slightly decreased BER and improved range accuracy, the slight effects do not outweigh the added cost and complexity.

The main results presented in this Thesis have been published in three peer-reviewed international journals ranking in the top 25th percentile (Q1) by citation index, as well as four peer-reviewed international conference proceedings.

The findings of this Thesis are an important contribution to the field of UWB-based ISAC-capable systems and can be extended to the field of deep space communications, which increasingly relies on time-tagging technology and PPM for long-range, robust, energy-efficient data links. In future applications, the dead time of the time-tagger (40 ns in the case of ESTT) must be decreased, as this is the main limiting factor of the range resolution (around 6 m in the presented research). Also, as attention is paid to higher throughput of such communication systems, significant software limitations must be resolved, as the break between the transfer frames significantly limits the achievable real-world data rate, even though the developed modulator is capable of multi-gigabit-per-second data transfer rates at the hardware level.

# REFERENCES


[1] Yang, L., and Giannakis, G. "Ultra-wideband communications: an idea whose time has come." *IEEE Signal Processing Magazine* 21.6 (2004), pp. 26–54. DOI: 10.1109/MSP.2004.1359140.

[2] Yajnanarayana, V., and Handel, P. "Joint Estimation of TOA and PPM Symbols Using Sub-Nyquist Sampled IR-UWB Signal." *IEEE Communications Letters* 21.4 (Apr. 2017), pp. 949–952. ISSN: 1089-7798. DOI: 10.1109/LCOMM.2017.2650231.

[3] Jajodia, B., Mahanta, A., and Ahamed, S. R. "IEEE 802.15.6 WBAN Standard Compliant IR-UWB Time-Hopping PPM Transmitter using SRRC signaling pulse." *AEU – International Journal of Electronics and Communications* 117 (Apr. 2020), p. 153119. ISSN: 1434-8411. DOI: 10.1016/J.AEUE.2020.153119.

[4] Youssef, A. A. "Adaptive LDPC coded high data rate based IR-UWB combined with VMIMO system for vehicular communication links." *AEU – International Journal of Electronics and Communications* 169 (Sept. 2023), p. 154747. ISSN: 16180399. DOI: 10.1016/j.aeue.2023.154747.

[5] Somov, A., and Baraev, A. "Consist-to-Consist communications in the trains: Is it time to use ultra wide-band?" *Computers & Electrical Engineering* 72 (Nov. 2018), pp. 965–975. ISSN: 0045-7906. DOI: 10.1016/J.COMPELECENG.2018.02.023.

[6] Salmento, M. L. G. et al. "An enhanced receiver for an impulsive UWB-based PLC system for low-bit rate applications." *Digital Signal Processing* 70 (Nov. 2017), pp. 145–154. ISSN: 1051-2004. DOI: 10.1016/J.DSP.2017.08.003.

[7] Duan, S. et al. "Ultra-Wideband Radio Channel Characteristics for Near-Ground Swarm Robots Communication." *IEEE Transactions on Wireless Communications* 19.7 (July 2020), pp. 4715–4726. ISSN: 1536-1276. DOI: 10.1109/TWC.2020.2986446.

[8] Rendevski, N., and Cassioli, D. "Potentials of low-complexity Rake receivers for 60 GHz UWB wireless communication systems." *2015 IEEE 1st International Forum on Research and Technologies for Society and Industry, RTSI 2015 – Proceedings* (2015), pp. 94–99. DOI: 10.1109/RTSI.2015.7325077.

[9] Ghavami, M., Michael, L. B., and Kohno, R. *Ultra Wideband Signals and Systems in Communication Engineering*. John Wiley & Sons, Ltd, 2004. DOI: 10.1002/0470867531.

[10] Nguyen, C., and Miao, M. *Design of CMOS RFIC Ultra-Wideband Impulse Transmitters and Receivers*. Springer International Publishing, 2017. DOI: 10.1007/978-3-319-53107-6.

[11] Chandrakasan, A. P. et al. “Low-Power Impulse UWB Architectures and Circuits.” *Proceedings of the IEEE* 97.2 (Feb. 2009), pp. 332–352. DOI: 10.1109/jproc.2008.2008787.

[12] Black, H. S. et al. “A Multichannel Microwave Radio Relay System.” *Transactions of the American Institute of Electrical Engineers* 65.12 (Dec. 1946), pp. 798–806. DOI: 10.1109/t-aiee.1946.5059251.

[13] Mahdiraji, G. A., and Zahedi, E. “Comparison of Selected Digital Modulation Schemes (OOK, PPM and DPIM) for Wireless Optical Communications.” *2006 4th Student Conference on Research and Development*. June 2006, pp. 5–10. DOI: 10.1109/SCORED.2006.4339297.

[14] Barnwell, N. et al. “The miniature optical communication transceiver-A compact, power-efficient lasercom system for deep space nanosatellites.” *Aerospace* 6.1 (2019). ISSN: 22264310. DOI: 10.3390/aerospace6010002.

[15] Elganimi, T. Y. “Studying the BER performance, power- and bandwidth- efficiency for FSO communication systems under various modulation schemes.” *2013 IEEE Jordan Conference on Applied Electrical Engineering and Computing Technologies, AEECT 2013. IEEE Computer Society.* (2013). DOI: 10.1109/AEECT.2013.6716426.

[16] Cui, S., Goldsmith, A., and Bahai, A. “Energy-Efficiency of MIMO and Cooperative MIMO Techniques in Sensor Networks.” *IEEE Journal on Selected Areas in Communications* 22.6 (Aug. 2004), pp. 1089–1098. DOI: 10.1109/jsac.2004.830916.

[17] Hamkins, J. *Pulse Position Modulation*. Nov. 2007. DOI: 10.1002/9781118256053.ch32.

[18] Dai, L. et al. “Research on the Pulse-position Modulation in the Digital Communication System.” *2021 International Conference on Wireless Communications and Smart Grid (ICWCSG)*. 2021, pp. 8–12. DOI: 10.1109/ICWCSG53609.2021.00009.

[19] Huan, L. “Simulation on the design of digital pulse position modulation system.” *International Conference on Neural Networks, Information, and Communication Engineering (NNICE 2022)*. Ed. by Tiwari, R. SPIE, July 2022. DOI: 10.1117/12.2640677.

[20] Proakis, J., and Salehi, M. *Digital Communications, 5th edition*. McGraw-Hill Higher Education, 2008.

[21] Karp, S., and Gagliardi, R. “The Design of a Pulse-Position Modulated Optical Communication System.” *IEEE Transactions on Communications* 17.6 (Dec. 1969), pp. 670–676. DOI: 10.1109/tcom.1969.1090162.

[22] Jing, M., Li-ying, T., and Siyuan, Y. "Technologies and applications of free-space optical communication and space optical information network." *Journal of communications and information networks* (June 2016). DOI: 10.11959/j.issn.2096-1081.2016.005.

[23] Wilson, B., and Ghassemlooy, Z. "Pulse time modulation techniques for optical communications: a review." *IEE Proceedings J Optoelectronics* 140.6 (1993), p. 346. DOI: 10.1049/ip-j.1993.0055.

[24] Saeed, R. et al. "Ultra Wide Band (UWB) Ad-hoc Networks: Review and Trends." *Journal of Computer Science* 1.1 (Jan. 2005), pp. 35–39. DOI: 10.3844/jcssp.2005.35.39.

[25] *Pulse Position Modulation : Block Diagram, Circuit, Working, Generation with PWM & Its Applications*. URL: https://www.elprocus.com/pulse-position-modulation/.

[26] Green, R. J. "Comparison of pulse position modulation and pulse width modulation for application in optical communications." *Optical Engineering* 46.6 (June 2007), p. 065001. DOI: 10.1117/1.2746010.

[27] Ai-ping, H. et al. "A differential pulse position width modulation for optical wireless communication." *2009 4th IEEE Conference on Industrial Electronics and Applications*. 2009, pp. 1773–1776. DOI: 10.1109/ICIEA.2009.5138501.

[28] Sacko, D., and Kéïta, A. A. "Techniques of Modulation: Pulse Amplitude Modulation, Pulse Width Modulation, Pulse Position Modulation." *IJEAT* 7.2 (Dec. 2017), p. 9. URL: https://www.ijeat.org/wp-content/uploads/papers/v7i2/B5251127217.pdf.

[29] Jahid, A., Alsharif, M. H., and Hall, T. J. "A contemporary survey on free space optical communication: Potentials, technical challenges, recent advances and research direction." *Journal of Network and Computer Applications* 200 (Apr. 2022), p. 103311. DOI: 10.1016/j.jnca.2021.103311.

[30] Fu, X. et al. "Research and Simulation of PPM Modulation and Demodulation System on Spatial Wireless Optical Communication." *2010 Symposium on Photonics and Optoelectronics*. IEEE, June 2010. DOI: 10.1109/sopo.2010.5504142.

[31] Tang, W. et al. "The Research Process, Application, and the Future Development of Pulse-Position Modulation." *Journal of Physics: Conference Series* 2384.1 (Dec. 2022), p. 012026. DOI: 10.1088/1742-6596/2384/1/012026.

[32] Wang, Y. et al. "Research on PPM Modulation Performance of Deep Space Optical Communication." *2021 International Conference on Electronic Information Engineering and Computer Science (EIECS)*. 2021, pp. 5–8. DOI: 10.1109/EIECS53707.2021.9588043.

[33] Simon, W. P. et al. “Field-Programmable Gate Array Implementation of a Single Photon-Counting Receive Modem.” *Free-Space Laser Communications XXXVI*. Ed. by Hemmati, H., and Robinson, B. S. San Francisco, United States: SPIE, Mar. 2024, p. 58. DOI: 10.1117/12.3001097.

[34] Jhaidri, M.-A. et al. “Implementation of High-Photon-Efficiency Optical Modem for ESA’s Technology Demonstration of Deep-Space Optical Communication with the NASA Psyche Spacecraft.” *International Conference on Space Optics – ICSO 2024*. Antibes Juan-les-Pins, France: SPIE, July 2025, p. 211. DOI: 10.1117/12.3075346.

[35] Sodnik, Z., Furch, B., and Lutz, H. “Free-space laser communication activities in Europe: SILEX and beyond.” *Conference Proceedings – Lasers and Electro-Optics Society Annual Meeting-LEOS (pp. 78–79)*. (2006). DOI: 10.1109/LEOS.2006.278845.

[36] Cryan, R. A., and Unwin., R. T. “Optical Employing Space Communications Pulse Position Modulation.” *IEE Colloquium on Advanced Modulation and Coding Techniques for Satellite Communications*. (1992).

[37] Guelman, M. et al. “Acquisition and Pointing Control for Inter-Satellite Laser Communications.” *IEEE Transactions on Aerospace and Electronic Systems* 40.4 (Oct. 2004), pp. 1239–1248. ISSN: 1557-9603. DOI: 10.1109/TAES.2004.1386877.

[38] Al Zaman, A., and Islam, N. “Modulation Schemes and Pulse Shaping in Ultra-Wideband.” *IEEE SoutheastCon 2008*. Apr. 2008, pp. 142–146. DOI: 10.1109/SECON.2008.4494274.

[39] Huo, X. et al. “C-Band 200 Gbit/s/$\lambda$ PS-PAM-8 Transmission Over 2-km SSMF for Optical Interconnections.” *IEEE Photonics Journal* 16.3 (2024), pp. 1–7. DOI: 10.1109/JPHOT.2024.3381232.

[40] Pan, S., and Yao, J. “UWB-Over-Fiber Communications: Modulation and Transmission.” *Journal of Lightwave Technology* 28.16 (2010), pp. 2445–2455. DOI: 10.1109/JLT.2010.2043713.

[41] Pan, S., and Yao, J. “Performance evaluation of UWB signal transmission over optical fiber.” *IEEE Journal on Selected Areas in Communications* 28.6 (2010), pp. 889–900. DOI: 10.1109/JSAC.2010.100813.

[42] Abraha, S. T. et al. “Performance Evaluation of IR-UWB in Short-Range Fiber Communication Using Linear Combination of Monocycles.” *Journal of Lightwave Technology* 29.8 (2011), pp. 1143–1151. DOI: 10.1109/JLT.2011.2120595.

[43] Edwards, B. L. “Latest Status of the CCSDS Optical Communications Working Group.” *2022 IEEE International Conference on Space Optical Systems and Applications, ICSOS 2022*. IEEE, Mar. 2022, pp. 1–6. ISBN: 9781665434393. DOI: 10.1109/ICSOS53063.2022.9749734.

[44] Kim, M.-J. et al. “Performance Analysis and Implementation of Biased MC-PPM for Optical Energy Transfer and Communication System.” *Physical Communication* 71 (Aug. 2025), p. 102684. ISSN: 1874-4907. DOI: 10.1016/j.phycom.2025.102684.

[45] Huang, J. et al. “Real-Time and High-Speed Underwater Photon-Counting Communication Based on SPAD and PPM Symbol Synchronization.” *IEEE Photonics Journal* 13.5 (Oct. 2021), pp. 1–9. ISSN: 1943-0655. DOI: 10.1109/JPHOT.2021.3113659.

[46] Kaszubowska-Anandarajah, A. et al. “An IR-UWB Photonic Distribution System.” *IEEE Photonics Technology Letters* 20.22 (Nov. 2008), pp. 1884–1886. ISSN: 1941-0174. DOI: 10.1109/LPT.2008.2004989.

[47] Fujiwara, Y. “Self-Synchronizing Pulse Position Modulation With Error Tolerance.” *IEEE Transactions on Information Theory* 59.9 (Sept. 2013), pp. 5352–5362. ISSN: 1557-9654. DOI: 10.1109/TIT.2013.2262094.

[48] Mietzner, J., and Lampe, L. “Nested PPM for Visible Light Communication With Heterogeneous Optical Receivers.” *IEEE Photonics Journal* 16.4 (2024), pp. 1–12. DOI: 10.1109/JPHOT.2024.3406156.

[49] Dix-Matthews, B. P. et al. “Ultra-Wideband Free-Space Optical Phase Stabilization.” *IEEE Communications Letters* 25.5 (May 2021), pp. 1610–1614. ISSN: 1089-7798. DOI: 10.1109/LCOMM.2021.3053943.

[50] Landolsi, T., and Elrefaie, A. F. “Effects of pointing errors and channel fading on the performance of free-space optically-preamplified PPM systems.” *International Journal of Communication Systems* 29.15 (Oct. 2016), pp. 2313–2324. ISSN: 1074-5351. DOI: 10.1002/dac.3166.

[51] Wen, Y. et al. “Free Space Optical Integrated Sensing and Communication Based on LFM and CPM.” *IEEE Communications Letters* 28.1 (Jan. 2023), pp. 43–47. ISSN: 15582558. DOI: 10.1109/LCOMM.2023.3332658.

[52] Qaisar, M. U. F. et al. “The Role of ISAC in 6G Networks: Enabling Next-Generation Wireless Systems.” *IEEE Transactions on Network Science and Engineering* 13 (2026), pp. 7825–7861. DOI: 10.1109/TNSE.2026.3666665.

[53] Perez Santacruz, J. “Analog Radio-over-Fiber for 5G/6G Millimeter-Wave Communications.” Ph. D. Thesis. Eindhoven University of Technology, 2022.

[54] Singh, G. et al. “Toward 6G-V2X: Aggregated RF-VLC for Ultra-Reliable and Low-Latency Autonomous Driving.” *IEEE Communications Standards Magazine* 8.4 (2024), pp. 80–87. DOI: 10.1109/MCOMSTD.0001.2300005.

[55] Colson, S., and Hoff, H. “Ultra-Wideband Technology for Defence Applications.” *2005 IEEE International Conference on Ultra-Wideband*. Sept. 2005, pp. 615–620. DOI: 10.1109/ICU.2005.1570059.

[56] Kaushik, A. et al. “Integrated Sensing and Communications for IoT: Synergies with Key 6G Technology Enablers.” *IEEE Internet of Things Magazine* 7.5 (2024), pp. 136–143. DOI: 10.1109/IOTM.001.2400052.

[57] Campbell, S. P. *Integrated Sensing and Communications (ISAC) Report*. Tech. rep. Findings from the National ISAC Workshop, April 9–10, 2025. George Mason University, Office of Research, Innovation, and Economic Impact, May 2025. URL: https://rt.cto.mil/wp-content/uploads/2025/07/ISAC-Report-from-Apr-2025-Workshop.pdf.

[58] Liu, F. et al. “ISAC With UWB: Reliable Decoupling and Target Sensing.” *IEEE Transactions on Wireless Communications* 23.11 (2024), pp. 15957–15972. DOI: 10.1109/TWC.2024.3435070.

[59] Wang, X. et al. “Fundamental Limits on Joint Delay and Doppler Characterization in UWB ISAC Systems.” *2023 IEEE 98th Vehicular Technology Conference (VTC2023-Fall)*. 2023, pp. 1–6. DOI: 10.1109/VTC2023-Fall60731.2023.10333549.

[60] Cai, S. et al. “Pulse-Based ISAC: Data Recovery and Ranging Estimation for Multi-Path Fading Channels.” *IEEE Transactions on Communications* 71.8 (2023), pp. 4819–4838. DOI: 10.1109/TCOMM.2023.3277039.

[61] Yu, M. et al. “FPGA-Based Dual-Pulse Anti-Interference Lidar System Using Digital Chaotic Pulse Position Modulation.” *IEEE Photonics Technology Letters* 33.15 (2021), pp. 757–760. DOI: 10.1109/LPT.2021.3093109.

[62] Yeo, J. et al. “A Flash LiDAR with SA-Based Pulse Position Modulation for Multi-user Interference Cancellation.” *2025 IEEE International Symposium on Circuits and Systems (ISCAS)*. 2025, pp. 1–5. DOI: 10.1109/ISCAS56072.2025.11044208.

[63] Alabd, M. B. et al. “Modified Pulse Position Modulation for Joint Radar Communication Based on Chirp Sequence.” *IEEE Microwave and Wireless Components Letters* 32.10 (2022), pp. 1247–1250. DOI: 10.1109/LMWC.2022.3169287.

[64] Shi, X. et al. “BER Performance Analysis of Non-Coherent Q-Ary Pulse Position Modulation Receivers on AWGN Channel.” *Sensors* 21.18 (2021). DOI: 10.3390/s21186102.

[65] Pulkkinen, M. et al. “45.2% Energy efficiency improvement of UWB IR Tx by use of differential PPM in 180nm CMOS.” *2016 IEEE International Symposium on Circuits and Systems (ISCAS)*. 2016, pp. 193–196. DOI: 10.1109/ISCAS.2016.7527203.

[66] Li, L., and Townsend, J. K. “M-Ary PPM for Transmitted Reference Ultra-Wideband Communications.” *IEEE Transactions on Communications* 58.7 (July 2010), pp. 1912–1917. ISSN: 1558-0857. DOI: 10.1109/TCOMM.2010.07.080675.

[67] Luo, X., and Giannakis, G. B. "Achievable rates of transmitted-reference ultra-wideband radio with PPM." *IEEE Transactions on Communications* 54 (9 Sept. 2006), pp. 1536–1541. ISSN: 00906778. DOI: 10.1109/TCOMM.2006.881203.

[68] Aliaberi, A., Sofotasios, P. C., and Muhaidat, S. "Modulation Schemes for Visible Light Communications." *2019 International Conference on Advanced Communication Technologies and Networking (CommNet)*. Apr. 2019, pp. 1–10. DOI: 10.1109/COMMNET.2019.8742376.

[69] Dahri, F. A., Ali, S., and Jawaid, M. M. "A Review of Modulation Schemes for Visible Light Communication." *IJCSNS International Journal of Computer Science and Network Security* 18.2 (2018), pp. 117–125.

[70] *Optical communications coding and synchronization*. 1st ed. Recommended Standard CCSDS 142.0-B-1. Consultative Committee for Space Data Systems. Washington, DC, USA, Aug. 2019. URL: https://ccsds.org/Pubs/142x0b1.pdf.

[71] Tiwari, S., Jain, V. K., and Kar, S. "Performance evaluation of different Pulse Position Modulation schemes in atmospheric turbulence channel for ground-to-satellite optical communication." *2012 International Conference on Optical Engineering* (2012). DOI: 10.1109/ICOE.2012.6409599.

[72] Xu, Z., Shen, L., and Wang, J. "An improved differential pulse position modulation using soft-decision decoding." *2007 International Conference on Wireless Communications, Networking and Mobile Computing, WiCOM 2007* (2007). DOI: 10.1109/WICOM.2007.348.

[73] Pulkkinen, M. et al. "Low-Power Wireless Transceiver with 67-nW Differential Pulse-Position Modulation Transmitter." *IEEE Transactions on Circuits and Systems I* (2020). DOI: 10.1109/TCSI.2020.3013065.

[74] Urkowitz, H. "Energy detection of unknown deterministic signals." *Proceedings of the IEEE* 55.4 (1967), pp. 523–531. DOI: 10.1109/proc.1967.5573.

[75] Dillard, G. "Pulse-Position Modulation Based on Energy Detection." *IEEE Transactions on Aerospace and Electronic Systems* AES-9.4 (July 1973), pp. 499–503. DOI: 10.1109/taes.1973.309631.

[76] Durisi, G., and Benedetto, S. "Comparison between coherent and noncoherent receivers for UWB communications." *Eurasip Journal on Applied Signal Processing* 2005.3 (2005), pp. 359–368. ISSN: 11108657. DOI: 10.1155/ASP.2005.359.

[77] Hussein, S. S., youssif, A., and M., G. H. H. "Performance Analysis and Evaluation of TH-PPM and TH-BPSK under Dynamic Channel Environment." *International Journal of Future Computer and Communication* (2012), pp. 352–355. ISSN: 20103751. DOI: 10.7763/IJFCC.2012.V1.94.

[78] Khani, H. “Improved Detection Schemes for Non-coherent Pulse-Position Modulation.” *Wireless Personal Communications* 131.3 (Aug. 2023), pp. 2173–2192. ISSN: 0929-6212. DOI: 10.1007/s11277-023-10537-7.

[79] Munirathinam, R. et al. “Chaotic Non-Coherent Pulse Position Modulation Based Ultra-Wideband Communication System.” *2021 IEEE Microwave Theory and Techniques in Wireless Communications (MTTW)*. IEEE, 2021, pp. 52–57. DOI: 10.1109/mttw53539.2021.9607075.

[80] Cassioli, D. et al. “Low Complexity Rake Receivers in Ultra-Wideband Channels.” *IEEE Transactions on Wireless Communications* 6.4 (Apr. 2007), pp. 1265–1275. ISSN: 1536-1276. DOI: 10.1109/TWC.2007.348323.

[81] Zheng, Y. et al. “A 0.18 um CMOS Dual-Band UWB Transceiver.” *2007 IEEE International Solid-State Circuits Conference. Digest of Technical Papers*. IEEE, Feb. 2007, pp. 114–590. ISBN: 1-4244-0852-0. DOI: 10.1109/ISSCC.2007.373614.

[82] Lee, F., and Chandrakasan, A. “A 2.5nJ/b 0.65V 3-to-5GHz Sub banded UWB Receiver in 90nm CMOS.” *Int. Solid State Circuits Conference (ISSCC 07)*. 2007, pp. 116–117.

[83] Shariat, M. et al. “Comparison Between Several Methods of PPM Demodulation Based on Iterative Techniques.” *Telecommunications and Networking – ICT 2004*. Springer Berlin Heidelberg, 2004, pp. 554–559. DOI: 10.1007/978-3-540-27824-5_75.

[84] Sushchik, M. et al. “Chaotic pulse position modulation: a robust method of communicating with chaos.” *IEEE Communications Letters* 4.4 (Apr. 2000), pp. 128–130. DOI: 10.1109/4234.841319.

[85] Wang, W. et al. “Under-Sampling of PPM-UWB Communication Signals Based on CS and AIC.” *Circuits, Systems, and Signal Processing* 34.11 (Nov. 2015), pp. 3595–3609. ISSN: 0278-081X. DOI: 10.1007/s00034-015-0026-4.

[86] Kalisz, J. “Review of methods for time interval measurements with picosecond resolution.” *Metrologia* 41.1 (Dec. 2003), pp. 17–32. DOI: 10.1088/0026-1394/41/1/004.

[87] Mahjoubfar, A. et al. “Time stretch and its applications.” *Nature Photonics* 11.6 (June 2017), pp. 341–351. DOI: 10.1038/nphoton.2017.76.

[88] Jonass, J., Bespal’ko, V., and Lapkovskis, V. “Precision Time Meters for Ground and Space Applications.” *Space-Based Lidar Remote Sensing Techniques and Emerging Technologies*. Cham: Springer Nature Switzerland, 2024, pp. 309–318. DOI: 10.1007/978-3-031-53618-2_27.

[89] Steindorfer, M. A. et al. “Space Debris and Satellite Laser Ranging Combined Using a Megahertz System.” *Nature Communications* 16.1 (Jan. 2025), p. 575. ISSN: 2041-1723. DOI: 10.1038/s41467-024-55777-8.

[90] Piedra, M. A. S. et al. “First Results from the Newly Modernized San Fernando Laser Station: Commemorating 45 Years of Service.” *9th European Conference on Space Debris*. Vol. 9. Bonn, Germany, ESA Space Debris Office, Apr. 2025.

[91] Merz, R., Botteron, C., and Farine, P.-A. “A novel low complexity data demodulation algorithm for pulse position modulation.” *Digital Signal Processing* 22.3 (May 2012), pp. 535–543. DOI: 10.1016/j.dsp.2011.08.008.

[92] Kim, J., and Clerckx, B. “Wireless Information and Power Transfer for IoT: Pulse Position Modulation, Integrated Receiver, and Experimental Validation.” *IEEE Internet of Things Journal* 9.14 (July 2022), pp. 12378–12394. DOI: 10.1109/jiot.2021.3135712.

[93] ScioSense B.V. *Datasheet of TDC-GPX2*. 2018. URL: https://www.sciosense.com/wp-content/uploads/documents/TDC-GPX2-Datasheet.pdf.

[94] Mezerins, A., and Bespal’ko, V. “Estimation of analog-to-time and time-to-digital conversion efficiency in analog optical communication system testbed.” *Proceedings – 2015 Advances in Wireless and Optical Communications, RTUWO 2015*. IEEE, Nov. 2015, pp. 211–214. ISBN: 9781467374316. DOI: 10.1109/RTUWO.2015.7365754.

[95] Solovjova, T. et al. “Picosecond Pulse Expansion Using The Low-Pass Filter in Event Timer-Based PPM Communication System.” *Proceedings of 2022 Workshop on Microwave Theory and Techniques in Wireless Communications, MTTW 2022*. IEEE, Oct. 2022, pp. 29–34. DOI: 10.1109/MTTW56973.2022.9942566.

[96] Hamil, H. et al. “Design and FPGA real-time implementation of PWM and PPM modulation for Ultra Wide Band applications.” *2019 6th International Conference on Image and Signal Processing and their Applications (ISPA)*. 2019, pp. 1–5. DOI: 10.1109/ISPA48434.2019.8966916.

[97] Roche, R. J. et al. “Reconfigurable, intelligently-adaptive, communication system, an SDR platform.” *34th AIAA International Communications Satellite Systems Conference, 2016*. 2016. ISBN: 9781624104572. DOI: 10.2514/6.2016-5718.

[98] Schlemmer, H. et al. “Results from a CCSDS-compliant High Photon Efficiency Downlink SDR Platform.” *2019 8th International Workshop on Tracking, Telemetry and Command Systems for Space Applications (TTC)*. IEEE, Sept. 2019, pp. 1–5. ISBN: 978-1-7281-3700-1. DOI: 10.1109/TTC.2019.8895458.

[99] *Optical communications physical layer*. 1st ed. Recommended Standard CCSDS 141.0-B-1. Consultative Committee for Space Data Systems. Washington, DC, USA, Aug. 2019. URL: https://ccsds.org/Pubs/141x0b1.pdf.

[100] Spolitis, S. et al. "Demonstration of 512-TR-PPM Fiber Optical Transmission Link." *2023 Photonics & Electromagnetics Research Symposium (PIERS)*. 2023, pp. 1416–1422. DOI: 10.1109/PIERS59004.2023.10221307.

[101] Li, T., Zhou, H., and Yi, M. "Gray coded PPM performance with imperfect slot synchronization in optical communication." *Pacific Rim Conference on Lasers and Electro-Optics, CLEO - Technical Digest*. IEEE, Aug. 2009, pp. 1–2. ISBN: 9781424438303. DOI: 10.1109/CLEOPR.2009.5292732.

[102] Lv, L. et al. "Asymmetric Dual-Mode Constellation and Protograph LDPC Code Design for Generalized Spatial MPPM Systems." *IEEE Transactions on Communications* 71.6 (2023), pp. 3165–3177. DOI: 10.1109/TCOMM.2023.3253687.

[103] Ajewole, B. D., Owolawi, P. A., and Srivastava, V. M. "Error performance of coded BPSK OFDM-FSO system under atmospheric turbulence." *Journal of Communications* (2019), pp. 936–944. DOI: 10.12720/jcm.14.10.936-944.

[104] Jeong, J.-D. et al. "Design of block-coded group PPM modem for low-power and low-cost home energy management." *2016 International Conference on Information and Communication Technology Convergence (ICTC)*. IEEE, Oct. 2016, pp. 78–81. ISBN: 978-1-5090-1325-8. DOI: 10.1109/ICTC.2016.7763440.

[105] He., Z. et al. "Probabilistic Amplitude Shaping for IM/DD System Using Hard-Decision Decoding." *24th OptoElectronics and Communications Conference/International Conference Photonics in Switching and Computing*. IEEE, 2019. DOI: 10.23919/PS.2019.8817784.

[106] Kiasaleh, K., Yan, T.-Y., and Srinivasan, M. "Trellis-coded pulse-position modulation for optical communication systems impaired by pulsewidth inaccuracies." *Journal of Lightwave Technology* 17.8 (1999), pp. 1336–1346. DOI: 10.1109/50.779155.

[107] Sics, P. E. et al. "Programmable Delay Line Based High-speed PPM Modulator with 50 ps Time Resolution." *2023 Photonics & Electromagnetics Research Symposium (PIERS)*. 2023, pp. 1779–1786. DOI: 10.1109/PIERS59004.2023.10221245.

[108] Barrett, T. W. "History of Ultra Wideband Communications and Radar: Part I, UWB Communications." *Microwave Journal* (Jan. 2001), pp. 22–56.

[109] Barrett, T. W. "History of Ultra Wideband Communications and Radar: Part II, UWB Radars and Sensors." *Microwave Journal* (Feb. 2001), pp. 22–52.

[110] O'Meara, T. R. "The synthesis of band-pass, all-pass time delay networks with graphical approximation techniques." *Research Rept. 114* (1959).

[111] Hoffswell, R. A. "A Microstrip Line Stretcher." *Review of Scientific Instruments* 41.9 (Nov. 2003), pp. 1330–1331. DOI: 10.1063/1.1684808.

[112] Caputi, W. J. "Stretch: A Time-Transformation Technique." *IEEE Transactions on Aerospace and Electronic Systems* AES-7.2 (1971), pp. 269–278. DOI: 10.1109/TAES.1971.310366.

[113] Ishii, M., Yamada, G., and Miyatake, H. "US Patent No. US20130141148A1, Pulse stretching circuit and method." 2011. URL: https://patents.google.com/patent/US20130141148A1/en.

[114] Xiang, B. et al. "An integrated Ku-band nanosecond time-stretching system using improved dispersive delay line (DDL)." *2012 IEEE 12th Topical Meeting on Silicon Monolithic Integrated Circuits in RF Systems*. 2012, pp. 151–154. DOI: 10.1109/SiRF.2012.6160140.

[115] Zverev, A. I. *Handbook of Filter Synthesis*. John Wiley and Sons, Inc., 1967.

[116] Monti, G., and Tarricone, L. "Negative Group Velocity in a Split Ring Resonator-Coupled Microstrip Line." *Progress In Electromagnetics Research* 94 (2009), pp. 33–47. DOI: 10.2528/PIER09052801.

[117] Regalia, P., Mitra, S., and Vaidyanathan, P. "The digital all-pass filter: a versatile signal processing building block." *Proceedings of the IEEE* 76.1 (1988), pp. 19–37. DOI: 10.1109/5.3286.

[118] Caloz, C. et al. "Analog Signal Processing: A Possible Alternative or Complement to Dominantly Digital Radio Schemes." *IEEE Microwave Magazine* 14.6 (2013), pp. 87–103. DOI: 10.1109/MMM.2013.2269862.

[119] Elamien, M. B. et al. "Synthesis of Wideband High-Quality Factor Delay- Tunable Fully Differential All-Pass Filters." *IEEE Transactions on Microwave Theory and Techniques* 68.10 (2020), pp. 4348–4360. DOI: 10.1109/TMTT.2020.3011723.

[120] França Ferreira, J. A. de et al. "Design and Synthesis of Arbitrary Group Delay Filters for Integrated Analog Signal Processing." *2018 25th IEEE International Conference on Electronics, Circuits and Systems (ICECS)*. 2018, pp. 613–616. DOI: 10.1109/ICECS.2018.8617912.

[121] Zhang, Q., Gupta, S., and Caloz, C. "Synthesis of Narrowband Reflection-Type Phasers With Arbitrary Prescribed Group Delay." *IEEE Transactions on Microwave Theory and Techniques* 60.8 (2012), pp. 2394–2402. DOI: 10.1109/TMTT.2012.2198486.

[122] Zhang, Q., Sounas, D. L., and Caloz, C. “Synthesis of Cross-Coupled Reduced-Order Dispersive Delay Structures (DDSs) With Arbitrary Group Delay and Controlled Magnitude.” *IEEE Transactions on Microwave Theory and Techniques* 61.3 (2013), pp. 1043–1052. DOI: 10.1109/TMTT.2013.2241785.

[123] Gupta, S. et al. “Group-Delay Engineered Noncommensurate Transmission Line All-Pass Network for Analog Signal Processing.” *IEEE Transactions on Microwave Theory and Techniques* 58.9 (2010), pp. 2392–2407. DOI: 10.1109/TMTT.2010.2058933.

[124] Avignon-Meseldzija, E., Anastasov, J., and Milic, D. “A linear group delay filter with tunable positive slope for analog signal processing.” *International Journal of Circuit Theory and Applications* 49.5 (2021), pp. 1307–1326. DOI: https://doi.org/10.1002/cta.2995.

[125] Mondal, I., and Krishnapura, N. “Expansion and Compression of Analog Pulses by Bandwidth Scaling of Continuous-Time Filters.” *IEEE Transactions on Circuits and Systems I: Regular Papers* 65.9 (2018), pp. 2703–2714. DOI: 10.1109/TCSI.2018.2799080.

[126] Pactitis, S. A. *Active Filters: Theory and Design*. CRC Press, 2007.

[127] Rauscher, C. “Microwave Active Filters Based on Transversal and Recursive Principles.” *IEEE Transactions on Microwave Theory and Techniques* 33.12 (1985), pp. 1350–1360. DOI: 10.1109/TMTT.1985.1133225.

[128] Xia, J., Law, C. L., and Jiang, J. “A Novel 3–5 GHz Active Matched Filter for Impulse Radio Ultra-Wideband.” *IEEE Microwave and Wireless Components Letters* 19.7 (2009), pp. 458–460. DOI: 10.1109/LMWC.2009.2022133.

[129] Jarjar, M., and Ouazzani, N. P. el. “Three branch microwave channelized active bandpass filter.” *2019 International Conference on Wireless Networks and Mobile Communications (WINCOM)*. 2019, pp. 1–5. DOI: 10.1109/WINCOM47513.2019.8942576.

[130] Gomez-Garcia, R. et al. “Flexible Filters: Reconfigurable-Bandwidth Bandpass Planar Filters with Ultralarge Tuning Ratio.” *IEEE Microwave Magazine* 15.5 (2014), pp. 43–54. DOI: 10.1109/MMM.2014.2321094.

[131] Thomson, W. “Delay networks having maximally flat frequency characteristics.” English. *Proceedings of the IEE - Part III: Radio and Communication Engineering* 96 (44 Nov. 1949), 487–490(3). ISSN: 0369-8947. URL: https://digital-library.theiet.org/content/journals/10.1049/pi-3.1949.0101.

[132] Mini-circuits. *Low Pass Filter SLP-2400+*. URL: https://www.minicircuits.com/pdfs/SLP-2400+.pdf.

[133] Paschotta, R. *Pulse Stretchers*. URL: https://www.rp-photonics.com/pulse_stretchers.html.

[134] Steed, R. *Modelling of Optical Pulse Stretching using Circulating Cavities*. Feb. 2015. DOI: 10.13140/2.1.3310.4169.

[135] Ulyanov, I., Przhiialkovskii, D. V., and Butov, O. V. "Point-by-point inscription of chirped apodized fiber Bragg gratings for application as ultrashort pulse stretchers." *Results in Physics* 32 (2022), p. 105101. ISSN: 2211-3797. DOI: https://doi.org/10.1016/j.rinp.2021.105101.

[136] Williamson, A. P., and Kiefer, J. "Polarization-controlled optical ring cavity (PORC) tunable pulse stretcher." *Optics Communications* 372 (2016), pp. 98–105. ISSN: 0030-4018. DOI: https://doi.org/10.1016/j.optcom.2016.03.091.

[137] Saraceno, C. "Pulse stretching and compressing using grating pairs." *Photonics and Ultrafast Laser Science*. Ibsen Photonics A/S, 2017, pp. 1–8. URL: https://ibsen.com/wp-content/uploads/White-paper-Pulse-stretching-and-compressing-using-grating-pairs_v1.pdf.

[138] Lim, C. et al. "Evolution of Radio-Over-Fiber Technology." *Journal of Lightwave Technology* 37.6 (2019), pp. 1647–1656. DOI: 10.1109/JLT.2018.2876722.

[139] Beas, J. et al. "Millimeter-Wave Frequency Radio over Fiber Systems: A Survey." *IEEE Communications Surveys &amp Tutorials* PP (Mar. 2013), pp. 1–27. DOI: 10.1109/SURV.2013.013013.00135.

[140] ITU-R. *Report ITU-R M.2516-0: Future technology trends of terrestrial International Mobile Telecommunications systems towards 2030 and beyond*. Nov. 2022.

[141] Wikström, G. et al. "Challenges and Technologies for 6G." *2020 2nd 6G Wireless Summit (6G SUMMIT)*. 2020, pp. 1–5. DOI: 10.1109/6GSUMMIT49458.2020.9083880.

[142] Puerta, R. et al. "Analog Mobile Fronthaul for 6G and Beyond." *Journal of Lightwave Technology* (2024), pp. 7458–7467. DOI: 10.1109/JLT.2024.3435770.

[143] Podbregar, L. et al. "Advances in and Applications of Microwave Photonics in Radar Systems: A Review." *Photonics* 12.6 (2025). ISSN: 2304-6732. DOI: 10.3390/photonics12060529.

[144] Nakamura, K. et al. "Verification of Applicability of 90 GHz Band Millimeter-Wave for Obstacle Detection to Railway." *IEEJ Transactions on Electrical and Electronic Engineering* 18.6 (2022), pp. 960–969. DOI: https://doi.org/10.1002/tee.23766.

[145] Kohmura, A. et al. "Optical fiber connected millimeter-wave radar for FOD detection on runway." *2013 European Radar Conference*. 2013, pp. 41–44.

[146] Kawanishi, T. et al. “Optical fiber network-connected distributed mm-wave radar system.” *2017 IEEE Photonics Society Summer Topical Meeting Series (SUM)*. 2017, pp. 197–198. DOI: 10.1109/PHOSST.2017.8012718.

[147] Ostrovskis, A. et al. “Experimental Demonstration of Hybrid Photonics-BasedARoF System for 5G and B5G Networks.” *2022 International Conference on Software, Telecommunications and Computer Networks (SoftCOM)*. 2022, pp. 1–5. DOI: 10.23919/SoftCOM55329.2022.9911478.

[148] Jiang, W., and Schotten, H. D. “Full-Spectrum Wireless Communications for 6G and Beyond: From Microwave, Millimeter-Wave, Terahertz to Lightwave.” *2023 IEEE 3rd International Conference on Computer Communication and Artificial Intelligence (CCAI)*. 2023, pp. 353–357. DOI: 10.1109/CCAI57533.2023.10201316.

[149] Li, W. et al. “Over 100 Gb/s mm-wave delivery with 4600 m wireless distance based on dual polarization multiplexing.” *Science China Information Sciences* 66.224301 (2023), pp. 1869–1919. DOI: 10.1007/s11432-023-3834-5.

[150] Jia, S. et al. “Integrated Dual-Laser Photonic Chip for High-Purity Carrier Generation Enabling Ultrafast Terahertz Wireless Communications.” *Nature Communications* 13.1 (Mar. 2022), p. 1388. ISSN: 2041-1723. DOI: 10.1038/s41467-022-29049-2.

[151] Jiang, T. et al. “Photonics-Enabled 6G Distributed MIMO: Experimental Study in an Indoor Environment.” *2024 International Topical Meeting on Microwave Photonics (MWP)*. 2024, pp. 1–5. DOI: 10.1109/MWP62612.2024.10736285.

[152] Anes, B., and Riad, B. A. “A new bidirectional analog radio over fiber transmission for 5G millimeter wave communication systems.” *2022 International Conference of Advanced Technology in Electronic and Electrical Engineering (ICATEEE)*. 2022, pp. 1–6. DOI: 10.1109/ICATEEE57445.2022.10093741.

[153] Perez-Galacho, D., Sartiano, D., and Sales, S. “Analog Radio over Fiber Links for Future 5G Radio Access Networks.” *2019 21st International Conference on Transparent Optical Networks (ICTON)*. 2019, pp. 1–4. DOI: 10.1109/ICTON.2019.8840516.

[154] Delmade, A. et al. “Expanded Gain-Switched Comb Source for 180 – 260 GHz Sub-THz Analog Radio-over-Fiber 6G Wireless System.” *2024 Optical Fiber Communications Conference and Exhibition (OFC)*. 2024, pp. 1–3.

[155] de Souza Lopes, C. H., Saia Lima, E., and Sodré Junior, A. C. “RoF/FSO-based Fronthaul for 5G Systems and Beyond.” *2021 SBMO/IEEE MTT-S International Microwave and Optoelectronics Conference (IMOC)*. Oct. 2021, pp. 1–3. DOI: 10.1109/IMOC53012.2021.9624921.

[156] Yao, J. “Microwave Photonics.” *Journal of Lightwave Technology* 27.3 (Feb. 2009), pp. 314–335. ISSN: 1558-2213. DOI: 10.1109/JLT.2008.2009551.

[157] Nguyen, D.-N. et al. “Optical Hybrid Fiber/Free-Space and 25 GHz Wireless Transmission Using LTE M-QAM Signals.” *2019 22nd International Symposium on Wireless Personal Multimedia Communications (WPMC)*. Nov. 2019, pp. 1–6. DOI: 10.1109/WPMC48795.2019.9096169.

[158] Azizpour, R. et al. “Multi-Channel Radio-Over-Fiber Communication Systems Through Modulation Instability Phenomenon.” *IEEE Photonics Journal* 16.5 (2024), pp. 1–13. DOI: 10.1109/JPHOT.2024.3446314.

[159] Jia, Z., Yu, J., and Chang, G.-K. “A Full-Duplex Radio-over-Fiber System Based on Optical Carrier Suppression and Reuse.” *IEEE Photonics Technology Letters* 18.16 (Aug. 2006), pp. 1726–1728. ISSN: 1941-0174. DOI: 10.1109/LPT.2006.879946.

[160] Eventech LTD. *ESTT 7 Series*. URL: https://eventechsite.com/products/%5C#estt7series.

[161] Srivastav, A., and Mandal, S. “Radars for Autonomous Driving: A Review of Deep Learning Methods and Challenges.” *IEEE Access* 11 (2023), pp. 97147–97168. DOI: 10.1109/ACCESS.2023.3312382.

[162] Enayati, J., Asef, P., and Wilson, P. “Resilient Multi-Range Radar Detection System for Autonomous Vehicles – A New Statistical Method.” *Journal of Electrical Engineering and Technology* 19 (May 2023), p. 15. DOI: 10.1007/s42835-023-01567-z.

[163] Ruiz-Carregal, G. et al. “Ku-Band SAR-Drone System and Methodology for Repeat-Pass Interferometry.” *Remote Sensing* 16.21 (2024). DOI: 10.3390/rs16214069.

[164] Nandana, V. et al. “Characterization of Drop Size Distribution in Urban Heavy Rainfall Event Using Doppler Weather Radar and Laser Precipitation Monitor.” *Remote Sensing in Earth Systems Sciences* 9 (Nov. 2025). DOI: 10.1007/s41976-025-00251-2.

[165] Gini, F. “Grand Challenges in Radar Signal Processing.” *Frontiers in Signal Processing* 1 (Mar. 2021). DOI: 10.3389/frsip.2021.664232.

[166] Yuksekkaya, F., Franchi, N., and Lubke, M. “On the Detection of Vulnerable Road Users—Simulating Limits of an FMCW Radar.” *Electronics* 13 (June 2024), p. 2547. DOI: 10.3390/electronics13132547.

[167] Santacruz, J. P. et al. “Analysis and Compensation of Phase Noise in FMCW LiDAR Sensors.” *J. Lightwave Technol.* 43.12 (June 2025), pp. 5636–5644.

[168] Bauduin, M., and Bourdoux, A. “Impact of Phase Noise on FMCW and PMCW Radars.” *2023 IEEE Radar Conference (RadarConf23)*. 2023, pp. 1–6. DOI: 10.1109/RadarConf2351548.2023.10149598.

[169] Tschapek, P. et al. “Detailed Analysis and Modeling of Phase Noise and Systematic Phase Distortions in FMCW Radar Systems.” *IEEE Journal of Microwaves* 2.4 (2022), pp. 648–659. DOI: 10.1109/JMW.2022.3195574.

[170] Liu, F. et al. “Seventy Years of Radar and Communications: The road from separation to integration.” *IEEE Signal Processing Magazine* 40.5 (2023), pp. 106–121. DOI: 10.1109/MSP.2023.3272881.

[171] *Super High Frequency (SHF) Communication Market Report, Industry and Market Size & Revenue, Share, Forecast 2024–2030*. Published August 2025; Report ID: 12970351; Historical Data: 2017–2023. Strategic Market Research, 2025. URL: https://www.strategicmarketresearch.com/market-report/super-high-frequency-communication-market.

[172] Rieländer, D. et al. “ESA Ground Infrastructure for the NASA/JPL PSYCHE Deep-Space Optical Communication Demonstration.” *International Conference on Space Optics – ICSO 2022*. Ed. by Minoglou, K., Karafolas, N., and Cugny, B. Dubrovnik, Croatia: SPIE, July 2023, p. 13. DOI: 10.1117/12.2688805.

[173] Khatri, F. I. et al. “Space-to-Ground Optical Interface Verification for the Orion Artemis II Optical (O2O) Communications Demonstration.” *2023 IEEE International Conference on Space Optical Systems and Applications (ICSOS)*. Oct. 2023, pp. 26–30. DOI: 10.1109/ICSOS59710.2023.10491223.

[174] Fokoua, E. N. et al. “How to make the propagation time through an optical fiber fully insensitive to temperature variations.” *Optica* 4.6 (June 2017), pp. 659–668. DOI: 10.1364/OPTICA.4.000659.

[175] Slavík, R. et al. “Ultralow Thermal Sensitivity of Phase and Propagation Delay in Hollow Core Optical Fibres.” *Scientific Reports* 5.1 (Oct. 2015), p. 15447. ISSN: 2045-2322. DOI: 10.1038/srep15447.

[176] Khudiakov, M. et al. “Optimization of the Pulse Position Modulation High-Power Compact Laser Source.” *International Conference on Space Optics – ICSO 2024*. Antibes Juan-les-Pins, France: SPIE, July 2025, p. 245. DOI: 10.1117/12.3075380.

[177] Chen, P. et al. “Range-Velocity Measurement Accuracy Improvement Based on Joint Spatiotemporal Characteristics of Multi-Input Multi-Output Radar.” *Remote Sensing* 16.14 (July 2024). ISSN: 2072-4292. DOI: 10.3390/rs16142648.

[178] Jacobs, L. et al. “On the Accuracy of Automotive Radar Tracking.” *2023 IEEE 97th Vehicular Technology Conference (VTC2023-Spring)*. June 2023, pp. 1–6. DOI: 10.1109/VTC2023-Spring57618.2023.10200523.

[179] Singh, P. et al. “Comprehensive Survey on Radar Systems and Its Target Classification Techniques.” *Journal of Electronics and Electrical Engineering* (Feb. 2025), pp. 234–269. ISSN: 2972-3280. DOI: 10.37256/jeee.4120255934.

[180] Blanche, P.-A. et al. “A 300 THz Tabletop Radar Range System with Sub-Micron Distance Accuracy.” *Scientific Reports* 8.1 (Sept. 2018), p. 14443. ISSN: 2045-2322. DOI: 10.1038/s41598-018-32846-9.

# ANNEXES

**Annex 1**

©2022 IEEE. Reprinted, with permission, from Migla, S., Selis, O., Sics, P. E., Pudzs, M., Zeltins, M., and Aboltins, A. “A Design of UWB Communication Testbed with Event Timer-based PPM Demodulator.” *2022 IEEE 2nd Ukrainian Microwave Week (UkrMW)*. 2022, pp. 691–694. DOI: 10.1109/UkrMW58013.2022.10037100

# A design of UWB communication testbed with event timer-based PPM demodulator

Sandis Migla
*Institute of Radioelectronics*
*Riga Technical University*
Riga, Latvia
sandis.migla@rtu.lv

Oskars Selis
*Institute of Radioelectronics*
*Riga Technical University*
Riga, Latvia
oskars.selis@rtu.lv

Pauls Eriks Sics
*Institute of Radioelectronics*
*Riga Technical University*
Riga, Latvia
paulssics@gmail.com

Mihails Pudzs
*Institute of Radioelectronics*
*Riga Technical University*
Riga, Latvia
mihails.pudzs@rtu.lv

Maris Zeltins
*Institute of Radioelectronics*
*Riga Technical University*
Riga, Latvia
maris.zeltins@rtu.lv

Arturs Aboltins
*Institute of Radioelectronics*
*Riga Technical University*
Riga, Latvia
aboltins@rtu.lv

***Abstract*—Ultra-wideband (UWB) communication achieves significantly lower power consumption compared to narrow-band technologies. However, the achievable transfer speed is much lower due to the limitations of UWB receivers. The employment of high-order pulse position modulation (PPM) in conjunction with a high-accuracy event timer at the demodulator side allows for radically increased transfer speed without compromising the power consumption. The purpose of the given paper is to present an implementation of a modular software framework and initial testbed for the exploration of high-order PPM communication which employs an event timer-based time-to-digital converter (TDC) at the receiver side. The architecture of the software framework, along with its integration with Eventech A033-ET event timer and Diglent Digital Discovery instruments, are presented. Assessment of the performance of the testbed is provided in terms of stability of the operation and bit error ratio (BER).**

***Keywords*—Communication systems, pulse position modulation, Python, instruments, timing, energy efficiency, RF signals**

## I. Introduction

Energy efficiency is an essential aspect of a communication system, and it is crucial in applications with limited power budgets i.e. space communications, sensor networks, and other autonomous systems. However, with the transition to millimeter-wave carrier frequencies, power consumption plays an increasingly important role [1]. On the other hand, the availability of the spectrum at a millimeter band and the possibility of transmitting focused beams of optical or radio signals make ultra-wideband (UWB) technology an attractive choice. Moreover, UWB signals allow making for very accurate time-of-flight (TOF) measurements and precise localization, which is the feature of high demand.

To provide exceptional energy efficiency, the transmitted pulses must be as short as possible, and the only limitation is the communication channel's available bandwidth and the transceiver's capabilities. In radio communications, the bandwidth is determined by the radio frequency (RF) part and antenna. Nowadays, the bandwidth of the radio communication channel can reach hundreds of GHz. Therefore, pulses with a duration of few picoseconds, theoretically, can be used. In the case of optical transmission, the length of the pulses can be below 1ps.

The objective of the given research is to develop a software framework and testbed for exploring pulse position modulation (PPM) communication using short electrical pulses with a duration between 20 and 40 ns. The main difference from existing work is the employment of a high-accuracy event timer for the demodulation.

## II. Related work

Generation of PPM signal with pulse duration above 100ps can be made using specific integrated RF circuitry [2]. The methodology of digital PPM signal generation can be borrowed from the analog world where pulse width modulation (PWM) or pulse amplitude modulation (PAM) signal is generated first and later converted to the PPM. In [3], authors propose an easy-to-implement combination of track-and-hold amplifier AD9100 and comparator ADCMP561 to generate analog PPM signal with pulses having a duration of about 1 ns. PPM signal can be synthesized directly by software running on high-speed field-programmable gate arrays (FPGAs) SoC with a digital-to-analog converter (DAC) [4]. Using modern FPGAs, the jitter can be minimized below 30 ps.

Correlation receiver is one of the most common approaches to the demodulation of UWB RF signals [5].In the RAKE receivers, which are widely used in UWB and code division multiple access (CDMA) systems [6], demodulation is performed by correlation with multiple copies of the locally generated template. Designing a template signal is difficult as linear and nonlinear distortions corrupt the received signal. Moreover, the correlation receiver has to track and record the energy of as many replicas as possible for better performance [7]. Non-coherent UWB modulation schemes [7], [8], which involve

transmitted reference (TR) pulses along with an information-carrying UWB pulse train [5] allow to overcome those issues. According to the TR scheme, the PPM transmitter sends a pair of pulses i.e. reference pulse at the beginning of the symbol and data pulse located at a certain time slot. The non-coherent receiver uses the first pulse as a reference for demodulation and recovering the information encoded in the second pulse time offset. Since both pulses will be distorted the same way, the matching process is much simpler, and strict timing synchronization between the transmitter and receiver is unnecessary.

Detection of high-speed PPM signals with a large number of symbol positions using digital correlation-based methods becomes impractical due to computational complexity and speed requirements. Moreover, high accuracy timing is necessary for distinguishing pulse positions (and symbol timing in case of coherent demodulation). If the communication channel is not multipath, such as point-to-point radio or optical link in free space or optical fiber, the signal propagation by the main path is much stronger than reflections. Such signal has well-defined edges and can be demodulated by time-to-digital converter (TDC). In the publication [4], the authors present the demodulation of PPM signal with 100 ps time slot using timer TDC-GPX2 from ScioSense which has accuracy 20ps RMS [9]. For the detection of pulses with a time slot duration of 50 ps and less, timer with accuracy less than 10 ps is required. Event timer A033-ET™ can detect events with accuracy about 3ps RMS. Using this timer, it is possible to register events at the rate of 20M events per second. This timer can be used for the demodulation of high-order digital PPM signals. The first attempt to use this timer for PPM was made in 2015 [3].

## III. Event timer based PPM testbed

### A. Overall design

*1) Hardware:* Experiment hardware consists of Digital Discovery™ (DD) device, produced by Digilent, with additional circuity at digital output pins to provide sufficient signal voltage to ensure that the timer will receive the incoming signal, Eventech A033-ET event timer, and source of white Gaussian noise (WGN). Moreover, there are computers with Python 3 and A033-ET software connected to the appropriate devices, as illustrated in Fig. 3. The signal from DD is added to the signal of the WGN generator and finally sent to the event timer's input.

*2) Software:* A Python script performs communication with the DD device using WaveForms software development kit (SDK). Communication with the A033-ET event timer is made by our Python scripts using TCP/IP messages sent over the network to the timer's PC software which controls the USB connection with the event timer. The flowchart of the testbed control algorithm can be seen in Fig. 2.

### B. Signal structure

The transmission is carried in packets of transmitted reference pulse-position modulation (TR-PPM) symbols, where each data symbol consists of a reference pulse and data pulse.

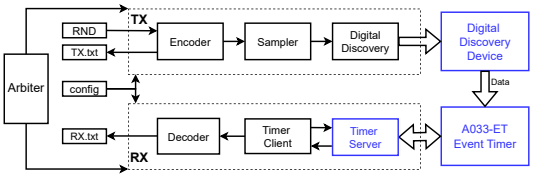



Fig. 1. Python modules (black boxes) and external software components (blue boxes) of the testbed.

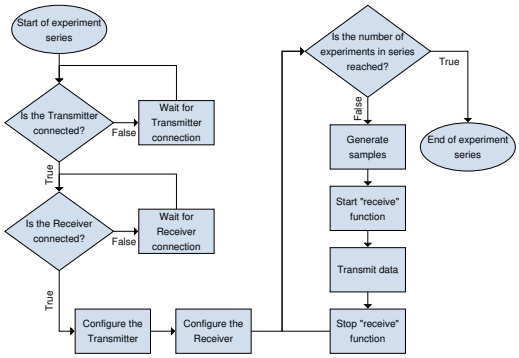



Fig. 2. Testbed operation algorithm

The employed packet structure for TR-PPM mode is shown in Fig. 4. The packet always begins with a start symbol consisting of just one pulse. Each data symbol is symmetrically split in half, where the first half begins with a start pulse and the second half consists of payload interval and guard interval $T_d$, which is necessary for the information processing. The total duration $T$ of the symbol can be calculated as $T = 2(M \cdot \tau + T_d)$, where $M$ is the count of positions, and $\tau$ is the width of one position. The time $t_x$ between the start pulse and data impulse corresponds to the encoded value added to half-symbol time $T/2$.

Generally, $\delta$ and $\tau$ are independent as $\delta$ is determined by the bandwidth of the communication system, whereas $\tau$

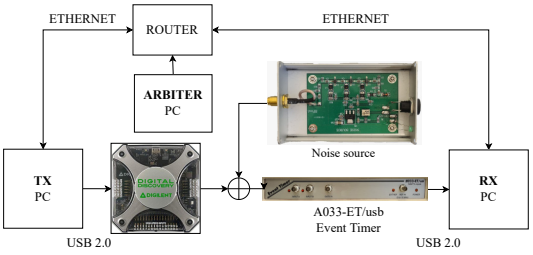



Fig. 3. Hardware components of the testbed.

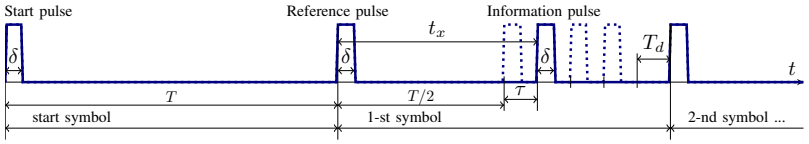



Fig. 4. Structure of TR-PPM signaling packet

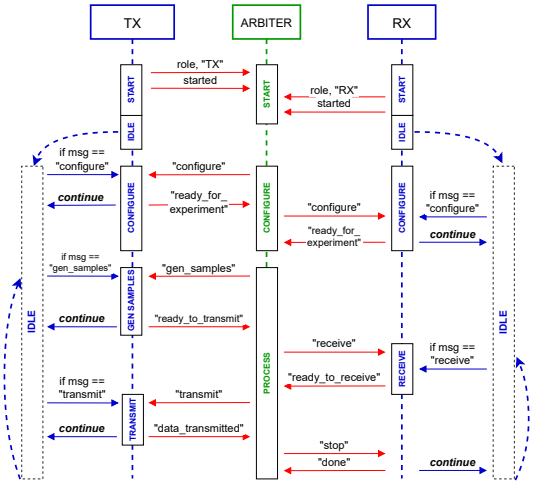



Fig. 5. Sequence diagram of Arbiter.

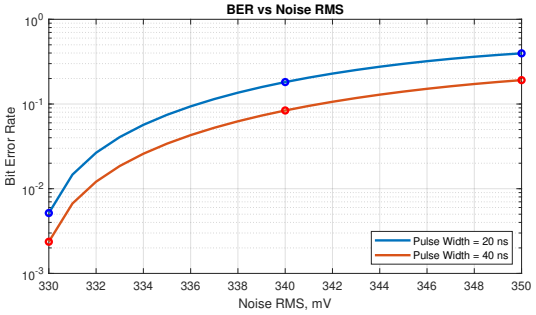



Fig. 6. Dependence of communication BER from the intensity of the additive WGN.

is determined by the resolution of digital-to-time converter (DTC) and TDC. As it was mentioned before, in PPM, the duration of the pulse does not play any role in the signaling, therefore, to save energy, pulses must be as short as possible. Since maximum sample rate of DD is 100 MSa/s and analog bandwidth about 50 MHz, minimal time slot $\tau$ is 10 ns and duration of the generated pulse $\delta$ is 20 ns. In our experiments, we employ a simplified scheme where $\delta = \tau$ i.e., the pulse duration is equal to the time slot for one position.

### C. Arbiter

The experiment is controlled by an arbiter program written in Python. The communication between Arbiter, Transmitter and Receiver programs is handled using TCP/IP sockets as illustrated in Fig. 5. First, the Arbiter opens a TCP/IP socket connection to both Transmitter and Receiver. When the connection is established, the Arbiter instructs the Transmitter and Receiver to configure for the experiment using a specified configuration file and issues respective commands.

### D. Transmitter

After receiving the appropriate command, the "Encoder" module of the Transmitter (see Fig. 1) generates a random binary string of specified length, converts it to Gray code, generates relative time tags for the impulses, and after that "Sampler" module creates a list of samples for DD device. Finally, the "Digital Discovery" module loads the generated samples in the DD device memory and instructs the DD device to create the waveform.

### E. Receiver

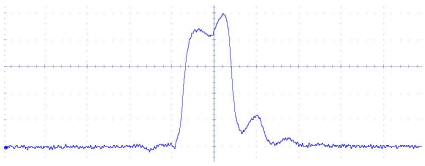
After pulses are received at the A033-ET timer, it processes and sends measurement results (time tags) to the "Timer Server" program on the PC (see Fig. 1). The "Timer Client" module of the Receiver calculates absolute intervals between each time tag with an accuracy of timer resolution, which in ideal conditions is 2-4 ps. After that, the absolute intervals are recalculated to relative times, and an empty symbol is searched at the start of the packet (see Fig. 4). When the beginning of the packet is found, the data is passed to the "Decoder" module, where the positions are converted to Gray codes and then to binary codes, which are saved in a separate file for offline comparison with the transmitted data.

## IV. Experimental verification

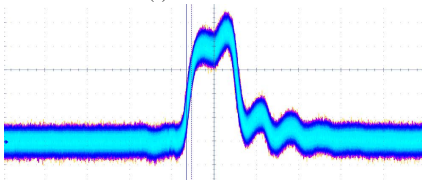
Verification of the testbed has been performed using transmission of pseudo-random bit sequences stored in a file. The configuration parameters of the testbed for this particular experiment are shown in Table I. Pulse duration and duration of the time slot are limited by the sample rate of DD. The number of symbols in the packet was chosen following the "Timer Server" program requirements. It can detect 64 pulses at a time, so we can send not more than 31 symbols, considering the empty symbol with one pulse and payload symbols with two pulses. By the timer's documentation, the

TABLE I
PARAMETERS OF THE EXPERIMENT

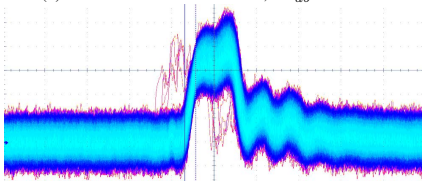
| Parameter | Parameter symbol | Parameter value |
|---|---|---|
| Number of positions | $M$ | 32 |
| Pulse duration | $\delta$ | 20 ns (40 ns) |
| Position duration | $\tau$ | |
| Symbols per packet | $N_{fr}$ | 31 |
| Guard time | $T_d$ | 40 ns (80ns) |



(a) Without WGN.



(b) With WGN. $SNR = 13$ dB, $\Delta t_{ab} = 1.1$ ns.



(c) With WGN. $SNR = 7$ dB, $\Delta t_{ab} = 2.6$ ns.

Fig. 7. Waveform of 20 ns pulse. (700mV/div, 10ns/div, 50Ω, 10GS/s)

Guard time, also known as the timer's dead time, is less than 40 ns. The additive WGN has been controlled manually with 10 mV RMS step.

As Fig. 6 shows, the first errors appear at 330 mV RMS and continue to rise by increasing the noise intensity. The use of 40 ns pulses leads to a lower bit-error rate than the 20 ns pulse sequence. With 20 ns pulses the signal RMS is approximately 730 mV, whereas with 40 ns – 980 mV. Therefore, it can be observed that, unfortunately, the amplitude of the DD output signal strongly depends on bandwidth. Moreover, the signal waveform is imperfect and oscillates, as shown in Fig. 7a.

The jitter of the pulses increases as signal-to-noise ratio (SNR) of the signal decreases. As shown in Fig. 7, at $SNR =$ 13 dB is $\Delta t_{ab} = 1.1$ ns, at $SNR = 7$ dB - $\Delta t_{ab} = 2.6$ ns.

## V. CONCLUSIONS

The main reason why the BER starts to rise is that the timer has a threshold voltage of around 1.2 V at which it reacts to incoming pulses. Fig. 7c shows that the WGN peaks can already reach the threshold voltage and cause a false timer's reaction and false time tags. As visible from Fig. 6, in ideal conditions, the RMS of WGN might not exceed 330 mV. Unfortunately, there are oscillations after the falling edge of the pulse at DD output. If the RMS of WGN is slightly higher than acceptable for data transmission, they can cause false time tags too. In this modulation scheme, the program can filter false time tags because the time between the pulses can not be less than guard time $T_d$. Because of the smaller signal RMS of DD's output when using narrower pulses, the 20 ns pulses will require higher SNR for achieving certain BER.

From Fig. 7c can be concluded that the jitter $\Delta t_{ab}$ of the rising edge does not exceed 2.8 ns. Therefore, the jitter does not affect the timer's decisions and does not decrease BER.

The limitation for the employment of shorter pulses is at the transmitter side. The maximum sample rate of DD, which is used as DTC in the transmitter, is 100 MSa/s. For the use of shorter pulses and, hence, more and shorter PPM bins, PPM bins, it is necessary to use more advanced arbitrary waveform generator (AWG) and develop respective Python modules for interfacing with AWG.

The proposed concept is suitable for a broader application and can be adapted to other modulation types and waveforms by developing respective interfacing modules.

## ACKNOWLEDGMENT

This research was funded by the Latvian Council of Science, grant No. lzp-2021/1-0475, "Picosecond-resolution pulse position modulation for beyond-the-limits energy efficiency of communications."

## REFERENCES

[1] N. Rendevski and D. Cassioli, "Potentials of low-complexity Rake receivers for 60 GHz UWB wireless communication systems," *2015 IEEE 1st International Forum on Research and Technologies for Society and Industry, RTSI 2015 - Proceedings*, pp. 94–99, 2015.

[2] H. Song, D. Liu, Y. Zhang, W. Rhee, and Z. Wang, "A 6.5-8.1-GHz Communication/Ranging VWB Transceiver for Secure Wireless Connectivity with Enhanced Bandwidth Efficiency and ΔΣ Energy Detection," *IEEE Journal of Solid-State Circuits*, vol. 55, no. 2, pp. 219–232, feb 2020.

[3] A. Mezerins and V. Bespal'ko, "Estimation of analog-to-time and time-to-digital conversion efficiency in analog optical communication system testbed," in *Proceedings - 2015 Advances in Wireless and Optical Communications, RTUWO 2015*. IEEE, nov 2015, pp. 211–214.

[4] N. Barnwell, T. Ritz, S. Parry, M. Clark, P. Serra, and J. W. Conklin, "The miniature optical communication transceiver-A compact, power-efficient lasercom system for deep space nanosatellites," *Aerospace*, vol. 6, no. 1, 2019.

[5] G. Durisi and S. Benedetto, "Comparison between coherent and noncoherent receivers for UWB communications," *Eurasip Journal on Applied Signal Processing*, vol. 2005, no. 3, pp. 359–368, 2005.

[6] D. Cassioli, M. Win, F. Vatalaro, and A. Molisch, "Low Complexity Rake Receivers in Ultra-Wideband Channels," *IEEE Transactions on Wireless Communications*, vol. 6, no. 4, pp. 1265–1275, apr 2007.

[7] Y. Zheng, K.-W. Wong, M. A. Asaru, D. Shen, W. H. Zhao, Y. J. The, P. Andrew, F. Lin, W. G. Yeoh, and R. Singh, "A 0.18μm CMOS Dual-Band UWB Transceiver," in *2007 IEEE International Solid-State Circuits Conference. Digest of Technical Papers*. IEEE, feb 2007, pp. 114–590.

[8] F. Lee and A. Chandrakasan, "A 2.5nJ/b 0.65V 3-to-5GHz Sub banded UWB Receiver in 90nm CMOS," in *Int. Solid State Circuits Conference (ISSCC'07)*, 2007, pp. 116–117.

[9] ScioSense B.V., "Datasheet of TDC-GPX2," pp. 1–77, 2018. [Online]. Available: https://www.sciosense.com/wp-content/uploads/documents/TDC-GPX2-Datasheet.pdf

**Annex 2**

©2023 IEEE. Reprinted, with permission, from Selis, O., Migla, S., Sics, P. E., Zeltins, M., Spolitis, S., and Aboltins, A. "Demonstration of 50 ps Per-Position Differential Pulse Position Modulation Data Transmission." *2023 IEEE 10th Jubilee Workshop on Advances in Information, Electronic and Electrical Engineering (AIEEE)*. 2023, pp. 1–4. DOI: 10.1109/AIEEE58915.2023.10134802

# Demonstration of 50 ps Per-Position Differential Pulse Position Modulation Data Transmission

Oskars Selis
*Institute of Microwave Engineering and Electronics*
*Riga Technical University*
Riga, Latvia
oskars.selis@rtu.lv

Sandis Migla
*Institute of Microwave Engineering and Electronics*
*Riga Technical University*
Riga, Latvia
sandis.migla@rtu.lv

Pauls Eriks Sics
*Institute of Microwave Engineering and Electronics*
*Riga Technical University*
Riga, Latvia
pauls-eriks.sics@rtu.lv

Maris Zeltins
*Institute of Microwave Engineering and Electronics*
*Riga Technical University*
Riga, Latvia
maris.zeltins@rtu.lv

Sandis Spolitis
*Institute of Telecommunications*
*Riga Technical University*
Riga, Latvia
sandis.spolitis@rtu.lv

Arturs Aboltins
*Institute of Microwave Engineering and Electronics*
*Riga Technical University*
Riga, Latvia
aboltins@rtu.lv

***Abstract*—To prolong the lifespan of devices with a limited power budget, efficient modulation schemes, such as pulse position modulation (PPM), can be employed. High-order differential pulse position modulation (DPPM), which can be efficiently demodulated using an event timer, presents advantages over other PPM modulation methods because it can provide higher data rates and does not require synchronization. This research aims to demonstrate data transmission using high-order DPPM signal in a laboratory environment and measure bit error ratio (BER) for position widths 50-200 ps. In the theoretical part, an assessment of data transmission rate dependence from the position count and position width of DPPM signal with guard time is presented. Moreover, a theoretical comparison in terms of power efficiency and maximum data rate with other types of PPM, such as transmitted reference pulse-position modulation (TR-PPM), is made. In the experimental part, the performance measurements of DPPM communication system consisting of arbitrary waveform generator (AWG) as DPPM transmitter and Eventech A033-ET/USB event timer as digital-to-time converter (DTC) of DPPM receiver are presented.**

***Keywords*—Pulse position modulation, ultra-wideband, timing, energy efficiency, communication***

## I. Introduction

The need for network access from rural areas, maritime and aviation transport communications and a growing number of space applications has led to the rapid development of space communication networks. Due to the limited power budget and the necessity to transmit data over huge distances, space communication employs advanced modulation and coding schemes, which continue to evolve.

Ultra-wideband (UWB) technology is one of the most promising directions for space communications as it can provide versatile control of the transmitted signal's power efficiency and peak-to-average power ratio (PAPR). Pulse position modulation (PPM) is UWB technology where information is encoded into the absolute or relative time of the signalling pulses. Because in PPM, the pulse duration does not carry any information, average power and signal-to-noise ratio (SNR) of the transmitted signal do not directly affect the bit error ratio (BER). Instead, the instantaneous power of the signalling pulses plays a vital role in determining the communication system's performance. By shortening the signalling pulses, it is possible to decrease the average power and SNR without significant impact on BER [1]. Alternatively, it is possible to decrease BER, shortening the signalling pulses and increasing the instantaneous power. The benefits in both cases come at the expense of the frequency spectrum occupation. Therefore, there is no contradiction with the well-known Shannon formula for channel capacity.

PPM signalling scheme has several sub-types with different synchronization requirements and energy efficiencies. Differential pulse position modulation (DPPM) is one of the most efficient and simple PPM modulation types. It provides higher channel capacity compared to fixed-length symbol modulation types. This research aims to demonstrate data transmission using high-order DPPM signal in a laboratory environment. The motivation of the given research work is to present DPPM modulation scheme and demonstrate possibilities for demodulation of DPPM using the highly-accurate Eventech A033-ET/USB event timer, which was selected considering its accuracy.

This paper is structured as follows: Section II is devoted to the pre-existing relevant research to this work. Section III outlines the theoretical aspects of DPPM signal structure and achievable data transmission rates using PPM. Section IV is devoted to the hardware used in the experiment, and Section V reports the parameters and methodology used in the experiment and the results of the experiment. Section VI

draws conclusions made by the authors during this research.

## II. Related Work

In 1998 the European Space Agency launched its SILEX mission [2]. One of the mission's goals was to test communication links using PPM. The mission was meant to reach data transmission speeds up to 120 Mbps [3]. Since then, numerous studies have tried to assess the use of different signal modulation types in free space optical (FSO) communication systems. One such study examined the power efficiency of such modulation methods as binary phase-shift keying (BPSK), on-off keying (OOK), quadrature phase-shift keying (QPSK), PPM, pulse amplitude modulation (PAM). The results showed that PPM based methods prevailed as the more power-efficient method, making it a well-suited candidate for systems with a limited power budget [4]. Furthermore, the energy efficiency of PPM can be further improved using advanced modulation schemes, such as DPPM. Experiments have shown that DPPM is also more rigid against disturbance caused by atmospheric turbulence. There have been several cases in FSO communications where DPPM has been utilized because of its energy efficiency. For example, in 2012, a study on the influence of atmospheric turbulence on different PPM types in ground-to-satellite communication was conducted. The results showed that DPPM was less prone to errors when exposed to atmospheric turbulence. The SNR level when using DPPM was lower at the same BER values than in the case of classical PPM [5]. This makes DPPM a more power-efficient modulation technique of the two, especially when the real-life obstacles by the transmission medium are considered. Furthermore, the error rate of DPPM can be decreased using soft decision encoding. Studies show that soft decision decoding can improve the reliability of DPPM over wireless optical communication systems [6]. In 2020 electrical engineering students in Finland [7] made an ultra-low power transmitter using soft decision-making and DPPM. The transmitter proved to be 67% more efficient when compared to similar transmitters using OOK and only consumed 67 $\mathrm{nW}$. It has to be said that the transmission range was only 30 $\mathrm{m}$. With the transmission power increased to 27 $\mu\mathrm{W}$, the transmission distance could be extended as far as 200 $\mathrm{m}$. Examples like these make DPPM an attractive choice for implementation and use in large-scale DPPM communication systems. Results reported in [1] show a BER of 0.257 % at optical peak power of 176 $\mathrm{nW}$ for an optical communication system using PPM. This system was mainly made for nano-satellites, and it achieved a raw data rate up to 78.1 $\mathrm{Mbit/s}$ using 2.5 $\mathrm{ns}$ short pulses.

## III. Analysis of DPPM Modulation Scheme

DPPM, like the classical TR-PPM, uses timed intervals to encode information. Both methods send information via symbol frames, where each symbol consists of several time slots. A data pulse can be transmitted during every symbol in one of the slots. The difference between the two pulse position techniques methods is that TR-PPM sends symbols of fixed length, whereas DPPM cuts the part of the symbol that follows the pulse. Therefore, each new symbol in DPPM starts immediately after the data pulse, which at the same time, is the reference pulse for the next symbol. This improvement dramatically increases the amount of information that can be transmitted compared to TR-PPM. Nevertheless, such an approach requires more elaborate demodulation techniques.

The mean data rate of DPPM can be calculated using the formula (1), considering that $M$ positions are used. $T_{\text{mean}}$ represents the mean symbol duration in the DPPM sequence:

$$R_{\text{b}} = \frac{log_2 M}{T_{\text{mean}}} = \frac{2log_2 M}{\Delta(M+1)}. \tag{1}$$

For demodulation of high order DPPM, an event timer can be used as time-to-digital converter (TDC). Event timer Eventech A033-ET/USB, employed in this research, requires a 50 $\mathrm{ns}$ guard interval $T_g$ to measure the time. The guard interval significantly increases the time between the pulses, especially if the time bin $\Delta$ is substantially smaller than $T_g$. The DPPM signal structure is illustrated in Fig. 1. The data rate of the DPPM signal when the guard interval $T_g$ is applied to it can be calculated using the formula (2):

$$R_{\text{b,guard}} = \frac{2log_2 M}{2T_g + \Delta(M-1)}. \tag{2}$$

As Fig. 1 shows, the time between pulses varies from pulse position. The number of data bits within each pulse is determined by the number of time bins utilized in the modulation scheme. For instance, given a pulse coded with $N$ bits, there are $M = 2^N$ possible time bins where the pulse can be positioned within the symbol. The initial position is at a time of $T_g = 50$ $\mathrm{ns}$ from the previous pulse.

It is important to note that a pulse duration does not affect the demodulation process because the event timer registers the time tag at a rising edge of the pulse. However, pulse duration $\tau$ is an important parameter because it determines the average power consumption and frequency bandwidth of the DPPM link. In this research, a 100 $\mathrm{ps}$ pulse duration was determined by the capabilities of arbitrary waveform generator (AWG)-based digital-to-time converter (DTC). Unfortunately, the particular event timer can detect the pulse if its duration exceeds 700 $\mathrm{ps}$. Therefore, the pulse should be expanded before the timer-based TDC detection.

### A. DPPM Data Rate

Fig. 2 shows theoretically achievable average data rates for DPPM and TR-PPM. By Fig. 2, to achieve the highest data rate using DPPM, 10 bits per position should be considered in the case of 50 $\mathrm{ns}$ guard interval and position width 50 $\mathrm{ps}$. The same figure shows that the achievable data rate for TR-PPM is twice smaller than for DPPM, and the optimal number of bits is nine. This is because TR-PPM symbols, on average, are twice longer than in the case of DPPM.

The large dead time of the event timer limits the overall data rate of PPM. Our calculations have shown that in the case of 50 $\mathrm{ps}$ position width, for increasing DPPM data rate to 400 $\mathrm{Mbit/s}$, it is necessary to reduce the dead time of the event timer to approximately 8 $\mathrm{ns}$.

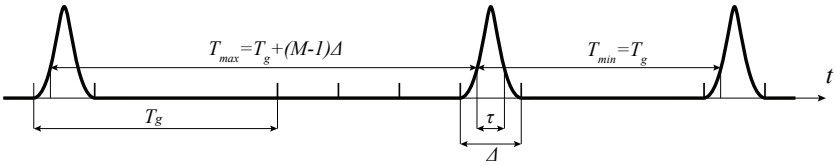



Fig. 1. Structure of DPPM signalling with guard interval.

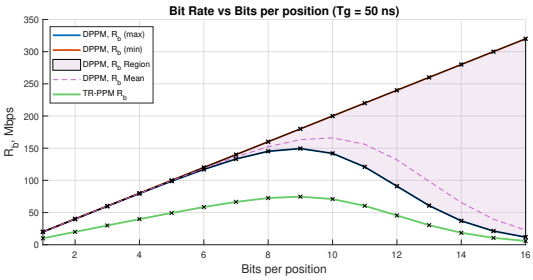



Fig. 2. Data rate comparison between DPPM and TR-PPM in case of position width $\Delta = 50$ps.

## IV. Experiment Setup

### A. Modulator

The transmitter DTC is based on Keysight M8195A AWG using the direct output of its first channel and the pulse expansion module (PEXM). The inverted output of the AWG first channel is used for monitoring the initially generated DPPM waveform. The direct and inverted outputs of channel 1 of the AWG are connected to the respective hardware (digital storage oscilloscope (DSO) or PEXM) using an 80 cm long pair of phase-matched coaxial radio frequency (RF) cables. As mentioned before, the inverted output of AWG channel 1 is connected to channel 1 of Keysight DSO (80 GSa/s sampling rate, 33 GHz analogue bandwidth) for monitoring the generated DPPM waveform. The direct output of channel 1 is connected to the experimental PEXM. The PEXM module contains the following hardware in such order:

1) 6 dB RF attenuator to remove possible back-reflection from custom low-pass filter (LPF),
2) In-house manufactured custom LPF [8],
3) VLFX-1300+ commercial LPF,
4) 30 dB RF amplifier with bandwidth 30-4000 MHz,
5) SHF BT45 broadband bias tee with bandwidth 20 kHz - 45 GHz.

### B. Demodulator

The demodulator is based on the Eventech A033-ET/USB event timer, a computer-based instrument for measuring time instants when input events occur as electrical pulses. The event timer has high precision with a single-shot RMS resolution better than 5 ps combined with a high measurement rate of up to 20 mega events (ME) in a burst. The A033-ET/USB uses a USB 2.0 interface. The incoming events are registered on the rising edge of a low-voltage transistor–transistor logic (LVTTL) signal. 50 ns guard (dead) time $T_g$ (see Section III) of the timer is a time interval which immediately follows the registered pulse. During this time interval, the event timer cannot register another received impulse. Every single measurement (time-tag) is represented in digital form with 1 ps least significant bit (LSB) resolution. The event timer is connected to a computer via USB 2.0 interface and communicates with the Timer Server software using TCP/IP communication protocol.

TABLE I
Results of data transmission tests using DPPM.

| Test nr. | $\tau$, ps | $\Delta$, ps | $M$ | $T_g$, ns | Total bits | BER |
|---|---|---|---|---|---|---|
| 1 | 100 | 200 | 128 | 50 | 4410 | 0 |
| 2 | 100 | 100 | 256 | 50 | 5041 | $7.935 \cdot 10^{-4}$ |
| 3 | 100 | 50 | 512 | 50 | 5670 | $1.781 \cdot 10^{-2}$ |

The software framework [9], which controlled the event timer via TCP/IP and performed DPPM demodulation, is written in Python. The event timer received the signal sequence with DPPM pulses at specific absolutes times (also known as time tags): $T_1, T_2, \cdots T_n$. From each time tag, guard time $T_g$ was subtracted, and the resulting time was divided by position width $\Delta$, obtaining relative time tags converted to the pulse positions. Finally, the positions were reversed to binary data.

The laboratory setup consisted of a DPPM modulator part, transmitting impulses through a cable. The cable was connected to the event timer's BNC, 50 Ω "B" input. The A033-ET/USB device is connected to the computer through a USB 2.0 cable. The computer runs the event timer's server program and DPPM demodulator software. Fig 3 shows the entire experimental setup.

## V. Experimental Validation

Experimental validation has been performed using UWB testbed reported in Section IV by transmitting pseudo-random bit sequences with parameters shown in Table I. Each experiment consists of one transmitted data packet of 63 data pulses. To ensure that a valid output signal is obtained, a periodic sequence of 100 ps pulses is transmitted to the DSO before data transmission. Each experiment file was loaded in AWG individually. At the same time, A033-ET/USB event

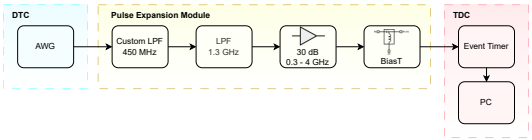



Fig. 3. Diagram of the experimental setup.

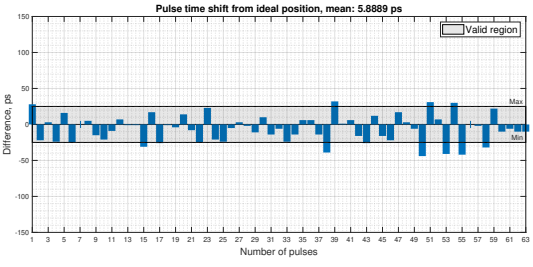



Fig. 4. Time drift of pulse positions in the case of 50 ps bin duration.

timer was being configured for event measurement. Using the laboratory setup, the AWG generated pulse was expended by PEXM to about 750 ps, which is an optimal and valid signal width for A033-ET/USB event detection. A 300 mV DC level to all signals is applied to ensure optimal signal level for the event timer because the event timer uses LVTTL signal levels, but PEXM output voltage is 1500 mV peak-to-peak, i.e., slightly above the threshold level. Signal parameters after the pulse expansion module were as follows: $V_{\text{pp}} = 1500\text{mV}$, $V_{\text{DC}} = 300\text{mV}$, $\tau = 750\text{ps}$, $t_{\text{rise}} = 350\text{ps}$. In the experiment, an internal reference clock was used.

First, a periodic pulse sequence has been received with graphical timer client software, illustrating the time intervals with points. The calculated RMS value was smaller when the DC offset voltage was set to 300 mV.

Table I summarizes the results of decoded DPPM test signals where BER was calculated for each test. The test did not detect any bit errors at position width (bin duration) $\Delta = 200$ ps. At 100 ps and 50 ps the error rate increases significantly $1.781 \cdot 10^{-2}$ and $7.935 \cdot 10^{-4}$ accordingly. Fig. 4 shows how each detected pulse is shifted from the expected time position. The shaded region denotes the time bin where the pulse should be registered. It shows that a maximum offset is less than one 50 ps time bin.

## VI. Conclusions

The implemented DPPM transmission test setup has demonstrated excellent results, as indicated by the low bit error rate observed. Despite the jitter and systematic timing error, the test system could accurately detect the pulses with an error rate of no more than one position.

The main contributing factor to the test's success was the robust design of the A033-ET/USB event timer, which could effectively detect events even in the presence of a noisy signal and an insufficiently steep rising edge of the expanded pulses. However, it should be noted that the signal amplitude could also impact the accuracy of the detection process, as the time walk may occur at different pulse amplitudes.

If compared with the results reported in [1] at a position duration of 100 ps, we observed 5-10 times improvement of the BER. When the position duration was reduced to 50 ps, the BER increased by about 22 times compared to the test with a position duration of 100 ps.

The achieved data rate in the case of 50 ps position width was about 160 Mbit/s, which is an improvement compared to [1] even considering relatively high BER. Nevertheless, the data rate was not the most critical aspect of these tests. What mattered most was to demodulate the DPPM at the narrowest bin times possible.

In future experiments, it will be necessary to carefully select positions that allow for a high data rate while also considering the effect of pulse width on the signal amplitude and rising edge. Reducing the width of a position can increase the data rate but with the risk of more errors. Therefore, the overall stability of the signal also needs to be looked at in the future. Overall, the results of this test demonstrate the viability of using an event timer as high-precision TDC for PPM demodulation.

## Acknowledgment

This research was funded by Riga Technical University Master Grant program No. ZM-2023/33.

## References

[1] N. Barnwell, T. Ritz, S. Parry, M. Clark, P. Serra, and J. W. Conklin, "The miniature optical communication transceiver-A compact, power-efficient lasercom system for deep space nanosatellites," *Aerospace*, vol. 6, no. 1, 2019.

[2] Z. Sodnik, B. Furch, and H. Lutz, "Free-space laser communication activities in europe: Silex and beyond." *Conference Proceedings - Lasers and Electro-Optics Society Annual Meeting-LEOS (pp. 78–79).*, 2006.

[3] R. A. Cryan and R. T. Unwin., "Optical Employing Space Communications Pulse Position Modulation," *IEE Colloquium on Advanced Modulation and Coding Techniques for Satellite Communications.*, 1992.

[4] T. Y. Elganimi, "Studying the BER performance, power- and bandwidth-efficiency for FSO communication systems under various modulation schemes." *2013 IEEE Jordan Conference on Applied Electrical Engineering and Computing Technologies, AEECT 2013. IEEE Computer Society.*, 2013.

[5] S. Tiwari, V. K. Jain, and S. Kar, "Performance evaluation of different Pulse Position Modulation schemes in atmospheric turbulence channel for ground-to-satellite optical communication," *2012 International Conference on Optical Engineering*, 2012.

[6] Z. Xu, L. Shen, and J. Wang, "An improved differential pulse position modulation using soft-decision decoding." *2007 International Conference on Wireless Communications, Networking and Mobile Computing, WiCOM 2007*, 2007.

[7] M. Pulkkinen, T. Haapala, J. Salomaa, and K. Halonen, "Low-Power Wireless Transceiver with 67-nW Differential Pulse-Position Modulation Transmitter," *IEEE Transactions on Circuits and Systems I*, 2020.

[8] T. Solovjova, J. Semenako, D. Prigunovs, D. Ortiz, S. Spolitis, and A. Aboltins, "Picosecond Pulse Expansion Using The Low-Pass Filter in Event Timer-Based PPM Communication System," in *Proceedings of 2022 Workshop on Microwave Theory and Techniques in Wireless Communications, MTTW 2022*. IEEE, oct 2022, pp. 29–34.

[9] S. Migla, O. Šēlis, P.-E. Šics, M. Pudzs, M. Zeltins, and A. Aboltins, "A design of uwb communication testbed with event timer-based ppm demodulator," in *2022 IEEE 2nd Ukrainian Microwave Week (UkrMW)*, 2022, pp. 691–694.

**Annex 3**

©2024 IEEE. Reprinted, with permission, from Sics, P. E., Tihomorskis, N., Migla, S., Ratners, J., Kurtenoks, V., and Aboltins, A. "Implementation of Reconfigurable 149Mbps TDC-Based PPM Transceiver." *2024 Joint European Conference on Networks and Communications & 6G Summit (EuCNC/6G Summit)*. 2024, pp. 706–710. DOI: 10.1109/EuCNC/6GSummit60053.2024.10597124

# Implementation of Reconfigurable 149Mbps TDC-Based PPM Transceiver

Pauls Eriks Sics
*Institute of Photonics, Electronics and Electronic Communications*
*Riga Technical University*
Riga, Latvia
pauls-eriks.sics@rtu.lv

Nikolajs Tihomorskis
*Institute of Photonics, Electronics and Electronic Communications*
*Riga Technical University*
Riga, Latvia
nikolajs.tihomorskis@rtu.lv

Sandis Migla
*Institute of Photonics, Electronics and Electronic Communications*
*Riga Technical University*
Riga, Latvia
sandis.migla@rtu.lv

Jakovs Ratners
*Institute of Photonics, Electronics and Electronic Communications*
*Riga Technical University*
Riga, Latvia
jakovs.ratners@rtu.lv

Viktors Kurtenoks
*Eventech Ltd.*
Riga, Latvia
juvitek@mail.com

Arturs Aboltins
*Institute of Photonics, Electronics and Electronic Communications*
*Riga Technical University*
Riga, Latvia
aboltins@rtu.lv

***Abstract*—This research is devoted to developing the pulse position modulation (PPM) modem, which utilizes an extremely small 40 ps position width to achieve a theoretical bitrate above 149 Mbps. In this work, we present a PPM modulator, implemented using software-controlled digital delay lines (DDLs) and the demodulator based on the high-precision event timer-based time-to-digital converter (TDC) with streaming capabilities. The versatility of the proposed solution is achieved by relying on software-defined radio (SDR) approach where the majority of modem functions are performed in software running on personal computer (PC) connected to the modem by USB3 interface. Unlike the traditional SDR, the proposed design relies on precise digital-to-time and time-to-digital conversion, which can cope with signals having up to 100 GHz bandwidth. Along with the design description, the use of Consultative Committee for Space Data Systems (CCSDS) standard-compliant Reed-Solomon error correcting code (ECC) for mitigating the timing errors is discussed. Results of laboratory testing of the PPM modem hardware prototype are presented and explained.**

***Index Terms*—Ultra wideband communication, Software radio, Free-space optical, Communication systems**

## I. Introduction

Space communications are witnessing rapid growth due to the necessity to provide global network coverage for Internet of Things (IoT) and robotic systems, such as various aerial, terrestrial and maritime autonomous vehicles. This market segment, mainly covered by low Earth orbit (LEO) satellites with a limited power budget, exhibits a strong need for energy-efficient high-speed free-space optical communication technologies. Power efficiency is even more critical in deep space communications, where the distance between the ground station and spacecraft could reach millions of kilometers [1], and it is necessary to use optical signals with very high peak power.

Ultra-wideband (UWB) technology provides efficient means for creating power-efficient radio and optical communication systems. Well-known impulse radio ultra-wideband (IR-UWB) modulation schemes like IEEE 802.15.4a and its derivatives [2], [3] are designed for short-range wireless personal area networks (WPANs) and provide data rates of about 0.5 $\mathrm{Mbit/s}$. There is numerous research for applying IR-UWB schemes and commercial devices for vehicle-to-vehicle (V2V) communications [4], railway consist-to-consist (C2C) [5], power line communication (PLC) [6], etc. However, due to limitations in achievable bitrate, impulse radio (IR) has not gained much popularity in high-speed terrestrial and space radio links, and most of the current research is concentrated on the employment of IR-UWB for localization and ranging [7]. However, with the introduction of 6G mobile networks, where it is predicted that integrated sensing and communication (ISAC) will be one of the core functions of the radio network, excellent capabilities of IR-UWB for the localization can facilitate the use of this technology also for the communication [2].

Pulse position modulation (PPM) is a type of UWB modulation where information is encoded in time between the reference clock and data pulse (coherent PPM), reference pulse and data pulse (transmitted reference pulse-position modulation (TR-PPM), [8]), two data pulses (differential pulse position modulation (DPPM) [9]). Combining PPM with free space optical (FSO) physical layer allows for competitive bitrate [10] suitable for space communication, IoT applications and underwater optical communications to be achieved [11]. The most significant challenges for transitioning to optical communication are providing high pointing accuracy and mitigating the atmospheric turbulence impact [12], [13]. The latest developments of optical ISAC for space and ground applications are highlighted in work [14].

The most classical approach for PPM demodulation relies on a correlator-based system [15]. Advanced methods like compressed sensing (CS) theory can be employed for the demodulation of PPM signal using low-speed analog-to-digital converter (ADC) [16]. On the transmitter side, along with the classical digital-to-analog converter (DAC) approach, hardware-based pulse generators with advanced pulse shaping schemes are widely used [3].

The novelty of the proposed PPM modem lies in the implementation of event timer-based time-to-digital converter (TDC) for the demodulation and digital delay line (DDL)-based digital-to-time converter (DTC) for the modulation of the PPM signal. The employment of these technologies allows the integration of software-defined radio (SDR) concepts to UWB, which, in turn, allows to easily switch between different PPM modulation formats and bandwidths. ADC/DAC-based SDR designs for PPM and space communications are reported in [17], [18]. Typical SDR bottleneck is the interface between ADC/DAC and the computer. Also, in the proposed design, both TDC and DTC hardware must be capable of streaming the time tags at very high speed between the computer running the software and hardware performing TDC/DTC functions.

The rest of this paper is organized as follows: In Section II, the functional design of the PPM transceiver is presented, and Section III explains the implementation of the modulator. Section IV describes the implementation of the demodulator. Section V presents results obtained from the conducted tests of the PPM transceiver in a laboratory environment. Finally, Section VI draws overall conclusions about the research.

## II. Functional design of transceiver

The transceiver comprises the modulator, the demodulator, and associated software packages. The modulator is implemented as a custom-made printed circuit board (PCB), and the Eventech Stream Time Tagger (ESTT) 7 Series event timer is used as the demodulator. The block diagram of the transceiver can be seen in Fig. 1.

The modulator board receives the pulse position values, which are calculated in real-time on personal computer (PC) according to the input binary data and error correcting code (ECC). The PPM pulses are generated based on the reference clock signal and delayed by the necessary time interval.

On the receiver side, ESTT, which is connected to the PC via a fast USB 3.0 interface, continuously registers absolute times (time tags) of all incoming pulses. On request, the time tag vector is sent to the PC for processing and demodulation. Time tags are necessary for calculating the DPPM symbol values and are obtained by subtracting each previous time tag from the next one. The demodulation of DPPM can be expressed by the following equation:

$$\hat{s_i} = \lfloor (t_i - t_{\mathrm{g}} + d_{\mathrm{w}}/2) / d_{\mathrm{w}} \rfloor , \tag{1}$$

where $\hat{s_i}$ is the recovered value of the symbol $i$, $t_i$ is an $i$ time interval, $t_{\mathrm{g}}$ is a guard time in $\mathrm{ns}$ (due to TDC dead time) and $d_{\mathrm{w}}$ is a position width.

After recovering the values of all received symbols, Gray decoding is applied for each symbol. After that, Reed-Solomon (RS)(255,223) decoding is completed. The resulting recovered bits $\hat{b}$ are then saved in the binary data file. These bits can represent any transmitted data and be further decoded to output data in text, image or video formats.

It is worth noticing that since PPM modulation and demodulation are performed in software, given PPM transceiver is capable of using different PPM modulation schemes. Currently we have implemented coherent PPM, incoherent TR-PPM [19] and DPPM [9]. Other modulation schemes like multi-pulse position modulation (M-PPM) and serially-concatenated pulse position modulation (SCPPM) [20], [21] can be added by writing respective software modules.

### A. The use of error correcting code

For forward error correction (FEC), RS(255,223) code with 8-bit symbols has been chosen, with 223 bytes of encoded data and 32 bytes of parity data. This ECC can detect and correct up to 16 bytes containing any number of error bits within these bytes. This encoding type is well suited for burst errors when many bits are flipped in succession.

In the transmitter part, written in C++, RS(255,223) code encodes binary data previously converted to decimal data with 8 bits per symbol before Gray code is applied. The receiver part of the software is written in Python, so for RS(255,223), parameters were chosen for both codes to be compatible. In the receiver, RS code is decoded after Gray code decoding as seen in Fig. 1. After RS(255,223) decoding, one of the two possible outcomes will happen:

- If the number of error bytes is less or equal to 16, error-less data is recovered;
- If the number of error bytes exceeds 16, the data part of the encoded data is retrieved without any error correction.

In the best-case scenario, when all error bits wholly occupy all 16 bytes, it is possible to recover all 128 bits when 8-bit symbols are used. In a more random distribution of error bits, when errors are present in more than 16 bytes, nothing will be corrected; thus, when dealing with received data having high bit error ratio (BER) that exceeds the FEC limit, this ECC would not be able to significantly lower BER of that data reception.

## III. Implementation of the modulator

A custom PCB has been developed for generating PPM signals, which is controlled by a PC. The main components of the real-time PPM modulator are the MC100EP196B high-precision programmable DDL, SI5394J-A phase-locked loop (PLL) jitter attenuator and Cyclone IV field-programmable gate array (FPGA) system-on-chip (SoC). The jitter attenuator features an ultra-low jitter of 69 $\mathrm{fs}$ and a frequency output range of up to 1028 MHz and delivers a 0.09 $\mathrm{ps}$ RMS phase jitter performance with a 0 ppm error.

The Altera Cyclone IV FPGA SoC controls and commands the modulator. FPGA was chosen because of its high-speed digital logic capabilities. It interprets the commands and serves

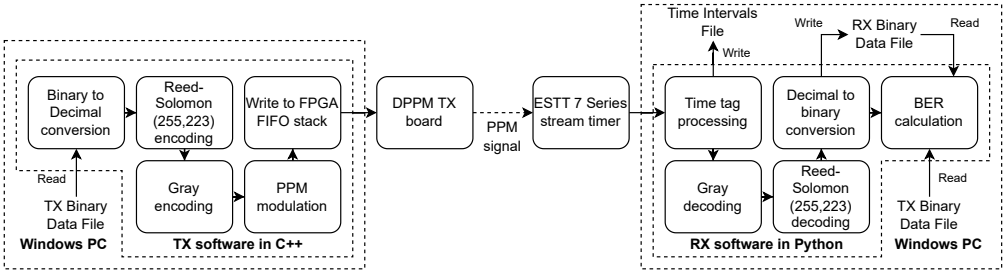



Fig. 1. Block diagram of a transceiver.

TABLE I
PARAMETERS OF THE MODULATOR.

| Parameter | Value |
|---|---|
| DTC granularity (minimum step) | 10 ps |
| Maximum precision delay | 10450 ps |
| Bits for precision delay | 10 |
| Maximal coarse delay | 655.35 µs |
| Bits for coarse delay | 16 |
| Maximal number of pulses per second | $10^6$ |
| Minimal pulse repetition interval | 10 ns |

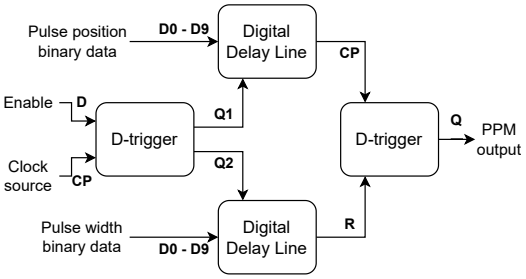



Fig. 2. Block diagram of the pulse position and width adjustment circuit.

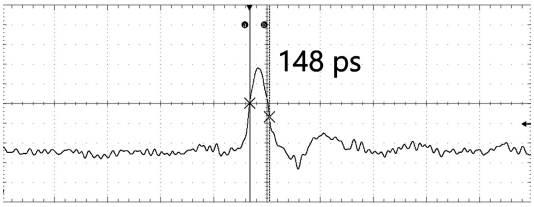



Fig. 3. Output waveform of the modulator.

as an interface between the PC and the rest of the modulator board. The connection to the PC is achieved using USB 3.0. The FT601Q USB 3.0 Super-Speed to 32-bit Sync FIFO was selected for the interface due to its high speed (66 MHz) and 32-bit bus width. The software architecture of the FPGA SoC part of the modulator is implemented as Nios® II virtual processor with custom IO procedures written in VHDL. Employment of Nios® soft microprocessor allows part of the software modules to be developed in C++.

The use of the DDLs as a DTC for generating PPM signals has been proven successful in the past [22]. Therefore, this approach was chosen. The MC100EP196B high-precision programmable DDL has a maximum time resolution of 10 ps and a programmable range of 10450 ps when using all data inputs (D0 to D9). The total delay range of the DTC is 2.2 ns to 12.4 ns, including the minimum fixed delay.

For each PPM symbol, a pulse is generated based on the 10 MHz reference clock, which can be delayed in 10 ns increments (coarse delay) and also delayed by the DDLs to achieve fine control over the pulse location in time (precision delay). The modulator's parameters can be seen in Table I.

The pulse width can be adjusted by using a second DDL in parallel with the DDL used to precisely adjust pulse location in time. The delay value set in the second DDL is the sum of the delay required in the PPM symbol and the desired pulse width. The second DDL output is used to reset a D-trigger, generating a short pulse with the required width. The block diagram of such an arrangement can be seen in Fig. 2 and the waveform of its output pulse, where the width was set to 150 ps to satisfy PPM demodulator minimum pulse width requirement, can be seen in Fig. 3.

## IV. IMPLEMENTATION OF THE DEMODULATOR

For the reception of PPM signal, ESTT 7 Series event timer was used. This event timer works in the "stream mode," which allows processing events immediately after their occurrence and provides an ability to use the event timer as a TDC in real-time. ESTT connects to the PC via a USB 3.0 interface that provides fast data rate transmission between the two devices [23]. ESTT parameters are compiled in Table II.

The software part of the demodulator is based on the software [8], [9] used for the previous Eventech Ltd. event timer A033-ET [23] and is written in Python. This software has been updated for use with ESTT, as this event timer can stream the time tags to PC in real time.

TABLE II
PARAMETERS OF THE ESTT 7 SERIES EVENT TIMER.

| Parameter | Value |
|---|---|
| Single-shot RMS resolution | 2.2 – 2.3 ps (max 2.5 ps) |
| Dead time | 40 ns |
| Impulse duration | $\geq$ 125 ps |
| Measurement rate | 20 MEPS |
| Single input time tag drift | $<$ 2 ps/C° |
| Input to input offset drift | $<$ 0.05 ps/C° |

TABLE III
TRANSCEIVER TEST FIXED PARAMETERS.

| Parameter | Description | Value |
|---|---|---|
| Modulation scheme | Modulation scheme | DPPM [9] |
| Bit count | Number of bits sent | $10^6$ |
| $t_g$ | Guard time, ns | 50 |
| $\tau$ | Pulse duration, ps | 150 |
| x | Bit pattern | Pseudo-random |

For the ability to test the performance of the developed system, BER computation was implemented in software to calculate BER in real-time via the comparison of binary data from the files used in transmission and demodulated data.

## V. LABORATORY TESTING

### A. Test setup

The PPM transceiver has been tested in a laboratory environment. In these tests, the output of the modulator was connected directly to the input of the event timer, as seen in Fig. 4. For all tests, a pseudo-random bit sequence (PRBS) was used with the length of one million bits. The impact of different time bin duration values and number of positions with various FEC codes has been explored, and BER calculated for each case. The fixed parameters of the tests can be seen in Table III.

### B. Results

The BER of experimental DPPM link at three different sizes of PPM symbols are depicted in Fig. 5. The results show that the PPM transceiver provides real-time data communication, and the implemented error correction algorithms are working as intended. The most significant impact on the BER is achieved using Gray code used in error correction, further enhanced by the RS error correction algorithm. When combined, these error correction schemes provide a BER of




Fig. 4. Test setup with the connection of PPM modulator board and ESTT 7 Series event timer.

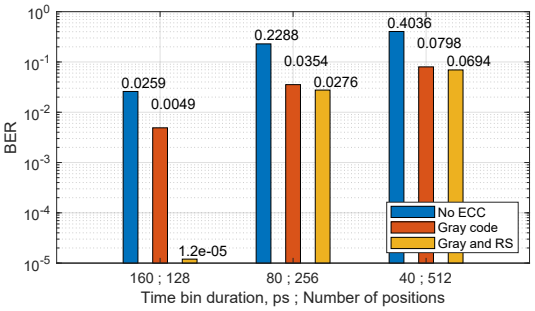



Fig. 5. Transceiver test results.

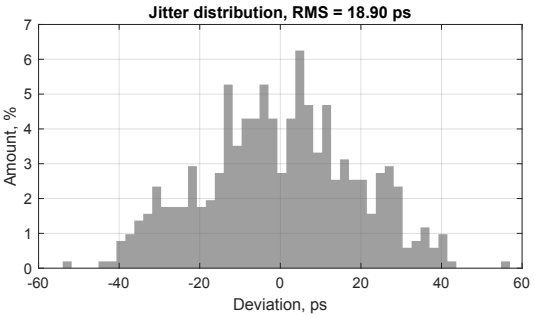



Fig. 6. Jitter distribution across the whole range of pulse positions, obtained by comparing measured and expected pulse positions.

$1.2 \cdot 10^{-5}$ at a position width of 160 ps. Even for extremely small 40 ps position width, using ECC, it is possible to reduce BER to 0.07, which can be further reduced using more advanced codes, such as low-density parity check (LDPC).

Considering at least 50 ns pause between two adjacent pulses due to dead time of TDC, given DPPM modulation scheme can theoretically achieve data rate up to 149 Mbit/s using 512 positions and a position width of 40 ps [9]. In practice, the developed transceiver prototype achieved a real-time transmission speed of about 10 Mbit/s due to PC software limitations.

The jitter distribution shown in Fig. 6 was obtained by analyzing the deviations of measured pulse positions from expected ones. The resulting root mean square (RMS) of pulse position deviation is 18.9 ps. Considering that the jitter distribution is close to normal, 99.7% of deviations fall within the $3\sigma$ range, i.e., 56.7 ps.

Demonstration of live video transmission using the above presented DPPM modem can be seen on the project website [24].

## VI. CONCLUSIONS

The given contribution presents a high-speed PPM modem design for optical and radio communications. The main feature

of the proposed design is versatility, which is achieved by adhering to SDR design concepts where most of the functions are offloaded to the software. However, unlike traditional SDR, which relies on DAC/ADC, the proposed design relies on precise high-speed DTC/TDC for converting information between the analog and digital domains.

Laboratory testing exhibited great potential for the proposed approach. However, due to the relatively large dead time of TDC, data rates above 150 $\mathrm{Mbit/s}$ are impractical due to the very small position width required. For example, to reach a data transmission rate of 200 $\mathrm{Mbit/s}$ at TDC dead time of 50 $\mathrm{ns}$, it is necessary to use a 5 $\mathrm{ps}$ position width.

Employment of the event timer, primarily designed for satellite laser ranging (SLR), sets limitations in size, control interface, data transfer bitrate and modulation format. Therefore, it is planned to improve the characteristics of the PPM modem in future versions.

The presented PPM transceiver can serve as a prototype for developing energy-efficient communication systems for deep space, IoT, and underwater optical communications. Moreover, the given prototype can be used to implement UWB-based ISAC designs, which will be an important part of future terrestrial and space networks. An essential aspect of developing a PPM modem for space applications is compliance with international standards, such as Consultative Committee for Space Data Systems (CCSDS) 141.0-B-1 and 142.0-B-1 [10] for high photon efficiency (HPE) systems.

The plans for the near future include integrating the developed PPM modem with the optical system of SLR station and conducting a test of simultaneous laser ranging and data transmission.

## ACKNOWLEDGMENT

This research was made possible by the funding provided by the Latvian Council of Science grant No. lzp-2021/1-0475, "Picosecond-resolution pulse position modulation for beyond-the-limits energy efficiency of communications", Riga Technical University's Master Grant program (No. ZM-2023/34) and the valuable support from Eventech Ltd.

## REFERENCES

[1] A. Biswas, M. Srinivasan, R. Rogalin, S. Piazzolla, J. Liu, B. Schratz, A. Wong, E. Alerstam, M. Wright, W. T. Roberts, J. Kovalik, G. Ortiz, A. Na-Nakornpanom, M. Shaw, C. Okino, K. Andrews, M. Peng, D. Orozco, and W. Klipstein, "Status of NASA's deep space optical communication technology demonstration," in *2017 IEEE International Conference on Space Optical Systems and Applications, ICSOS 2017*. IEEE, nov 2018, pp. 23–27.

[2] V. Yajnanarayana and P. Handel, "Joint Estimation of TOA and PPM Symbols Using Sub-Nyquist Sampled IR-UWB Signal," *IEEE Communications Letters*, vol. 21, no. 4, pp. 949–952, apr 2017.

[3] B. Jajodia, A. Mahanta, and S. R. Ahamed, "IEEE 802.15.6 WBAN Standard Compliant IR-UWB Time-Hopping PPM Transmitter using SRRC signaling pulse," *AEU - International Journal of Electronics and Communications*, vol. 117, p. 153119, apr 2020.

[4] A. A. Youssef, "Adaptive LDPC coded high data rate based IR-UWB combined with VMIMO system for vehicular communication links," *AEU - International Journal of Electronics and Communications*, vol. 169, p. 154747, sep 2023.

[5] A. Somov and A. Baraev, "Consist-to-Consist communications in the trains: Is it time to use ultra wide-band?" *Computers & Electrical Engineering*, vol. 72, pp. 965–975, nov 2018.

[6] M. L. G. Salmento, E. Pestana de Aguiar, Â. Camponogara, and M. V. Ribeiro, "An enhanced receiver for an impulsive UWB-based PLC system for low-bit rate applications," *Digital Signal Processing*, vol. 70, pp. 145–154, nov 2017.

[7] S. Duan, R. Su, C. Xu, Y. Chen, and J. He, "Ultra-Wideband Radio Channel Characteristics for Near-Ground Swarm Robots Communication," *IEEE Transactions on Wireless Communications*, vol. 19, no. 7, pp. 4715–4726, jul 2020.

[8] S. Migla, O. Selis, P. E. Sics, M. Pudzs, M. Zeltins, and A. Aboltins, "A Design of UWB Communication Testbed with Event Timer-based PPM Demodulator," in *2022 IEEE 2nd Ukrainian Microwave Week (UkrMW)*, 2022, pp. 691–694.

[9] O. Selis, S. Migla, P. E. Sics, M. Zeltins, S. Spolitis, and A. Aboltins, "Demonstration of 50 ps Per-Position Differential Pulse Position Modulation Data Transmission," in *2023 IEEE 10th Jubilee Workshop on Advances in Information, Electronic and Electrical Engineering (AIEEE)*, 2023, pp. 1–4.

[10] B. L. Edwards, "Latest Status of the CCSDS Optical Communications Working Group," in *2022 IEEE International Conference on Space Optical Systems and Applications, ICSOS 2022*. IEEE, mar 2022, pp. 1–6.

[11] J. Huang, C. Li, J. Dai, R. Shu, L. Zhang, and J. Wang, "Real-Time and High-Speed Underwater Photon-Counting Communication Based on SPAD and PPM Symbol Synchronization," *IEEE Photonics Journal*, vol. 13, no. 5, pp. 1–9, oct 2021.

[12] B. P. Dix-Matthews, D. R. Gozzard, S. F. E. Karpathakis, C. T. Gravestock, and S. W. Schediwy, "Ultra-Wideband Free-Space Optical Phase Stabilization," *IEEE Communications Letters*, vol. 25, no. 5, pp. 1610–1614, may 2021.

[13] T. Landolsi and A. F. Elrefaie, "Effects of pointing errors and channel fading on the performance of free-space optically-preamplified PPM systems," *International Journal of Communication Systems*, vol. 29, no. 15, pp. 2313–2324, oct 2016.

[14] Y. Wen, F. Yang, J. Song, and Z. Han, "Free Space Optical Integrated Sensing and Communication Based on LFM and CPM," *IEEE Communications Letters*, vol. 28, no. 1, pp. 43–47, jan 2023.

[15] H. Khani, "Improved Detection Schemes for Non-coherent Pulse-Position Modulation," *Wireless Personal Communications*, vol. 131, no. 3, pp. 2173–2192, aug 2023.

[16] W. Wang, S. Wang, J.-a. Yang, and H. Liu, "Under-Sampling of PPM-UWB Communication Signals Based on CS and AIC," *Circuits, Systems, and Signal Processing*, vol. 34, no. 11, pp. 3595–3609, nov 2015.

[17] R. J. Roche, M. J. Shalkhauser, J. P. Hickey, and J. C. Briones, "Reconfigurable, intelligently-adaptive, communication system, an SDR platform," in *34th AIAA International Communications Satellite Systems Conference, 2016*, 2016.

[18] H. Schlemmer, N. Stamenic, B. Ferenczi, and M. Schoenhuber, "Results from a CCSDS-compliant High Photon Efficiency Downlink SDR Platform," in *2019 8th International Workshop on Tracking, Telemetry and Command Systems for Space Applications (TTC)*. IEEE, sep 2019, pp. 1–5.

[19] S. Spolitis, D. Prigunovs, S. Migla, D. Ortiz, O. Selis, P. E. Sics, A. Ostrovskis, T. Solovjova, J. Semenjako, and A. Aboltins, "Demonstration of 512-TR-PPM Fiber Optical Transmission Link," in *2023 Photonics & Electromagnetics Research Symposium (PIERS)*, 2023, pp. 1416–1422.

[20] M. F. Barsoum, B. Moision, M. Fitz, D. Divsalar, and J. Hamkins, "Iterative Coded Pulse-Position-Modulation for Deep-Space Optical Communications," in *2007 IEEE Information Theory Workshop*. IEEE, sep 2007, pp. 66–71.

[21] J. M. Nappier and N. C. Lantz, "Development of an optical slice for an RF and optical software defined radio," in *SPIE Photonics West*, 2018, p. 51.

[22] P. E. Sics, O. Selis, S. Migla, M. Zeltins, S. Spolitis, V. Kurtenoks, and A. Aboltins, "Programmable Delay Line Based High-speed PPM Modulator with 50 ps Time Resolution," in *2023 Photonics & Electromagnetics Research Symposium (PIERS)*, 2023, pp. 1779–1786.

[23] "Key Products," https://eventechsite.com/products/.

[24] "Live video transmission using PPM," http://www.picoppm.org/?p=164.

**Annex 4**

©2024 IEEE. Reprinted, with permission, from Migla, S., Selis, O., Sics, P. E., and Aboltins, A. “Error Analysis and Correction Techniques for PPM Communication Links with Jitter and Clock Drift.” *2024 IEEE International Conference on Microwaves, Communications, Antennas, Biomedical Engineering and Electronic Systems (COMCAS)*. 2024, pp. 1–4. DOI: 10.1109/COMCAS58210.2024.10666259

# Error Analysis and Correction Techniques for PPM Communication Links with Jitter and Clock Drift

Sandis Migla
*Institute of Microwave Engineering and Electronics*
*Riga Technical University*
Riga, Latvia
sandis.migla@rtu.lv

Oskars Selis
*Institute of Microwave Engineering and Electronics*
*Riga Technical University*
Riga, Latvia
oskars.selis@rtu.lv

Pauls Eriks Sics
*Institute of Microwave Engineering and Electronics*
*Riga Technical University*
Riga, Latvia
pauls-eriks.sics@rtu.lv

Arturs Aboltins
*Institute of Microwave Engineering and Electronics*
*Riga Technical University*
Riga, Latvia
aboltins@rtu.lv

***Abstract*—This paper addresses two significant challenges associated with high-speed data transmission using pulse position modulation (PPM): systematic errors caused by clock drift and random errors resulting from signal jitter. We present a comprehensive theoretical framework that encompasses the error distribution and causal analysis of PPM links, along with algorithms for error correction. To address systematic errors, we introduce an original algorithm, while for combating random errors, we evaluate the effectiveness of forward error correction (FEC). We derive precise bit error ratio (BER) curves for various combinations of the proposed error correction methods through simulations based on device measurements. Our results highlight the practical significance of the proposed solutions, demonstrating their efficacy in real-world scenarios.**

***Index Terms*—ultra wideband communication, Reed-Solomon codes, time measurement, jitter, clocks, forward error correction**

## I. Introduction

The ever-growing need for data correction algorithms in high-speed data links means that advanced methods of improving data transmission links are needed. Along with custom, application-specific estimation and correction algorithms, forward error correction (FEC) is widely used in pulse position modulation (PPM)-based free space optical (FSO) communication and other systems that use transmission channels that are noisy and can be unreliable. Furthermore, the errors in the received information tend to increase when moving closer to the limits of the data transmission capacity for the channel. The FEC algorithm must be selected depending on the application and computational capabilities of the communication modem. This contribution is devoted to the theoretical study and simulation of custom error-correction algorithms in conjunction with FEC for the improvement of transmitted reference pulse-position modulation (TR-PPM) transmission links [1]. In the following section, we will review major PPM link degradation reasons and respective mitigation methods. Special attention will be paid to FEC methods and their suitability to PPM communication links.

The main contributions of this paper are as follows: First, a theoretical framework describing the impact of the jitter and systematic errors, such as clock drift, on the performance of PPM link is developed. Second, using computer simulation, the contribution of Gray coding and Consultative Committee for Space Data Systems (CCSDS) Reed-Solomon (RS) coding to the reduction of bit error ratio (BER) of TR-PPM communication link with event timer-based demodulator is found.

## II. Related work

Atmospheric turbulence caused by variation in temperature, pressure, wind, etc., can lead to jitter and data errors due to inhomogeneity in the FSO transmission channels [2]. As coherent PPM uses a separate clock signal for synchronization, any clock drift can cause synchronization issues which lead to data corruption. The primary source of the clock drift is the instability of local oscillators in the transmitter and receiver. Clock drift can also be caused by relative motion between transmitter and receiver stations [3], i.e., the Doppler effect.

There is a great variety of FEC algorithms, and this area continues evolving. The most straightforward approach, which is widely used in communications, is Gray coding [4], where adjacent symbols are encoded by maximally similar bit combinations. In the 1950s, one of the first FEC codes was introduced by American engineer Richard Hamming. Since then, several FEC codes have been developed. Low density parity check (LDPC) was one of the first error correction codes that allowed the achievement of data transmission rates close to transmission channels' maximum capacity, which is dictated by the Shannon theorem. For the last 30 years, Turbo and RS coding has been widely used in 3G/4G mobile communications, deep space satellite communication, and other data transmission environments. Studies [5] have shown that Turbo coding has significantly increased channel reliability under extreme turbulence conditions in FSO system. There have also been studies that have shown that by using RS hard decision coding for FEC, it is possible to greatly increase the sensitivity of the receiver in FSO applications [6], [7]. There are also FEC methods that combine RS and Turbo coding. Paper [8] explores the possibility of using Trellis-coded pulse-position modulation

(T-PPM) for improving the performance of optical communication systems that employ high-power Q-switched lasers and in which pulse width inaccuracies are present. The authors conclude that T-PPM can reduce data loss caused by reduced signal intensity. In the research [9], authors analyze the employment of Photograph LDPC codes for FSO communication systems employing PPM.

## III. Theoretical framework

Pulse position modulation PPM is a modulation technique that encodes information based on the position of the pulse in the time domain. The pulse can be coded in $M = 2^N$ positions, where $N$ represents the number of bits per symbol. Therefore, a symbol length is equal to $l_s = \Delta M$ where $\Delta$ is the position width of a single position. It is important to mention that the pulse width does not affect the encoded information. Such signal design allows the utilization of event timers for the demodulation of PPM signal [10]. However, employment of the event timer for demodulation usually has a side effect – the PPM signal must contain a quiescent time $T_Q$ during which the timer is busy with measurement and unable to register new events. In modern event timers [11], $T_Q$ falls within the range of 40-50 ns. A time domain entity containing both symbol length and quiescent time further will be regarded as PPM frame, and its length could be calculated using formula (1):

$$l_{\mathrm{F}} = \Delta \cdot M + T_Q. \tag{1}$$

where $\Delta$ is position width and $M$ is number of positions per frame, i.e. order of PPM signal. In the setups where PPM position width below 100 ps is used, it is challenging to maintain precision due to various conditions that can cause position errors. For instance, temperature can affect the internal circuitry, which generates clock signals, resulting in position errors. Additionally, errors may occur as a result of the inability of the generator to provide an exact clock divisor, leading to tiny pulse shifts in time. Also, the movement of the transmitter and receiver stations will lead to various issues.

Moreover, these errors can arise if a jitter is introduced in the signal, causing the receiver to detect the pulse position differently from what was expected. Earlier tests [12] have shown that the values of the jitter are distributed approximately normally. The BER of PPM data transmission can be found via calculation of the probability of the pulse appearing at different positions using the formula (2).

$$P(\sigma,\mu) = 1 - \int_{-\frac{1}{2}\Delta}^{\frac{1}{2}\Delta} \frac{1}{\sigma\sqrt{2\pi}} e^{-\frac{1}{2}(\frac{x-\mu}{\sigma})^2}\, dx. \tag{2}$$

where $x$ is the deviation from ideal position, $\mu$ is systematic error caused by the clock drift, $\sigma$ is standard deviation of the jitter. For the normal distribution function, 99.73% of cases are within $\pm 3\sigma$ interval. If we limit the jitter in range $(-t_j/2, t_j/2)$, using the $3\sigma$ rule, the standard deviation can be found as $\sigma = t_j/6$, where $t_j$ is the jitter amplitude.

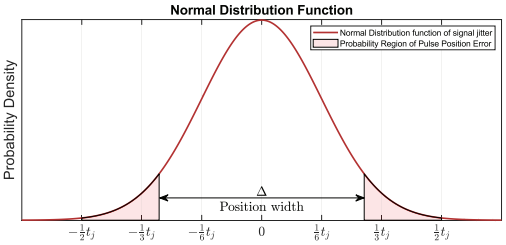



Fig. 1. Distribution of deviations from the ideal position in PPM signal.

If the PPM signal structure where bits per symbol $N = 8$ is used, and a position error occurs where the time drift does not exceed $\frac{3}{2}\Delta$, then a one-bit error will be determined in 8-bit symbol. If deviation $x$ does not exceed one position, and it leads to only a 1-bit error, the BER $B$ can be calculated by using the formula (3):

$$B(\sigma,\mu) = \frac{P(\sigma,\mu)}{N} = \frac{1}{N} - \frac{1}{N}\int_{-\frac{1}{2}\Delta}^{\frac{1}{2}\Delta} \frac{1}{\sigma\sqrt{2\pi}} e^{-\frac{1}{2}(\frac{x-\mu}{\sigma})^2} dx. \tag{3}$$

If the time shifts from expected positions are linear for all pulses, a simple time shift averaging method called the zero position interval method could be used. This method requires a certain number of frames in which the pulse is fixed at the first symbol position. Based on the PPM parameters, an average time shift for several frames containing fixed interval pulses can be calculated. A higher number of fixed intervals will result in more precise averaging. The receiver will apply this average value to the remaining pulses, assuming that the other pulses have the same average time shift. If an averaging is performed on the time intervals, which corrects the described clock drift $\mu$, it is possible to calculate the improvement $\gamma$ of the correction by the formula (4).

$$\gamma = \frac{B(\sigma,\mu)}{B(\sigma,0)}. \tag{4}$$

Due to the high probability of position error if $t_j \geq \Delta$, appropriate FEC codes should be implemented. If the PPM pulse is detected in a different position, the binary code of the symbol will change respective to the new position. Employment of Gray coding of the PPM positions ensures that one position shift will result in a single-bit error.

A much more advanced technique is the RS code, an error correction code widely used in communications. This error correction adds redundant correction bits to the data to be used for the decoding process. It encodes and decodes the data by symbols, which are perfect for PPM communication since they consist of $N$ bits each. RS encoding requires two parameters: the total symbol length $n$ and the number of redundant bits $k$. These parameters are usually determined by the expected error rate and the length of the signal frame block. The data symbols are separated into blocks, with each block transformed into coefficients of a polynomial

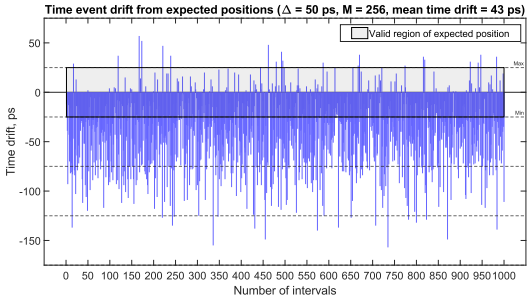



Fig. 2. Data pulse deviation from the expected position before correction.

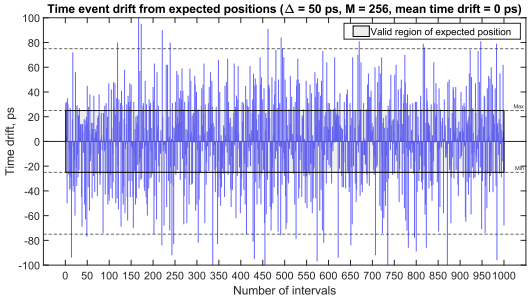



Fig. 3. Data pulse deviation from the expected position after correction.

representing the data. The block length determines the degree of the polynomial. The redundant bits are generated based on the polynomial, which means the redundant symbols act as coefficients that are part of the polynomial. This data block is then sent to the receiver for decoding.

## IV. Validation of Clock Drift Correction

The experimental validation of the clock drift correction algorithm has been performed using the pulse pattern generator (PPG) and high-precision event stream timer Eventech ESTT-01, connected via a Bias T as reported in [13].

A calibration sequence consisting of five TR-PPM data frames in the ”0” position was used before the main data frame sequence. The receiver software corrected the clock drift error by comparing the expected time interval between the reference and data pulses and the actual received interval for each calibration frame. The average difference was calculated and applied to the entire TR-PPM data sequence. The deviation from expected intervals before correction is shown in Fig. 2 and after correction in Fig. 3. The results show that clock drift error manifests as an offset of the entire TR-PPM by a specific value. The implemented correction algorithm can determine the offset, and applying the correction leads to significantly lower BER as reported in [13].

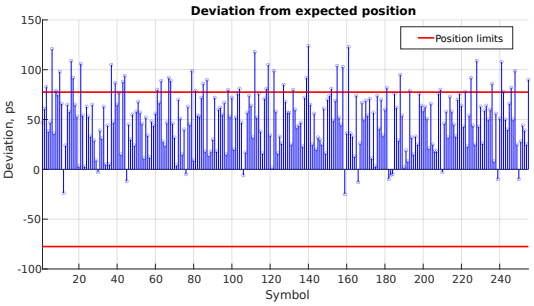



Fig. 4. Pulse deviation from expected positions within simulated clock drift.

## V. Validation of Forward Error Correction

A simulation was performed in a Matlab environment and employed experimentally determined jitter and clock drift values of the custom-designed programmable delay-line based TR-PPM modulator board, reported in [12], which is used for generating the TR-PPM waveform. The board can generate a TR-PPM waveform with a minimum position width of 155 ps and a frame duration of 400 ns, the jitter RMS of the modulator was about 40 ps. In the hardware prototype, the deviation of the data pulses from their expected positions was distributed semi-normally. In contrast, the errors introduced by the clock drift were almost constant during one PPM frame. As the clock drift does not significantly increase for the duration of the TR-PPM sequence, it can be modeled as a constant offset from the expected data pulse position values. The illustration of simulated jitter and clock drift can be seen in Fig. 4.

In the simulation CCSDS 131.0-B-3 Section 4 compliant RS error correction algorithm was implemented. The RS(255, 223) code was used, in which a block consists of 223 data bits with 255 total bits. The experiment was repeated using various parameters listed in Table I. The position count in all experiments was 256 and position width 155 ps. The transmitted data was generated as a 255 symbol long (8 bits per symbol, 1784 total bits) pseudo-random bit sequence (PRBS) and encoded using RS(225, 223) code and Gray code, if applicable for the specific experiment. The

TABLE I
Experiment parameters.

| Test nr. | Jitter RMS range, ps | Clock drift, ps | Error correction used |
|---|---|---|---|
| 1 | 30-55 | 0 | No error correction |
| 2 | 30-55 | 0 | Gray code |
| 3 | 30-55 | 0 | Reed-Solomon code |
| 4 | 30-55 | 0 | Reed-Solomon code and Gray code |
| 5 | 10-22 | 43 | No error correction |
| 6 | 10-22 | 43 | Gray code |
| 5 | 10-22 | 43 | Reed-Solomon code |
| 6 | 10-22 | 43 | Reed-Solomon code and Gray code |

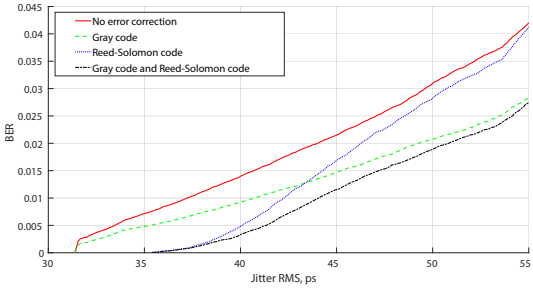



Fig. 5. BER vs jitter RMS for various error correction methods in PPM system without clock drift.

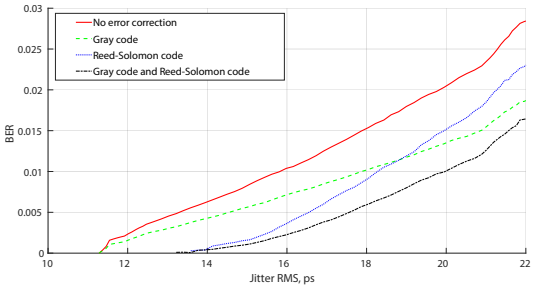



Fig. 6. BER vs jitter RMS for various error correction methods in PPM system with mean clock drift 43 ps.

event stream timer Eventech ESTT-01 was simulated using the known parameters of the event timer, i.e., by adding 3 ps RMS jitter to the simulated received data [13]. The experimentally obtained BER as a function of jitter RMS for the previously mentioned error correction schemes without clock drift error can be seen in Fig. 5 and with added clock drift error in Fig. 6. The results show that RS error correction scheme performs well up to a jitter RMS of about 45 ps. As the jitter further increases, the gain from the error correction is minimal. In contrast, bit errors emerge at a jitter RMS of 32 ps in case of no error correction and Grey code only. This is expected, as errors should appear when the deviation exceeds position limits. The Gray code provides the most significant decrease of the BER as it provides for a single bit error in the TR-PPM symbol in case the data pulse is shifted by a value equal to or less than one position duration.

## VI. Conclusions

This research was devoted to the development and validation of error correction algorithms for data communication links that employ PPM signaling scheme. Methods for mitigating systematic errors caused by the clock drift and random errors caused by the jitter were proposed.

Clock drift correction via averaging offsets from the ideal positions significantly reduces BER. However, it requires data-aided estimation of the clock drift via transmission of known training sequences before sending actual data. In TR-PPM, time measurement between the reference pulses can be employed to estimate the clock drift without sending the training sequence.

FEC based on RS code allows for the reduction of bit errors caused by both jitter and clock drift. However, after a certain point, RS code cannot correct the bit error caused by the jitter since RS(255,223) code can correct 16-bit error per block. For this reason, data should also be encoded using Gray code since it improved in BER over the whole range of jitter RMS values used in this experiment.

## Acknowledgment

This research was made possible by the funding provided by Riga Technical University's Master Grant program (No. ZM-2023/26) and the valuable support from Eventech Ltd.

## References

[1] S. Spolitis, D. Prigunovs, S. Migla, D. Ortiz, O. Selis, P. E. Sics, A. Ostrovskis, T. Solovjova, J. Semenjako, and A. Aboltins, "Demonstration of 512-tr-ppm fiber optical transmission link," in *2023 Photonics & Electromagnetics Research Symposium (PIERS)*, 2023, pp. 1416–1422.

[2] A. S. Alatawi, A. A. Youssef, M. Abaza, M. A. Uddin, and A. Mansour, "Effects of atmospheric turbulence on optical wireless communication in neom smart city," *Photonics*, vol. 9, no. 4, 2022.

[3] M. S. Bashir and S. S. Muhammad, "Time Synchronization in Photon-Limited Deep Space Optical Communications." *IEEE Transactions on Aerospace and Electronic Systems*, pp. 30–40, 2020.

[4] T. Li, H. Zhou, and M. Yi, "Gray coded PPM performance with imperfect slot synchronization in optical communication," in *Pacific Rim Conference on Lasers and Electro-Optics, CLEO - Technical Digest*. IEEE, aug 2009, pp. 1–2.

[5] B. D. Ajewole, P. A. Owolawi, and V. M. Srivastava, "Error performance of coded BPSK OFDM-FSO system under atmospheric turbulence." *Journal of Communications*, p. 936–944, 2019.

[6] J.-D. Jeong, J. Han, C.-S. Choi, W.-K. Park, I.-W. Lee, and J.-W. Chong, "Design of block-coded group PPM modem for low-power and low-cost home energy management," in *2016 International Conference on Information and Communication Technology Convergence (ICTC)*. IEEE, oct 2016, pp. 78–81.

[7] Z. He., Y. Yu., T. Bo., and H. Kim, "Probabilistic Amplitude Shaping for IM/DD System Using Hard-Decision Decoding." in *24th OptoElectronics and Communications Conference/International Conference Photonics in Switching and Computing*. IEEE, 2019.

[8] K. Kiasaleh, T.-Y. Yan, and M. Srinivasan, "Trellis-coded pulse-position modulation for optical communication systems impaired by pulsewidth inaccuracies," *Journal of Lightwave Technology*, vol. 17, no. 8, pp. 1336–1346, 1999.

[9] L. Lv, Y. Fang, L. Dai, Y. Li, and M. Guizani, "Asymmetric Dual-Mode Constellation and Protograph LDPC Code Design for Generalized Spatial MPPM Systems," *IEEE Transactions on Communications*, vol. 71, no. 6, pp. 3165–3177, 2023.

[10] S. Migla, O. Selis, P.-E. Sics, M. Pudzs, M. Zeltins, and A. Aboltins, "A Design of UWB Communication Testbed with Event Eimer-based PPM Demodulator," in *2022 IEEE 2nd Ukrainian Microwave Week, UkrMW 2022 - Proceedings*. IEEE, nov 2022, pp. 691–694.

[11] Eventech Ltd, *Event Timer A033-ET / usb*. [Online]. Available: http://eventechsite.com/en/products/event-timer-a033-et/

[12] P. E. Sics, O. Selis, S. Migla, M. Zeltins, S. Spolitis, V. Kurtenoks, and A. Aboltins, "Programmable delay line based high-speed ppm modulator with 50 ps time resolution," in *2023 Photonics & Electromagnetics Research Symposium (PIERS)*, 2023, pp. 1779–1786.

[13] O. Selis, S. Migla, P. E. Sics, M. Zeltins, S. Spolitis, and A. Aboltins, "Demonstration of 50 ps per-position differential pulse position modulation data transmission," in *2023 IEEE 10th Jubilee Workshop on Advances in Information, Electronic and Electrical Engineering (AIEEE)*, 2023, pp. 1–4.

**Annex 5**

Aboltins, A., Solovjova, T., Semenako, J., Kusnins, R., Migla, S., Sics, P. E., Selis, O., Tihomorskis, N., Prigunovs, D., Ostrovskis, A., and Spolitis, S. “Passive Electrical and Optical Methods of Ultra-Short Pulse Expansion for Event Timer-Based TDC in PPM Receiver.” *Electronics* 12.22 (2023). DOI: 10.3390/electronics12224634

*electronics*

MDPI

*Article*

# Passive Electrical and Optical Methods of Ultra-Short Pulse Expansion for Event Timer-Based TDC in PPM Receiver

**Arturs Aboltins [1,*], Tatjana Solovjova [1], Janis Semenako [1], Romans Kusnins [1], Sandis Migla [1], Pauls Eriks Sics [1], Oskars Selis [1], Nikolajs Tihomorskis [1], Dmitrijs Prigunovs [2], Armands Ostrovskis [2] and Sandis Spolitis [2]**

[1] Institute of Microwave Engineering and Electronics, Riga Technical University, 12 Azenes Street, LV-1048 Riga, Latvia; tatjana.solovjova@rtu.lv (T.S.); janis.semenako@rtu.lv (J.S.); romans.kusnins@rtu.lv (R.K.); sandis.migla@rtu.lv (S.M.); pauls-eriks.sics@rtu.lv (P.E.S.); oskars.selis@rtu.lv (O.S.); nikolajs.tihomorskis@rtu.lv (N.T.)

[2] Institute of Telecommunications, Riga Technical University, 12 Azenes Street, LV-1048 Riga, Latvia; dmitrijs.prigunovs@rtu.lv (D.P.); sandis.spolitis@rtu.lv (S.S.)

* Correspondence: aboltins@rtu.lv

**Abstract:** The energy efficiency of a communication system using pulse position modulation (PPM) can be increased by reducing the duration of the pulses transmitted over the communication channel to several tens of picoseconds. The employment of an event timer device as a time-to-digital converter (TDC) for demodulation allows the use of PPM with many pulse positions and achieves competitive data transfer speeds. However, along with several-picosecond accuracy of modern event timers, they require a pulse duration of several hundred picoseconds for precise detection. This research is devoted to developing passive techniques for precise pulse expansion from tens of picoseconds to hundreds of picoseconds. We propose two methods: the electrical method, which employs a microstrip low-pass filter (LPF), and the optical method, which uses fiber Bragg grating (FBG). This research offers a detailed analysis of distortion-free pulse expansion requirements, the design of prototypes meeting these requirements, and experimental design verification. Theoretical background, mathematical models, and results of experimental validation of the proposed pulse expansion methods within the laboratory transmitted reference pulse-position modulation (TR-PPM) communication system are provided.

**Keywords:** ultra-wideband communication; pulse-position modulation; event timers; Bragg gratings; microstrip filters; electromagnetics; energy efficiency

check for updates

**Citation:** Aboltins, A.; Solovjova, T.; Semenako, J.; Kusnins, R.; Migla, S.; Sics, P.E.; Selis, O.; Tihomorskis, N.; Prigunovs, D.; Ostrovskis, A.; et al. Passive Electrical and Optical Methods of Ultra-Short Pulse Expansion for Event Timer-Based TDC in PPM Receiver. *Electronics* **2023**, *12*, 4634. https://doi.org/10.3390/electronics12224634

Academic Editor: Nakkeeran Kaliyaperumal

Received: 19 October 2023
Revised: 8 November 2023
Accepted: 10 November 2023
Published: 13 November 2023

**Copyright:** © 2023 by the authors. Licensee MDPI, Basel, Switzerland. This article is an open access article distributed under the terms and conditions of the Creative Commons Attribution (CC BY) license (https://creativecommons.org/licenses/by/4.0/).

## 1. Introduction

Over the last decade, the amount of transmitted data and the data transmission speed have increased significantly. The urgency of the energy consumption associated with data transmission has increased correspondingly. Nowadays, communication systems designed to perform bandwidth-intensive high-speed data transmission extensively exploit microwave and optical frequency bands, thereby becoming increasingly demanding in energy consumption.

The overall energy consumption of a communication system consists of the energy lost in the system's transmitter circuitry, transmission channel, and receiver circuitry. In long-distance communication, the energy lost in the communications channel exceeds the power consumed by the circuitry of the transmitter and receiver. On the other hand, in short-distance communication, the amount of energy absorbed by the circuitry is more significant than that associated with the transmission channel [1]. PPM is a modulation technique that allows theoretically unlimited energy savings at the cost of spectrum occupation, which makes the proposed modulation technique of particular interest to users with limited energy resources and significant signal power losses in the communication channel, for example,

deep space communications, terrestrial and underwater optical wireless sensor networks, etc. It might also be important for other users since using the proposed modulation method can reduce overall energy consumption. However, the demodulation of a PPM signal by employing extremely short pulses is challenging as it requires fast electronic circuitry, such as comparators and triggers with bandwidths of tens of gigahertz. As PPM pulse duration does not carry information, the problem can be tackled by increasing the duration of the received pulses just before the demodulation.

This paper focuses on the expansion techniques of 50–100 ps short pulses using passive electrical and optical devices for subsequent use in PPM demodulators. As shown in the next sections, distortionless expansion of pulses with bandwidths above 10 GHz is a challenging task due to the high bandwidth and difficulties with the use of active methods. The main contribution of this research is to demonstrate that passive techniques can be successfully applied for high-bandwidth pulse expansion in both optical and electrical domains. A novel technique for developing requirements and calculating electrical LPF is validated by fabricating and testing filters in a real-time PPM communication system. To the authors' best knowledge, the suitability of passive pulse expanders for work in event timer-based PPM demodulators was explored for the first time.

This paper is organized as follows: Section 2 provides a short introduction to PPM, Section 3 is devoted to the literature analysis and the state-of-the-art in the field of precise pulse duration expansion, and consists of Section 3.1, which provides a theoretical foundation for electrical pulse expansion, and Section 3.2, which is devoted to the optical pulse expansion, also known as stretching. Section 4 is focused on the experimental validation of the proposed solutions using data transfer in laboratory conditions. Finally, Sections 4.2 and 5 summarize the research and conclude.

## 2. Overview of PPM Technique

Among the many different modulation techniques employed in communication systems, the PPM technique [2,3] is one of the most generally used ultra-wideband (UWB) modulation techniques and achieves energy savings via the use of very short pulses [4]. This efficiency comes at the cost of increased frequency bandwidths and higher bandwidth requirements for the receiver, transmitter frontend, and propagation media. The employment of PPM in optical communication systems is especially appealing as optical circuitry naturally operates at large frequency bandwidths, and optical fibers typically have very low signal attenuation. At the same time, traditional on–off keying modulation techniques have higher optical power utilization and lower sensitivity to nonlinear distortions.

The PPM technique encodes the information by the time of the transmitted pulse. The term "pulse position modulation (PPM)" was first coined in 1946 [5], and initially, it was mainly utilized in military applications. While PPM was originally employed in analog low-frequency radio and microwave systems [6], it has subsequently found use in digital communications [7–9] and microwave applications. In the optical frequency range, PPM is used in free-space optical communication and wired communications [10–12]. Furthermore, PPM is still in use in semi-analog radio control systems [13].

An overview of the benefits, disadvantages, and applications of PPM can be found in [14]. The main advantage of PPM is that it ensures higher energy efficiency than other modulation techniques and is tolerant of nonlinear distortions [15–17]. Those properties provide a solid foundation for future use of PPM, as pointed out in [6,18,19]. The development of the PPM technique has led to novel hybrid modulation types, such as multi-pulse-position modulation [20], where the symbol is composed of several pulses. It is worth mentioning that pulse-position modulation can be combined with pulse-amplitude modulation and pulse-width modulation techniques to increase the spectral efficiency of the transmission.

The operation principle of PPM is straightforward, as shown in Figure 1. The $\log_2(M)$ message bits are encoded by transmitting a single pulse with a duration of $\tau$ in one of $M$ possible time positions that have a duration $\Delta$ over a symbol time interval of length

$T = M \cdot \Delta + T_s$, where $T_s$ is a guard time required for data processing and $M \cdot \Delta$ is the payload interval in which the pulse is transmitted. In the PPM technique, there is no stringent requirement to maximally preserve the shape of the generated pulse being transmitted via a channel to the receiver unit, provided that the pulse shape variations do not vary considerably between the pulses; one only needs to ensure that the change in the pulse shape is not too significant to provide correct demodulation. These conditions are not unacceptably stringent and depend on the implemented PPM demodulation method.

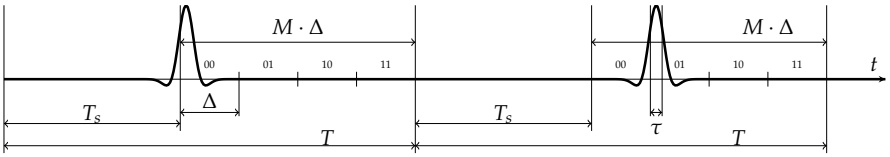



**Figure 1.** Structure of example PPM signal having $M = 4$, encoding "00" and "01".

There are several methods for PPM signal demodulation [6,12,19]. Early PPM demodulators employed energy-based detection [21,22]. This method can be used in communication channels where the received pulses' exact arrival time and shape are unknown. However, the most commonly used technique in low-speed applications is first to convert pulse-position modulation to pulse-width modulation, then use an integrator circuit to produce an approximation of the message signal. When the number of positions is small, the Rake receiver can be employed [23]. In this case, the signal is demodulated using matched filtering in several branches that have different delays. This method is especially attractive in the case of non-coherent TR-PPM because the received signal provides the reference pulse for the matched filtering, mitigating the impact of multi-path propagation [24]. Other, more advanced approaches have been developed, including iterative demodulation methods [25] and even chaotic synchronization-based techniques [26].

One of the most elegant ways to implement a highly efficient digital PPM demodulator is to employ a TDC [27,28]. This method is based on the idea of direct time measurement using an event timer device [29,30]. The employment of accurate event timers [31] allows the use of a virtually unlimited number of positions in the symbol, achieving a very low duty cycle and exceptional energy efficiency. However, two major challenges exist when using an event timer to demodulate the PPM signal. Firstly, the timer imposes specific requirements concerning the minimal pulse duration at the input of the timer. If the pulse duration is too small, the event timer will not detect the event (incoming pulse). Secondly, time measurement by the event timers requires a relatively large guard time ($T_s$ in Figure 1), during which the timer estimates the time and does not react to the incoming signal. This time, sometimes called "dead time", cannot be efficiently employed for data transfer and affects the achievable bitrate.

## 3. Electrical and Optical Pulse Expansion Methods

In this research, we employ one of the most precise commercially available event stream timers: Eventech Stream Time Tagger [32]. The event timer can reliably record the signal arrival intervals between pulses without much jitter if the PPM pulse duration is at least 150 ps. In addition, the pulse waveform must be smooth enough, with the first transition duration (rise time) as small as possible, so there is little measurement jitter and a low impact from the additive noise. In contrast, the second transition duration (fall time) is less critical; nevertheless, ripples in the pulse tail are highly undesirable. Additionally, to ensure an adequate event timer response, it is highly desirable for the overshoots and undershoots in the pre-transition and post-transition aberration regions of the incoming pulse to be as small as possible.

In this work, pulses with a duration of 50 ps are used in the PPM transmission channel, providing significant energy savings. As the particular event timer requires a pulse width of

more than 150 ps, the pulses must be expanded or stretched at least three times. Therefore, it is necessary to develop a device that satisfies the following requirements:

1. The full width at half maximum (FWHM) duration of the input pulse is 40–60 ps.
2. The bandwidth of the input pulse is at most 25 GHz.
3. The FWHM duration of the output pulse is at least 150 ps.
4. The rise of the output pulse time is at most 50 ps.
5. The fall time of the output pulse is at most 100 ps.
6. The ripples and overshoots of the output pulse are at most 10% of pulse amplitude.
7. The jitter of the output pulse rising edge is less than 5 ps.

It is worth stressing that in PPM, the pulse duration does not carry any information and can be manipulated freely. Figure 2 illustrates the structure of a PPM signal at the input of the event timer. The occupation of several time positions by the single incoming expanded pulse does not create any issues with PPM demodulation, as only the rising edge of the pulse carries the information.

There are many methods of pulse expansion using passive or active devices. In this paper, we address the employment of electrical LPF and optical techniques, namely, FBG, for pulse duration expansion. In the following sections, we will look at these technologies.

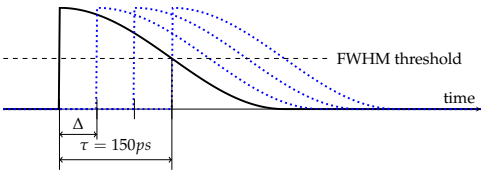



**Figure 2.** Pulse duration versus position duration before the demodulation.

### *3.1. Electrical Pulse Expansion*

Many modern electrical and optical systems—such as UWB communication devices; signal processing circuits; radar and chirped radar communication; indoor localization and radar systems, used for through-wall imaging and ground penetration; various detectors, including neutrino detectors, sensors, time measurement systems, etc.—are dealing with the transmission, measurement, and processing of pulses [33,34].

These operations often require the pulse to be expanded or compressed with minimal waveform distortion. Various delay lines [35] and other devices operating in the frequency domain (for example, filters) and making changes to it [36] and combinations of delay lines and filters are widely used for pulse expansion. Both digital and analog signal processing techniques are used, and each has advantages and disadvantages.

Here, we will mainly look at the methods used to expand analog signals without significantly affecting their waveform. The various dispersive delay lines have been handy devices in communication systems for decades, and the simplest of them are coaxial or microstrip delay lines [37]. There are several methods where two or more dispersive elements and a mixer are required. Delay and summation of delayed pulses allow the creation of a composite output signal whose duration is larger than the input signal. Using this technique, signals can be slowed down, sped up, or reversed in time with corresponding changes in the spectrum [38,39]. Today, active delay lines are also used to implement an on-chip time stretching system in the microwave band [40]. Some studies demonstrate the possibilities of influencing propagating pulse shape in the transmission line coupled a with split ring resonator in situations where negative group velocity is created; however, such devices are difficult to implement in practical applications [41].

Signals can be processed by passive filters whose magnitude and group delay responses are determined by the requirements for the waveform and spectrum of the pulse. All-pass filters (APFs) are widely used for passing through the signal without affecting its magnitude spectrum, providing phase shift and subsequently allowing the tailoring of the group delay response of the circuit. Digital APFs, which are used in digital sig-

nal processing (DSP) [42] and in many subsequent publications cited in this work, have gained widespread adoption in many applications. Various types of DSP filters have been developed and are widely used. Although DSP filters have taken an essential place in signal processing technologies, DSP suffers from some significant drawbacks, such as costly analog-to-digital conversion and digital-to-analog conversion, high power consumption, and inadequate performance at high frequencies.

As an alternative to DSP in the microwave range, microwave analog signal processing (ASP) technology has been proposed [43]. ASP devices are based on phaser devices, which ideally have an arbitrary group delay with a flat and lossless magnitude. Phaser synthesis aims to realize a response as close to ideal as possible for various applications. The practical implementation of the phaser is not easy and requires controllable dispersion for efficient group delay engineering. In ASP applications, various analog filters are widely used for signal spectrum transformation, which includes dispersive delay structures with controlled magnitude for analog signals. In [44], a fully differential second-order voltage-mode active APF topology was proposed. The filter consists of the generic two-transistor common-source differential pair, using all possible combinations of the surrounding impedances to obtain a second-order APF circuit. In [45], procedures are proposed for the design and synthesis of broadband filters with arbitrary group delay or phase response, allowing the implementation of the analog filters in integrated circuits. In [46], a closed-form synthesis method is proposed for the design of reflection-type phasers with arbitrary prescribed group delay response, and in [47], a systematic synthesis method is proposed for dispersive delay structures with controlled magnitudes for analog signal processing applications. In these two papers, a prototype waveguide filter was built and tested. In [48], a group-delayed, two-port, all-pass transmission line network application is presented, analytically modeled, and experimentally demonstrated. There are sections where all-pass network group delay synthesis examples and experimental results using genetic algorithm design are shown. In [49], all-pass network circuits have been synthesized and applied to on-chip technologies using a high-level architecture where the designed filter consists of eight second-order all-pass cells.

The circuits used in all APF implementations are complex, as they are primarily universal and offer many possibilities to manipulate pulses and apply them in many specific applications. For example, Ref. [50] demonstrates a completely on-chip implementation of the expansion and compression of continuous-time, wideband analog pulses. This work uses a cascade of a seventh-order APF coupled with a fifth-order LPF.

Another option for pulse shaping involves using filters that influence the pulse magnitude spectrum. Passive and active filters [51,52] can be utilized for this purpose. The simplest active filters are built around transistor and op-amp circuits as their fundamental components [53], although, in most cases, they tend to be more complex [54]. Active filters offer greater flexibility, allowing for reconfigurable bandwidths ranging from narrow/mid-band to ultra-wideband states, as described in [55]. Active filters can implement intricate filter functions such as low-pass, band-pass, and various filter types, and they can be designed with a reconfigurable magnitude response and phase-frequency dependence. However, active filters also come with some notable disadvantages. Due to the presence of active components, they tend to be more costly than passive filters. Additionally, they require an external power supply, which can introduce noise or interference. Furthermore, active filters have limited bandwidth since their performance is influenced by the characteristics and limitations of the active devices.

Much simpler designs than the use of APFs and conventional active filters can be successfully used for pulse expansion in many applications, as has been done in this research. As mentioned above, to realize the ideas of our work, i.e., ensure an unambiguous event timer response and the minimum possible jitter in time interval detection as well as the stable operation of the event timer and initial state recovery, it is necessary to ensure that the initial pulse is extended to about 150 ps, that the filtered pulse does not have

noticeable ripples or a long tail, and that the rising edge of the filtered pulse is preferably as steep as possible.

LPFs perform the signal's energy accumulation, leading to a situation where the signal at the output of the filter lasts longer than excitation. Therefore, when unipolar pulses are used in the PPM transmission channel, one of the most rational ways for pulse expansion is to utilize a LPF. As will be shown below, it is sufficient to design a filter whose attenuation in the passband (up to the cutoff frequency $f_c$) is almost constant, whose stopband up to the frequency $3f_c$ decreases by 10 dB, and whose group delay has minimal variations up to the frequency $2f_c$.

Using the software presented in [56], several pulses with different waveforms have been modeled, and numerical calculations have been carried out for different types of filters with various cutoff frequencies and filter orders. Analytical derivations and numerical modeling in [56] have confirmed that, of all the filter types, the Bessel-type filter is the most suitable for pulse expansion, as it has a maximally flat group delay and a maximally linear phase response. Those characteristics ensure negligible ringing in the impulse response [57] and minimize overshoots in the pre-transition and post-transition aberration regions of the expanded PPM pulses. Before developing the custom pulse expander, our research group performed experiments with commercially available LPFs to determine if an off-the-shelf filter could be used for pulse expansion. An example of pulse expansion using the Mini-circuits$^{TM}$ SLP-2400+ filter [58] is shown in Figure 3. As can be seen from the figure, the commercial filter introduced noticeable oscillations in the post-transition region. Moreover, it significantly flattened the pulse's rising edge, increasing the timer's sensitivity to the additive noise. Experiments with commercial filters showed that it would be difficult to find a suitable filter, so it was decided to design and build a custom filter. Microstrip technology was chosen because its fabrication is possible without the involvement of complicated and expensive technological processes.

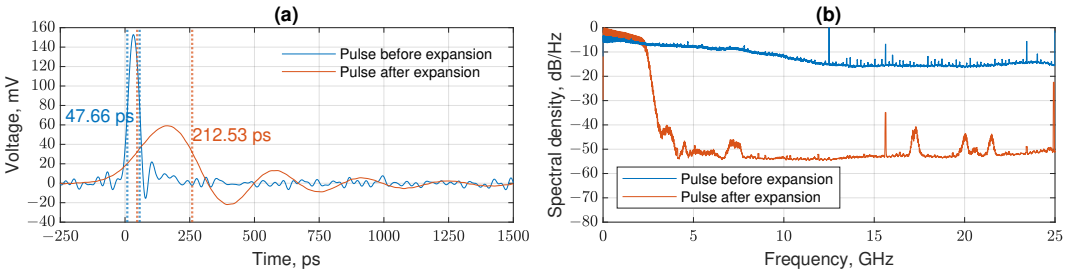



**Figure 3.** Pulse generated by Keysight M8195A arbitrary waveform generator (AWG) and expanded using Mini-circuits SLP-2400 filter. (**a**) Waveforms of the pulses acquired by Keysight DSAZ334A digital storage oscilloscope (DSO). (**b**) Normalized magnitude spectra calculated using fast Fourier transform (FFT).

### 3.1.1. Design of Custom LPFs

In this study, we designed two microstrip LPF filters to extend the pulse duration from 50 ps up to about 170 ps, which is slightly above the event timer's minimum pulse duration threshold of 150 ps, to ensure that the timer will definitely respond. Analytical and numerical calculations, computer modeling, and measurements showed that the third-order Bessel LPF capacitor–inductor–capacitor filter, which is normalized by the group delay (hereafter called Classical), is the most suitable for the expansion task. First, the filter's group delay was normalized, so that in the passband, it is $1/\omega_c$, where $1/\omega_c$ is the angular cutoff frequency, which was chosen to give the required pulse extension. The normalization of the second filter (hereafter called Magnitude-Normalized) was performed using the traditional magnitude normalization methodology, where the gain is $-3$ dB at the cutoff frequency).

To carry out simulations with Ansys HFSS software that calculate the scattering matrix elements and characteristics of a microstrip filter, it is necessary to specify at least the approximate physical lengths of the elements. The more accurately these lengths are calculated as initial values, the better and faster the result can be achieved in the Ansys HFSS simulations.

In this paper, a software package has been developed that consists of two modules, the first of which allows the effective permeability of the microstrip line used to be calculated. This software has been produced based on publications on the calculation of microstrip lines [59–62]. The second software module calculates the physical lengths of the selected microstrip filter's capacitive and inductive elements, considering parasitic inductance and capacitance. Some important microstrip quasi-illuminated elements are discussed in [63].

Any electrically short (physical length much smaller than the wavelength) microstrip line discontinuity always has both capacitance and inductance. It can be replaced by one of two equivalent circuits: T-shaped or Π-shaped.

The inductance of the divider is proportional to the line's characteristic impedance, and the capacitance is inversely proportional to it. Since the characteristic impedance increases with decreasing line width, inductive elements can be realized using narrow line sections. Of course, these elements also have capacitance, but this can be reduced by decreasing the line width. It is more convenient to describe an inductive line segment with an equivalent Π-shaped circuit, where the series element represents the inductance and the two shunt elements represent the parasitic capacitances (see Figure 4).

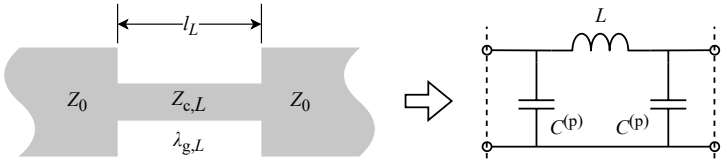



**Figure 4.** High-impedance inductive element and its equivalent Π-shaped circuit.

The inductance $L$ and the two parasitic capacities $C^{(p)}$ are calculated as

$$L = \frac{Z_{c,L}}{\omega} \sin\left(\frac{2\pi}{\lambda_{g,L}} l_L\right), \qquad C^{(p)} = \frac{1}{\omega Z_{c,L}} \tan\left(\frac{\pi}{\lambda_{g,L}} l_L\right), \tag{1}$$

where $Z_0$ is line impedance (source and load impedances), $Z_{c,L}$ is inductance line's characteristic impedance, $\lambda_{g,L}$ is wavelength of the inductance line, and $l_L$ is the inductance line element's physical length.

Capacitive elements are realized using wide microstrip line segments with very low characteristic impedance. It is more convenient to replace such an inductance with an equivalent T-shaped circuit, where the series elements represent the parasitic inductances and the shunt element represents the capacitance (see Figure 5).

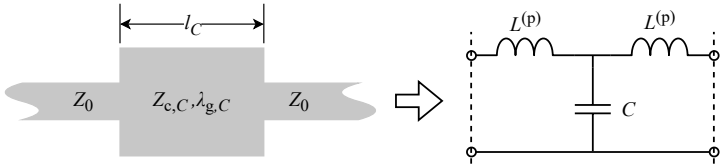



**Figure 5.** Low impedance capacitive element and its equivalent T-shaped circuit.

The capacity of the element $C$ and two parasitic inductivities is calculated as

$$C = \frac{1}{Z_{c,C}} \sin\left(\frac{2\pi}{\lambda_{g,C}} l_C\right), \qquad L^{(p)} = Z_{c,C} \tan\left(\frac{\pi}{\lambda_{g,C}} l_C\right), \tag{2}$$

where $Z_{c,C}$ is capacitance line characteristic impedance, $\lambda_{g,C}$ is wavelength in capacitance line, and $l_C$ is the capacitance line element's physical length.

The calculation of the third-order Bessel filter is described below. The capacitor–inductor–capacitor topology was chosen because the inductor–capacitor–inductor topology requires inductive elements with a very high characteristic impedance, consequently, very narrow line segments with a width less than 0.4 mm, and successively, increased requirements for the tolerance. Such elements were difficult to fabricate using the available milling machine. The filters' prototype values were selected by the methodology in [36,64], and the lumped values of the filters were calculated using the element transformations described in [36], chapter 3.

First, the element lengths are calculated, ignoring parasitic inductances and capacitances:

$$\omega_c C_1 = \frac{1}{Z_{c1}} \sin\left(\frac{2\pi}{\lambda_{g1}} l_1\right) \Rightarrow l_1 = \frac{\lambda_{g1}}{2\pi} \sin^{-1}(\omega_c Z_{c1} C_1), \tag{3}$$

$$\omega_c L_2 = \frac{1}{Z_{c2}} \sin\left(\frac{2\pi}{\lambda_{g2}} l_2\right) \Rightarrow l_2 = \frac{\lambda_{g2}}{2\pi} \sin^{-1}(\omega_c Z_{c2} L_2), \tag{4}$$

$$\omega_c C_3 = \frac{1}{Z_{c3}} \sin\left(\frac{2\pi}{\lambda_{g3}} l_3\right) \Rightarrow l_3 = \frac{\lambda_{g3}}{2\pi} \sin^{-1}(\omega_c Z_{c3} C_3), \tag{5}$$

where guided wavelengths in striplines are:

$$\lambda_{g1} = \frac{c}{f_c \sqrt{\varepsilon_{eff,1}}}, \qquad \lambda_{g2} = \frac{c}{f_c \sqrt{\varepsilon_{eff,2}}}, \qquad \lambda_{g3} = \frac{c}{f_c \sqrt{\varepsilon_{eff,3}}}, \tag{6}$$

where $c$ is the light speed in free space, $f_c = \omega_c/(2\pi)$ is the cutoff frequency, and $\varepsilon_{eff}$ is the relative effective dielectric constant, which depends on dimensions of the lines and the parameters of the substrate. The relative effective permittivity $\varepsilon_{eff}$ and impedances of the lines $Z_0$ or $Z_c$ are calculated using the calculation expressions given by [59–62].

Using the initial values of the element lengths $l_1$, $l_2$, $l_3$ calculated according to the Formulas (3)–(5), the parasitic inductances and capacities of the elements can be calculated:

$$L_1^{(p)} = \frac{Z_{c1}}{\omega_c} \tan\left(\frac{\pi}{\lambda_{g1}} l_1\right), \quad C_2^{(p)} = \frac{1}{\omega_c Z_{c2}} \tan\left(\frac{\pi}{\lambda_{g2}} l_2\right), \quad L_3^{(p)} = \frac{Z_{c3}}{\omega_c} \tan\left(\frac{\pi}{\lambda_{g3}} l_3\right). \tag{7}$$

Although elements $C_2^{(p)}$ and $C_1$ are not connected in parallel, the shunt inductance $L_1^{(p)}$ is so small that they can be assumed to be connected in parallel and can therefore be combined. The same applies to elements $L_1^{(p)}$ and $L_2$: they can be assumed to be connected in series.

In the next step, the lengths of the elements are calculated according to the parasitic parameters:

$$
\begin{aligned}
C_1 &= \frac{1}{\omega_c Z_{c1}} \sin\left(\frac{2\pi}{\lambda_{g1}} \hat{l}_1\right) + C_2^{(p)} = \frac{1}{\omega_c Z_{c1}} \sin\left(\frac{2\pi}{\lambda_{g1}} \hat{l}_1\right) + \frac{Z_{c2}}{\omega_c} \sin\left(\frac{2\pi}{\lambda_{g2}} l_2\right) \Rightarrow \\
\hat{l}_1 &= \frac{\lambda_{g1}}{2\pi} \sin^{-1}\left(\omega_c Z_{c1} \left[C_1 - \frac{Z_{c2}}{\omega_c} \sin\left(\frac{2\pi}{\lambda_{g2}} l_2\right)\right]\right),
\end{aligned} \tag{8}
$$

$$
\begin{aligned}
L_2 &= \frac{Z_{c2}}{\omega_c} \sin\left(\frac{2\pi}{\lambda_{g2}} \hat{l}_2\right) + L_1^{(p)} + L_3^{(p)} \\
&= \frac{Z_{c2}}{\omega_c} \sin\left(\frac{2\pi}{\lambda_{g2}} \hat{l}_2\right) + \frac{1}{\omega_c Z_{c1}} \sin\left(\frac{2\pi}{\lambda_{g1}} l_1\right) + \frac{1}{\omega_c Z_{c3}} \sin\left(\frac{2\pi}{\lambda_{g3}} l_3\right) \Rightarrow \\
\hat{l}_2 &= \frac{\lambda_{g2}}{2\pi} \sin^{-1}\left(\omega_c Z_{c2} \left[L_2 - \frac{1}{\omega_c Z_{c1}} \sin\left(\frac{2\pi}{\lambda_{g1}} l_1\right) - \frac{1}{\omega_c Z_{c3}} \sin\left(\frac{2\pi}{\lambda_{g3}} l_3\right)\right]\right),
\end{aligned} \tag{9}
$$

$$
\begin{aligned}
C_3 &= \frac{1}{\omega_c Z_{c3}} \sin\left(\frac{2\pi}{\lambda_{g3}} \hat{l}_3\right) + C_2^{(p)} = \frac{1}{\omega_c Z_{c3}} \sin\left(\frac{2\pi}{\lambda_{g3}} \hat{l}_3\right) + \frac{Z_{c2}}{\omega_c} \sin\left(\frac{2\pi}{\lambda_{g2}} l_2\right) \Rightarrow \\
\hat{l}_3 &= \frac{\lambda_{g3}}{2\pi} \sin^{-1}\left(\omega_c Z_{c3} \left[C_1 - \frac{Z_{c2}}{\omega_c} \sin\left(\frac{2\pi}{\lambda_{g2}} l_2\right)\right]\right).
\end{aligned} \tag{10}
$$

The last step of the procedure can be repeated to obtain even more accurate lengths. However, the results obtained this way are usually very little different from the previous ones. Therefore, it is not always practical to recalculate the length values.

The next and final step in calculating the physical dimensions of the LPF for pulse duration expansion was modeling using the Ansys HFSS software. The widths of the lines are selected beforehand, considering that the width of the inductive element is smaller than that of the capacitive element.

The simulations were carried out with respect to the physical sizes of the elements until the desired result was obtained (quasi-parametric modulation). It should be noted, however, that the relatively precise calculations carried out beforehand for the initial lengths of the elements are an essential condition for obtaining results in Ansys HFSS fast enough, as even with a good approximation of initial sizes, the optimization can take a few hours.

The calculation of the numerical values of elements and physical sizes of two microstrip filters, Classical (group delay normalized) and Magnitude-Normalized, was performed. The cutoff frequency $f_c = 1.8$ GHz was set to the same value for both filters, and the source and load impedances were requested at $Z = 50\ \Omega$. The results obtained after optimization and modeling by Ansys HFSS are shown in Figure 6.

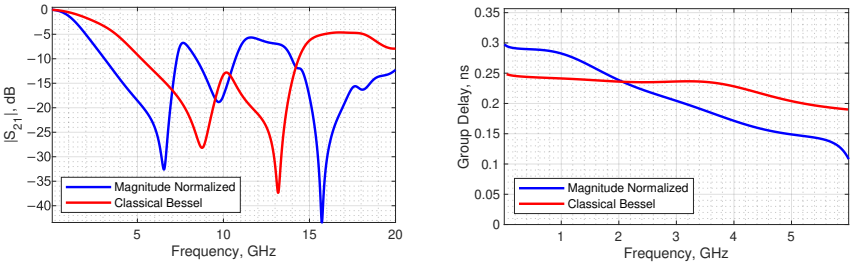



**Figure 6.** Ansys HFSS modeling results. Magnitude $|S_{21}|$ and group delay of designed filters.

The simulation result curves in Figure 6 show that the attenuation for the Classical filter and the Magnitude-Normalized filter differ minimally in the passband. Still, immediately after the passband and up to a frequency of 6 GHz, the attenuation for the Magnitude-Normalized filter is significantly higher, which means that the Classical filter cuts out

fewer incoming pulse spectrum components in this band. Above 6 GHz, the attenuation of the Magnitude-Normalized filter decreases rapidly and fluctuates more, while for the Classical filter, the attenuation decreases and fluctuation is noticeable above the frequency of 9 GHz. The group delay curve for the Classical filter is significantly flatter than for the Magnitude-Normalized filter in the spectrum range of 0–6 GHz. As will be seen below, these differences are significant and determine the time duration and waveform of the filtered pulse.

Based on the results obtained by modeling with Ansys HFSS, two microstrip LPF were fabricated: Magnitude-Normalized and Classical third-order Bessel filters (see Figure 7). FR4-type printed circuit board laminate has been used for the substrate of the filters.

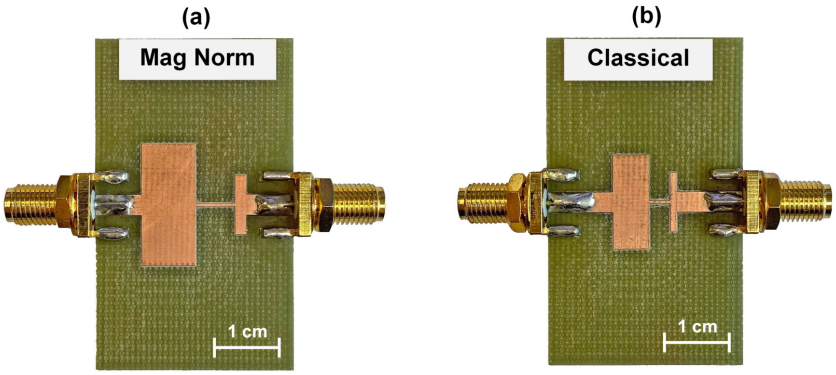



**Figure 7.** Custom-designed Bessel third-order LPF filters: (**a**) Magnitude-Normalized and (**b**) Classical, with cutoff frequencies $f_c = 1.8$ GHz.

Simulated and measured curves of the transmission coefficient magnitude $|S_{21}|$ and group delay for both filters are shown, respectively, in Figures 8 and 9. For the Classical filter, the simulation and the measured results agree well for the magnitude curves (see Figure 8). In contrast, for the Magnitude-Normalized filter, differences are visible, which could be explained by the fact that the actual permittivity of the FR-4 material did not correspond to the one used in the simulation (the manufacturer specifies the relative permittivity of FR-4 in the range from 3.8 to 5). The group delay curves obtained in the simulation and the experimental ones (see Figure 9) are in good agreement if the slopes of the curves are compared. The differences in group delay seen in the figures are almost constant across the whole frequency range, and they can be caused by different reference planes used in the simulation and experiments, as the actual board included the SMA connectors but the simulations did not.

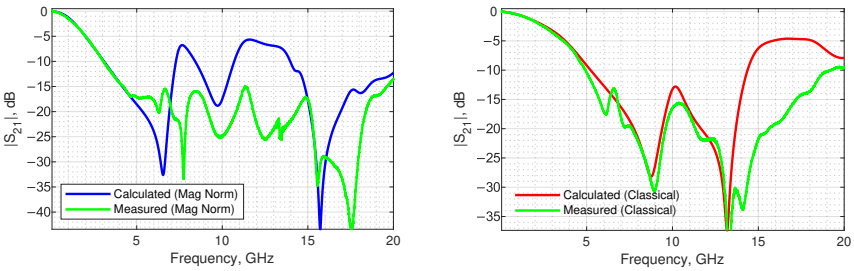



**Figure 8.** Ansys HFSS simulation results and custom-designed filter measurement results for $|S_{21}|$ magnitude.

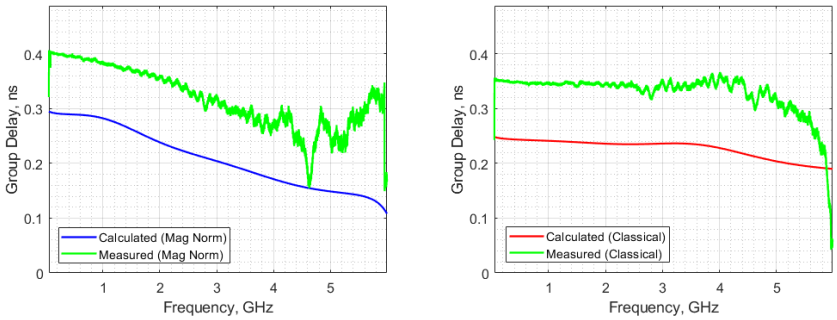



**Figure 9.** Ansys HFSS simulation results and custom-designed filter measurement results for group delay.

3.1.2. Experimental Electrical Pulse Expansion

Figure 10 shows the block diagram of the LPF-based electrical pulse expansion test setup. Both are third-order Bessel filters with equal cutoff frequencies of 1.8 GHz. The results of a 50 ps input pulse expansion by the Classical LPF filter can be seen in Figure 11, whereas those of the Magnitude-Normalized LPF filter can be seen in Figure 12. It can be seen that the pulse expanded by the Classical filter to 146 ps is close to the desired pulse waveform as it meets the waveform requirements set out in this paper. The Magnitude-Normalized filter expands the pulse to 237 ps, and this pulse waveform has a first transition duration that is too large, a long tail, and ripples in the tail. Simulations with this type of filter showed that, by increasing the cutoff frequency, the duration of this pulse can be obtained at close to 150 ps. However, its waveform first transition duration will still have worse indicators (it is longer) than the pulse extended with the Classical filter. The explanation for these differences can be seen in the curves in Figures 8 and 9. The group delay of the Classical filter is less variable across the frequency range, and the transfer coefficient magnitude is flatter and significantly larger at frequencies above 3 GHz compared to the Magnitude-Normalized filter. Those features affect the pulse waveform, especially the rise time, which should be small enough to comply with the parameters set out in this paper.

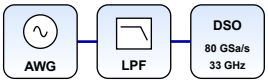



**Figure 10.** Block diagram of electrical pulse expansion test setup by LPF.

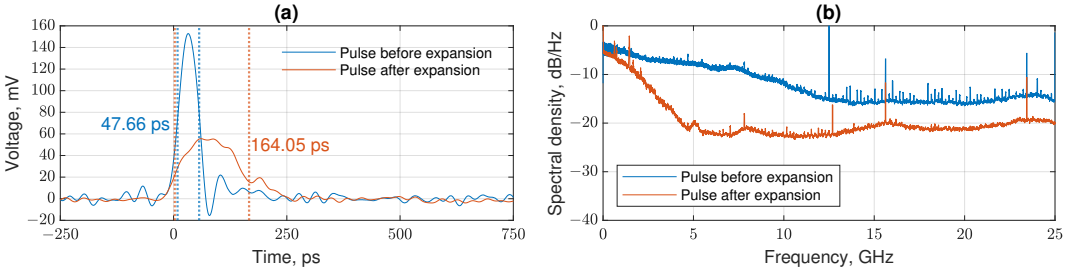



**Figure 11.** Pulse generated by Keysight M8195A AWG and expanded using Classical custom-designed filter. (**a**) Waveforms of the pulses acquired by Keysight DSAZ334A DSO. (**b**) Normalized magnitude spectra calculated using FFT.

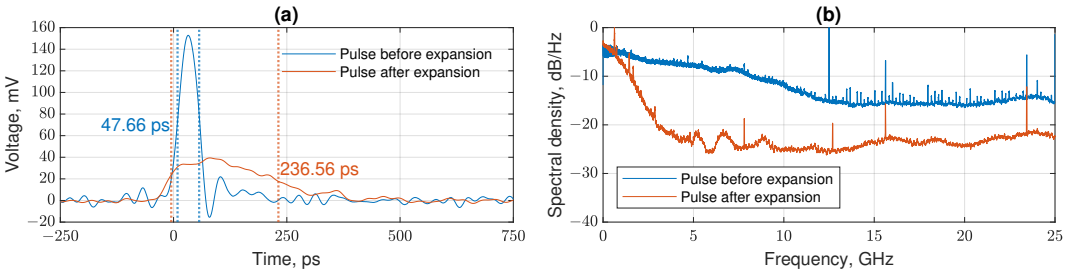



**Figure 12.** Pulse generated by Keysight M8195A AWG and expanded using Magnitude-Normalized custom-designed filter. (**a**) Waveforms of the pulses acquired by Keysight DSAZ334A DSO. (**b**) Normalized magnitude spectra calculated using FFT.

### *3.2. Optical Pulse Expansion*

PPM pulses can be expanded not only in the electrical domain but also in the optical domain when signal transmission over optical fiber is realized. To increase optical pulse duration, so-called optical pulse stretchers or techniques are used [65,66]. Stretching optical pulses can be helpful in scenarios where it is necessary to increase the duration of a pulse without altering its waveform. These are crucial elements, for example, in ultra-fast lasers, to expand the pulse in the time domain and reduce the pulse's peak power, eliminating adverse nonlinear effects [67]. Also, optical pulse stretching is a commonly employed technique to safeguard the input faces of optical fibers from damage [68]. In general, pulse stretchers can be classified into two categories: coherent and incoherent. Coherent pulse stretchers, such as grating pulse stretchers, stretch a pulse in a way that can later be undone. They provide positive or negative group delay dispersion and typically are based on dispersive elements like diffraction grating pairs, grisms (grating and prism), FBG, chirped Bragg gratings, or ring resonators. On the other hand, incoherent pulse stretchers irreversibly stretch a pulse [65,69]. For example, an incoherent pulse stretcher can be realized by circulating cavities, which divide an incident pulse into many smaller pulses spread over a time period [66]. In our application, we will apply tunable FBG to introduce positive dispersion and broaden the input optical PPM pulses.

#### Experimental Optical Pulse Expansion

Our target in this experiment was to expand 50 ps optical PPM pulses up to at least 150 ps. As mentioned in Section 2, this is necessary as the duration of the incoming PPM pulse on the input of the event timer should be at least 150 ps to provide stable operation. This experiment employed a tunable FBG dispersion compensation module (Teraxion Clear Spectrum TDCMX) for optical pulse expansion or stretching. The experiment setup consisted mainly of the transmitter and receiver sides.

The transmitter side included AWG *Keysight M8195A*, radio frequency (RF) amplifier *SHF 810* with 29 dB gain, *Photline 40* GHz Mach–Zehnder modulator (MZM) intensity modulator, *Cobrite DX4* continuous wave (CW) C-band laser tuned at 193.1 THz central frequency (1552.52 nm) and +3 dBm out power, and power supplies used for the operation of the RF amplifier and setting the bias of MZM. The MZM is biased at 1.2 V to obtain the maximum amplitude and quality of the generated PPM pulses. The receiver part contained a linear variable optical attenuator *Keysight FVA-3150* with 2 dB insertion loss at 1550 nm, optical power meter, *Amonics PR10G* 10 Gbit/s ac-coupled photo-receiver p-i-n photodiode (PIN) with a typical sensitivity of −20 dBm and maximum ac output voltage swing of around 350 mVpp, and *Keysight DSAZ334A* DSO (80 GSa/s, 33 GHz) with connected DC blocker. As one can see in Figure 13, tunable FBG was placed right between the transmitter and receiver sides of the experimental scheme. As this section exclusively focuses on the optical pulse expansion, more detailed parameters of the experimental setup are provided in Section 4 of the article.

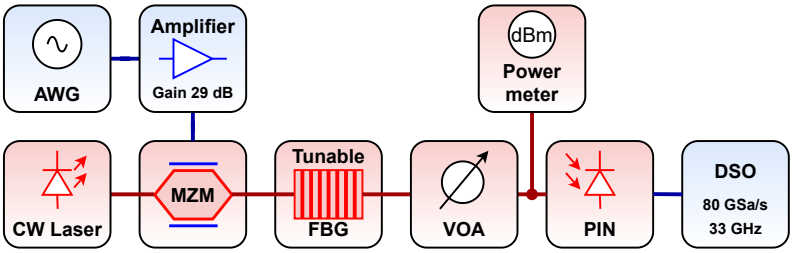



**Figure 13.** Block diagram of optical PPM pulse expansion test setup by tunable fiber Bragg grating (FBG) dispersion compensation unit. PPM signal is generated by an arbitrary waveform generator (AWG), the optical part consists of continuous wave (CW) laser, Mach–Zehnder modulator (MZM), FBG, variable optical attenuator (VOA), p-i-n photodiode (PIN), and an optical power meter. The detection part consists of a digital storage oscilloscope (DSO).

Figure 14 shows the waveforms and spectra of electrical PPM pulses on the output of PIN when the amount of added chromatic dispersion (CD) by tunable FBG module is 0 ps/nm or +1200 ps/nm.

The PIN used in our experiment is typical for 10 Gbit/s intensity-modulated on–off keying signals with a high-frequency cutoff of around 8 GHz. The RF bandwidth of this PIN is lower than the RF bandwidth occupied by the original PPM signal. This limited PIN bandwidth also increased the PPM pulse duration from originally 50 ps (which occupies up to ≈20 GHz RF bandwidth) to around 76.76 ps (which occupies up to ≈13 GHz RF bandwidth).

CD, the value at +1200 ps/nm, was equal to around the dispersion value introduced by 75 km of standard ITU T G.652 single mode optical fiber. As a result, FBG set to this value of CD expanded the PPM pulses up to 154.03 ps. From the spectra shown in Figure 14, it can be concluded that FBG behaved as a slight band-rejection filter with a center frequency around 6 GHz.

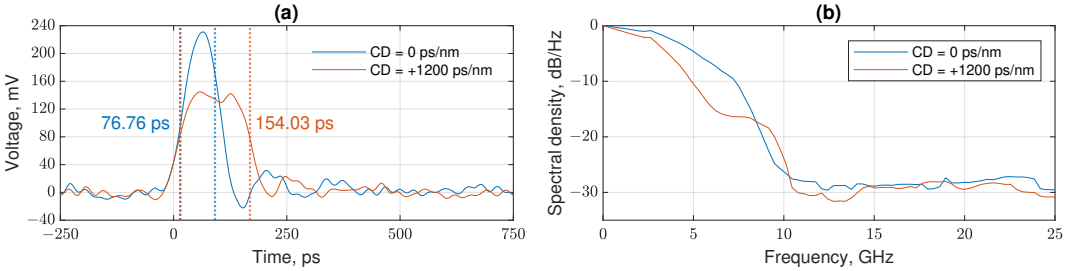



**Figure 14.** Pulse expansion using tunable FBG (**a**) captured waveform of PPM pulse at the output of PIN, and (**b**) normalized magnitude spectra calculated using FFT.

We have shown the optical pulse expansion capacity of the tunable FBG module. The following section will provide deeper insight into the realized experimental setup and validate the use of the proposed pulse expanders in optical UWB communication systems.

## 4. Experimental Validation Using PPM Data Transmission

### *4.1. Experimental Setup*

The TR-PPM transmission experiments have been carried out using optical and electrical pulse expansion methods. PPM pulses were kept as short as possible to demonstrate energy-efficient transmission. As stated in Section 2, if the event timer is used for the detection, the received pulse must be sufficiently long to ensure proper timer triggering.

The block diagram of the proposed and investigated PPM transmission system is illustrated in Figure 15. Key components of the system are a pulse expander module (optical FBG or electrical LPF) and a high-precision event timer used for the demodulation. AWG acts as a PPM transmitter, generating the desired signal waveform following our loaded sampled data. This study used unipolar PPM pulses with a time duration of 50 ps. The difference between the setup in Figure 15 and that previously shown in Figure 13 is that (a) the pulse expansion was also realized by our custom-designed LPF, and (b) both pulse expansion methods, namely, optical (using a FBG) and electrical (using a LPF), are assessed by the connected event timer device. When pulse expansion was realized by the LPF, the CD value of FBG was set to 0 ps/nm.

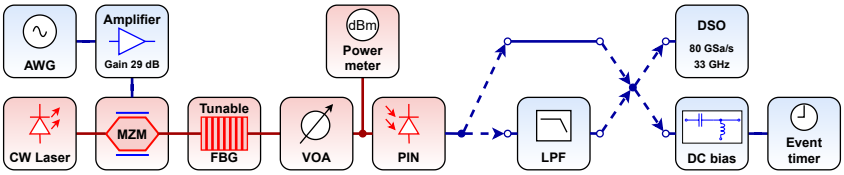



**Figure 15.** Block diagram of a PPM transmission link with event timer for the demodulation, where the electrical part is shown in blue and the optical part is shown in red. PPM signal is generated by an arbitrary waveform generator (AWG) and amplified as necessary to drive the Mach–Zehnder modulator (MZM). The optical part consists of a continuous wave (CW) laser, MZM, tunable fiber Bragg grating (FBG) dispersion compensation module, variable optical attenuator (VOA), p-i-n photodiode (PIN), and optical power meter. The detection part consists of the custom-made low-pass filter (LPF), digital storage oscilloscope (DSO), direct current (DC) bias tee, and event timer. Dashed lines indicate the realized electrical connections for demonstrated pulse expansion and detection scenarios.

First, the ideal 50 ps pulses with a rectangular shape and intervals between pulses determined by the random data were generated by MATLAB. Then, the waveform was saved into an AWG-specific file format and loaded into its memory. Next, the prepared waveform was played on AWG's output port at a maximal sampling speed of 65 GSa/s. The AWG output signal was amplified by a 38 GHz SHF 810 RF amplifier to drive the 40 Gbit/s MZM intensity modulator. The optical MZM output was connected to the Teraxion FBG module. The output of this module was connected to a variable optical attenuator and through a 10%/90% optical coupler to a 10 Gbit/s photoreceiver, where the optical signal was converted to electrical. The 10% port of the optical coupler was connected to the optical power meter. The PPM pulse duration on the output of the PIN was measured to be about 76.76 ps due to the limited bandwidth of the PIN, which was lower than the bandwidth of the original signal generated by AWG.

The next step was to test our custom-made electrical LPFs' pulse expansion capability in this experimental setup. To do so, the microstrip LPF with Classical design (see Section 3.1) was connected to the PIN output. A DSO was connected to the output of the LPF to capture the broadened PPM pulse. As one can see in Figure 16, the PPM pulse at the output of LPF expanded up to 169.24 ps, which is similar to the pulse expansion result shown in Figure 11.

After validating both pulse expansion techniques, the next step was verifying the novel expansion filters in the PPM communication system. The bias tee (BiasT, 20–45 GHz, SHF BT45) circuit was connected before the event timer to adjust the PPM signal's DC level so that the half-magnitude of the incoming pulses was approximately at the timer-triggering threshold of 1.2 V.

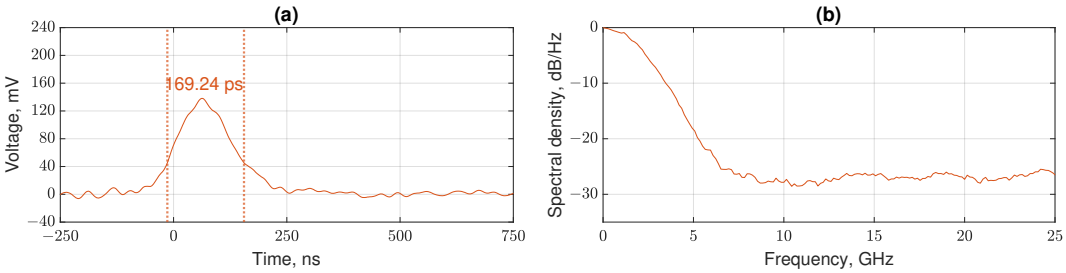



**Figure 16.** Pulse expansion using electrical LPF with Classical design in optical transmission system (**a**) captured waveform of PPM pulse at the output of LPF, and (**b**) normalized magnitude spectra calculated using FFT.

### *4.2. Results and Discussion*

The experiment has been conducted using TR-PPM waveforms [70] with the parameters listed in Table 1 by employing optical or electrical pulse expansion methods. In both cases, bit error ratio (BER) measurements were respective to the average optical power received before the PIN, as shown in Figure 15. The BER versus the average received optical power with optical pulse expansion for multiple position width values can be seen in Figure 17, whereas in the case of electrical pulse expansion, the results can be seen in Figure 18. The range of the average received optical power values was selected to represent the region around which the data transmission transitions from error-free to completely unintelligible (BER value of 0.5). This range was experimentally determined for the given system and corresponds to the amplitude values of the electrical pulse on the edge of the detection threshold of the event timer.

**Table 1.** Experiment parameters.

| Number of Positions, $N$ | Position Width $\Delta$, ps | Pulse Width $\tau$, ps | Expansion Method |
|---|---|---|---|
| 512 | 50 | 50 | Optical |
| 256 | 100 | 50 | Optical |
| 128 | 200 | 50 | Optical |
| 512 | 50 | 50 | Electrical |
| 256 | 100 | 50 | Electrical |
| 128 | 200 | 50 | Electrical |

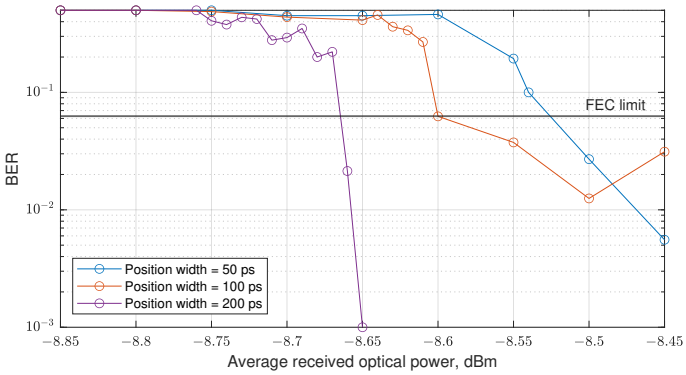



**Figure 17.** BER versus average received optical power with optical pulse expansion with FBG module.

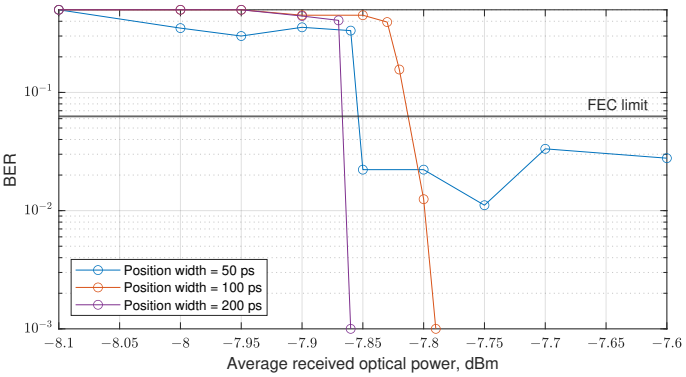



**Figure 18.** BER versus average received optical power with electrical pulse expansion with LPF.

The forward error correction (FEC) limit shown in Figures 17 and 18 represents the BER threshold, at which the Reed–Solomon RS(255, 223) FEC algorithm is capable of correcting the errors in the received data pattern. This BER value is $6.27 \times 10^{-2}$ as the RS(255, 223) algorithm can correct up to 16 erroneous symbols in the block. It was decided to represent this FEC limit, as the Reed–Solomon FEC algorithm is widely used.

For the experiments conducted using a position width of 200 ps, the results reveal a distinct point where the data transmission becomes error-free. This happens when the incoming PPM signal at the input of the event timer significantly exceeds the threshold set by the DC bias voltage so that no adverse effects, such as noise and jitter, significantly impact the BER. In contrast, if the magnitude of the incoming pulses, which corresponds to the certain average received optical power, falls below the voltage threshold of the event timer, very low BER values are observed in all cases. The threshold effect is observable at a position width of 200 ps. In contrast, in the case of position widths of 50 and 100 ps, the experiments show an error floor, especially in the case of optical pulse expansion. This is expected behavior, as smaller position widths require more precise modulation in the transmitter and demodulation in the receiver. Adverse effects such as jitter and additive noise in all system components considerably impact the PPM signal with smaller position widths. As the position widths of PPM pulses decrease, the jitter can more likely cause the estimated pulse position in the receiver to shift to a different pulse position than the one generated by the modulator. The additive noise in the signal waveform can also cause errors by falsely triggering the event timer when the time corresponds to a different pulse position. The effect of the noise is especially pronounced when considering position widths smaller than the pulse width, as this provides a large time window (the entire pulse) where noise may falsely trigger the timer.

The authors have recognized that an automatic gain control system or a similar circuit could eliminate the effect of DC biasing in the experiment results. Ideally, the electrical pulse amplitude at the input of the event timer should be constant across a wide range of average received optical power values.

Nevertheless, the results validate the concept of both electrical and optical pulse expansion methods for use with the event timer, as the BER values even at very small position widths of 50–100 ps are acceptable. The lower BER values in the case of electrical pulse expansion at a similar average received optical power can be attributed to the excellent pulse shape at the output of the custom LPF, which leads to higher accuracy in the triggering of the event timer, resulting in less error-prone transmission. Employment of new pulse expansion techniques in conjunction with more capable TDC allowed us to achieve much lower BER compared to the results presented in [71].

## 5. Conclusions and Future Work

This research explores the employment of passive electrical or optical filters for picosecond-range pulse expansion to support demodulation in an event timer-based PPM communication system. The quality and characteristics of the proposed designs are examined through the acquisition of time-domain waveforms and the calculation of spectra. The suitability of the designed solutions for PPM signal processing is validated through data transmission tests in laboratory conditions.

The given research contributes to a detailed analysis of the requirements for distortion-free pulse expansion in the time domain, the design of microstrip filter prototypes according to requirements, and experimental verification of the proposed designs.

For expansion in the optical domain, an off-the-shelf FBG-based pulse stretcher is examined, whereas for electrical expansion, two custom-designed microstrip LPFs are proposed. The results have shown that both FBG-based optical and custom-designed LPF-based designs are capable of expanding the pulses to at least 150 ps and comply with the requirements of the Eventech Stream Time Tagger used as the TDC in the PPM demodulator.

The designed pulse expanders can satisfy requirements for at most 50 ps rising edge and oscillations after the main peak below 10% of pulse amplitude. The authors conclude that applied passive electrical and optical expansion are viable and cost-efficient methods to preprocess signals in UWB communication and sensing systems that employ event timer-based TDC.

The employment of advanced filters for the development of pulse expanders that preserve the steepness of the output pulse's rising edge is one of the most prospective future development directions. In this case, the filter's magnitude response needs to have several peaks, and such devices are no longer low-pass filters.

The expansion of pulses with a duration of 10 ps or less has great potential as shorter pulses save energy in PPM transmissions. This will become an important problem after the widespread adoption of terahertz technologies in transmission channels. Implementing such expanders in the electrical domain would require the employment of more advanced techniques to suppress spurious modes and cope with fabrication tolerances.

**Author Contributions:** Conceptualization, A.A., J.S. and S.S.; Data curation, T.S., S.M. and O.S.; Formal analysis, J.S. and R.K.; Funding acquisition, A.A.; Investigation, T.S., S.M., R.K., D.P. and A.O.; Project administration, A.A.; Resources, D.P. and S.S.; Software, T.S., S.M., O.S., R.K. and N.T.; Supervision, A.A. and S.S.; Validation, S.M., N.T. and A.O.; Visualization, T.S., R.K. and N.T.; Writing—original draft, T.S., J.S., S.M. and P.E.S.; Writing—review and editing, A.A. and S.S. All authors have read and agreed to the published version of the manuscript.

**Funding:** This research was funded by the Latvian Council of Science grant No. lzp-2021/1-0475, "Picosecond-resolution pulse position modulation for beyond-the-limits energy efficiency of communications", and by Riga Technical University Master Grant program.

**Data Availability Statement:** Data are contained within the article. The data used to support the findings of this study are available from the first author upon request.

**Conflicts of Interest:** The authors declare no conflict of interest.

## Abbreviations

The following abbreviations are used in this manuscript:

| | |
|---|---|
| APF | all-pass filter |
| ASP | analog signal processing |
| AWG | arbitrary waveform generator |
| BER | bit error ratio |
| CD | chromatic dispersion |
| CW | continuous wave |
| DC | direct current |
| DSO | digital storage oscilloscope |

| | |
|---|---|
| DSP | digital signal processing |
| FBG | fiber Bragg grating |
| FEC | forward error correction |
| FFT | fast Fourier transform |
| FWHM | full width at half maximum |
| LPF | low-pass filter |
| MZM | Mach–Zehnder modulator |
| PIN | p-i-n photodiode |
| PPM | pulse-position modulation |
| RF | radio frequency |
| TDC | time-to-digital converter |
| TR-PPM | transmitted reference pulse-position modulation |
| UWB | ultra-wideband |
| VOA | variable optical attenuator |

## References


1. Cui, S.; Goldsmith, A.; Bahai, A. Energy-Efficiency of MIMO and Cooperative MIMO Techniques in Sensor Networks. *IEEE J. Sel. Areas Commun.* **2004**, *22*, 1089–1098. [CrossRef]
2. Ghavami, M.; Michael, L.B.; Kohno, R. *Ultra Wideband Signals and Systems in Communication Engineering*; John Wiley & Sons, Ltd.: Hoboken, NJ, USA, 2004. [CrossRef]
3. Nguyen, C.; Miao, M. *Design of CMOS RFIC Ultra-Wideband Impulse Transmitters and Receivers*; Springer International Publishing: Berlin/Heidelberg, Germany, 2017. [CrossRef]
4. Chandrakasan, A.P.; Lee, F.S.; Wentzloff, D.D.; Sze, V.; Ginsburg, B.P.; Mercier, P.P.; Daly, D.C.; Blazquez, R. Low-Power Impulse UWB Architectures and Circuits. *Proc. IEEE* **2009**, *97*, 332–352. [CrossRef]
5. Black, H.S.; Beyer, J.W.; Grieser, T.J.; Polkinghorn, F.A. A Multichannel Microwave Radio Relay System. *Trans. Am. Inst. Electr. Eng.* **1946**, *65*, 798–806. [CrossRef]
6. Hamkins, J. *Pulse Position Modulation*; Wiley: Hoboken, NJ, USA, 2007. [CrossRef]
7. Dai, L.; Liu, Z.; Meng, S.; Zhao, Y. Research on the Pulse-position Modulation in the Digital Communication System. In Proceedings of the 2021 International Conference on Wireless Communications and Smart Grid (ICWCSG), Hangzhou, China, 13–15 August 2021; pp. 8–12. [CrossRef]
8. Huan, L. Simulation on the design of digital pulse position modulation system. In Proceedings of the International Conference on Neural Networks, Information, and Communication Engineering (NNICE 2022), Qingdao, China, 25–27 March 2022; Tiwari, R., Ed.; SPIE: Bellingham, WA, USA, 2022. [CrossRef]
9. Proakis, J.; Salehi, M. *Digital Communications*, 5th ed.; McGraw-Hill Higher Education: Columbus, OH, USA, 2008.
10. Karp, S.; Gagliardi, R. The Design of a Pulse-Position Modulated Optical Communication System. *IEEE Trans. Commun.* **1969**, *17*, 670–676. [CrossRef]
11. Jing, M.; Li-ying, T.; Siyuan, Y. Technologies and applications of free-space optical communication and space optical information network. *J. Commun. Inf. Netw.* **2016**, *1*, 61–71. [CrossRef]
12. Wilson, B.; Ghassemlooy, Z. Pulse time modulation techniques for optical communications: A review. *IEE Proc. Optoelectron.* **1993**, *140*, 346. [CrossRef]
13. Saeed, R.; Khatun, S.; Ali, B.M.; Abduallah, M.K. Ultra Wide Band (UWB) Ad-hoc Networks: Review and Trends. *J. Comput. Sci.* **2005**, *1*, 35–39. [CrossRef]
14. Pulse Position Modulation: Block Diagram, Circuit, Working, Generation with PWM & Its Applications. Available online: https://www.elprocus.com/pulse-position-modulation/ (accessed on 9 November 2023).
15. Green, R.J. Comparison of pulse position modulation and pulse width modulation for application in optical communications. *Opt. Eng.* **2007**, *46*, 065001. [CrossRef]
16. Ai-ping, H.; Yang-Yu, F.; Yuan-Kui, L.; Meng, J.; Bo, B.; Qing-Gui, T. A differential pulse position width modulation for optical wireless communication. In Proceedings of the 2009 4th IEEE Conference on Industrial Electronics and Applications, Xi'an, China, 25–27 May 2009; pp. 1773–1776. [CrossRef]
17. Sacko, D.; Kéïta, A.A. Techniques of Modulation: Pulse Amplitude Modulation, Pulse Width Modulation, Pulse Position Modulation. *Int. J. Eng. Adv. Technol.* **2017**, *7*, 9.
18. Jahid, A.; Alsharif, M.H.; Hall, T.J. A contemporary survey on free space optical communication: Potentials, technical challenges, recent advances and research direction. *J. Netw. Comput. Appl.* **2022**, *200*, 103311. [CrossRef]
19. Fu, X.; Chen, G.; Tang, T.; Zhao, Y.; Wang, P.; Zhang, Y. Research and Simulation of PPM Modulation and Demodulation System on Spatial Wireless Optical Communication. In Proceedings of the 2010 Symposium on Photonics and Optoelectronics, Chengdu, China, 19–21 June 2010. [CrossRef]
20. Tang, W.; Wang, S.; Xu, Y.; Yu, Z. The Research Process, Application, and the Future Development of Pulse-Position Modulation. *J. Phys. Conf. Ser.* **2022**, *2384*, 012026. [CrossRef]
21. Urkowitz, H. Energy detection of unknown deterministic signals. *Proc. IEEE* **1967**, *55*, 523–531. [CrossRef]

22. Dillard, G. Pulse-Position Modulation Based on Energy Detection. *IEEE Trans. Aerosp. Electron. Syst.* **1973**, *AES-9*, 499–503. [CrossRef]
23. Hussein, S.S.; Youssif, A.; Ghouz, H.H.M. Performance Analysis and Evaluation of TH-PPM and TH-BPSK under Dynamic Channel Environment. *Int. J. Future Comput. Commun.* **2012**, *1*, 352–355. [CrossRef]
24. Munirathinam, R.; Aboltins, A.; Pikulins, D.; Grizans, J. Chaotic Non-Coherent Pulse Position Modulation Based Ultra- Wideband Communication System. In Proceedings of the 2021 IEEE Microwave Theory and Techniques in Wireless Communications (MTTW), Riga, Latvia, 7–8 October 2021; pp. 52–57. [CrossRef]
25. Shariat, M.; Ferdosizadeh, M.; Abdoli, M.J.; Makouei, B.; Yazdanpanah, A.; Marvasti, F. Comparison Between Several Methods of PPM Demodulation Based on Iterative Techniques. In *Telecommunications and Networking-ICT 2004*; Springer: Berlin/Heidelberg, Germany, 2004; pp. 554–559. [CrossRef]
26. Sushchik, M.; Rulkov, N.; Larson, L.; Tsimring, L.; Abarbanel, H.; Yao, K.; Volkovskii, A. Chaotic pulse position modulation: A robust method of communicating with chaos. *IEEE Commun. Lett.* **2000**, *4*, 128–130. [CrossRef]
27. Kalisz, J. Review of methods for time interval measurements with picosecond resolution. *Metrologia* **2003**, *41*, 17–32. [CrossRef]
28. Mahjoubfar, A.; Churkin, D.V.; Barland, S.; Broderick, N.; Turitsyn, S.K.; Jalali, B. Time stretch and its applications. *Nat. Photonics* **2017**, *11*, 341–351. [CrossRef]
29. Merz, R.; Botteron, C.; Farine, P.A. A novel low complexity data demodulation algorithm for pulse position modulation. *Digit. Signal Process.* **2012**, *22*, 535–543. [CrossRef]
30. Kim, J.; Clerckx, B. Wireless Information and Power Transfer for IoT: Pulse Position Modulation, Integrated Receiver, and Experimental Validation. *IEEE Internet Things J.* **2022**, *9*, 12378–12394. [CrossRef]
31. Event Timer A033-ET. Available online: https://eventechsite.com/products/a033-et/ (accessed on 9 November 2023).
32. Eventech Stream Time Tagger. Available online: https://eventechsite.com/products/ (accessed on 9 November 2023).
33. Barrett, T.W. History of Ultra Wideband Communications and Radar: Part I, UWB Communications. *Microw. J.* **2001**, *44*, 22–56.
34. Barrett, T.W. History of Ultra Wideband Communications and Radar: Part II, UWB Radars and Sensors. *Microw. J.* **2001**, *44*, 22–52.
35. O'Meara, T.R. *The Synthesis of Band-Pass, All-Pass Time Delay Networks with Graphical Approximation Techniques*; Research Report No. 114; Hughes Aircraft Company: Culver City, LA, USA, 1959.
36. Zverev, A.I. *Handbook of Filter Synthesis*; John Wiley and Sons, Inc.: Hoboken, NJ, USA, 1967.
37. Hoffswell, R.A. A Microstrip Line Stretcher. *Rev. Sci. Instrum.* **2003**, *41*, 1330–1331. [CrossRef]
38. Caputi, W.J. Stretch: A Time-Transformation Technique. *IEEE Trans. Aerosp. Electron. Syst.* **1971**, *AES-7*, 269–278. [CrossRef]
39. Ishii, M.; Yamada, G.; Miyatake, H. Pulse Stretching Circuit and Method. U.S. Patent No. US20130141148A1, 8 September 2015.
40. Xiang, B.; Kopa, A.; Fu, Z.; Apsel, A.B. An integrated Ku-band nanosecond time-stretching system using improved dispersive delay line (DDL). In Proceedings of the 2012 IEEE 12th Topical Meeting on Silicon Monolithic Integrated Circuits in RF Systems, Santa Clara, CA, USA, 16–18 January 2012; pp. 151–154. [CrossRef]
41. Monti, G.; Tarricone, L. Negative Group Velocity in a Split Ring Resonator-Coupled Microstrip Line. *Prog. Electromagn. Res.* **2009**, *94*, 33–47. [CrossRef]
42. Regalia, P.; Mitra, S.; Vaidyanathan, P. The digital all-pass filter: A versatile signal processing building block. *Proc. IEEE* **1988**, *76*, 19–37. [CrossRef]
43. Caloz, C.; Gupta, S.; Zhang, Q.; Nikfal, B. Analog Signal Processing: A Possible Alternative or Complement to Dominantly Digital Radio Schemes. *IEEE Microw. Mag.* **2013**, *14*, 87–103. [CrossRef]
44. Elamien, M.B.; Maundy, B.J.; Belostotski, L.; Elwakil, A.S. Synthesis of Wideband High-Quality Factor Delay- Tunable Fully Differential All-Pass Filters. *IEEE Trans. Microw. Theory Tech.* **2020**, *68*, 4348–4360. [CrossRef]
45. de França Ferreira, J.A.; Avignon-Meseldzija, E.; Ferreira, P.M.; Bénabès, P. Design and Synthesis of Arbitrary Group Delay Filters for Integrated Analog Signal Processing. In Proceedings of the 2018 25th IEEE International Conference on Electronics, Circuits and Systems (ICECS), Bordeaux, France, 9–12 December 2018; pp. 613–616. [CrossRef]
46. Zhang, Q.; Gupta, S.; Caloz, C. Synthesis of Narrowband Reflection-Type Phasers With Arbitrary Prescribed Group Delay. *IEEE Trans. Microw. Theory Tech.* **2012**, *60*, 2394–2402. [CrossRef]
47. Zhang, Q.; Sounas, D.L.; Caloz, C. Synthesis of Cross-Coupled Reduced-Order Dispersive Delay Structures (DDSs) With Arbitrary Group Delay and Controlled Magnitude. *IEEE Trans. Microw. Theory Tech.* **2013**, *61*, 1043–1052. [CrossRef]
48. Gupta, S.; Parsa, A.; Perret, E.; Snyder, R.V.; Wenzel, R.J.; Caloz, C. Group-Delay Engineered Noncommensurate Transmission Line All-Pass Network for Analog Signal Processing. *IEEE Trans. Microw. Theory Tech.* **2010**, *58*, 2392–2407. [CrossRef]
49. Avignon-Meseldzija, E.; Anastasov, J.; Milic, D. A linear group delay filter with tunable positive slope for analog signal processing. *Int. J. Circuit Theory Appl.* **2021**, *49*, 1307–1326. [CrossRef]
50. Mondal, I.; Krishnapura, N. Expansion and Compression of Analog Pulses by Bandwidth Scaling of Continuous-Time Filters. *IEEE Trans. Circuits Syst. I Regul. Pap.* **2018**, *65*, 2703–2714. [CrossRef]
51. Pactitis, S.A. *Active Filters: Theory and Design*; CRC Press: Boca Raton, FL, USA, 2007.
52. Rauscher, C. Microwave Active Filters Based on Transversal and Recursive Principles. *IEEE Trans. Microw. Theory Tech.* **1985**, *33*, 1350–1360. [CrossRef]
53. Xia, J.; Law, C.L.; Jiang, J. A Novel 3–5 GHz Active Matched Filter for Impulse Radio Ultra-Wideband. *IEEE Microw. Wirel. Components Lett.* **2009**, *19*, 458–460. [CrossRef]

54. Jarjar, M.; el Ouazzani, N.P. Three branch microwave channelized active bandpass filter. In Proceedings of the 2019 International Conference on Wireless Networks and Mobile Communications (WINCOM), Fez, Morocco, 29 October–1 November 2019; pp. 1–5. [CrossRef]
55. Gomez-Garcia, R.; Sanchez-Soriano, M.A.; Tam, K.W.; Xue, Q. Flexible Filters: Reconfigurable-Bandwidth Bandpass Planar Filters with Ultralarge Tuning Ratio. *IEEE Microw. Mag.* **2014**, *15*, 43–54. [CrossRef]
56. Solovjova, T.; Semenako, J.; Prigunovs, D.; Ortiz, D.; Spolitis, S.; Aboltins, A. Picosecond Pulse Expansion Using The Low-Pass Filter in Event Timer-Based PPM Communication System. In Proceedings of the 2022 Workshop on Microwave Theory and Techniques in Wireless Communications (MTTW), Riga, Latvia, 5–7 October 2022; pp. 29–34. [CrossRef]
57. Thomson, W. Delay networks having maximally flat frequency characteristics. *Proc. IEE-Part III Radio Commun. Eng.* **1949**, *96*, 487–490.
58. Mini-Circuits. Low Pass Filter SLP-2400+. Available online: https://www.minicircuits.com/pdfs/SLP-2400+.pdf (accessed on 9 November 2023).
59. Hammerstad, E.O. Equations for Microstrip Circuit Design. In Proceedings of the 1975 5th European Microwave Conference, Hamburg, Germany, 1–4 September 1975; pp. 268–272. [CrossRef]
60. Hammerstad, E.; Jensen, O. Accurate Models for Microstrip Computer-Aided Design. In Proceedings of the 1980 IEEE MTT-S International Microwave symposium Digest, Washington, DC, USA, 28–30 May 1980; pp. 407–409. [CrossRef]
61. Kirschning, M.; Jansen, R. Accurate Wide-Range Design Equations for the Frequency-Dependent Characteristic of Parallel Coupled Microstrip Lines. *IEEE Trans. Microw. Theory Tech.* **1984**, *32*, 83–90. [CrossRef]
62. Kirschning, M.; Jansen, R.; Koster, N. Accurate model for open end effect of microstrip lines. *Electron. Lett.* **1981**, *17*, 123–125. [CrossRef]
63. Hong, J.S.; Lancaster, M.J. *Microstrip Filters for RF/Microwave Applications*; John Wiley & Sons, Inc.: Hoboken, NJ, USA, 2001. [CrossRef]
64. Bond, C. Bessel Filters, Polynomials, Poles and Circuit Elements. 2003. Available online: http://www.crbond.com/papers/bsf2.pdf (accessed on 9 November 2023).
65. Paschotta, R. Pulse Stretchers. Available online: https://www.rp-photonics.com/pulse_stretchers.html (accessed on 9 November 2023).
66. Steed, R. Modelling of Optical Pulse Stretching Using Circulating Cavities. 2015. Available online: https://www.researchgate.net/publication/272292773_Modelling_of_Optical_Pulse_Stretching_using_Circulating_Cavities?channel=doi&linkId=54e0db5d0cf24d184b0e92cd&showFulltext=true (accessed on 9 November 2023).
67. Ulyanov, I.; Przhiialkovskii, D.V.; Butov, O.V. Point-by-point inscription of chirped apodized fiber Bragg gratings for application as ultrashort pulse stretchers. *Results Phys.* **2022**, *32*, 105101. [CrossRef]
68. Williamson, A.P.; Kiefer, J. Polarization-controlled optical ring cavity (PORC) tunable pulse stretcher. *Opt. Commun.* **2016**, *372*, 98–105. [CrossRef]
69. Saraceno, C. Pulse Stretching and Compressing Using Grating Pairs. Photonics and Ultrafast Laser Science, Ibsen Photonics A/S, 2017. Available online: https://ibsen.com/wp-content/uploads/White-paper-Pulse-stretching-and-compressing-using-grating-pairs_v1-2.pdf (accessed on 9 November 2023).
70. Luo, X.; Giannakis, G.B. Achievable rates of transmitted-reference ultra-wideband radio with PPM. *IEEE Trans. Commun.* **2006**, *54*, 1536–1541. [CrossRef]
71. Spolitis, S.; Prigunovs, D.; Migla, S.; Ortiz, D.; Selis, O.; Sics, P.E.; Ostrovskis, A.; Solovjova, T.; Semenjako, J.; Aboltins, A. Demonstration of 512-TR-PPM Fiber Optical Transmission Link. In Proceedings of the 2023 Photonics & Electromagnetics Research Symposium (PIERS), Prague, Czech Republic, 3–6 July 2023; pp. 1416–1422. [CrossRef]


**Disclaimer/Publisher's Note:** The statements, opinions and data contained in all publications are solely those of the individual author(s) and contributor(s) and not of MDPI and/or the editor(s). MDPI and/or the editor(s) disclaim responsibility for any injury to people or property resulting from any ideas, methods, instructions or products referred to in the content.

**Annex 6**

Migla, S., Rubuls, K., Tihomorskis, N., Salgals, T., Ozolins, O., Bobrovs, V., Spolitis, S., and Aboltins, A. “Ultra-Wideband Analog Radio-over-Fiber Communication System Employing Pulse-Position Modulation.” *Applied Sciences* 15.8 (2025). DOI: 10.3390/app15084222

*applied sciences*

MDPI

*Article*

# Ultra-Wideband Analog Radio-over-Fiber Communication System Employing Pulse-Position Modulation

**Sandis Migla [1], Kristaps Rubuls [1], Nikolajs Tihomorskis [1], Toms Salgals [1], Oskars Ozolins [1,2,3], Vjaceslavs Bobrovs [1], Sandis Spolitis [1] and Arturs Aboltins [1,*]**

[1] Institute of Photonics, Electronics and Telecommunications, Riga Technical University, 12 Azenes Street, LV-1048 Riga, Latvia; sandis.migla@rtu.lv (S.M.); kristaps.rubuls@rtu.lv (K.R.); nikolajs.tihomorskis@rtu.lv (N.T.); toms.salgals@rtu.lv (T.S.); oskars.ozolins@rtu.lv (O.O.); vjaceslavs.bobrovs@rtu.lv (V.B.); sandis.spolitis@rtu.lv (S.S.)
[2] Department of Applied Physics, KTH Royal Institute of Technology, 10691 Stockholm, Sweden
[3] RISE Research Institutes of Sweden, 16440 Kista, Sweden
* Correspondence: aboltins@rtu.lv

**Abstract:** This research presents a novel approach to 28 GHz impulse radio ultra-wideband (IR-UWB) transmission using pulse position modulation (PPM) over an analog radio-over-fiber (ARoF) link, investigating the impact of fiber-based fronthaul on the overall performance of the communication system. In this setup, an arbitrary waveform generator (AWG) is employed for PPM signal generation, while demodulation is performed with a commercial time-to-digital converter (TDC) based on an event timer. To enhance the reliability of transmitted reference PPM (TR-PPM) signals, the transmission system integrates Gray coding and Consultative Committee for Space Data Systems (CCSDS)-standard-compliant Reed-Solomon (RS) error correcting code (ECC). System performance was evaluated by transmitting pseudorandom binary sequences (PRBSs) and measuring the bit error ratio (BER) across a 5-m wireless link between two 20 dBi gain horn (Ka-band) antennas, with and without a 20 km single-mode optical fiber (SMF) link in transmitter side and ECC at the receiver side. The system achieved a BER of less than $8.17 \times 10^{-7}$, using a time bin duration of 200 ps and a pulse duration of 100 ps, demonstrating robust performance and significant potential for space-to-ground telecommunication applications.

**Keywords:** microwave communication; optical fiber communication; space communications; microwave photonics; energy efficiency; ultra wideband technology

check for updates

Academic Editors: Darius Plonis and Andrius Katkevičius

Received: 4 March 2025
Revised: 4 April 2025
Accepted: 8 April 2025
Published: 11 April 2025

**Citation:** Migla, S.; Rubuls, K.; Tihomorskis, N.; Salgals, T.; Ozolins, O.; Bobrovs, V.; Spolitis, S.; Aboltins, A. Ultra-Wideband Analog Radio-over-Fiber Communication System Employing Pulse-Position Modulation. *Appl. Sci.* **2025**, *15*, 4222. https://doi.org/10.3390/app15084222

**Copyright:** © 2025 by the authors. Licensee MDPI, Basel, Switzerland. This article is an open access article distributed under the terms and conditions of the Creative Commons Attribution (CC BY) license (https://creativecommons.org/licenses/by/4.0/).

## 1. Introduction

With the advent of current 5G Advanced and future 6G networks [1], fronthaul solutions, such as radio-over-fiber (RoF), have gained prominence as a means of enhancing communication systems [2]. RoF employs optical fibers to create the fronthaul links for radio frequency (RF) signal transmission, offering a sizable usable bandwidth and low attenuation. Employment of RoF alleviates bandwidth constraints while enabling the distribution of antenna units (AUs) over longer distances without frequent amplification [3]. Additionally, RoF technology can support centralized processing and signal generation [4], reducing the complexity and power consumption of the entire network.

A promising RoF technology for 5G Advanced and 6G networks is ARoF [4]. In ARoF, an analog waveform modulates the optical transmitter, generating an analog optical signal transmitted through the fronthaul link. This approach minimizes the need for power-hungry, high-speed analog-to-digital converters (ADCs) and digital-to-analog converters

(DACs) compared to traditional digital interfaces [4], enabling the use of low-complexity and energy-efficient AUs. For these reasons, ARoF technology offers a spectrally efficient, power-efficient, and low-complexity solution. As next-generation networks plan to utilize even higher frequency bands, this becomes particularly important [2]. Consequently, ARoF technology has been explored in recent research for millimeter-wave [5,6] and terahertz links [7,8]. Additionally, ARoF is being considered for future distributed multiple-input multiple-output (D-MIMO) systems in 6G networks [4,9], which rely heavily on a distributed AU architecture to enhance wireless coverage.

Applications of ARoF technology include wireless communications, distributed sensor networks, radars, space communication systems, and many other applications [10]. In Figure 1, a visualization of the physical and wireless RF connections between the central office, base station, and user equipment is provided, depicting a communication system for remote sensing and space applications involving low Earth orbit, geostationary Earth orbit, and deep space satellites.

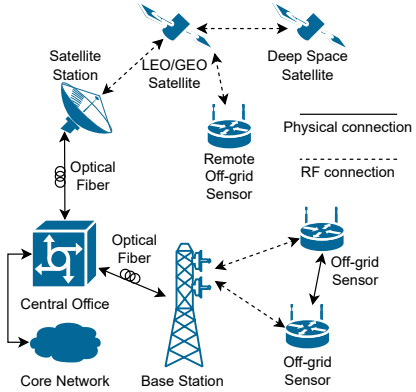



**Figure 1.** Usage scenarios for the proposed UWB ARoF technology.

ARoF is an increasingly popular solution for 5G Advanced and upcoming 6G telecommunication standards, leveraging millimeter-wave signals to support high-capacity broadband applications [11–13]. In [14], a hybrid architecture for 5G mobile networks based on the ARoF technological concept is described. The authors propose a long-range wireless communication solution with 1 km optical fiber and 20 m free-space optical communication (FSO) fronthaul, using quadrature amplitude modulation (QAM) signal with 700 MHz carrier, achieving 60 Mb/s data transmission rate.

The paper [15] demonstrates the seamless integration of ARoF with FSO and mm-wave wireless communication systems and shows satisfactory performance with QAM signals at simulated data transmission speeds exceeding 10 Gb/s.

ARoF technology can increase the performance of phased antenna arrays by using the modulation instability phenomenon [16]. The authors have demonstrated modulation instability gain of 38.1 dB by using 45 km long optical fiber. Another possibility is to use a single light source at the central office to achieve full duplex communication [17]. The presented system has achieved 2.5 Gb/s data transmission over 40 km long SMF.

Ultra-wideband (UWB) technology has emerged as a promising innovation for RF that allows for the use of ultra-short pulses for transmitting information, as well as applications in integrated sensing and communications (ISAC), radar technology, and distributed sensor networks [18].

Research on UWB modulation schemes [19,20] for use in ARoF communication systems has been conducted in the past. For example, paper [21] presents an UWB over fiber

communications system based on asymmetric Mach-Zehnder interferometer for optical modulation. It provides an overview of various UWB modulation schemes for use in ARoF systems, such as on-off keying (OOK), bi-phase modulation, pulse amplitude modulation, pulse shape modulation, and PPM. The authors have achieved error-free data transmission over a 20 km long SMF and 5 GHz wireless channel. In the paper [22], authors provide a performance evaluation of UWB signal transmission over SMF by using double-sided UWB and quasi single-sideband UWB (QSSB-UWB) monocycle pulses and analyzing the power spectral density of the signal at multiple transmission distances. The authors have found that QSSB-UWB pulses are more suitable for use with OOK and PPM. In paper [23], a low-complexity IR-UWB pulse generation method based on a linear combination of two monocycle pulses is presented, and transmission over SMF is evaluated. Error-free performance was achieved over 25 km long fiber at the speed of 2 Gb/s.

The PPM modulation scheme is widely used in RF and optical IR-UWB communication systems [24,25]. This modulation scheme encodes data as a time interval and allows ultra-short pulses to transmit data, increasing the power efficiency [26]. There are many types of PPM, such as coherent PPM, differential PPM, TR-PPM [27,28], variable PPM [29], overlap PPM and more [30]. Paper [31] proposes a nested PPM scheme for use in visible light communication systems, which simplifies the transmitter and receiver structure, therefore making nested PPM an attractive choice for a wide range of applications where energy efficiency and low cost are crucial.

Another application of PPM is in joint radar communication, which was experimentally validated with the employment of chirp sequences [32]. PPM transceiver can be set up as a joint radar communication system, using the receiving antenna unit as a radar. In this implementation, the transmitted signal will be locally used for symbol synchronization of the received waveform. Depending on the received reflections and pulses from other transmitters, distances and velocities of objects and receivers can be measured. This theoretical PPM communication system with radar capabilities will work as an ISAC system, adjusting, for example, the power of transmitted pulses, depending on the distance to the receiver, for power conservation purposes. In deep space communications, the position of a directional antenna may be adjusted, depending on the received pulses' power [33]. In terrestrial applications, PPM pulses may also be used for the localization of mobile objects, essentially working as a radar on top of the PPM communication [34].

This research presents a novel, experimentally validated communication system employing TR-PPM transmission over ARoF. In this research implementation, the central office is equipped with a local analog RoF transmitter; in turn, the base station consists of an remote antenna unit (RAU) serving as the RF transmitter in the access network. The demodulation of PPM signal is performed by TDC based on a commercial event timer. The presented system functions as a testbed for the investigation of IR-UWB communication and future use cases of UWB ISAC.

The manuscript is organized as follows: Section 2 discusses the use of PPM in ARoF applications, Section 3 describes the experimental setup used in this research, Section 4 shows the results of the conducted experiments, and finally, Section 5 provides conclusions about the presented research.

## 2. The Use of PPM

In this paper, TR-PPM is employed, where data are encoded by allocating pulses of duration $\tau$ (s) into time bins of duration $\Delta$ (s). Each of $M = 2^b$ positions (time bins) represents a different symbol described by a predefined number of bits $b$. An additional reference pulse at the beginning of each frame helps to calculate the value of the received symbols. The first time bin starts after $\mathrm{M} \cdot \Delta + T_g$ seconds from the reference pulse, where

guard time, denoted as $T_g$ (s), is introduced to ensure a safe interval between the pulses. This interval compensates for the hardware's inherent dead time, encompassing signal propagation delays and the duration required for processing. An example of a TR-PPM frame, which provides reference and symbol pulses with $M = 4$ positions, is shown in Figure 2.

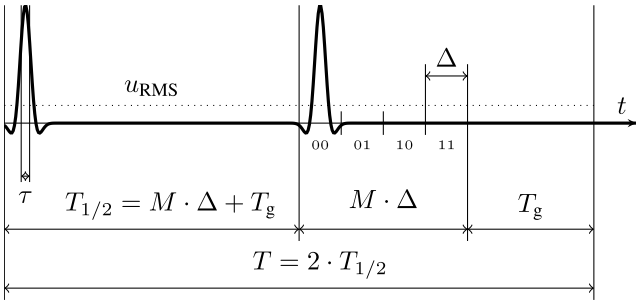



**Figure 2.** Example structure of one TR-PPM frame with $M = 4$.

The allocation of data symbols into the time between short pulses, measured in picoseconds (ps), significantly enhances energy efficiency per symbol. The root mean square (RMS) of the signal is defined as $u_{\mathrm{RMS}} = \sqrt{\int_0^{T/2} u(t)^2\, dt}$, where duration $T_{1/2} = M \cdot \Delta + T_g$ and $T = 2 \cdot T_{1/2}$ represent frame duration consisting of two halves of a TR-PPM symbol duration $T_{1/2}$, (s). The decrease in signal RMS $u_{\mathrm{RMS}}$, achieved by using pulses with minimal pulse duration $\tau$, enables an increase in transmission distance while maintaining the same mean power consumption compared to conventional modulation schemes like OOK. By decreasing the time bins' width $\Delta$, more data in PPM can be allocated, increasing data transmission speed. It is worth noticing that although in some PPM applications, a simplified scheme with $\Delta = \tau$ is used, the information is carried solely by the timing of the pulses' rising edges. Hence, the pulse width $\Delta$ is not critical from an information-carrying perspective. However, pulse width affects both the link's energy efficiency and the signal's frequency bandwidth. Consequently, the narrower pulses create more energy-efficient transmission, whereas longer pulses require smaller bandwidth and are easier to detect. In the latter case, the pulse width shouldn't exceed guard time $T_g$ to avoid overlapping the pulses.

As PPM encodes data in the time domain, precise time-to-digital conversion is essential for its demodulation. Ideally, each pulse has equal and constant amplitude and steep rising edge, allowing for pulse detection with a constant threshold that triggers precisely on one of the pulse's edges. As demodulation is performed by TDC, the precision of TDC significantly influences the speed of PPM communication. To avoid symbol errors, the time interval $\Delta$ must be adjusted according to the TDC precision, ensuring that the measured time does not drift into adjacent pulse time bins.

Pulse threshold detection with precise time recording is what the Eventech Stream Time Tagger (ESTT) 7 Series event timer [35] provides. This event timer was used as TDC for PPM demodulation in previous papers [36,37], and it was also chosen as a TDC for PPM demodulation in this research. ESTT's time precision is around 1.5 ps with a dead time of 40 ns, which must be defined as the guard-time $T_g$ in PPM.

Recently, a space-rated version of the ESTT–Eventech Space Ready Timing Module (ESRTM) was developed and is available for use in space applications where precise time measurement is needed [38]. ESRTM enables the implementation of a PPM receiver for Earth orbit and deep space satellites without the need to develop a dedicated system. ESRTM was launched with the European Space Agency's Hera mission [39] on 7 October 2024.

## 3. Experimental Setup

A series of captured experimental illustrations of the setup is shown in Figure 3. At the same time, a block diagram of the developed ARoF-based UWB communication system employing PPM is depicted in Figure 4, where the optical part is shown in red, the electrical part is displayed in blue, and the digital part is depicted in gray. The experimental system mainly consists of three parts: (a) ARoF transmitter, (b) RAU transmitter, and (c) RAU receiver. In the experimental setup, the following primary assumptions have been made: firstly, the radio channel is exclusive to our experiment; secondly, both the transmitter and receiver remain stationary; and, thirdly, multipath propagation effects are negligible due to the controlled environment. These assumptions align with the experimental constraints and ensure the system's performance is evaluated close to ideal conditions.

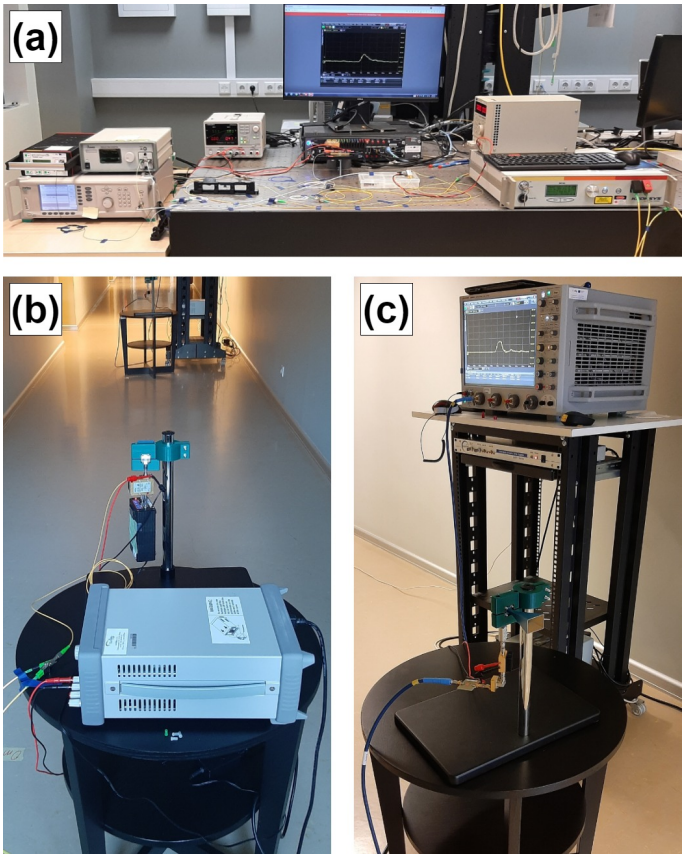



**Figure 3.** Captured experimental illustrations of ARoF-based UWB communication system employing PPM, (**a**) ARoF transmitter, (**b**) RAU transmitter, (**c**) RAU receiver.

### *3.1. ARoF Transmitter*

The optical output (∼1550 nm wavelength) from the Cobrite DX-1 (ID Photonics, Neubiberg, Germany) continuous wave (CW) laser, with a linewidth of 25 kHz and an output power of +16 dBm, was first directly connected to a Mach-Zehnder modulator (MZM)—a 40 GHz MX-LN-40 intensity modulator (Exail Technologies, Paris, France) that has a 3.5 dB insertion loss and a 20 dB extinction ratio. The bias point was adjusted near its zero level. A sinusoidal signal generator MG3690C (Anritsu, Vienna, Austria), producing

a 14 GHz sinusoidal electrical signal (half of the proposed intermediate frequency), was directly connected to the electrical signal input of the first MZM. As a result, the desired RF of 28 GHz was achieved between the generated tones in the optical domain at the output of the first MZM. Polarization controllers were positioned before and after the first MZM to precisely adjust the polarization states of the optical signal during the experiment. The output of the first MZM, comprising two equal optical tones (carriers) spaced 28 GHz apart, was subsequently amplified using an erbium-doped fiber amplifier (EDFA) to compensate for optical power loss. The optical signal was then modulated with the TR-PPM waveform using a second MZM (Covega 10G, Jessup, MD, USA). The TR-PPM waveform was generated using the M8195A AWG (Keysight, Colorado Springs, CO, USA) with a 25 GHz analog bandwidth and a 65 GSa/s sampling rate. Due to the limited output power (maximum 1 V-pp) of the AWG, an RF broadband amplifier (SHF 100 BP, 17 dB gain, up to 25 GHz) was used to amplify the TR-PPM waveform before launching it into the RT input of the second MZM.

An optical signal pre-amplification by a second EDFA with an optimized gain was performed before launching the optical signal into a 20 km long ITU-T G.652 rec. compliant SMF span, which has 0.02 dB/km attenuation and a 17 ps/nm/km dispersion coefficient at 1550 nm.

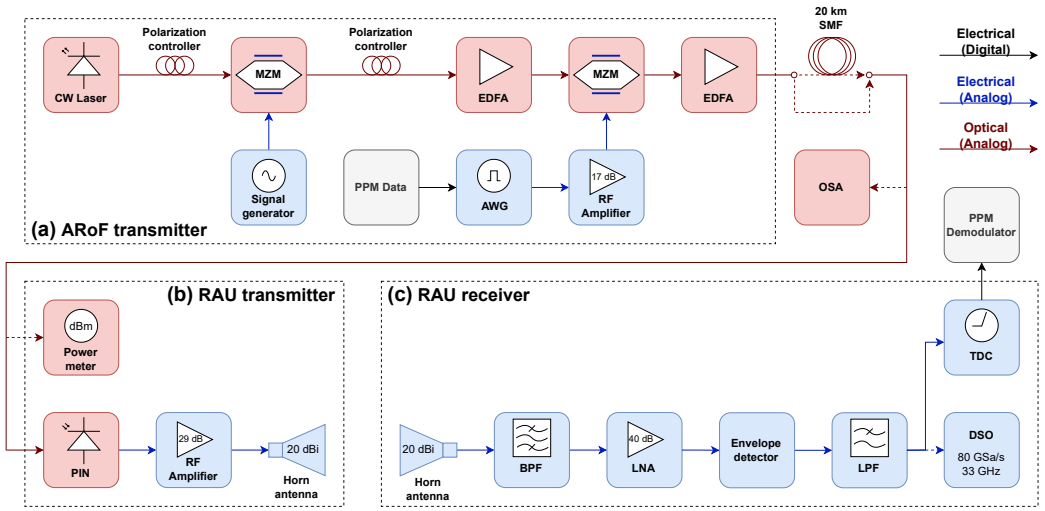



**Figure 4.** Experiment setup of ARoF-based UWB communication system employing PPM, (**a**) ARoF transmitter, (**b**) RAU transmitter, (**c**) RAU receiver.

### *3.2. RAU Transmitter*

As for the optical receiver, a Discovery Semiconductors DSC10H p-i-n photodiode (PIN) with 50 GHz 3-dB electrical bandwidth with a sensitivity level +4 dBm for BER of $10^{-12}$, the dark current of 5 nA and responsivity of 0.65 A/W was used, which realized the photodetection-based RF generation from the optical beat-note. A broadband optical power meter and an optical spectrum analyzer were used at the end of the fiber line to measure and optimize the received optical power, which was later disconnected and replaced by the PIN after optimization. The optical spectra before the PIN can be seen in Figure 5. The RF signal output power from the PIN was limited. Therefore, the RF signal is amplified by a 38 GHz and +29 dB gain broadband amplifier (SHF 810) before being transmitted to the Ka-band (26.5–40 GHz) horn-type antenna with 20 dBi gain. Free space path loss of the transmitted 28 GHz signal at 5 m was 35.36 dB; at 10 m, it was 41.38 dB, and at 20 m it was

47.40 dB. As one can see from the calculations, the most critical insertion losses are at the beginning of the transmission distance.

In Figure 5, the Kerr nonlinear optical effects (NOE), e.g., the four-wave mixing (FWM) impact on the PPM modulated intermediate frequency optical signal, is illustrated, which affects the signal transmission through the optical distribution network. Additional spectrum peaks are caused by the high optical power level output (∼+15 dBm) of the second EDFA before launching the optical signal in the 20 km long SMF optical distribution network and are more pronounced than in the case of the back-to-back setup due to the nonlinear coefficient and the mode effective area of the SMF. Nevertheless, this does not significantly impact the BER, as NOE does not considerably affect PPM signals. The optical power of the three optical tones after the 20 km long SMF is about 3 dB lower due to the attenuation in the fiber.

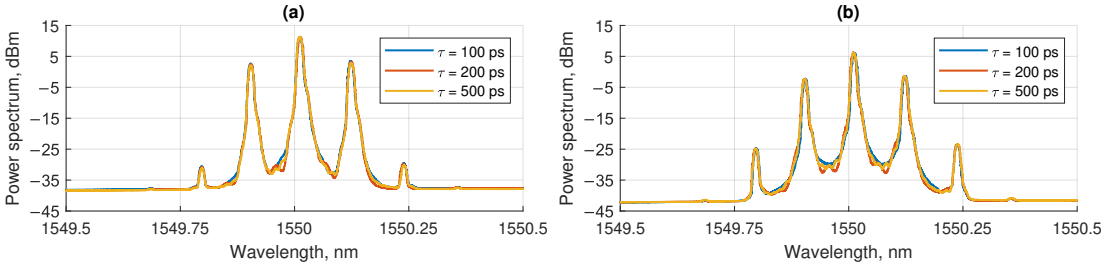



**Figure 5.** Optical spectrum before PIN for (**a**) back-to-back setup, (**b**) setup with 20 km SMF.

### *3.3. RAU Receiver*

The receiver was located 5 m away from the RAU transmitter. The transmitted mm-wave signal was received by an identical Ka-band antenna and filtered using the bandpass filter (BPF) (Marki, Morgan Hill, CA, USA), which has a center frequency of 27.38 GHz and a 3-dB passband of 8.3 GHz. After filtering, the signal at a central frequency of 28 GHz was amplified by the SAGE SBL low-noise amplifier (LNA) with a gain of 40 dB, allowing further processing in the mm-wave RAU receiver. The amplified signal was then sent to the envelope detector (Spacek Labs, Santa Barbara, CA, USA) with 13.5 GHz bandwidth, which performed frequency down-conversion of the 28 GHz intermediate frequency signal. The down-converted baseband signal was then sent to the digital storage oscilloscope (DSO) and the ESTT 7 Series [35] event timer via a custom-made low-pass filter (LPF) with a bandwidth of up to 1.8 GHz for analysis. This specific LPF [40] was purposefully utilized to broaden the received pulses for accurate detection with the ESTT, as the group delay of this filter remains nearly constant for frequencies up to 3 GHz, thus reducing pulse shape distortions. The magnitude response of the ARoF communication system, including the custom LPF, can be seen in Figure 6. Additionally, the Keysight DSOZ334A DSO, with a sample rate of 80 GSa/s and a bandwidth of 33 GHz, was initially used for signal visualization and optimization after wireless transmission and was later replaced with the ESTT for experimental measurements. The pulse waveforms for various pulse duration values $\tau$, captured by the DSO, for the back-to-back experimental setup and the setup involving 20 km SMF, can be seen in Figure 7 and Figure 8, respectively.

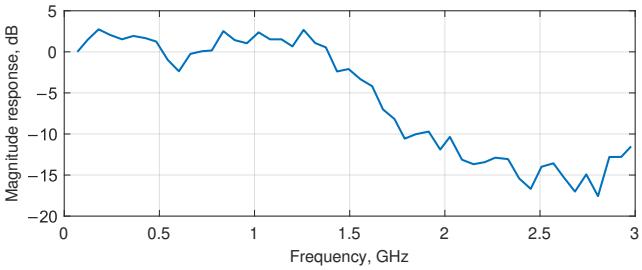



**Figure 6.** Magnitude response of the ARoF system.

As shown in Figures 7 and 8, the pulses after the LPF in the RAU receiver are broadened to approximately 500 ps, facilitating their detection by the ESTT. However, the expansion comes at the cost of the pulse waveform amplitude.

In the presented receiver RAU, ESTT is working as a TDC, triggering at the incoming pulses and converting the absolute times of the events into digital numerical values in ps, called "time tags". ESTT uses a variable voltage threshold, which can be set by software in a range between −2 V and 3 V with step 1.2 mV. In the case of PPM, where pulses are transmitted with high amplitude, this device successfully works as a TDC, as presented in Section 4 of this and our previous research [37].

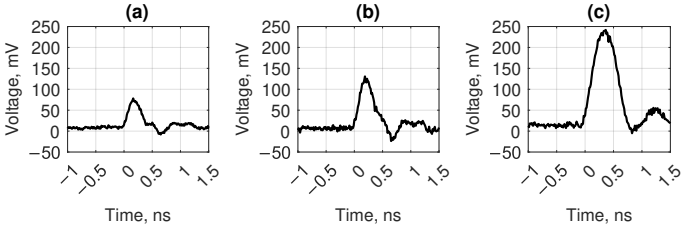



**Figure 7.** Pulse waveforms after the envelope detector for back-to-back experiment setup with (**a**) $\tau = 100$ ps, (**b**) $\tau = 200$ ps, (**c**) $\tau = 500$ ps.

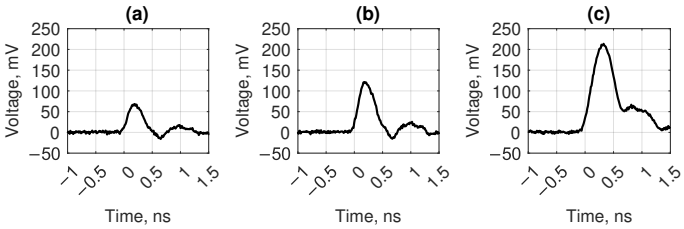



**Figure 8.** Pulse waveforms after the envelope detector for experiment setup with 20 km SMF with (**a**) $\tau = 100$ ps, (**b**) $\tau = 200$ ps, (**c**) $\tau = 500$ ps.

ESTT is connected to the PC via a USB 3.0 interface, providing fast real-time transfer of time tags to PC. TR-PPM demodulation from time tags and forward error correction (FEC) is done in the receiver's software part, written in C++20 and running on the PC.

### *3.4. Data Preparation*

The transmitted data were generated as a $1.224 \times 10^6$ bit long PRBS using the Mersenne Twister pseudo-random number generator with the order of 623, establishing a minimum detectable BER of $8.17 \times 10^{-7}$ corresponding to a single error in the demodulated data. There data were saved for later comparison with the demodulated data. The TR-PPM

waveforms were generated offline in MATLAB 2024a with pulse durations varying from 500 ps to 100 ps and time bin durations ranging from 200 ps to 50 ps and then loaded into the AWG. The number of pulse positions was adjusted for each configuration to achieve optimal data rates for the given parameters [36]. Additionally, these waveforms were generated with and without ECC. Error correction was implemented using Gray code alone and Gray code with CCSDS "Blue book" 131.0-B-5 Section 4 standard-compliant RS ECC, which can correct up to 16 error bytes in the encoded data. In the case of RS encoding, the waveform was generated with the number of positions $M = 256$, so that one byte of data takes up an entire TR-PPM frame and is not split across multiple frames.

## 4. Experimental Results

Two sets of experiments were performed, with and without a 20 km SMF link and BER measurements were made with and without ECC. The results are presented in Figures 9 and 10 and summarized in Table 1. For error-free demodulation, the BER is reported as $<8.17 \times 10^{-7}$, as lower BER values cannot be measured with the given data set size.

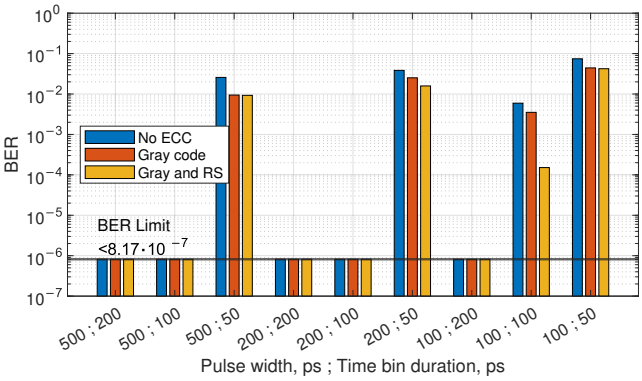



**Figure 9.** BER measurement results for TR-PPM transmission over ARoF experiments, using PRBS, for setup with 20 km SMF. Bars shown at BER limit $8.17 \times 10^{-7}$ have 0 errors in the received data.

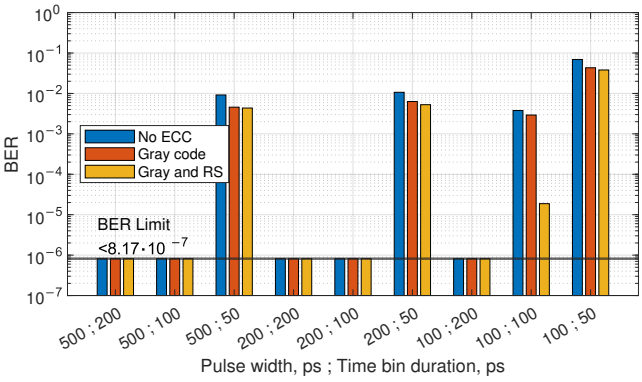



**Figure 10.** BER measurement results for TR-PPM transmission over ARoF experiments, using PRBS, for back-to-back setup. Bars shown at BER limit $8.17 \times 10^{-7}$ have 0 errors in the received data.

All measurements with a time bin duration of 200 ps demonstrate error-free transmission. Error-free transmission was also achieved with both 500 ps and 200 ps pulse widths, using a time bin duration of 100 ps.

It can be seen that the employment of Gray code, which ensures that only one bit is flipped if the received pulse is located in the adjacent time bin, slightly decreases the BER, which is further reduced by the use of RS (255, 223) code. Employment of RS code significantly reduces the BER for measurements with the pulse width of 100 ps and time bin duration of 100 ps. For all measurements involving the time bin duration of 50 ps, the impact of RS code is negligible, which can be attributed to the high amount of flipped bits in the TR-PPM frames which carry the parity bytes. When considering time bin durations smaller than the pulse width, the effect of the additive noise is especially significant, as the detection threshold may be reached over a time span longer than the time bin duration in systems employing a timer-based TDC.

Comparing measurements with and without the 20 km SMF, the back-to-back measurements result in a lower overall BER than when the 20 km fiber is connected. BER degradation in the latter case can be attributed to dispersion in the fiber, which causes degradation of the pulse shape and a reduction in the steepness of the rising edge. This, in turn, increases sensitivity to additive noise, resulting in errors in pulse position measurements by the ESTT.

**Table 1.** Results of the TR-PPM transmission over ARoF experiments, using PRBS for back-to-back setup and setup with 20 km SMF.

| ECC | Pulse Duration $\tau$, ps | Time Bin Duration $\Delta$, ps | Number of Positions $M$ | 20 km Fiber BER | Back-to-Back BER |
|---|---|---|---|---|---|
| **No ECC** | 500 | 200 | 128 | $<8.17 \times 10^{-7}$ | $<8.17 \times 10^{-7}$ |
| | 500 | 100 | 256 | $<8.17 \times 10^{-7}$ | $<8.17 \times 10^{-7}$ |
| | 500 | 50 | 512 | $2.578 \times 10^{-2}$ | $9.169 \times 10^{-3}$ |
| | 200 | 200 | 128 | $<8.17 \times 10^{-7}$ | $<8.17 \times 10^{-7}$ |
| | 200 | 100 | 256 | $<8.17 \times 10^{-7}$ | $<8.17 \times 10^{-7}$ |
| | 200 | 50 | 512 | $3.848 \times 10^{-2}$ | $1.068 \times 10^{-2}$ |
| | 100 | 200 | 128 | $<8.17 \times 10^{-7}$ | $<8.17 \times 10^{-7}$ |
| | 100 | 100 | 256 | $5.936 \times 10^{-3}$ | $3.781 \times 10^{-3}$ |
| | 100 | 50 | 512 | $7.436 \times 10^{-2}$ | $6.931 \times 10^{-2}$ |
| **Gray code** | 500 | 200 | 128 | $<8.17 \times 10^{-7}$ | $<8.17 \times 10^{-7}$ |
| | 500 | 100 | 256 | $<8.17 \times 10^{-7}$ | $<8.17 \times 10^{-7}$ |
| | 500 | 50 | 512 | $9.433 \times 10^{-3}$ | $4.572 \times 10^{-3}$ |
| | 200 | 200 | 128 | $<8.17 \times 10^{-7}$ | $<8.17 \times 10^{-7}$ |
| | 200 | 100 | 256 | $<8.17 \times 10^{-7}$ | $<8.17 \times 10^{-7}$ |
| | 200 | 50 | 512 | $2.518 \times 10^{-2}$ | $6.317 \times 10^{-3}$ |
| | 100 | 200 | 128 | $<8.17 \times 10^{-7}$ | $<8.17 \times 10^{-7}$ |
| | 100 | 100 | 256 | $3.524 \times 10^{-3}$ | $2.924 \times 10^{-3}$ |
| | 100 | 50 | 512 | $4.427 \times 10^{-2}$ | $4.318 \times 10^{-2}$ |
| **Gray code and RS** | 500 | 200 | 256 | $<8.17 \times 10^{-7}$ | $<8.17 \times 10^{-7}$ |
| | 500 | 100 | | $<8.17 \times 10^{-7}$ | $<8.17 \times 10^{-7}$ |
| | 500 | 50 | | $9.285 \times 10^{-3}$ | $4.356 \times 10^{-3}$ |
| | 200 | 200 | | $<8.17 \times 10^{-7}$ | $<8.17 \times 10^{-7}$ |
| | 200 | 100 | | $<8.17 \times 10^{-7}$ | $<8.17 \times 10^{-7}$ |
| | 200 | 50 | | $1.584 \times 10^{-2}$ | $5.267 \times 10^{-3}$ |
| | 100 | 200 | | $<8.17 \times 10^{-7}$ | $<8.17 \times 10^{-7}$ |
| | 100 | 100 | | $1.514 \times 10^{-4}$ | $1.875 \times 10^{-5}$ |
| | 100 | 50 | | $4.226 \times 10^{-2}$ | $3.804 \times 10^{-2}$ |

The results strongly agree with previously published findings [40–42] in that in PPM data transmission, pulse shape plays a vital role in the overall system performance. The presented pulse waveforms after the RF transmission show distortions not dissimilar to

existing research on RoF systems, where waveforms were captured after the optical transmission network.

## 5. Conclusions

This research demonstrates the use of TR-PPM for data transmission in an ARoF system, with signal detection carried out by a commercial time tagger. The experimental results confirm the feasibility of this approach and highlight the potential of PPM over RoF for wireless communication applications, as well as the possibility of extending this concept to PPM-based ISAC implementations.

The primary factor influencing the performance of the ARoF TR-PPM communication system is the time bin duration, which directly determines the system's tolerance to jitter. The results validate the effectiveness of the implemented encoding algorithms, as enabling ECC reduces the BER in both the 20 km SMF and back-to-back setups. Tests with a 20 km SMF show only a slight BER increase over the back-to-back setup, which remains negligible for data transmission. In both configurations, multiple combinations of pulse widths and time bin durations resulted in a BER of $<8.17 \times 10^{-7}$, which is below the threshold corresponding to a single bit error after PPM signal demodulation. Within the context of this research, all BER values below this limit can be interpreted as error-free data transmission.

**Supplementary Materials:** The following supporting information can be downloaded at: https://www.mdpi.com/article/10.3390/app15084222/s1.

**Author Contributions:** Conceptualization, S.M., S.S. and T.S.; methodology, T.S. and O.O.; software, S.M. and N.T.; validation, S.M., N.T., S.S. and K.R.; formal analysis, S.M. and K.R.; investigation, K.R., S.M. and N.T.; resources, A.A., S.S., V.B. and O.O.; data curation, S.M., N.T. and K.R.; writing—original draft preparation, S.M., K.R. and N.T.; writing—review and editing, A.A., S.M., N.T. and S.S.; visualization, N.T. and S.M.; supervision, A.A. and V.B.; project administration, A.A.; funding acquisition, A.A. All authors have read and agreed to the published version of the manuscript.

**Funding:** This research was funded by the Latvian Council of Science grant No. lzp-2021/1-0475, "Picosecond-resolution pulse position modulation for beyond-the-limits energy efficiency of communications".

**Institutional Review Board Statement:** Not applicable.

**Informed Consent Statement:** Not applicable.

**Data Availability Statement:** The original contributions presented in this study are included in the article and Supplementary Materials. Further inquiries can be directed to the corresponding author.

**Conflicts of Interest:** The authors declare no conflict of interest.

## Abbreviations

The following abbreviations are used in this manuscript:

| | |
|---|---|
| ADC | analog-to-digital converter |
| ARoF | analog radio-over-fiber |
| AU | antenna unit |
| AWG | arbitrary waveform generator |
| BER | bit error ratio |
| BPF | bandpass filter |
| CCSDS | Consultative Committee for Space Data Systems |
| CW | continuous wave |
| DAC | digital-to-analog converter |
| D-MIMO | distributed multiple-input multiple-output |

| | |
|---|---|
| DSO | digital storage oscilloscope |
| ECC | error correcting code |
| EDFA | erbium-doped fiber amplifier |
| ESRTM | Eventech Space Ready Timing Module |
| ESTT | Eventech Stream Time Tagger |
| FEC | forward error correction |
| FSO | free-space optical communication |
| FWM | four-wave mixing |
| IR-UWB | impulse radio ultra-wideband |
| ISAC | integrated sensing and communications |
| LNA | low-noise amplifier |
| LPF | low-pass filter |
| MZM | Mach-Zehnder modulator |
| NOE | nonlinear optical effects |
| OOK | on-off keying |
| PIN | p-i-n photodiode |
| PPM | pulse position modulation |
| PRBS | pseudorandom binary sequence |
| QAM | quadrature amplitude modulation |
| QSSB-UWB | quasi single-sideband UWB |
| RAU | remote antenna unit |
| RF | radio frequency |
| RMS | root mean square |
| RoF | radio-over-fiber |
| RS | Reed-Solomon |
| SMF | single-mode optical fiber |
| TDC | time-to-digital converter |
| TR-PPM | transmitted reference PPM |
| UWB | ultra-wideband |

## References


1. ITU-R. *Report ITU-R M.2516-0: Future Technology Trends of Terrestrial International Mobile Telecommunications Systems Towards 2030 and Beyond*; ITU-R: Geneva, Switzerland, 2022.
2. Wikström, G.; Peisa, J.; Rugeland, P.; Johansson, N.; Parkvall, S.; Girnyk, M.; Mildh, G.; Da Silva, I.L. Challenges and Technologies for 6G. In Proceedings of the 2020 2nd 6G Wireless Summit (6G SUMMIT), Levi, Finland, 17–20 March 2020; pp. 1–5. [CrossRef]
3. Lim, C.; Tian, Y.; Ranaweera, C.; Nirmalathas, T.A.; Wong, E.; Lee, K.L. Evolution of Radio-Over-Fiber Technology. *J. Light. Technol.* **2019**, *37*, 1647–1656. [CrossRef]
4. Puerta, R.; Jiang, T.; Joharifar, M.; Ostrovskis, A.; Salgals, T.; Rubuls, K.; Schatz, R.; Djupsjöbacka, A.; Pittalà, F.; Gruen, M.; et al. Analog Mobile Fronthaul for 6G and Beyond. *J. Light. Technol.* **2024**, *42*, 7458–7467. [CrossRef]
5. Ostrovskis, A.; Salgals, T.; Rubuls, K.; Skladova, L.; Bobrovs, V.; Spolitis, S. Experimental Demonstration of Hybrid Photonics-BasedARoF System for 5G and B5G Networks. In Proceedings of the 2022 International Conference on Software, Telecommunications and Computer Networks (SoftCOM), Split, Croatia, 22–24 September 2022; pp. 1–5. [CrossRef]
6. Jiang, W.; Schotten, H.D. Full-Spectrum Wireless Communications for 6G and Beyond: From Microwave, Millimeter-Wave, Terahertz to Lightwave. In Proceedings of the 2023 IEEE 3rd International Conference on Computer Communication and Artificial Intelligence (CCAI), Taiyuan, China, 26–28 May 2023; pp. 353–357. [CrossRef]
7. Li, W.; Yu, J.; Ji, X.; Liu, J.; Wang, F.; Zhu, B.; Zhou, W.; Zhao, F.; Yu, J. Over 100 Gb/s mm-wave delivery with 4600 m wireless distance based on dual polarization multiplexing. *Sci. China Inf. Sci.* **2023**, *66*, 1869–1919. [CrossRef]
8. Jia, S.; Lo, M.C.; Zhang, L.; Ozolins, O.; Udalcovs, A.; Kong, D.; Pang, X.; Guzman, R.; Yu, X.; Xiao, S.; et al. Integrated Dual-Laser Photonic Chip for High-Purity Carrier Generation Enabling Ultrafast Terahertz Wireless Communications. *Nat. Commun.* **2022**, *13*, 1388. [CrossRef] [PubMed]
9. Jiang, T.; Rubuls, K.; Joharifar, M.; Ostrovskis, A.; Djupsjöbacka, A.; Salgals, T.; Zvěřina, J.; Halmo, L.; Spolitis, S.; Bobrovs, V.; et al. Photonics-Enabled 6G Distributed MIMO: Experimental Study in an Indoor Environment. In Proceedings of the 2024 International Topical Meeting on Microwave Photonics (MWP), Pisa, Italy, 17–20 September 2024; pp. 1–5. [CrossRef]
10. Yao, J. Microwave Photonics. *J. Light. Technol.* **2009**, *27*, 314–335. [CrossRef]

11. Anes, B.; Riad, B.A. A new bidirectional analog radio over fiber transmission for 5G millimeter wave communication systems. In Proceedings of the 2022 International Conference of Advanced Technology in Electronic and Electrical Engineering (ICATEEE), M'sila, Algeria, 26–27 November 2022; pp. 1–6. [CrossRef]
12. Perez-Galacho, D.; Sartiano, D.; Sales, S. Analog Radio over Fiber Links for Future 5G Radio Access Networks. In Proceedings of the 2019 21st International Conference on Transparent Optical Networks (ICTON), Angers, France, 9–13 July 2019; pp. 1–4. [CrossRef]
13. Delmade, A.; Vargas, C.; Kearney, A.; Nellen, S.; Kohlhaas, R.B.; Schell, M.; Coffey, D.; Smyth, F.; Barry, L.P. Expanded Gain-Switched Comb Source for 180–260 GHz Sub-THz Analog Radio-over-Fiber 6G Wireless System. In Proceedings of the 2024 Optical Fiber Communications Conference and Exhibition (OFC), San Diego, CA, USA, 24–28 March 2024; pp. 1–3.
14. de Souza Lopes, C.H.; Saia Lima, E.; Sodré Junior, A.C. RoF/FSO-based Fronthaul for 5G Systems and Beyond. In Proceedings of the 2021 SBMO/IEEE MTT-S International Microwave and Optoelectronics Conference (IMOC), Fortaleza, Brazil, 24–27 October 2021; pp. 1–3. [CrossRef]
15. Nguyen, D.N.; Bohata, J.; Komanec, M.; Zvanovec, S.; Ortega, B.; Ghassemlooy, Z. Optical Hybrid Fiber/Free-Space and 25 GHz Wireless Transmission Using LTE M-QAM Signals. In Proceedings of the 2019 22nd International Symposium on Wireless Personal Multimedia Communications (WPMC), Lisbon, Portugal, 24–27 November 2019; pp. 1–6. [CrossRef]
16. Azizpour, R.; Zakeri, H.; Moradi, G.; Alibakhshikenari, M.; Falcone, F.; Liu, B.; Dendini, T.A.; Park, I.; Koziel, S.; Limiti, E. Multi-Channel Radio-Over-Fiber Communication Systems Through Modulation Instability Phenomenon. *IEEE Photonics J.* **2024**, *16*, 7201813. [CrossRef]
17. Jia, Z.; Yu, J.; Chang, G.K. A Full-Duplex Radio-over-Fiber System Based on Optical Carrier Suppression and Reuse. *IEEE Photonics Technol. Lett.* **2006**, *18*, 1726–1728. [CrossRef]
18. Yang, L.; Giannakis, G. Ultra-wideband communications: An idea whose time has come. *IEEE Signal Process. Mag.* **2004**, *21*, 26–54. [CrossRef]
19. Al Zaman, A.; Islam, N. Modulation Schemes and Pulse Shaping in Ultra-Wideband. In Proceedings of the IEEE SoutheastCon 2008, Huntsville, AL, USA, 3–6 April 2008; pp. 142–146. [CrossRef]
20. Huo, X.; Xiang, M.; Zhou, G.; Li, J.; Li, J.; Qin, Y.; Fu, S. C-Band 200 Gbit/s/$\lambda$ PS-PAM-8 Transmission Over 2-km SSMF for Optical Interconnections. *IEEE Photonics J.* **2024**, *16*, 7200807. [CrossRef]
21. Pan, S.; Yao, J. UWB-Over-Fiber Communications: Modulation and Transmission. *J. Light. Technol.* **2010**, *28*, 2445–2455. [CrossRef]
22. Pan, S.; Yao, J. Performance evaluation of UWB signal transmission over optical fiber. *IEEE J. Sel. Areas Commun.* **2010**, *28*, 889–900. [CrossRef]
23. Abraha, S.T.; Okonkwo, C.; Yang, H.; Visani, D.; Shi, Y.; Jung, H.D.; Tangdiongga, E.; Koonen, T. Performance Evaluation of IR-UWB in Short-Range Fiber Communication Using Linear Combination of Monocycles. *J. Light. Technol.* **2011**, *29*, 1143–1151. [CrossRef]
24. Kaszubowska-Anandarajah, A.; Perry, P.; Barry, L.P.; Shams, H. An IR-UWB Photonic Distribution System. *IEEE Photonics Technol. Lett.* **2008**, *20*, 1884–1886. [CrossRef]
25. Fujiwara, Y. Self-Synchronizing Pulse Position Modulation With Error Tolerance. *IEEE Trans. Inf. Theory* **2013**, *59*, 5352–5362. [CrossRef]
26. Mahdiraji, G.A.; Zahedi, E. Comparison of Selected Digital Modulation Schemes (OOK, PPM and DPIM) for Wireless Optical Communications. In Proceedings of the 2006 4th Student Conference on Research and Development, Shah Alam, Malaysia, 27–28 June 2006; pp. 5–10. [CrossRef]
27. Li, L.; Townsend, J.K. M-Ary PPM for Transmitted Reference Ultra-Wideband Communications. *IEEE Trans. Commun.* **2010**, *58*, 1912–1917. [CrossRef]
28. Luo, X.; Giannakis, G. Achievable Rates of Transmitted-Reference Ultra-Wideband Radio with PPM. *IEEE Trans. Commun.* **2006**, *54*, 1536–1541. [CrossRef]
29. Aliaberi, A.; Sofotasios, P.C.; Muhaidat, S. Modulation Schemes for Visible Light Communications. In Proceedings of the 2019 International Conference on Advanced Communication Technologies and Networking (CommNet), Rabat, Morocco, 12–14 April 2019; pp. 1–10. [CrossRef]
30. Dahri, F.A.; Ali, S.; Jawaid, M.M. A Review of Modulation Schemes for Visible Light Communication. *IJCSNS Int. J. Comput. Sci. Netw. Secur.* **2018**, *18*, 117–125.
31. Mietzner, J.; Lampe, L. Nested PPM for Visible Light Communication with Heterogeneous Optical Receivers. *IEEE Photonics J.* **2024**, *16*, 7302112. [CrossRef]
32. Alabd, M.B.; Nuss, B.; de Oliveira, L.G.; Diewald, A.; Li, Y.; Zwick, T. Modified Pulse Position Modulation for Joint Radar Communication Based on Chirp Sequence. *IEEE Microw. Wirel. Compon. Lett.* **2022**, *32*, 1247–1250. [CrossRef]
33. Guelman, M.; Kogan, A.; Kazarian, A.; Livne, A.; Orenstein, M.; Michalik, H. Acquisition and Pointing Control for Inter-Satellite Laser Communications. *IEEE Trans. Aerosp. Electron. Syst.* **2004**, *40*, 1239–1248. [CrossRef]

34. Colson, S.; Hoff, H. Ultra-Wideband Technology for Defence Applications. In Proceedings of the 2005 IEEE International Conference on Ultra-Wideband, Zurich, Switzerland, 5–8 September 2005; pp. 615–620. [CrossRef]
35. Eventech. Key Products. Available online: https://eventechsite.com/products/ (accessed on 27 March 2025).
36. Selis, O.; Migla, S.; Sics, P.E.; Zeltins, M.; Spolitis, S.; Aboltins, A. Demonstration of 50 ps Per-Position Differential Pulse Position Modulation Data Transmission. In Proceedings of the 2023 IEEE 10th Jubilee Workshop on Advances in Information, Electronic and Electrical Engineering (AIEEE), Vilnius, Lithuania, 27–29 April 2023; pp. 1–4. [CrossRef]
37. Sics, P.E.; Tihomorskis, N.; Migla, S.; Ratners, J.; Kurtenoks, V.; Aboltins, A. Implementation of Reconfigurable 149 Mbps TDC-Based PPM Transceiver. In Proceedings of the 2024 Joint European Conference on Networks and Communications & 6G Summit (EuCNC/6G Summit), Antwerp, Belgium, 3–6 June 2024; pp. 706–710. [CrossRef]
38. Eventech. Eventech Space Ready Timing Module. Available online: https://eventechsite.com/wp-content/uploads/2024/08/Eventech-Space-Ready-Timing-Module-2024.pdf (accessed on 27 March 2025).
39. European Space Agency. Hera's Asteroid Deck and instruments. Available online: https://www.esa.int/Space_Safety/Hera/Hera_s_Asteroid_Deck_and_instruments (accessed on 27 March 2025).
40. Aboltins, A.; Solovjova, T.; Semenako, J.; Kusnins, R.; Migla, S.; Sics, P.E.; Selis, O.; Tihomorskis, N.; Prigunovs, D.; Ostrovskis, A.; et al. Passive Electrical and Optical Methods of Ultra-Short Pulse Expansion for Event Timer-Based TDC in PPM Receiver. *Electronics* **2023**, *12*, 4634. [CrossRef]
41. Liu, Y.; Wang, C. The Research on Transmission Effect of Different Pulse Shapes in MPPM. In Proceedings of the 2022 14th International Conference on Computer Research and Development (ICCRD), Shenzhen, China, 7–9 January 2022; pp. 373–377. [CrossRef]
42. Cho, S.; Kwak, J. Performance Comparison of M-Ary PPM Ultra-Wideband Multiple Access System Using an Intelligent Pulse Shaping Techniques. In *International Conference on Knowledge-Based and Intelligent Information and Engineering Systems*; Springer: Berlin/Heidelberg, Germany, 2005; pp. 1094–1103.


**Disclaimer/Publisher's Note:** The statements, opinions and data contained in all publications are solely those of the individual author(s) and contributor(s) and not of MDPI and/or the editor(s). MDPI and/or the editor(s) disclaim responsibility for any injury to people or property resulting from any ideas, methods, instructions or products referred to in the content.

**Annex 7**

Migla, S., Tihomorskis, N., Rubuls, K., Cirjulina, D., Murans, I., Kurtenoks, V., Braunfelds, J., Spolitis, S., Ozolins, O., Vovchuk, D., Salgals, T., Ginzburg, P., Bobrovs, V., and Aboltins, A. "Demonstration of Integrated Sensing and Communications in an ARoF-Based Radar System Utilizing Pulse Position Modulation." *IEEE Access* 14 (2026), pp. 76251–76264. DOI: 10.1109/ACCESS.2026.3693952

IEEE Access
Multidisciplinary ⋮ Rapid Review ⋮ Open Access Journal

Received 30 April 2026, accepted 10 May 2026, date of publication 15 May 2026, date of current version 21 May 2026.

*Digital Object Identifier 10.1109/ACCESS.2026.3693952*

RESEARCH ARTICLE

# Demonstration of Integrated Sensing and Communications in an ARoF-Based Radar System Utilizing Pulse Position Modulation

**SANDIS MIGLA[1], (Graduate Student Member, IEEE), NIKOLAJS TIHOMORSKIS[1], (Graduate Student Member, IEEE), KRISTAPS RUBULS[1], DARJA CIRJULINA[1], (Graduate Student Member, IEEE), INTS MURANS[1], VIKTORS KURTENOKS[2], JANIS BRAUNFELDS[1,3], SANDIS SPOLITIS[1], OSKARS OZOLINS[1,4], (Senior Member, IEEE), DMYTRO VOVCHUK[1,5], (Member, IEEE), TOMS SALGALS[1], PAVEL GINZBURG[5], (Member, IEEE), VJACESLAVS BOBROVS[1], (Member, IEEE), AND ARTURS ABOLTINS[1], (Senior Member, IEEE)**

[1]Institute of Photonics, Electronics and Telecommunications, Riga Technical University, 1048 Riga, Latvia
[2]Eventech Ltd., 1007 Riga, Latvia
[3]Fiber Optical Sensor Research Group (RTU FiberSens), Riga Technical University, 1048 Riga, Latvia
[4]RISE Research Institutes of Sweden, Kista, 16440 Stockholm, Sweden
[5]School of Electrical Engineering, Tel Aviv University, Tel Aviv-Yafo 6997801, Israel

Corresponding author: Sandis Migla (sandis.migla@rtu.lv)

This work was supported by European Union (EU) Recovery and Resilience Facility within the Project No 5.2.1.1.i.0/2/24/I/CFLA/003 under Academic Career Doctoral Grant 1008.

**ABSTRACT** Integrated sensing and communications (ISAC) is a key enabling technology for 6G networks, as it unifies radar sensing and data transmission within a shared infrastructure. Analog radio-over-fiber (ARoF) has emerged as a crucial technology for extending radar coverage and enabling distributed radar sensing. By incorporating pulse position modulation (PPM), it is possible to simultaneously measure the target's range and transmit data, thereby increasing the energy efficiency of such systems. In this research, we present a novel analog radio-over-fiber (ARoF)-based integrated sensing and communications (ISAC)-capable pulse radar system that features a custom-built PPM modulator employing a digital-to-time converter, and a high-accuracy time tagger as the demodulator, allowing for pulse time of arrival measurements with an root mean square accuracy up to 1.5 ps. The experimental results show a 5 Mbit/s data transmission along with a bit error ratio less than $5.86 \times 10^{-7}$ at a 95% confidence level, using a PPM slot duration of 750 ps in an optical system featuring more than 40 km of single-mode optical fiber and a simultaneous range measurement with error less than 0.86 cm. In addition to ISAC exploration, the impact of fiber-induced chromatic dispersion on the PPM signal is studied, and the system is validated in an outdoor environment with a moving target.

**INDEX TERMS** Pulse position modulation (PPM), integrated sensing and communications (ISAC), analog radio-over-fiber (ARoF), pulse radar, time tagger.

## I. INTRODUCTION

Integrated sensing and communications (ISAC) systems present a wide range of perspectives in the pursuit of launching 6G networks [1], [2] which promise to focus on more than just a communication-only standpoint, but

The associate editor coordinating the review of this manuscript and approving it for publication was Yogendra Kumar Prajapati.

© 2026 The Authors. This work is licensed under a Creative Commons Attribution 4.0 License.
For more information, see https://creativecommons.org/licenses/by/4.0/

to utilize existing infrastructure for novel applications, e.g., vehicle-to-everything (V2X) communication [3], internet of things [4], and unmanned aerial vehicle surveillance [5]. ISAC has proven itself as a valuable method for enhancing energy and spectrum efficiency in impulse radio ultra-wideband systems and is used for range and Doppler shift sensing, as well as data transmission [6], [7]. The study [8] shows the feasibility of pulse-based ISAC systems with a symbol duration of 100 ns, a bit rate of 100 kbit/s, and sensing accuracies of around 10 cm.

Pulse position modulation (PPM), in which data is encoded in the time intervals between short pulses, is one of the modulation formats used in ISAC applications, such as simultaneous communication and LiDAR [9], [10], or radar sensing based on chirp sequences [11], with its key advantages being high energy efficiency and resilience [12]. The study [13] shows a 45.2% energy efficiency improvement compared to on-off keying. The detector employed in [11] relies on an analog-to-digital converter (ADC) with inherent power efficiency and performance bottlenecks. The study [14] presents a field-programmable gate array (FPGA)-based PPM modulator, one of its advantages being low power consumption achieved by asynchronous design. In study [15], a free-space optical (FSO) communication system employing PPM is presented, and achieved bit error ratio (BER) values as low as $10^{-4}$ at a distance of 10 m. PPM is also used in space communications [16], [17], [18], and study [18] shows the implementation of a PPM modem capable of using a slot width as narrow as 0.5 ns for deep space communication experiment. Widely used FPGAs for PPM signal generation are limited in available PPM slot width and accuracy, whereas ADCs used for PPM signal sampling often require high sampling rates and suffer from limited accuracy when dealing with slot durations in the picosecond range. A prospective development for pulse detection are time-to-digital converters (TDCs), employed in event timers, also known as time taggers, which are widely used in time measurement applications where precise time measurements, and therefore distance measurements, are crucial, particularly for time-of-flight (ToF) measurements [19], such as satellite laser ranging (SLR) [20], [21], LiDAR, and ISAC applications.

Achieving such tight sub-nanosecond timing tolerances for distributed sensing is challenging. To address this issue, fiber-optic technologies provide low-jitter, long-distance physical links with an established functional model: radio-over-fiber (RoF) [22], [23]. RoF has gained considerable popularity as optical fiber links and passive optical network (PON) infrastructure are deployed to consolidate these technologies in centralized radio access network topologies. Additionally, RoF has already proven itself to be a valuable addition to interconnected radar architectures [24], enabling simplified radar data transmission [25], [26], [27]. The study [25] presents a 90 GHz RoF-based radar system for railway obstacle detection with an accuracy of 500 mm for a human target 200 m from the radar node. Radio-over-fiber (RoF)-based radars for airport foreign object debris detection are presented in [26] and [27], achieving resolutions of less than 8 cm but they also require antennas with gain above 40 dBi. A sub-branch of RoF, ARoF, further simplifies the system by sending an analog signal directly over an optical fiber without analog-to-digital conversion. This approach preserves the signal's continuous form and analog nature, which can be beneficial for subsequent signal processing and synchronization, especially in PPM-based systems, which require high timing accuracy.

Despite the mentioned technological advances, their integration to overcome their individual limitations has not been extensively studied. The main novelty of the given research is the first implementation of an ARoF-based ISAC-capable radar system utilizing PPM, with a custom-built modulator and a high-precision time tagger, the Eventech Stream Time Tagger (ESTT) 7 Series [28], enabling sub-nanosecond PPM slot durations and transmission over a long single-mode optical fiber (SMF) span, significantly expanding our previous work [29]. Using high-precision range data, the target velocity was calculated for a moving target in a field environment.

Compared to commonly used radar sensing solutions, such as those used in autonomous driving, aerial and ground object monitoring, and weather monitoring [30], [31], [32], [33], namely frequency modulated continuous wave (FMCW) and pulse-Doppler radars, both of which offer range and velocity measurement capabilities, the proposed architecture addresses several limitations. Frequency modulated continuous wave (FMCW) radars are usually quite power-hungry due to continuous transmission and reception and require complex remote antenna units (RAUs); meanwhile, pulse-Doppler radars encounter limitations in performing precise absolute range measurements and in detecting slow-moving targets as they rely on Doppler shifts [34], [35]. The proposed architecture achieves precise range measurements by directly measuring the pulse time of arrival (ToA) even for low-velocity or stationary targets. When combined with ARoF, the PPM waveform used mitigates the phase noise accumulation issue in optical FMCW systems [36], [37], [38].

In this work, a 6.6 GHz pulse radar is studied due to the extensive super-high-frequency (SHF) infrastructure [39], [40], which can be easily repurposed for ISAC systems. This study investigates the impact of long SMF spans on the quality of the PPM signal, measured BER, and range accuracy. The impact of fiber-induced chromatic dispersion compensation in the optical subsystem is evaluated, given that PON systems are intrinsically designed and assessed with dispersion effects accounted for.

This paper is organized as follows: Section II is devoted to the PPM format, as well as implemented digital-to-time converter (DTC) and TDC technologies, Section III describes detailed experimental hardware setup, parameters and configurations, meanwhile Section IV provides the data transmission and range measurement results in indoor and

outdoor environments. Section V provides the conclusion of the presented research.

## II. SYSTEM ARCHITECTURE

The conceptual system architecture is shown in Fig. 1. It consists of the Transmitter, the Transmission network, and the Receiver. The modulation format is described in detail in Subsection II-A. The custom-designed DTC-based device as PPM modulator is described in Subsection II-B. The transmission network consists of an optical/radio frequency (RF) link, and the impact of this link on the transmitted PPM signal is systematically analyzed. Subsection II-C is devoted to ESTT 7 Series as PPM receiver.

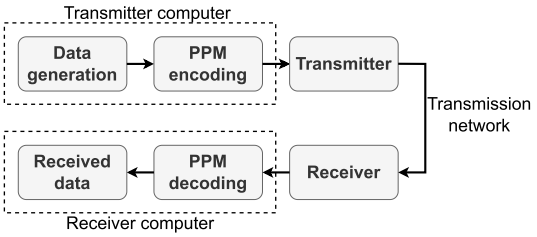



**FIGURE 1.** Conceptual diagram of the PPM data transmission system.

### A. MODULATION FORMAT

In this work, PPM following the Consultative Committee for Space Data Systems (CCSDS) recommended standard 142.0-B-1 "Optical communications coding and synchronization," [41] was used. An example signal structure is shown in Fig. 2. The sequence of pulses, called a PPM transfer frame, consists of a start pulse, with respect to which all time tags are calculated, and $N$ PPM subframes that contain the data pulses. In a PPM symbol, which is part of the subframe, the pulse can be located in one of $M$ time slots with the slot duration $\Delta$. The number of time slots $M$ is determined by how many bits are encoded in a single PPM symbol $M = 2^b$, where $b$ is the number of bits per symbol. The total symbol duration is $M \cdot \Delta$. Together with the guard slot duration $T_g$, the symbol makes up the subframe with the duration [12], [42]:

$$T_{sf} = M \cdot \Delta + T_g \,, \tag{1}$$

where $T_{sf}$ is the subframe duration, $M$ is modulation order, $\Delta$ is the slot duration and $T_g$ is the guard slot duration.

The time tags for each pulse in the sequence [41] with respect to the PPM transfer frame start pulse can be calculated as:

$$t_k = k \cdot T_{sf} + K \cdot \Delta \,, \tag{2}$$

where $t_k$ is the time tag with the index $k$ (1 to $N$) and $K$ is the encoded decimal data (0 to $M-1$) in the subframe.

It should be noted that in PPM, the pulse duration $\tau$ carries no information and can be made as short as practically possible to achieve the maximum energy efficiency in the transmission channel.

For this modulation format, the maximum achievable continuous data transfer speed can be calculated by equation (3), derived from [43]:

$$R_b = \frac{N \cdot \log_2 M}{(N+1) \cdot T_{sf} + T_{break}} \,, \tag{3}$$

where $R_b$ is the bit rate, $M$ is modulation order, $N$ is the number of symbols in the PPM transfer frame, and $T_{break}$ is the time between subsequent PPM transfer frames.

In PPM data transmission, bit errors may arise from jitter in the transmission network, leading to a pulse being detected in a time slot corresponding to a different value. In our previous research [42], [44], it was shown that the deviations from the expected ToA of the pulse to the actual ToA are distributed approximately normally.

Additionally, clock drift in the transmitter and receiver can cause the time slots across the entire PPM transfer frame to contract or expand slightly, which, over short PPM transfer frames, appears as a constant offset between the expected and actual ToAs, and, over longer transfer frames, as a constantly increasing or decreasing offset. This effect can be mitigated by using a common reference clock, which may not be feasible in long-distance transmission networks; therefore, an alternative solution is required.

The jitter's impact on BER can be reduced using Gray coding. In this case, if a pulse shifts to an adjacent time slot, only a single bit error occurs in the received PPM symbol. The probability $P(\sigma,\ \mu)$ that a pulse will land in a neighboring time slot can be calculated, assuming that the PPM transfer frame is relatively short compared to the clock drift, and the jitter present in the system is distributed normally [42]:

$$P(\sigma, \mu) = 1 - \int_{-\frac{1}{2}\Delta}^{\frac{1}{2}\Delta} \frac{1}{\sigma\sqrt{2\pi}} e^{-\frac{1}{2}(\frac{t-\mu}{\sigma})^2} dt \,, \tag{4}$$

where $\Delta$ is the slot duration, $\sigma$ is the jitter standard deviation, $\mu$ is the jitter mean and $t$ is the pulse deviation from the expected position.

### B. DIGITAL-TO-TIME CONVERSION

The PPM signal, with the structure shown in Fig. 2, was generated using a custom PPM modulator incorporating a DTC board designed based on our previous research [44], [45], that utilized the same core component – digital delay line (DDL). The DTC is a device that can output electrical pulses of predetermined duration at specified times. The conceptual diagram of the DTC part of the board is shown in Fig. 3. The device is compliant with CCSDS recommended standard 141.0-B-1 "Optical communications physical layer" [46].

The core of the DTC is the MC100EP196B programmable DDL with the programmable delay range 0 – 10.24 ns in 10 ps increments, and it features a ±11 ps linearity across the whole delay range. The purpose of the DDL is to delay a pulse at its

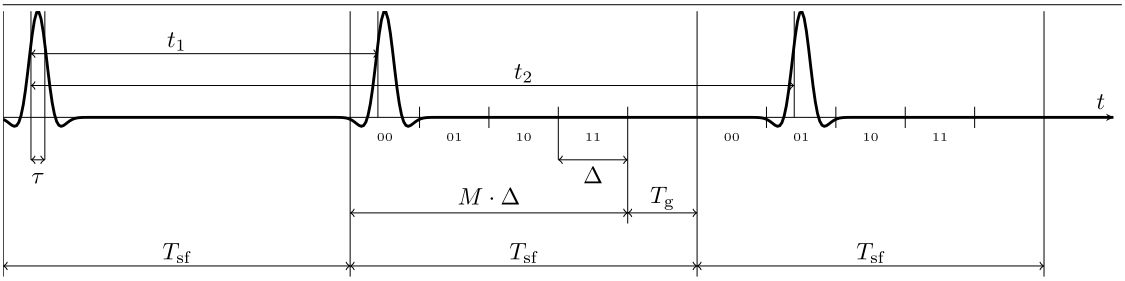



**FIGURE 2.** Structure of a PPM signal with $M = 4$, where the transfer frame start pulse and two sub-frames are shown - with the pulse in position "0" and in position "1".

input by a specified time interval, set via the 10-bit-wide input bus, allowing 1024 unique delay values.

The DDL receives the clock signal from a highly stable D flip-flop. The flip-flop is clocked by a 100 MHz signal generated by a very low-jitter phase locked loop (PLL), while its "D" input is driven by the FPGA. The clock phase is slightly delayed relative to the FPGA reference clock of the same frequency. This technique minimizes the contribution of FPGA output jitter.

For precise control of the pulse duration, the signal at the output of the DDL is split using a fanout buffer, one output of which ("Q1") is directly connected to the "CLK" input of a D flip-flop, and the other output ("Q2") is passed through a second DDL of the same model and then connected to the reset ("R") input of the flip-flop as shown in Fig. 3. This arrangement allows for adjustment of the pulse full width at half maximum (FWHM) in the range of 2.4 – 12.6 ns, as there is a 2.4 ns inherent propagation delay in the DDL even with "0" delay set on the input bus.

The DTC is controlled by the Altera Cyclone IV FPGA, which is connected to the personal computer (PC) via a USB 3.0 interface. A custom software, built in C++ and running on the PC, is responsible for data preparation and transfer to the FPGA. When the software initiates a transmission, an entire PPM transfer frame is sent to the FPGA and stored in memory. Each PPM symbol in the transfer frame is stored at a separate memory address as a 24-bit binary number, where 10 bits specify the pulse delay from the start of the current clock cycle and 14 bits specify the number of clock cycles until the next pulse in the sequence. At the start of the PPM transfer frame, a start pulse is generated, from which the clock cycles are counted. At this time, the FPGA also already prepares and outputs the 10-bit delay value for the next pulse in the sequence. When the FPGA receives a set number of clock cycles (14 bits in the memory address), it sets the "D" input of the flip-flop for one clock cycle, thereby generating a single pulse which is delayed by the value already set in the DDL. Then the FPGA moves to the next memory address, where the data for the next pulse in the sequence is stored, and the same process repeats until the end of the PPM transfer frame. The pulse duration

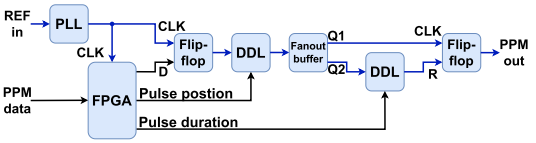



**FIGURE 3.** Conceptual diagram of the DTC implementation.

can be set separately via a 10-bit register that stores the pulse duration value.

Since the operating clock frequency is 100 MHz, corresponding to the clock period 10 ns, and the programmable delay range of the DDL is 0 – 10.24 ns, all possible time slots can be covered with the step of 10 ps by setting the DDL delay value and counting the clock cycles.

As the pulse duration can be programmatically controlled, the given modulator enables the use of advanced ultra-wideband (UWB) modulation schemes, such as the pulse-width and pulse-position modulation (PWPM).

The device can transmit a 16000-symbol-long PPM transfer frame at a time, with about 20 ms between PPM transfer frames, a software limitation that can be further improved to significantly increase the continuous data transfer rate. For example, with $M = 16$ and $\Delta = 100$ ps, the modulator can achieve a data transfer speed of 2 Gbit/s if the guard slot duration and break are nearly eliminated.

Initial testing was performed by connecting the modulator directly to the ESTT via a coaxial cable, in an electrical back-to-back (B2B) configuration. The jitter distribution and pulse position deviation from expected values over a 16000-symbol-long PPM transfer frame are presented in Fig. 4. The red line in Fig. 4a represents the distribution of jitter. As can be observed, the pulse position jitter is approximately normally distributed, with a root mean square (RMS) jitter of 7.65 ps.

### C. TIME-TO-DIGITAL CONVERSION

The PPM signal was demodulated using the ESTT, which was connected to the PC, enabling real-time data transfer. The ESTT serves as the TDC—a device that converts the

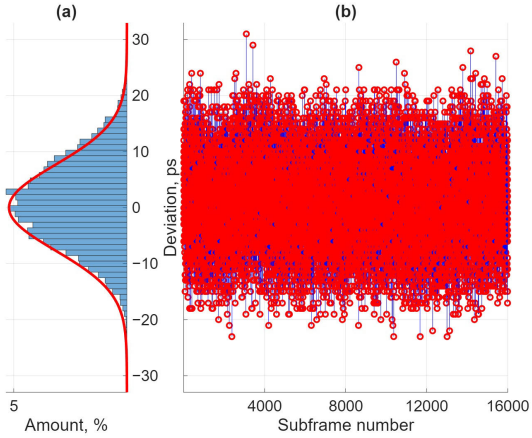



**FIGURE 4.** Jitter distribution (a), where the red line denotes normal distribution, and pulse deviation from the expected positions (b) over a 16000-symbol-long PPM transfer frame.

measured ToA of the incoming pulse rising edges to absolute time tags. Eventech Stream Time Tagger (ESTT) features a single-shot RMS accuracy of 1.5 ps and has a dead time of 40 ns, which was the key limiting factor when selecting the PPM parameters, especially the subframe duration $T_{sf}$. The dead time of TDC designates the time interval after a pulse is captured, during which no new incoming pulses can be registered. Dead time is one of the most significant limitations, as it limits the maximum achievable bit rate.

The ESTT features two inputs, thereby enabling ToF and range calculations for ISAC. The event is triggered by a programmatically set voltage threshold value in the range of −2 V to 3 V with a step of 1.2 mV. Different threshold values can be set for the two inputs, allowing the use of signals with varying amplitudes. As the ESTT triggers on the rising edge of the pulse, it is critical to have an edge with as short a rise time as possible, but the pulse duration is not crucial, as long as it is above the minimum required duration of 150 ps.

The PPM demodulation and range data processing were performed in real-time on the PC using custom C++ software. The time tags from the two channels were saved as separate files on the PC, allowing for later processing and range estimation. Additionally, the decoded data was saved, enabling BER calculation.

## III. EXPERIMENTAL SETUP

### A. HARDWARE SETUP AND DATA PROCESSING

The experimental system consists of the central office (CO), where the optical carrier and the RF signals are generated and detected, and the RAU, which radiates and receives the RF signal. The conceptual block diagram of the ARoF-based pulse radar setup featuring CO and RAU is shown in Fig. 5. The photo illustrations of the experimental setup are shown in Fig. 6.

The transmitted pseudorandom binary sequence (PRBS) was generated in MATLAB software, using the 623-order Mersenne Twister pseudo-random number generator. In total, $5.12 \times 10^6$ bits were generated, saved as 40 data files, each containing 16000 PPM symbols (one symbol being 8 bits long, therefore the modulation order $M = 256$), and loaded into the modulator control software on the PC.

In the CO, the baseband PPM waveform with an amplitude of 1 V was generated using the custom modulator described in Subsection II-B. The PPM waveform was mixed with the 6.6 GHz RF carrier, using the Mini-Circuits ZX05-153MH-S+ mixer with an operating frequency range 3.2 GHz to 15 GHz, 6.5 dB typical conversion loss, and 36 dB typical LO-RF port isolation. The carrier was generated by the Anritsu MG3690C signal generator, which served as the local oscillator (LO). The up-converted signal was then filtered using the Mini-Circuits VHF-6010+ high-pass filter (HPF) with the cutoff frequency of 6.3 GHz to remove any remaining baseband components. The filtered signal was amplified using the Mini-Circuits ZX60-06183LN+ low-noise amplifier (LNA) with 18 dB gain, a typical noise figure of 2.2 dB, and ±1.3 dB gain flatness. The amplified signal was fed into the RF input port of the Mach-Zehnder modulator (MZM). An Exail Technologies MX-LN-40 MZM with a 40 GHz bandwidth, 20 dB extinction ratio, and 3.5 dB insertion loss was used to modulate the optical carrier with the up-converted PPM waveform. The optical carrier was generated using an ID Photonics Cobrite DX-4 continuous wave (CW) laser, which has a line width of 25 kHz. The optical carrier wavelength was 1550 nm and the laser's optical output power was +12 dBm. The optical carrier was split by an optical splitter (ratio: 50/50) to use the same laser source for both the transmitter and receiver links, and then passed through polarization controllers. The optical output of the MZM was routed to an EXFO FVA-3150 variable optical attenuator (VOA), which was used to precisely control the optical power incident on the photodetector (PD) in the RAU, maintaining a consistent level of −15 dBm across all connection scenarios. This optical power level enabled the PD to receive the signal without saturation or amplitude clipping. The optical signal was passed to the RAU through a 400 m long SMF span with the option to add an additional 20 km of SMF.

In the RAU, the optical signal from the CO was split by an optical splitter (ratio: 90/10), with 10% of the output sent to the optical power meter (OPM). The signal was converted to the electrical domain using the Conquer KG-PT-10G-SM-FA InGaAs/InP planar structure PIN PD which features 10 GHz 3-dB bandwidth, −11 dBm saturation, 10 nA dark current, and responsiveness of 0.9 A/W at 1550 nm. The AC-coupled electrical output of the PD was amplified using the SHF 810 broadband RF amplifier with 38 GHz bandwidth, 29 dB gain, 6 dB noise figure, and ±1 dB gain ripple. The amplified signal was then radiated by the Pasternack WR-159 horn antenna with 20 dBi gain and frequency range of 4.9 GHz to 7.05 GHz.

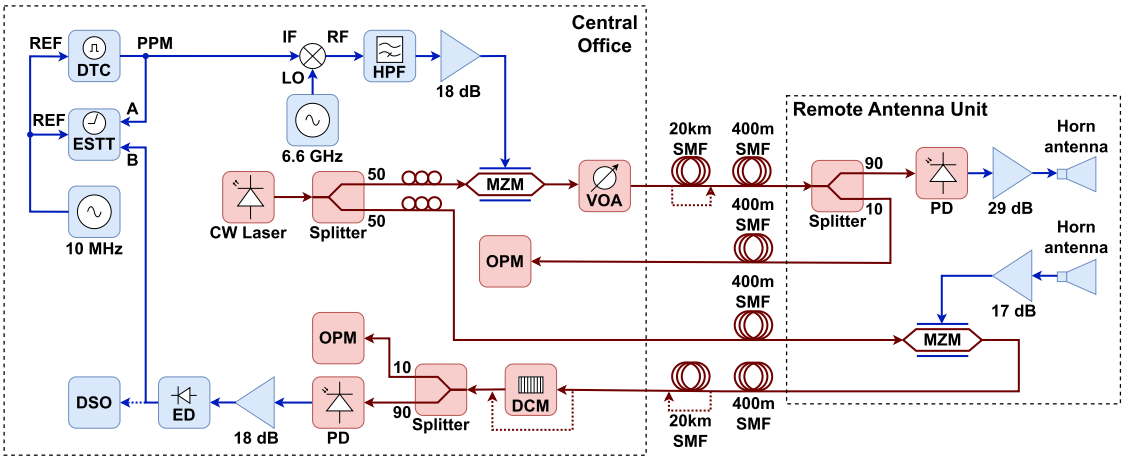



**FIGURE 5.** Block diagram of the experiment setup where the electrical part is shaded in blue, and the optical part in red.

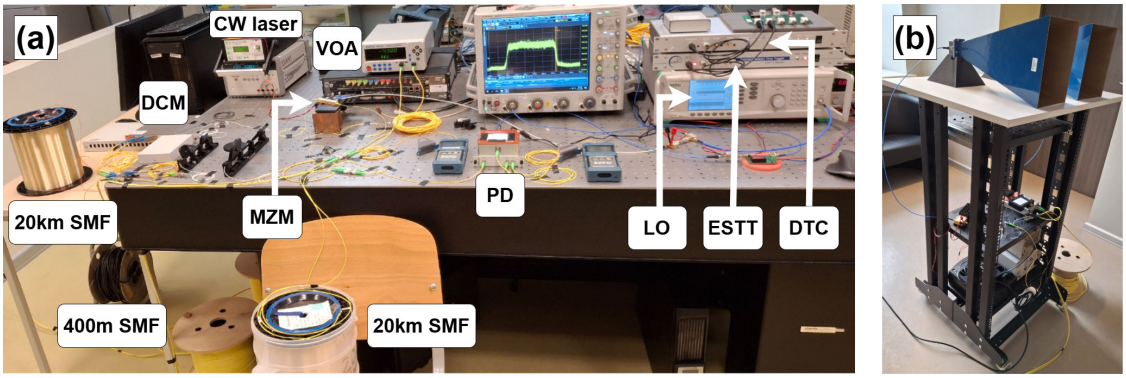



**FIGURE 6.** Photo illustrations of the experimental ARoF-based pulse radar setup, (a) central office, (b) remote antenna unit.

On the receiver side, the same type of antenna as in the transmitter was used. The antennas were located next to each other, and the measured isolation between the antennas was 40 dB. The received signal was amplified using the SHF 100 BP broadband amplifier, which has a 25 GHz bandwidth and 17 dB gain. The amplified signal was fed into the RF input of another MZM, which receives the optical carrier from the CO. The optical output of the MZM was fed into a TeraXion Clear Spectrum TDCMX tunable dispersion compensation module (DCM), which could be bypassed and replaced with a 3 dB optical attenuator to preserve the same −15 dBm optical power at the PD. The signal propagated through a 400 m SMF span, with the option to add 20 km of SMF. The total dispersion for both 20 km SMF (total 40 km) spools was measured to be 681 ps/nm at 1550 nm. The optical signal was subsequently delivered to the PD, and the resulting electrical signal was amplified and down-converted using a custom-built envelope detector (ED). Waveform monitoring and capture were performed with a Keysight DSOZ334A digital storage oscilloscope (DSO), which offers a 33 GHz bandwidth and 80 GSa/s sampling rate.

The received and down-converted signal was sent to the "B" input of the ESTT described in Subsection II-C, whereas the "A" input of the ESTT was connected to the modulator to record the time tags of the transmitted pulses, which are necessary for range estimation. Both the custom-built modulator and the ESTT were connected to the same ultra-stable 10 MHz reference signal generator with stability of less than ±0.5 ppb, to exclude possible clock drift caused errors, as the internal clocks of the two devices do not share exactly the same clock frequency. It slightly varies over time, which is highly problematic when working with slot durations in the sub-nanosecond range.

### B. EXPERIMENTAL PARAMETERS

The subframe duration $T_{sf} = 300$ ns was chosen as such to make sure that at every tested slot duration $\Delta$, pulses do not arrive within the dead time window of the ESTT. Although the subframe duration can be adjusted to maximize bit rate, to maintain consistency, it was kept constant.

The slot duration range of 10—1000 ps was chosen, as $\Delta = 10$ ps is the shortest possible slot duration that can be generated by the custom-built modulator, due to the limitation of the used DDL integrated circuit (IC). The upper limit of slot duration equal to 1000 ps was chosen as it represents the lower end of the typical slot durations used in real-world state-of-the-art PPM data transmission systems, such as those used by National Aeronautics and Space Administration (NASA) and European Space Agency (ESA) [17], [18], [47]. The presented system can achieve an undetectable low error rate at this slot duration.

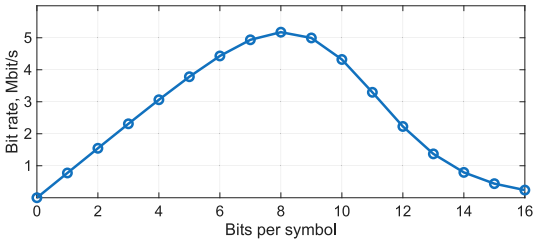



**FIGURE 7.** Calculated bit rate dependent on the number of bits per PPM symbol.

The PPM transfer frame size was set to the maximum allowable by the DTC, meaning that $128 \times 10^3$ bits were transmitted in a single transfer frame.

To find the optimal PPM order in terms of bit rate, equation (3) was used with the known DTC parameters. The calculated bit rate as a function of the bits per PPM symbol is shown in Fig. 7. As can be observed, the optimal number of bits per symbol is 8; therefore, the modulation order $M = 256$.

The maximum bit rate for the given set of constraints ($T_{sf} = 300$ ns, $T_{break} = 20$ ms, $N = 16000$) is around 5 Mbit/s, and, as such, the bit rate is acceptable and close to other practically implemented systems [48]. The main experimental parameters are summarized in Table 1.

### C. EXPERIMENTAL CONFIGURATIONS

#### 1) INDOOR MEASUREMENTS

The indoor measurements were conducted with a static metallic reflector located 4 m from the RAU due to space constraints, as shown in Fig. 8. This distance provides optimal pulse amplitude at the receiver for data transmission and ranging tests.

The data transmission experiments were conducted with and without Gray coding in four system connection configurations:

**TABLE 1.** Summary of the main experimental parameters.

| Parameter | Value |
|---|---|
| Modulation type | PPM |
| Slot duration $\Delta$ | 10 – 1000 ps |
| Modulation order $M$ | 256 |
| Bits per symbol | 8 |
| PPM transfer frame size $N$ | 16000 symbols |
| Subframe duration $T_{sf}$ | 300 ns |
| Number of transfer frames sent | 40 |
| Total number of bits sent | $5.12 \times 10^6$ |
| Pulse FWHM $\tau$ | 2.5 ns |
| RF carrier frequency | 6.6 GHz |
| Distance to the static reflector | 4 m |
| Optical B2B distance | 800 m |
| Total distance with SMF | 40.8 km |
| Optical carrier wavelength | 1550 nm |
| DCM value | −681 ps/nm |

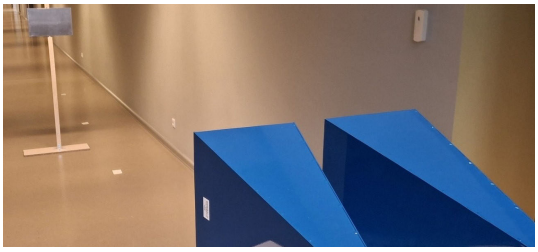


**FIGURE 8.** Test setup with the static reflector and the RAU located indoors.

1) electrical back-to-back (B2B) connection, where the modulator was directly connected to the ESTT via a coaxial cable;
2) optical B2B connection, where the optical transmission network shown in Fig. 5 was connected with only the 800 m (400 m each direction) SMF;
3) optical connection with 40 km SMF, where 20 km spools were added in the optical branches that carry the PPM signal in each direction;
4) optical connection with 40 km SMF and DCM.

The range measurements were conducted using the setup shown in Fig. 8 for all three optical connection scenarios by measuring the ToA of the pulses on both channels of the ESTT and calculating the ToF. The actual ToF in the RF channel can be calculated by subtracting the system propagation delay from the measured time difference. The propagation delay was measured by the ESTT: 4.005752 µs for the optical B2B connection, 202.374635 µs for the connection with 40 km SMF, and 202.418792 µs for the connection with a 40 km SMF with DCM. The average ToF was calculated over each PPM transfer frame to eliminate relatively large range discrepancies that can be present when considering each transmitted and received pulse individually. The distance $d$ was calculated by knowing the propagation velocity, i.e., the speed of light:

$$d = \frac{(t_m - t_0)}{2} \cdot c\,, \tag{5}$$

where $t_m$ is the measured average time difference between the transmitted and received pulses, $t_0$ is the propagation delay in the system, and $c$ is the speed of light.

Importantly, the static propagation delay is also temperature dependent, which is especially noticeable in long SMF links. Since the propagation time through standard (solid-core) SMF optical fiber changes by approximately 40 ps/km/K at 1550 nm [49], [50]. Therefore, the 40 km SMF link configuration can experience a delay drift of approximately 1.6 ns/K (e.g., $t_m - t_0$). From equation (5), this corresponds to an uncompensated apparent range shift or inaccuracy of about 24 cm/K (e.g., $d$). Thus, to maintain sub-centimeter range accuracy, the residual error in the static propagation delay must be kept below approximately 67 ps. In practice, this can be achieved by periodically or continuously recalibrating the static propagation delay using an optical loop-back system. The measured drift can then be subtracted from the subsequent range measurements to maintain sub-centimeter accuracy over time.

While the ESTT offers picosecond-level timing accuracy that enables centimeter-level range accuracy, its ability to resolve multiple targets is limited by the 40 ns dead time, which corresponds to about 6 m separation between detectable targets. If we eliminated the dead time of the ESTT, the range resolution $\Delta R$ is limited by the formula $\Delta R = c \cdot \tau/2$, where $c$ is the speed of light and $\tau$ is the pulse duration.



**FIGURE 9.** Test setup with the RAU located outdoors and the vehicle in the starting position.

#### 2) OUTDOOR MEASUREMENTS

The outdoor experiments, intended as a proof-of-concept validation, were conducted using the setup shown in Fig. 9. The system was configured for the optical B2B connection, in which only 800 m (400 m in each direction) of SMF was used. The target was a passenger vehicle in controlled motion scenarios—accelerating from a stationary position or decelerating towards the RAU.

The target's range can be calculated from time measurements, and its velocity $V$ can be inferred from a series of range measurements:

$$V_n = \frac{d_n - d_{n-1}}{t_n - t_{n-1}}, \tag{6}$$

where $t$ is the average time tag for the PPM transfer frame and $n$ is the index.

As the ESTT produces time tags with absolute values, we can estimate the target's average velocity at that time, corresponding to the middle of the PPM transfer frame, with high accuracy.

## IV. RESULTS

### A. PRELIMINARY TESTING

First, the impact of the pulse duration $\tau$ on the BER was explored, by measuring the BER in system connection configurations 2 to 4 and with pulse durations 2.5 ns, 5 ns, 7.5 ns and 10 ns, at slot duration $\Delta = 250$ ps. The chosen pulse durations represent the lower end of those actually used [51]. The measurements were conducted without Gray coding and the results are shown in Fig. 10, from which we observe that the BER remains almost constant across all tested pulse durations. This is expected, as the pulse duration $\tau$ should not affect the BER, notwithstanding other system factors such as available bandwidth, since the time tagger reacts only on the rising edge of the pulse. The approximate bandwidth of the shortest tested pulse is about 400 MHz, so this pulse duration can be used in further experiments.

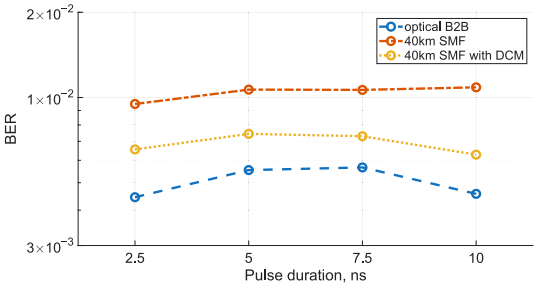



**FIGURE 10.** Measured BER dependent on pulse duration.

Signal waveforms with a pulse duration of $\tau = 2.5$ ns were captured with the DSO for all system connection configurations and are displayed in Fig. 11.

In Figs. 11b–11d we can observe a slight pulse expansion effect, with the FWHM of the pulse being expanded to about 3.1 ns. In all cases, the width of the falling edge was measured to quantify the system's jitter. The falling edge was measured because the jitter is the same for both edges of the pulse, and the DSO was triggered from the rising edge. In Fig. 11a, an edge width of 47 ps can be observed, which matches well with the jitter measurements using the ESTT, as shown in Fig. 4. However, all three optical connection scenarios featured significantly increased jitter. For the optical B2B scenario, the recorded edge width was 227 ps. For the 40 km SMF scenario, the edge width increased to 318 ps due to accumulated positive chromatic dispersion along the fiber. In this case, the resulting group-velocity dispersion caused different spectral components of the signal to propagate at

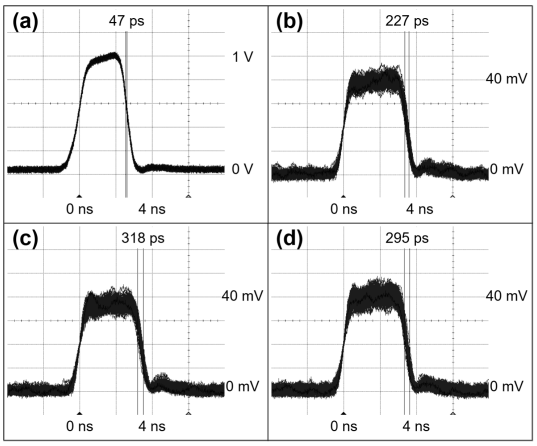



**FIGURE 11.** DSO captured waveforms for (a) electrical B2B connection, (b) optical B2B connection, (c) optical connection with 40 km SMF, (d) optical connection with 40 km SMF and DCM.

different velocities, leading to temporal pulse broadening and reduced edge slope, and thereby increasing the measured jitter due to larger noise susceptibility. Meanwhile, with the introduction of the DCM, the edge width decreased to 295 ps, as the applied negative dispersion only partially compensated the accumulated higher-order dispersion, slightly reducing the temporal spread of the pulse. Although the nominal dispersion values were matched, complete restoration of the original edge width could not be achieved due to residual higher-order dispersion and dispersion slope mismatch between the SMF and DCM.

The observed transition width increase can be explained by the chromatic dispersion effect in a double-sideband intensity modulation / direct detection (IM/DD) ARoF link. Chromatic dispersion is strongly dependent on signal bandwidth, increasing approximately quadratically with increasing bandwidth or data rate. However, under these conditions, the impact of chromatic dispersion remains sufficiently limited to allow signal transmission over optical links exceeding 100 km. Chromatic dispersion introduces deterministic frequency-dependent phase shifts and group-delay differences among the optical carrier and modulation sidebands. After square-law photodetection, this phase distortion is converted into a frequency-dependent electrical magnitude response or dispersion-induced RF power fading. Consequently, the signal components contributing to the pulse transition are delayed and attenuated non-uniformly, which causes temporal pulse broadening, increases the transition time, and reduces the edge slope at the detection threshold. Since the RMS timing jitter of a threshold-triggered receiver due to additive voltage noise can be approximated as the voltage-noise RMS divided by the signal slope at the threshold crossing, the reduced slope directly increases the measured timing jitter. Using the measured transition widths as a first-order inverse indicator of edge slope, the increase from 227 ps in the optical B2B case to 318 ps after 40 km SMF corresponds to an approximately 29% normalized slope reduction and an expected jitter increase factor of about 1.4. With DCM, the transition width decreased to approximately 295 ps, corresponding to a partial slope recovery of about 8%, which confirms that dispersion compensation partially restores the pulse transition.

### B. DATA TRANSMISSION

The data transmission measurement results without Gray coding are shown in Fig. 12a, while the results with Gray coding are shown in Fig. 12b. The estimated BER lower limit is $5.86 \times 10^{-7}$ at a 95% confidence level, given the number of bits sent.

As shown in the reported results, in the electrical B2B configuration, zero errors were observed over $5.12 \times 10^6$ bits at $\Delta = 100$ ps, meaning the modulator achieved error-free transmission with and without Gray coding, whereas at $\Delta = 50$ ps slot duration, the Gray code significantly reduced the BER. The optical transmission network significantly degraded the BER, achieving error-free transmission only at $\Delta = 500$ ps for the optical B2B case and at $\Delta = 750$ ps for cases with 40 km SMF.

Considering the existing methodology and testing approaches [17], [18], which focus on high photon efficiency and present the BER as a function of photons per slot, the presented PPM modulator and the transmission network show improved performance in terms of BER and meet the CCSDS 141.0-B-1 requirement [46] of the jitter RMS $\leq$10% of the slot duration at $\Delta \geq 100$ ps, in the electrical B2B configuration, which is the lower than the 125 ps slot duration allowed by the standard and much lower than ones practically used (1 ns). In the optical configurations, improvements were observed at $\Delta \geq 750$ ps slot durations. For all cases, when the BER does not approach the established limit, the 95% confidence interval is less than 6%.

It can be seen that adding a 40 km SMF span slightly degrades performance compared to the optical B2B connection scenario. The impact is not significant, as the system achieves error-free transmission at $\Delta \geq 750$ ps. This degradation is consistent with the observed edge broadening in Fig. 11, where accumulated chromatic dispersion reduced the edge slope and increased jitter, leading to slightly increased BER in this case.

The results obtained with the 40 km SMF and DCM value of $-681$ ps/nm, which nominally compensated the accumulated second-order dispersion at the carrier wavelength, show a slight improvement in BER. The performance did not fully return to the level observed in the optical B2B case due to residual higher-order dispersion and practical device limitations.

### C. INDOOR RANGE MEASUREMENTS

The range measurement errorbox plots for all three optical measurement scenarios are presented in Fig. 13. The mean,

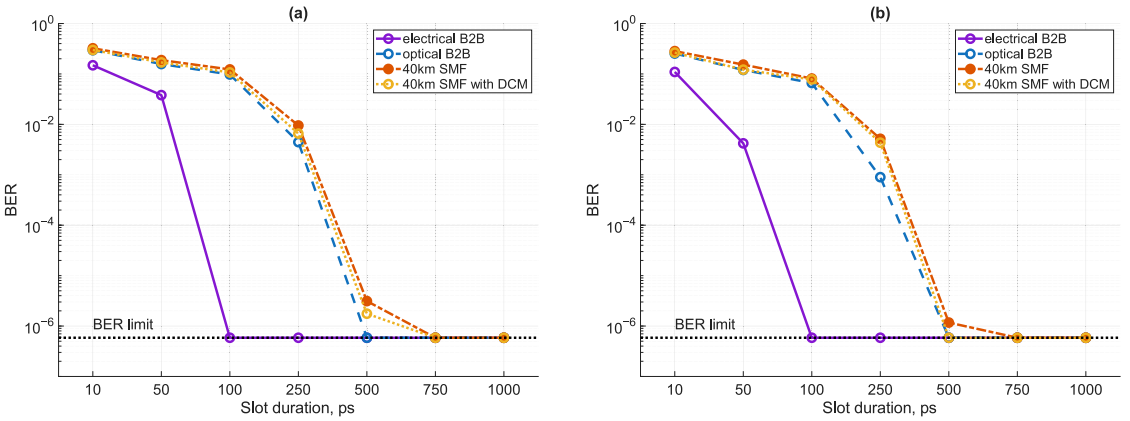



**FIGURE 12.** Measured BER for slot durations 10–1000 ps, (a) without Gray coding, (b) with Gray coding.

**TABLE 2.** Range measurement results.

| Connection | Mean range, m | Absolute deviation, cm | Standard deviation, cm | Interquartile range, cm |
|---|---|---|---|---|
| Optical B2B | 4.0198 | 0.6741 | 0.1803 | 0.2789 |
| 40 km SMF | 4.0189 | 0.8610 | 0.2405 | 0.3657 |
| 40 km SMF with DCM | 4.0188 | 0.6144 | 0.1858 | 0.3330 |

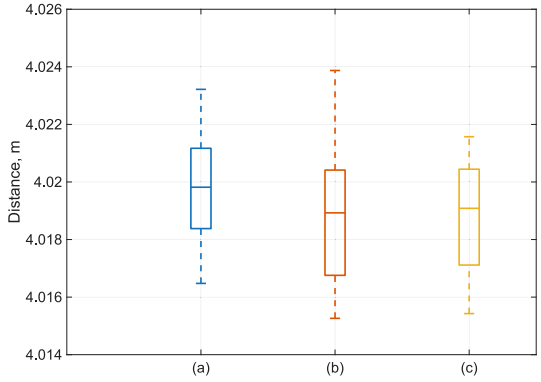



**FIGURE 13.** Measured distance to the target errorboxes for (a) optical B2B connection, (b) connection with 40 km SMF, (c) connection with 40 km SMF and DCM.

absolute deviation, standard deviation, and interquartile ranges for all measurements are presented in Table 2.

In the optical B2B connection, the absolute range deviation was approximately 0.6741 cm. With the addition of a 40 km SMF, the deviation increased slightly to 0.8610 cm, while incorporating the DCM reduced the deviation to 0.6144 cm, but in this case, the interquartile range was larger. The results are consistent with the previously described considerations and show that dispersion compensation can slightly improve the accuracy. The effect of the dispersion in the SMF is slight, at least in the tested distance, and the main factor impacting the range accuracy is the accuracy of the ESTT and the jitter introduced by other hardware (PD, envelope detector, etc.), as we only require the measurement of the relative ToA between the transmitted and received pulses, which is not impacted by the quality of the generated pulse sequence. Conversely, the jitter present in the transmission system degrades measurement accuracy, and it is not possible to achieve ToF measurement accuracy close to the stated RMS accuracy of the ESTT of about 1.5 ps.

The presented architecture shows improved accuracy compared to existing, more complex and costly solutions [52], [53], [54]; On the other hand, newer experimental terahertz systems report sub-micron accuracy [55] using interferometric ToF.

The broader and slightly shallower pulse rising edge, which results from the dispersion in the SMF, impacts the BER and range accuracy measurements as the ESTT triggers at a set threshold voltage; therefore, additive noise in the pulse waveform may cause the triggering event to happen at a time, which is slightly before or after the expected time.

### D. OUTDOOR RANGE AND VELOCITY MEASUREMENTS

The measured distance over a 40 s period, with the target stationary and accelerating away from and towards the RAU, is shown in Fig. 14a. The maximum working range of the presented system under these conditions is approximately 4 m, given the low transmit power and the smooth, curved shape of the target, which leads to significant scattering of the electromagnetic radiation away from the receiving antenna. The velocity estimation results are shown in Fig. 14b.

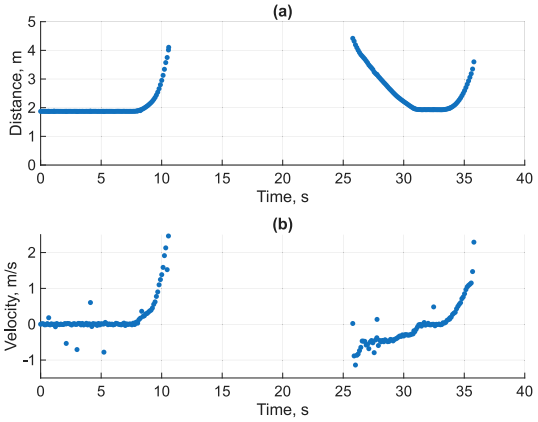



**FIGURE 14.** Results using the ESTT-based architecture with the passenger vehicle as the target, (a) measured distance, (b) interpreted velocity.

The results validate the system's ability to perform highly accurate range measurements in field conditions and to calculate the target's velocity. Notable outliers are observed in the calculated velocity graph because distance measurements are taken 20 ms apart, and even very small inaccuracies in the measured range can lead to significant errors in the calculated velocity. Such outliers are rare, and filtering techniques must be applied to minimize their impact.

## V. CONCLUSION

This research was devoted to the design, implementation, and demonstration of an ARoF-based ISAC-capable pulse radar system, featuring a custom-built PPM modulator and the commercial high-precision time tagger, ESTT, as the demodulator.

The modulator can achieve a jitter RMS of 7.65 ps, while producing up to 16000-symbol-long PPM transfer frames, with the minimum slot duration being 10 ps. The electrical B2B tests demonstrated error-free transmission at a slot duration of 100 ps.

Using the optical transmission network, error-free transmission was achieved at a slot duration of 500 ps, and with an additional 40 km of SMF, at 750 ps. The system outperforms existing solutions in both BER and the minimum usable slot duration, and is ISAC-capable. Gray coding reduced the resulting BER, making it effective for PPM data transmission.

The range measurement accuracy was 0.6741 cm in the optical B2B case and increased slightly to 0.8610 cm in the case with a 40 km SMF. The effect of dispersion compensation was tested and found to reduce the BER and to slightly increase the range accuracy. The improvement is slight and may not justify the added complexity and cost. The range accuracy achieved with the time tagger significantly outperforms that of widely used radar systems, and enables accurate range and velocity estimation with a lower power budget than an FMCW radar, without depending on Doppler-induced frequency shifts. The main limitation of the range resolution, currently 6 m for multi-target scenarios, is the dead time of the TDC. While the pulse duration does not carry information in PPM, reducing it is important for energy efficiency and range resolution in ISAC, given that the TDC dead time is kept low.

The PPM modulator is fully compliant with the CCSDS recommended standard 141.0-B-1 "Optical communications physical layer" [46], which is an important aspect for future works in the field of space communications and sensing. As the modulator's pulse durations can be programmatically controlled, advanced modulation schemes such as PWPM can be implemented. The bit rate can be further improved by optimizing the modulator's software and thereby reducing the break between PPM transfer frames by implementing data buffering and multi-threaded processing of stored data, with only limitation being hardware or processing overhead, at the cost of increased latency between transmitted and received PPM transfer frames. As we move towards longer transfer frames, a solution for synchronizing the transmitter and receiver must be implemented, such as a preamble in the transmitted data, since a shared reference clock generator will not be feasible for long-distance data transmission present in space applications.

Future work will involve designing a time tagger with significantly lower dead time by moving to a multi-channel TDC configuration where incoming pulses are switched between channels. While a channel receives and processes a pulse, with the channel's individual dead time still applying, the next channel in sequence is waiting for the next incoming pulse. This configuration will improve the system's range resolution and enable the use of the proposed architecture alongside other established sensing technologies in a sensor-fusion approach.

## REFERENCES

[1] M. U. F. Qaisar, W. Yuan, O. Günlü, T. Riihonen, Y. Cui, L. Zhang, N. Gonzalez-Prelcic, M. D. Renzo, and Z. Han, "The role of ISAC in 6G networks: Enabling next-generation wireless systems," *IEEE Trans. Netw. Sci. Eng.*, vol. 13, pp. 7825–7861, 2026.

[2] J. Perez Santacruz, "Analog radio-over-fiber for 5G/6G millimeter-wave communications," Ph.D. thesis, Dept. Elect. Eng., Eindhoven University of Technology, Eindhoven University of Technology, The Netherlands, 2022.

[3] G. Singh, A. Srivastava, V. A. Bohara, M. Noor-A-Rahim, Z. Liu, and D. Pesch, "Toward 6G-V2X: Aggregated RF-VLC for ultra-reliable and low-latency autonomous driving," *IEEE Commun. Standards Mag.*, vol. 8, no. 4, pp. 80–87, Dec. 2024.

[4] A. Kaushik, R. Singh, M. Li, H. Luo, S. Dayarathna, R. Senanayake, X. An, R. A. Stirling-Gallacher, W. Shin, and M. Di Renzo, "Integrated sensing and communications for IoT: Synergies with key 6G technology enablers," *IEEE Internet Things Mag.*, vol. 7, no. 5, pp. 136–143, Sep. 2024.

[5] S. P. Campbell, "Integrated sensing and communications (ISAC) report," Office of Research, Innovation, and Economic Impact, George Mason University, George Mason, VA, USA, Tech. Rep., May 2025. [Online]. Available: https://rt.cto.mil/wp-content/uploads/2025/07/ISAC-Report-from-Apr-2025-Workshop.pdf

[6] F. Liu, T. Zhang, Z. Zhang, Y. Shen, and Q. Zhang, "ISAC with UWB: Reliable decoupling and target sensing," *IEEE Trans. Wireless Commun.*, vol. 23, no. 11, pp. 15957–15972, Nov. 2024.

[7] X. Wang, F. Liu, Z. Zhang, and T. Zhang, "Fundamental limits on joint delay and Doppler characterization in UWB ISAC systems," in *Proc. IEEE 98th Veh. Technol. Conf. (VTC-Fall)*, Oct. 2023, pp. 1–6.

[8] S. Cai, L. Chen, Y. Chen, H. Yin, and W. Wang, "Pulse-based ISAC: Data recovery and ranging estimation for multi-path fading channels," *IEEE Trans. Commun.*, vol. 71, no. 8, pp. 4819–4838, Aug. 2023.

[9] M. Yu, M. Shi, W. Hu, and L. Yi, "FPGA-based dual-pulse anti-interference LiDAR system using digital chaotic pulse position modulation," *IEEE Photon. Technol. Lett.*, vol. 33, no. 15, pp. 757–760, Aug. 15, 2021.

[10] J. Yeo, S. Park, Y. Hong, J. Choi, J.-H. Chun, and S.-J. Kim, "A flash LiDAR with SA-based pulse position modulation for multi-user interference cancellation," in *Proc. IEEE Int. Symp. Circuits Syst. (ISCAS)*, May 2025, pp. 1–5.

[11] M. B. Alabd, B. Nuss, L. G. de Oliveira, A. Diewald, Y. Li, and T. Zwick, "Modified pulse position modulation for joint radar communication based on chirp sequence," *IEEE Microw. Wireless Compon. Lett.*, vol. 32, no. 10, pp. 1247–1250, Oct. 2022.

[12] X. Shi, Y. Sun, J. Tian, M. Chen, Y. Liu, N. Xie, and J. Zhang, "BER performance analysis of non-coherent Q-ary pulse position modulation receivers on AWGN channel," *Sensors*, vol. 21, no. 18, p. 6102, Sep. 2021.

[13] M. Pulkkinen, T. Haapala, J. Salomaa, and K. Halonen, "45.2% energy efficiency improvement of UWB IR Tx by use of differential PPM in 180 nm CMOS," in *Proc. IEEE Int. Symp. Circuits Syst. (ISCAS)*, May 2016, pp. 193–196.

[14] H. Hamil, M. S. Azzaz, S. Sakhi, A. Maali, Z. Zidelmal, and D. O. Abdeslam, "Design and FPGA real-time implementation of PWM and PPM modulation for ultra wide band applications," in *Proc. 6th Int. Conf. Image Signal Process. Appl. (ISPA)*, Nov. 2019, pp. 1–5.

[15] M.-J. Kim, T.-J. Lee, N.-Y. Hwang, P. Singh, and S.-Y. Jung, "Performance analysis and implementation of biased MC-PPM for optical energy transfer and communication system," *Phys. Commun.*, vol. 71, Aug. 2025, Art. no. 102684.

[16] Y. Wang, Z. Hao, J. Yu, and H. Li, "Research on PPM modulation performance of deep space optical communication," in *Proc. Int. Conf. Electron. Inf. Eng. Comput. Sci. (EIECS)*, Sep. 2021, pp. 5–8.

[17] W. P. Simon, J. N. Downey, N. C. Lantz, T. P. Bizon, M. A. Marsden, B. E. Vyhnalek, and D. Zeleznikar, "Field-programmable gate array implementation of a single photon-counting receive modem," *Proc. SPIE*, vol. 11180, p. 58, Mar. 2024.

[18] M.-A. Jhaidri, M. Llauro, B. Rouzaud, H. Ivanov, and S. Mejri, "Implementation of high-photon-efficiency optical modem for ESA's technology demonstration of deep-space optical communication with the NASA psyche spacecraft," *Proc. SPIE*, vol. 13699, p. 211, Jul. 2025.

[19] J. Jonass, V. Bespal'ko, and V. Lapkovskis, "Precision time meters for ground and space applications," in *Space-Based LiDAR Remote Sensing Techniques and Emerging Technologies*, U. N. Singh, G. Tzeremes, T. F. Refaat, and P. Ribes Pleguezuelo, Eds., Cham, Switzerland: Springer, 2024, pp. 309–318.

[20] M. A. Steindorfer, P. Wang, F. Koidl, and G. Kirchner, "Space debris and satellite laser ranging combined using a megahertz system," *Nature Commun.*, vol. 16, no. 1, p. 575, Jan. 2025.

[21] M. A. S. Piedra, S. Salata, J. Marín, M. Larrán, A. Blanco, R. Diego, B. Santamaría, M. Larrad, and M. A. Navarro, "First results from the newly modernized san Fernando laser station: Commemorating 45 years of service," in *Proc. 9th European Conf. Space Debris*, vol. 9, Apr. 2025, pp. 1–16.

[22] C. Lim, Y. Tian, C. Ranaweera, T. A. Nirmalathas, E. Wong, and K.-L. Lee, "Evolution of radio-over-fiber technology," *J. Lightw. Technol.*, vol. 37, no. 6, pp. 1647–1656, Mar. 15, 2019.

[23] J. Beas, G. Castanon, I. Aldaya, A. Aragon-Zavala, and G. Campuzano, "Millimeter-wave frequency radio over fiber systems: A survey," *IEEE Commun. Surveys Tuts.*, vol. 15, no. 4, pp. 1–27, 2013.

[24] L. Podbregar, B. Batagelj, A. Blatnik, and A. Lavric, "Advances in and applications of microwave photonics in radar systems: A review," *Photonics*, vol. 12, no. 6, p. 529, May 2025.

[25] K. Nakamura, K. Kawasaki, N. Iwasawa, D. Yamaguchi, K. Takeuchi, N. Shibagaki, Y. Sato, K.-I. Kashima, and M. Takahashi, "Verification of applicability of 90 GHz band millimeter-wave for obstacle detection to railway," *IEEJ Trans. Electr. Electron. Eng.*, vol. 18, no. 6, pp. 960–969, May 2023.

[26] A. Kohmura, S. Futatsumori, N. Yonemoto, and K. Okada, "Optical fiber connected millimeter-wave radar for FOD detection on runway," in *Proc. Eur. Radar Conf.*, Oct. 2013, pp. 41–44.

[27] T. Kawanishi, A. Kanno, N. Yamamoto, N. Yonemoto, N. Shibagaki, and K.-i. Kashima, "Optical fiber network-connected distributed mm-wave radar system," in *Proc. IEEE Photon. Soc. Summer Top. Meeting Ser.*, Jul. 2017, pp. 197–198.

[28] (2026). *ESTT 7 Series*. [Online]. Available: https://eventechsite.com/products/#estt7series

[29] S. Migla, K. Rubuls, N. Tihomorskis, T. Salgals, O. Ozolins, V. Bobrovs, S. Spolitis, and A. Aboltins, "Ultra-wideband analog radio-over-fiber communication system employing pulse-position modulation," *Appl. Sci.*, vol. 15, no. 8, p. 4222, 2025.

[30] A. Srivastav and S. Mandal, "Radars for autonomous driving: A review of deep learning methods and challenges," *IEEE Access*, vol. 11, pp. 97147–97168, 2023.

[31] J. Enayati, P. Asef, and P. Wilson, "Resilient multi-range radar detection system for autonomous vehicles—A new statistical method," *J. Electr. Eng. Technol.*, vol. 19, p. 15, May 2023.

[32] G. Ruiz-Carregal, M. Lort Cuenca, L. Yam, G. Masalias, E. Makhoul, R. Iglesias, A. Heredia, Á. González, G. Centolanza, A. Gili-Zaragoza, A. Faridi, D. Monells, and J. Duro, "Ku-band SAR-drone system and methodology for repeat-pass interferometry," *Remote Sens.*, vol. 16, no. 21, p. 4069, Oct. 2024.

[33] V. Nandana, K. V. Subrahmanyam, V. B. Rao, K. N. Ratna, R. K. Nayak, M. V. Ramana, and G. S. Rao, "Characterization of drop size distribution in urban heavy rainfall event using Doppler weather radar and laser precipitation monitor," *Remote Sens. Earth Syst. Sci.*, vol. 9, no. 1, pp. 1–16, Mar. 2026.

[34] F. Gini, "Grand challenges in radar signal processing," *Frontiers Signal Process.*, vol. 1, Mar. 2021, Art. no. 664232.

[35] F. Yuksekkaya, N. Franchi, and M. Lubke, "On the detection of vulnerable road users—Simulating limits of an FMCW radar," *Electronics*, vol. 13, no. 13, p. 2547, Jun. 2024.

[36] J. P. Santacruz, J. Romme, X. Zhang, E. V. Araujo, M. Dahlem, and R. M. Oldenbeuving, "Analysis and compensation of phase noise in FMCW LiDAR sensors," *J. Lightw. Technol.*, vol. 43, no. 12, pp. 5636–5644, Mar. 17, 2025.

[37] M. Bauduin and A. Bourdoux, "Impact of phase noise on FMCW and PMCW radars," in *Proc. IEEE Radar Conf. (RadarConf23)*, May 2023, pp. 1–6.

[38] P. Tschapek, G. Körner, C. Carlowitz, and M. Vossiek, "Detailed analysis and modeling of phase noise and systematic phase distortions in FMCW radar systems," *IEEE J. Microw.*, vol. 2, no. 4, pp. 648–659, Oct. 2022.

[39] F. Liu, L. Zheng, Y. Cui, C. Masouros, A. P. Petropulu, H. Griffiths, and Y. C. Eldar, "Seventy years of radar and communications: The road from separation to integration," *IEEE Signal Process. Mag.*, vol. 40, no. 5, pp. 106–121, Jul. 2023.

[40] (2025). *Super High FrequenCY (SHF) Communication Market Report, Industry and Market Size & Revenue, Share, Forecast 2024–2030*. [Online]. Available: https://www.strategicmarketresearch.com/market-report/super-high-frequency-communication-market

[41] *Optical Communications Coding and Synchronization*, Standard CCSDS 142.0-B-1, Consultative Committee for Space Data Systems, Washington, DC, USA, Aug. 2019. [Online]. Available: https://ccsds.org/Pubs/142x0b1.pdf

[42] S. Migla, O. Selis, P. E. Sics, and A. Aboltins, "Error analysis and correction techniques for PPM communication links with jitter and clock drift," in *Proc. IEEE Int. Conf. Microw., Commun., Antennas, Biomed. Eng. Electron. Syst. (COMCAS)*, Jul. 2024, pp. 1–4.

[43] O. Selis, S. Migla, P. E. Sics, M. Zeltins, S. Spolitis, and A. Aboltins, "Demonstration of 50 ps per-position differential pulse position modulation data transmission," in *Proc. IEEE 10th Jubilee Workshop Adv. Inf., Electron. Electr. Eng. (AIEEE)*, Apr. 2023, pp. 1–4.

[44] P. E. Sics, O. Selis, S. Migla, M. Zeltins, S. Spolitis, V. Kurtenoks, and A. Aboltins, "Programmable delay line based high-speed PPM modulator with 50 ps time resolution," in *Proc. Photon. Electromagn. Res. Symp. (PIERS)*, Jul. 2023, pp. 1779–1786.

[45] P. E. Sics, N. Tihomorskis, S. Migla, J. Ratners, V. Kurtenoks, and A. Aboltins, "Implementation of reconfigurable 149Mbps TDC-based PPM transceiver," in *Proc. Joint Eur. Conf. Netw. Commun. 6G Summit (EuCNC/6G Summit)*, Jun. 2024, pp. 706–710.

[46] *Optical Communications Physical Layer*, Standard CCSDS 141.0-B-1, Consultative Committee for Space Data Systems, Washington, DC, USA, Aug. 2019. [Online]. Available: https://ccsds.org/Pubs/141x0b1.pdf

[47] D. Rieländer, A. Di Mira, D. Alaluf, R. Daddato, S. Mejri, J. Piris, J. Alves, D. Antsos, A. Biswas, N. Karafolas, K.-J. Schulz, and C. Heese, "ESA ground infrastructure for the NASA/JPL PSYCHE deep-space optical communication demonstration," *Proc. SPIE*, vol. 12777, Jul. 2023, Art. no. 127770E.

[48] F. I. Khatri, D. O. Caplan, M. E. Grein, C. E. DeVoe, J. Torres, S. Constantine, B. S. Robinson, D. V. Murphy, R. T. Schulein, N. M. Desch, M. Bay, S. J. Horowitz, M. W. Wright, J. M. Kovalik, and A. Biswas, "Space-to-ground optical interface verification for the orion Artemis II optical (O2O) communications demonstration," in *Proc. IEEE Int. Conf. Space Opt. Syst. Appl. (ICSOS)*, Oct. 2023, pp. 26–30.

[49] E. N. Fokoua, M. N. Petrovich, T. Bradley, F. Poletti, D. J. Richardson, and R. Slavík, "How to make the propagation time through an optical fiber fully insensitive to temperature variations," *Optica*, vol. 4, no. 6, pp. 659–668, Jun. 2017.

[50] R. Slavík, G. Marra, E. N. Fokoua, N. Baddela, N. V. Wheeler, M. Petrovich, F. Poletti, and D. J. Richardson, "Ultralow thermal sensitivity of phase and propagation delay in hollow core optical fibres," *Sci. Rep.*, vol. 5, no. 1, p. 15447, Oct. 2015.

[51] M. Khudiakov, K. Zarekarizi, R. Safaei, S. Papernyi, W. R. L. Clements, and F. Légaré, "Optimization of the pulse position modulation high-power compact laser source," *Proc. SPIE*, vol. 13699, pp. 2630–2637, Jul. 2025.

[52] P. Chen, J. Song, Y. Bai, J. Wang, Y. Du, and L. Tian, "Range-velocity measurement accuracy improvement based on joint spatiotemporal characteristics of multi-input multi-output radar," *Remote Sens.*, vol. 16, no. 14, p. 2648, Jul. 2024.

[53] L. Jacobs, P. Veelaert, H. Steendam, and W. Philips, "On the accuracy of automotive radar tracking," in *Proc. IEEE 97th Veh. Technol. Conf.*, Jun. 2023, pp. 1–6.

[54] P. Singh, S. Menkudale, S. Soni, V. R. Tank, and A. A. B. Raj, "Comprehensive survey on radar systems and its target classification techniques," *J. Electron. Electr. Eng.*, vol. 2025, pp. 234–269, Feb. 2025.

[55] P.-A. Blanche, M. Neifeld, M. Tuo, H. Xin, and N. Peyghambarian, "A 300 THz tabletop radar range system with sub-micron distance accuracy," *Sci. Rep.*, vol. 8, no. 1, p. 14443, Sep. 2018.



**SANDIS MIGLA** (Graduate Student Member, IEEE) received the B.S. degree in engineering science in electrical science and the M.S. degree in electronics from Riga Technical University, Riga, in 2021 and 2023, respectively. He is currently pursuing the Ph.D. degree in engineering and technology. From 2020 to 2023, he was a Research Assistant with the Institute of Microwave Engineering and Electronics, Riga Technical University, and since 2023, he has been a Researcher. His research interests include ultra-wideband communication systems, integrated communications and sensing, space communications, and radar systems.



**NIKOLAJS TIHOMORSKIS** (Graduate Student Member, IEEE) received the bachelor's degree in computer control and computer science and the master's degree in electronics from Riga Technical University, Riga, Latvia, in 2021 and 2023, respectively. He is currently pursuing the Ph.D. degree in engineering and technology. He is a Researcher at the Institute of Photonics, Electronics and Telecommunications (IPET), Riga Technical University. His research interests include software-defined radio (SDR), wireless communications, and OTFS.



**KRISTAPS RUBULS** received the B.S. degree in electrical science and the M.S. degree in telecommunications from Riga Technical University (RTU), Riga, in 2021 and 2023, respectively, where he is currently pursuing the Ph.D. degree in telecommunications. He is a Researcher at RTU, affiliated with the Faculty of Computer Science, Information Technology and Energy, within the Institute of Photonics, Electronics, and Telecommunications. His research focuses on advanced wireless and optical communication technologies, including radio-over-fiber (RoF), MIMO systems, mobile networks, optical fiber communications, and silicon photonics.



**DARJA CIRJULINA** (Graduate Student Member, IEEE) received the Academic bachelor's degree in electrical engineering and the Professional master's degree in electronics from Riga Technical University (RTU), in 2020 and 2022, respectively. She is currently pursuing the Ph.D. degree in electronics, information and communication technologies. She received the qualification of a Lead Electronics Engineer from RTU. Since March 2019, she has been at RTU as a Researcher at the Institute of Photonics, Electronics and Telecommunications. Her research interests focus on chaos-based data transmission systems for IoT applications, as well as photonics, particularly high-speed IM/DD transmission systems.



**INTS MURANS** received the B.S. and M.S. degrees in telecommunications from Riga Technical University (RTU), Riga, Latvia, in 2021 and 2023, respectively, where he is currently pursuing the Ph.D. degree in telecommunications. He is a Researcher at the Institute of Photonics, Electronics and Telecommunications, Faculty of Computer Science, Information Technology and Energy (FCSITE), RTU. His research interests include optical communications, radio-over-fiber, and nanophotonics.



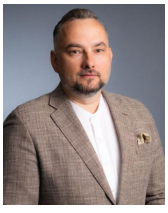
**VIKTORS KURTENOKS** received the M.S. degree in computer engineering from the University of Latvia, in 1992. He is the Chief Technical Officer with Eventech Ltd. His research interests include assembly languages, analog, digital, and mixed signal devices, networking devices, and embedded solutions.



**JANIS BRAUNFELDS** received the Industrial Ph.D. degree (Latvia) in telecommunication engineering from Riga Technical University. His Industrial Ph.D. thesis is devoted to FBG sensors and their integration into infrastructure's SHM. He is an Associate Professor and a Leading Researcher at RTU IPET. His main research interests are FBG sensors, fiber optical distributed sensors, sensor networks, passive optical networks, road pavements, and concrete SHM.



**SANDIS SPOLITIS** is a Leading (Senior) Researcher and a Professor at the Institute of Photonics, Electronics and Telecommunications, Faculty of Computer Science, Information Technology and Energy (FCSITE), Riga Technical University (RTU), Riga, Latvia. He currently holds the position of vice-dean for research at RTU FCSITE. His primary research focus encompasses the development and investigation of fiber-optic communication systems, optical interconnects, radio-over-fiber technologies, 5G/6G (THz) systems, passive optical network technologies, digital signal processing, nonlinear optics, optical frequency combs, optical amplifiers, and system modeling.



**OSKARS OZOLINS** (Senior Member, IEEE) received the Dr.sc.-Ing. degree in optical communications from Riga Technical University (RTU), Latvia, in 2013, and the Habilitation degree from the KTH Royal Institute of Technology, Sweden, in 2021. He is a full member (Academician) of Latvian Academy of Sciences and a Tenured Full Professor at RTU. He is a co-holder of eleven world records reported at the top conference post-deadline sessions. He is the author of around 300 international journal publications (including two Nature Communications articles), conference contributions, invited talks (more than 70), patents (more than 10), and book chapters. He was a TPC Member of ECOC 2022, 2024–2026, and OFC 2023–2025.



**DMYTRO VOVCHUK** (Member, IEEE) received the B.Sc. and M.Sc. degrees from Yuriy Fedkovych Chernivtsi National University, Chernivtsi, Ukraine, in 2012 and 2013, respectively, and the Ph.D. degree in electrical engineering. His current research interests include radars, superscattering and superdirectivity, micro-Doppler, and deterministic chaos for communication systems.



**TOMS SALGALS** is currently an Associate Professor with the Institute of Photonics, Electronics and Telecommunications (IPET), Faculty of Computer Science, Information Technology and Energy (FCSITE), Riga Technical University. He is also an Expert in high-speed fiber-optic systems, optical frequency combs (OFCs), integrated photonics, micro-/nano-photonics, and microwave photonics.



**PAVEL GINZBURG** (Member, IEEE) received the Ph.D. degree from Technion, Haifa, Israel, in 2011. He is currently an Associate Professor with Tel Aviv University, Tel Aviv-Yafo, Israel. He is also a former EPSRC Research Fellow, an International Newton Research Fellow, and a Rothschild Fellow with King's College London, London, U.K., and the Head of the "Dynamics of Nanostructures" Laboratory, Encompassing Theoretical Group, Optical Spectroscopy, and Radio Waves Laboratories. The laboratory runs multidisciplinary research in the fields of biophotonics, quantum mechanics, nanoplasmonics and metamaterials, and radio physics.



**VJACESLAVS BOBROVS** (Member, IEEE) received the M.Sc. degree in telecommunications and the Dr.sc.-Ing. degree in electronics and telecommunications from Riga Technical University, Riga, Latvia, in 2005 and 2010, respectively. He is currently a Professor and the Director of the Institute of Photonics, Electronics and Telecommunications; and a member of the RTU Science Council. He is also engaged at Latvian Council of Science, as an Expert in the area of engineering and computer science, sub-area electronics and telecommunications. He is the co-author of more than 350 articles in international journals and conferences. His research interests include nonlinear optics, photonics, fiber optical metro and access networks, radio-over-fiber technologies, digital signal processing, 5G, and beyond.



**ARTURS ABOLTINS** (Senior Member, IEEE) received the M.Sc. degree in telecommunications from Riga Technical University, in 1998. In 2013, he defended a Doctoral thesis, "Synchronization and equalization for multicarrier systems with parametric modulation based on generalized unitary rotation." From 1995 to 2004, he was a Telecommunications Engineer for the local telecom operator Lattelecom. From 2004 to 2008, he was a software developer for several international companies. Since 2023, he has been a Full Professor at Riga Technical University, and he is working on research projects in the field of signal processing for communications. Since 2021, he has been supervising and consulting on several projects focused on optical high-photon-efficiency communications for space and ground applications. He received the Best Student Paper in Physics and Mathematics Award from Latvian Academy of Sciences, in 1996.



**Sandis Migla** was born in 1999 in Riga. He earned a Bachelor's degree in Electrical Science (2021) and a Master's degree in Electronics and the Qualification of Lead Electronics Engineer (2023) from Riga Technical University. Since 2020, he has worked at Riga Technical University, currently holding the positions of researcher and lecturer. His research interests include integrated sensing and communications, space communications, and radar systems.